Searching for Reactor Antineutrino Flavor Oscillations with the Double Chooz Far Detector

Arthur James Franke

Submitted in partial fulfillment of the
requirements for the degree of
Doctor of Philosophy
in the Graduate School of Arts and Sciences

COLUMBIA UNIVERSITY

2013

ABSTRACT

Searching for Reactor Antineutrino Flavor Oscillations with the Double Chooz Far Detector

Arthur James Franke

This dissertation presents results from a search for reactor $\bar{\nu}_e$ flavor oscillations using the Double Chooz Far Detector. The search was performed by observing the rate and energy spectrum of $\bar{\nu}_e$ interacting via Inverse Beta Decay in a Gd-doped liquid scintillator detector, and comparing the observation to an expectation based on a prediction of the emitted reactor flux. The Columbia University neutrino group was instrumental in construction of the Double Chooz Outer Veto, as well as the analysis efforts leading to two oscillation measurement results. The most recent analysis is presented herein, focusing on 251.27 days of data (or 33.71 GW-ton-years of exposure). In these data, 8249 IBD candidates were observed, compared to a signal+background prediction of 8936.8. A fit to a two-neutrino oscillation model considering event rate, spectral shape, and time yields a best-fit value of $\sin^2(2\theta_{13}) = 0.109 \pm 0.030$ (stat.) ± 0.025 (syst.) at $\Delta m^2_{31} = 2.32 \times 10^{-3}$ eV^2, with χ^2_{RS}/d.o.f. $= 42.1/35$. A frequentist method deems the null-oscillation hypothesis excluded by the data at 99.8% C.L., or 2.9σ. These results are in agreement with the measurements of other modern reactor $\bar{\nu}_e$ experiments.

Table of Contents

List of Figures

List of Tables

Chapter 1

Introduction

Neutrinos are perhaps some of the most perplexing particles to have ever been discovered: they were theorized out of desperation, their discovery was elusive, and subsequent studies of them have provided abounding anomalies and tension. But with each anomaly has often come a resolution which pushes the Standard Model of particle physics towards its first necessary extensions. The most important such discovery was the observation of neutrino flavor oscillations.

The flavor oscillation phenomenon manifests as a time-varying probability that the neutrino will interact with other particles via a different weak eigenstate than the one which created it. If the neutrinos are propagating through space, the time-varying oscillatory behavior is easily rephrased as oscillations in distance and can be measured by placing a detector some distance from the neutrino source. These oscillations have been well-measured in neutrinos from the sun, from cosmic ray interactions, and from neutrinos produced by beams of accelerated particles. One critical parameter of the neutrino mixing model has thus far not been positively measured: θ_{13}, often phrased as the oscillation mixing amplitude $\sin^2(2\theta_{13})$. If measured to be nonzero, $\sin^2(2\theta_{13})$ would open the door to measurements of CP-violation in the neutrino sector.

This dissertation will describe how the Double Chooz experiment has searched for $\bar{\nu}_e \rightarrow \bar{\nu}_X$ flavor oscillations using a liquid scintillator detector placed at an average distance $L = 1050$ meters from two nuclear reactor cores. Emphasis will be placed on the statistical methods used to measure the oscillation amplitude $\sin^2(2\theta_{13})$ and establish con-

fidence intervals on it.

The dissertation is divided into four parts.

Part I will frame the measurement reviewing the theory and current experimental state of neutrino flavor oscillations. Chapter 2 will review how neutrinos fit into the Standard Model of particle physics, and develop the oscillation probability formulas relevant to measurements of θ_{13}. Chapter 3 will recap the experimental evidence for neutrino flavor oscillations, and summarize the modern techniques used by physicists to measure θ_{13}.

Part II will describe the Double Chooz experiment and how it is designed to measure θ_{13} to a better precision than previous reactor-based experiments. Chapter 4 describes the detector hardware and operation in detail, providing the basis for how $\bar{\nu}_e$ from the Chooz reactors are detected and their energies reconstructed. Chapter 5 will describe the Double Chooz Outer Veto, which was the Columbia University group's principal hardware contribution to the experiment.

Part III describes the statistical and analytical methods used to turn data from the Double Chooz Far Detector into a measurement of $\sin^2(2\theta_{13})$ with some uncertainty. Chapter 6 describes in detail the mathematical methods for predicting the number of $\bar{\nu}_e$ signal events observed in the detector, and evaluating the uncertainty on that prediction. Chapter 7 comprehensively describes the second, improved Double Chooz oscillation analysis and its measurement of $\sin^2(2\theta_{13})$. Closely related to this chapter is Appendix A, which describes in some detail the first analysis for the purposes of comparison.

Part IV concludes the dissertation by placing Double Chooz's measurements in the context of the state of the field. Chapter 8 recounts the chronology of events from when Double Chooz began taking data with its Far Detector in April 2011 and θ_{13} was still unknown, to the summer of 2012 when θ_{13} had become the most precisely-measured of all neutrino mixing angles. Chapter 9 summarizes what has been presented in this document.

Finally, a number of appendices provide in-depth detail into some aspects of the author's contribution to Double Chooz.

Double Chooz has performed a search for neutrino flavor oscillations in $\bar{\nu}_e$ from a nuclear reactor. The measurement was performed by observing the rate and energy spectrum of $\bar{\nu}_e$ interacting via Inverse Beta Decay in a Gd-doped liquid scintillator detector, and

comparing the observation to an expectation based on a prediction of the emitted reactor flux. With 251.27 days of data (or 33.71 GW-ton-years of exposure) a total of 8249 IBD candidates were observed, compared to a signal+background prediction of 8936.8. A fit to the $\sin^2(2\theta_{13})$-driven oscillation model was performed where IBD event rate, spectral shape, and time, were all accounted for in the goodness-of-fit statistic. The result is a best-fit value of $\sin^2(2\theta_{13}) = 0.109 \pm 0.030$ (stat.) ± 0.025 (syst.) at $\Delta m^2_{31} = 2.32 \times 10^{-3}$ eV^2, with χ^2_{RS}/d.o.f. $= 42.1/35$. Using a frequentist method, the null-oscillation hypothesis is excluded at 99.8% C.L., or 2.9σ. These results are in agreement with the measurements of other modern reactor $\bar{\nu}_e$ experiments. Double Chooz has nearly provided evidence for a nonzero θ_{13}.

Part I

Neutrino Oscillations & Experimental Searches

Chapter 2

Neutrino Flavor Oscillations

2.1 Neutrinos in the Standard Model of Particle Physics

While first proposed by W. Pauli as an energy conservation stop-gap in 1930, neutrinos did not become part of a mature theory of weak interactions until Fermi's work of 1934 [23]. It was then nearly 25 years until the first experimental evidence of neutrinos was observed in 1956 by the Reines and Cowan experiments [24], detecting $\bar{\nu}_e$ from a nuclear reactor. It would be a further few decades before the remaining two known types of neutrinos were discovered: the ν_μ in 1962 [25], and the ν_τ in 2001 [26]. Soon after the initial discovery, it was observed that neutrinos have predominantly left-handed helicity [27]. Neutrino scattering experiments in the late 1970's would confirm the $V - A$ nature of neutrino interactions [28, 29, 30]. Neutrino deep-inelastic scattering experiments around the same time also led to the discovery of neutral-current interactions [31, 32]. The combination of all this evidence has led to neutrinos included as a precisely-measured component of the Glashow-Weinberg-Salam model of electroweak interactions [33, 34, 35]. Combined with the quantum chromodynamics (QCD) theory of strong interactions [1], this is now known as the Standard Model of Particle Physics.

In the Standard Model, each of the three weak interaction neutrino flavors ν_i $(i = e,\ \mu,\ \tau)$ is one component of an $SU(2)_L$ fermionic doublet $\Psi_i = \begin{pmatrix} l_i^- \\ \nu_i \end{pmatrix}$, along with its charged

[1] See the review of Bethke *et. al.* in Section 9 of [36].

lepton partner l_i^-. This doublet is part of the ith fermion family, along with the left-handed quark fields of the same family. Following [36], the Standard Model Lagrangian for the fermion fields ψ_i is written down after gauge symmetry breaking (omitting strong interaction terms):

$$\begin{aligned} L_F &= \sum_{i=1}^{3} \bar{\psi}_i \left(i\partial\!\!\!/ - m_i - \frac{g m_i H}{2M_W} \right) \psi_i \\ &\quad - \frac{g}{2\sqrt{2}} \sum_{i=1}^{3} \bar{\Psi}_i \gamma^\mu \left(1-\gamma^5\right) \left(T^+ W_\mu^+ + T^- W_\mu^- \right) \Psi_i \\ &\quad - e \sum_{i=1}^{3} \bar{\psi}_i \gamma^\mu \psi_i A_\mu \\ &\quad - \frac{g}{2\cos\theta_W} \sum_{i=1}^{3} \bar{\psi}_i \gamma^\mu \left(g_V^i - g_A^i \gamma^5 \right) \psi_i Z_\mu. \end{aligned} \tag{2.1}$$

$$\tag{2.2}$$

The many components of this equation include: fermion mass parameters m_i; gauge coupling constants g and g'; the Weinberg angle $\theta_W = \tan^{-1}(g'/g)$; the positron charge $e = g\sin\theta_W$; the mass of the W boson $M_W = \frac{1}{2}gv$. The constant $v \approx 246.22$ GeV is related to breaking of electroweak symmetry by the Higgs mechanism [37]. Bosonic fields in Eq. 2.2 include: the gauge boson fields $W^i \sim (i = 1, 2, 3)$ and B^μ; the photon field $A = B\cos\theta_W + W^3 \sin\theta_W$; the charged weak bosons $W^\pm = (W^1 \mp iW^2)/\sqrt{2}$; and the weak neutral boson $Z = -B\sin\theta_W + W^3\cos\theta_W$. Two more couplings are the vector $g_V^i = t_{3L}(i) - 2q_i \sin^2\theta_W$ and axial-vector $g_A^i = t_{3L}(i)$, each of which depend on the weak isospin $t_{3L}(i)$ and charge q_i of fermion i. Finally, T^+ and T^- are the weak isospin raising and lowering operators. Detailed discussion of some components of this Lagrangian, such as the Higgs mechanism, renormalization, and symmetry breaking, are well-covered elsewhere; good references may be found in [36].

Massless neutrinos couple only to the weak interactions, thus the second and fourth terms of Eq. 2.2 are most relevant, describing charged-current and neutral-current weak interactions, respectively. It is worthwhile to note that at momenta small compared to M_W, the second term effectively behaves like the four-fermion interaction first described in [23]. In staying consistent with the ν_i having exclusively left-handed helicity, the neutrino masses are set to be zero in this Lagrangian.

2.2 Neutrino Flavor Mixing

Following a large accumulation of evidence (reviewed in Chapter 3), it is now well-accepted that neutrinos exhibit flavor oscillations as they propagate through space, which implies that at least two of the three known neutrinos have nonzero masses. In the following sections, we review the underlying mathematics behind flavor mixing, and derive formulas for the flavor oscillation probabilities relevant to measuring $\sin^2(2\theta_{13})$.

2.2.1 The PMNS Neutrino Mixing Matrix

The underlying theory describing neutrino mixing was first predicted by Maki, Nakagawa, and Sakata [38], and independently by Pontecorvo [39]. In this model, the weakly-interacting lepton flavor eigenstates of neutrinos ν_e, ν_μ, and ν_τ are each superpositions of three neutrino mass eigenstates ν_1, ν_2, and ν_3. The two bases are related by a unitary mixing matrix U, often called the "PMNS matrix" after its creators:

$$|\nu_\alpha\rangle = \sum_i U^*_{\alpha i} |\nu_i\rangle \tag{2.3}$$

where Greek indices denote the interaction basis (*i.e.* $W^+ \to \ell^+_\alpha + \nu_\alpha$) and Latin indices the mass basis, following the conventions of [36].

The true nature of neutrino masses, or whether neutrinos are Dirac or Majorana fermions, has subtle effects on the form of U. If the neutrinos are Majorana particles, each pair of mass eigenstates has between them one mixing angle θ_{ij} and one CP-violating phase ϕ_{ij} [40], similar to how CP violation arises in the quark sector [41]. Following [42], mixings may then be thought of as effectively 2×2 unitary operations ω_{ij} with 3×3 forms tailored to act on the relevant eigenstates, *e.g.* for the mixing between eigenstates 1 and 3:

$$\omega_{13} = \begin{pmatrix} \cos\theta_{13} & 0 & e^{i\phi_{13}}\sin\theta_{13} \\ 0 & 1 & 0 \\ -e^{-i\phi_{13}}\sin\theta_{13} & 0 & \cos\theta_{13} \end{pmatrix} \tag{2.4}$$

The three-neutrino mixing matrix can then be described as the product of the three ω_{ij} matrices. While this formalism is extensible to larger numbers of neutrinos, measurements of $Z \to \nu_\alpha \bar{\nu}_\alpha$ contributions to the Z decay width by experiments at LEP support only 3

active neutrinos [43]. It may be possible to have "sterile" neutrinos which do not couple to the Z, nor have leptonic partners, and interact only by oscillation processes [36]. However, for the sake of simplicity, these calculations will focus only on the 3 active neutrino case. The full matrix U is thus given by the product:

$$\begin{aligned} U &= \omega_{23}\omega_{13}\omega_{12} \qquad (2.5)\\ &= \begin{pmatrix} c_{12}c_{13} & s_{12}c_{13}e^{i\phi_{12}} & s_{13}e^{i\phi_{13}} \\ -s_{12}c_{23}e^{-i\phi_{12}} - c_{12}s_{13}s_{23}e^{i(\phi_{23}-\phi_{13})} & c_{12}c_{23} - s_{12}s_{13}s_{23}e^{i(\phi_{12}+\phi_{23}-\phi_{13})} & c_{13}s_{23}e^{i\phi_{23}} \\ s_{12}s_{23}e^{-i(\phi_{12}+\phi_{23})} - c_{12}s_{13}c_{23}e^{-i\phi_{13}} & -c_{12}s_{23}e^{-i\phi_{23}} - s_{12}s_{13}c_{23}e^{i(\phi_{12}-\phi_{13})} & c_{13}c_{23} \end{pmatrix} \end{aligned}$$

using the shorthand notation $c_{ij} = \cos\theta_{ij}$ and $s_{ij} = \sin\theta_{ij}$. While all three CP-violating phases have physical effects [42, 44], two of the phases are only relevant in processes involving neutrinoless double beta decay. It is then convention [36] in discussing oscillations to define $\delta_{CP} \equiv \phi_{12} + \phi_{23} - \phi_{13}$ and to set $\phi_{12} = \phi_{23} = 0$. The mixing matrix then takes the form:

$$U = \begin{pmatrix} c_{12}c_{13} & s_{12}c_{13} & s_{13}e^{-i\delta_{CP}} \\ -s_{12}c_{23} - c_{12}s_{13}s_{23}e^{i\delta_{CP}} & c_{12}c_{23} - s_{12}s_{13}s_{23}e^{i\delta_{CP}} & c_{13}s_{23} \\ s_{12}s_{23} - c_{12}s_{13}c_{23}e^{i\delta_{CP}} & -c_{12}s_{23} - s_{12}s_{13}c_{23}e^{i\delta_{CP}} & c_{13}c_{23} \end{pmatrix}. \qquad (2.6)$$

In this form, the lepton mixing matrix is equivalent to the quark mixing matrix, as first proposed in [38] and [39].

If neutrinos are Dirac fermions, a set of three flavor eigenstates has only one phase degree of freedom [40]. The mixing matrix U then automatically takes the form of Eq. 2.6. However, if any component of the neutrino masses take a Majorana form, a mixing matrix with three CP-violating phases as in Eq. 2.5 is necessary. Nevertheless, the extra phases have no effects on neutrino oscillations, so our choice to eliminate them stands valid.

2.2.2 Oscillation Probability Formulas

From the mixing matrix given in Eq. 2.6, it is straight-forward to calculate the probability for neutrino flavor oscillation due to mixing amplitudes related to θ_{13}. As discussed later in Section 3.2, the most relevant processes to measuring θ_{13} are $\bar{\nu}_e \to \bar{\nu}_e$ survival and $\nu_\mu \to \nu_e$ appearance.

For any process, the creation and detection of neutrinos is described in terms of the weak interaction eigenstates, while the propagation of neutrinos from creation point to detector

is described by the mass eigenstates and their Hamiltonians. So, for any process we must calculate the amplitude:

$$A\left(\nu_\alpha \to \nu_\beta\right) = \langle \nu_\beta | \nu_\alpha \rangle = \sum_i U^*_{\alpha i} e^{iH_i\tau_i} U_{i\beta} \tag{2.7}$$

For the survival case, $\alpha = \beta$, while for the appearance case $\alpha \neq \beta$. For the time being, H_i is the Hamiltonian for the mass eigenstate $|\nu_i\rangle$ propagating in vacuum. In calculating the probability for an oscillation process $P\left(\nu_\alpha \to \nu_\beta\right) = \left|A\left(\nu_\alpha \to \nu_\beta\right)\right|^2$ oscillating terms will survive only as phases proportional to differences between the mass eigenstate Hamiltonians $\eta_{ij} = H_i\tau_i - H_j\tau_j$ with $i \neq j$. Following [36], $H_i\tau_i = m_i\tau_i$ in the neutrino rest frame, or by Lorentz invariance $m_i\tau_i = E_i t - p_i L$ where E_i and p_i are the neutrino energy and momentum, and L and t are the distance and time in the lab frame traversed by the neutrino as it propagates from source to detector. Applying an approximation first shown in [45], $t \approx L\left(E_i + E_j\right) / \left(p_i + p_j\right)$, and approximating $E_i \approx p_i$ for highly-relativistic neutrinos, the phase differences become:

$$\eta_{ij} = \left(m_j^2 - m_i^2\right) \frac{L}{2E}. \tag{2.8}$$

The probability for flavor oscillation is then:

$$\begin{aligned} P\left(\nu_\alpha \to \nu_\beta\right) = \delta_{\alpha\beta} &- 4 \sum_{i \neq j} \mathrm{Re}\left(U^*_{\alpha i} U_{\beta i} U_{\alpha j} U^*_{\beta j}\right) \sin^2\left(\frac{1.27 \Delta m^2_{ij} L}{E}\right) \\ &+ 2 \sum_{i \neq j} \mathrm{Im}\left(U^*_{\alpha i} U_{\beta i} U_{\alpha j} U^*_{\beta j}\right) \sin\left(\frac{2.54 \Delta m^2_{ij} L}{E}\right) \end{aligned} \tag{2.9}$$

where $\Delta m^2_{ij} \equiv m^2_i - m^2_j$ is the mass-squared splitting in units of eV^2, E is the neutrino energy in GeV, and L is in km. All factors of c and $\hbar$ have been absorbed into the constants 1.27 and 2.54 in the oscillation terms. A cartoon of the flavor mixing parametrized in terms of the Δm^2_{ij} and mixing angles is shown in Figure 2.1.

Equation 2.9 may now be applied to the processes relevant to measuring θ_{13}. The disappearance process $\bar{\nu}_e \to \bar{\nu}_X$ used by reactor-based experiments is explained in Sec. 2.2.2.1, and the $\nu_\mu \to \nu_e$ appearance process used by accelerator-based experiments is explained in Sec. 2.2.2.2.

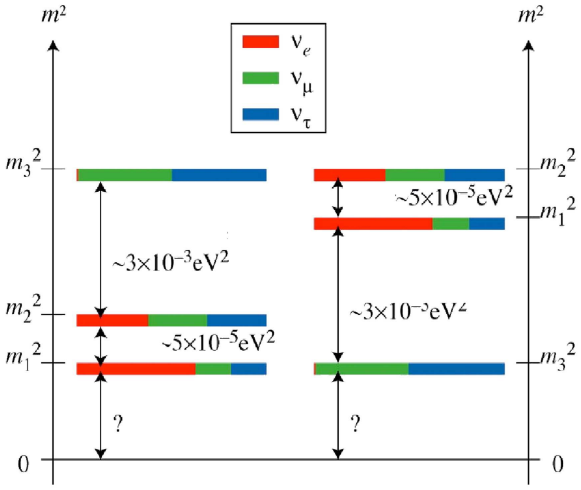

Figure 2.1: Illustration of the neutrino mass eigenstates as superpositions of the flavor eigenstates (colored regions). Mass-squared splittings shown are approximately those as observed by experiment (see Chapter 3). The ordering of the masses, or "mass hierarchy", is still undetermined: left-hand scenario is the "Normal Hierarchy", and right-hand scenario is the "Inverted Hierarchy". Figure from [1].

2.2.2.1 $\bar{\nu}_e \to \bar{\nu}_X$ Disappearance

While Eq. 2.9 was explicitly formulated for neutrinos, assuming CPT invariance allows consideration of the antineutrino case simply by taking $U \to U^*$. This implies $P(\nu_\alpha \to \nu_\beta) = P(\bar{\nu}_\alpha \to \bar{\nu}_\beta)$. For the $\bar{\nu}_e$ survival channel,

$$P(\bar{\nu}_e \to \bar{\nu}_e) = 1 - c_{13}^4 \sin^2 2\theta_{12} \sin^2\left(\frac{1.27\Delta m_{12}^2 L}{E}\right) - c_{12}^2 \sin^2 2\theta_{13} \sin^2\left(\frac{1.27\Delta m_{13}^2 L}{E}\right) - s_{12}^2 \sin^2 2\theta_{13} \sin^2\left(\frac{1.27\Delta m_{23}^2 L}{E}\right). \quad (2.10)$$

In practice, experiments seek to measure a deficit of events due to neutrinos oscillating to other flavors. The measured quantity is then the disappearance probability $P_{dis}(\bar{\nu}_e \to \bar{\nu}_X) = 1 - P(\bar{\nu}_e \to \bar{\nu}_e)$. As discussed later in Section 3.1, θ_{13} is less than 10°, so P_{dis} is often simplified:

$$P_{dis}(\bar{\nu}_e \to \bar{\nu}_X) \approx \sin^2 2\theta_{12} \sin^2\left(\frac{1.27\Delta m_{12}^2 L}{E}\right) + c_{12}^2 \sin^2 2\theta_{13} \sin^2\left(\frac{1.27\Delta m_{31}^2 L}{E}\right) + s_{12}^2 \sin^2 2\theta_{13} \sin^2\left(\frac{1.27\Delta m_{23}^2 L}{E}\right). \quad (2.11)$$

For the case of reactor $\bar{\nu}_e$ experiments at the $L \sim 1$ km baseline of Double Chooz, the equation can be further simplified in two ways. The first term may be dropped, as $\Delta m^2_{12} L/E << 1$ at this baseline. This leaves the latter two terms to be combined, using the approximation $|\Delta m^2_{31}| \approx |\Delta m^2_{32}|$ and leaving:

$$P_{dis}\left(\bar{\nu}_e \rightarrow \bar{\nu}_X\right) \approx \sin^2 2\theta_{13} \sin^2\left(\frac{1.27\Delta m^2_{31} L}{E}\right). \tag{2.12}$$

It is worthwhile to note that Eq. 2.10, and thus also Eq. 2.12, do not contain any terms proportional to δ_{CP}, and thus reactor experiments are not sensitive to that parameter.

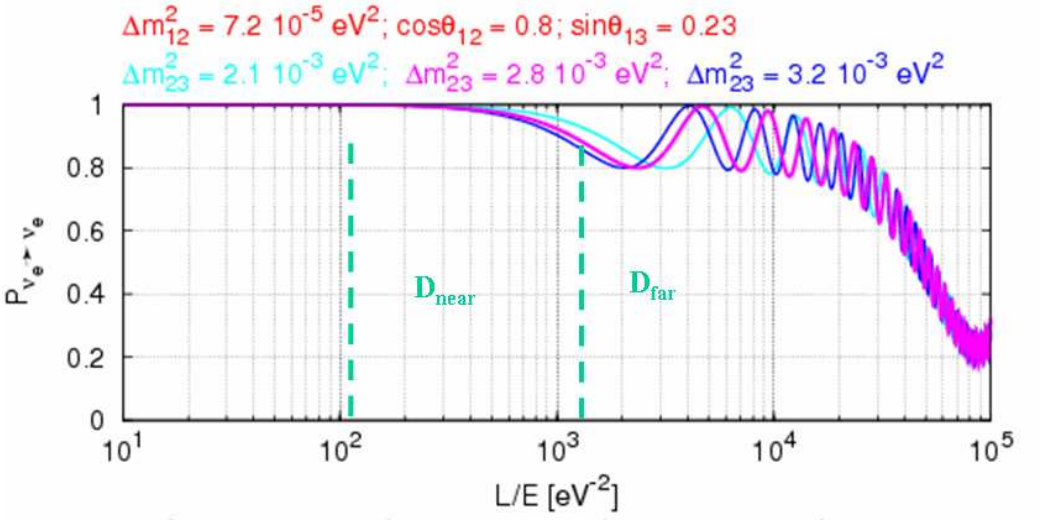

Figure 2.2: Traces of the survival probability $P\left(\bar{\nu}_e \rightarrow \bar{\nu}_e\right)$ as a function of the baseline-to-energy ration $L/E_{\bar{\nu}}$ for three different hypothetical sets of oscillation parameters. Dashed lines indicate optimal baseline distances D_{near} and D_{far} for the near and far detectors of a two-detector reactor experiment measuring $\sin^2(2\theta_{13})$. Note the effects of θ_{13}-driven oscillations at $2 \times 10^{-3}\text{eV}^{-2}$ while θ_{12}-driven oscillations are still negligible. Also note how θ_{13}-driven oscillations rapidly average out to a normalization factor in the region where θ_{12}-driven oscillations dominate. From [2].

2.2.2.2 $\nu_\mu \rightarrow \nu_e$ Appearance

Recall that accelerator-based neutrino experiments search for θ_{13} by looking for the appearance of ν_e in a nearly-pure beam of ν_μ. Calculation of the $\nu_\mu \rightarrow \nu_e$ appearance probability

in vacuum yields (with assistance from [46]):

$$
\begin{aligned}
P(\nu_\mu \to \nu_e) &= \sin^2 2\theta_{13} s_{23}^2 \sin^2 \frac{1.27\Delta m_{13}^2 L}{E} \\
&+ 8 c_{13}^2 s_{12} s_{13} s_{23} c_{12} c_{23} \cos\delta_{CP} \cos\frac{1.27\Delta m_{23}^2 L}{E} \sin\frac{1.27\Delta m_{31}^2 L}{E} \sin\frac{1.27\Delta m_{21}^2 L}{E} \\
&- 2\sin^2 2\theta_{13} s_{12}^2 s_{23}^2 \cos\frac{1.27\Delta m_{23}^2 L}{E} \sin\frac{1.27\Delta m_{31}^2 L}{E} \sin\frac{1.27\Delta m_{21}^2 L}{E} \\
&- 2 c_{13}^2 \sin 2\theta_{12} \sin 2\theta_{23} s_{13} \sin\delta_{CP} \sin\frac{1.27\Delta m_{32}^2 L}{E} \sin\frac{1.27\Delta m_{31}^2 L}{E} \sin\frac{1.27\Delta m_{21}^2 L}{E} \\
&+ 4 c_{13}^2 s_{12}^2 \left(c_{12}^2 c_{23}^2 + s_{12}^2 s_{23}^2 s_{13}^2 - 2 c_{12} c_{23} s_{12} s_{23} s_{13} \cos\delta_{CP}\right) \sin^2 \frac{1.27\Delta m_{12}^2 L}{E}.
\end{aligned}
\tag{2.13}
$$

With its abundance of terms, Eq. 2.13 provides a good starting point for discussing practical considerations which must be taken into account when choosing an experimental baseline L and neutrino energy E. To be sensitive to oscillation effects, an experiment should be configured such that the chosen L maximizes $P(\nu_\mu \to \nu_e)$ at the mean energy $\approx E$ of the neutrino source (or in the case of Eq. 2.11, maximizes P_{dis}). For instance, in cases where $\left|\Delta m_{21}^2\right| \ll \left|\Delta m_{31}^2\right|$ an experiment built to maximize the effects of the first term in Eq. 2.13 (and be sensitive to $\sin^2\theta_{13}$) will effectively suppress any oscillation contributions from the other terms, each of which is proportional to $\sin\left(1.27\Delta m_{21}^2 L/E\right)$. As discussed later in Section 3.1, this situation is close to that of the real world, with $\left|\Delta m_{21}^2\right|$ about two orders of magnitude less than $\left|\Delta m_{31}^2\right| \approx \left|\Delta m_{32}^2\right|$. This situation permits neutrino oscillations to often be treated as "quasi-two-neutrino oscillation," seeing only the effects of the larger mass-squared splitting [36].

2.2.2.3 Effects of δ_{CP}

While not directly relevant to the measurement being made by Double Chooz and the other reactor $\bar{\nu}_e$ experiments, the effects of the CP-violating phase δ_{CP} enters accelerator-based measurements of $\sin^2(2\theta_{13})$ as a yet-unconstrained parameter.

The effect of δ_{CP} on neutrino oscillations is most easily observed by comparing the oscillation probability of neutrinos $P(\nu_\mu \to \nu_e)$ with that of antineutrinos $P(\bar{\nu}_\mu \to \bar{\nu}_e)$. As in the calculation of Eq. 2.10, assuming CPT invariance allows the calculation of antineutrino oscillation probabilities by taking $U \to U^*$ in Eq. 2.9. This effectively takes $\delta_{CP} \to -\delta_{CP}$ in Eq. 2.13, so the CP-violating terms are those proportional to $\sin\delta_{CP}$. A simple calculation

yields the measure of leptonic CP violation:

$$\begin{aligned}\Delta P_{\mu e} &\equiv P\left(\nu_\mu \to \nu_e\right) - P\left(\bar{\nu}_\mu \to \bar{\nu}_e\right) \\ &= -4c_{13}^2 \sin 2\theta_{12} \sin 2\theta_{23} s_{13} \sin\delta_{CP} \sin\frac{1.27\Delta m_{32}^2 L}{E} \sin\frac{1.27\Delta m_{31}^2 L}{E} \sin\frac{1.27\Delta m_{21}^2 L}{E}.\end{aligned} \tag{2.14}$$

While the above form for $\Delta P_{\mu e}$ is explicitly for $\nu_\mu \to \nu_e$ processes, in general $\Delta P_{\alpha\beta} = -\Delta P_{\beta\alpha}$ has the same form for any cyclic permutation of two neutrino flavors e, μ, or τ [47, 48]. Also, it should be noted that CP violation cannot be observed by comparing $\nu_\alpha \to \nu_\alpha$ and $\bar{\nu}_\alpha \to \bar{\nu}_\alpha$ survival processes, as unlike Eq. 2.13, Eq. 2.10 contains no terms odd in δ_{CP}. In practice, Eq. 2.14 is often modified to a form known as the CP asymmetry [49]:

$$A_{CP} = \frac{P\left(\nu_\mu \to \nu_e\right) - P\left(\bar{\nu}_\mu \to \bar{\nu}_e\right)}{P\left(\nu_\mu \to \nu_e\right) + P\left(\bar{\nu}_\mu \to \bar{\nu}_e\right)} \approx \frac{1.27\Delta m_{12}^2 L}{E} \frac{\sin^2 2\theta_{12}}{\sin\theta_{13}} \sin\delta_{CP} \tag{2.15}$$

Both Equations 2.14 and 2.15 illustrate how any measure of δ_{CP} is dependent upon knowing θ_{13}. Since θ_{13} is known to be small, $\Delta P_{\mu e}$ will be a small effect, though A_{CP} may be large at low E. If $\theta_{13} = 0$, CP violation in the neutrino sector may only be measured through the observation of neutrinoless double beta decay.

2.2.2.4 Matter Effects

When discussing oscillation searches where the neutrino beam passes through a portion of the Earth, one must consider the influence of matter on neutrino propagation. During propagation, electron neutrinos and antineutrinos may forward-scatter via charged-current interactions with electrons in the surrounding matter medium.This phenomena was first considered by Mikheyev and Smirnov [50], and Wolfenstein [51], and is now known as the MSW effect. While most neutrinos observed in experiments pass through part of the Earth at some point, it has been been shown by [52] that matter effects only impact experiments with $L \sim 1000$ km. Thus, this effect has little effect on reactor $\bar{\nu}_e$ experiments where $L \sim$ 1km, but does need to be considered in accelerator-based neutrino experiments searching for $\nu_\mu \to \nu_e$ appearance at long baselines.

Any area of electron density N_α can be considered to contribute an effective potential term to the flavor-basis Hamiltonian $V_\alpha = \sqrt{2} G_F N_\alpha$, where G_F is the Fermi constant. Since

the Earth presents a density of only electrons, $V = \text{diag}\left(\sqrt{2}G_F N_e,\ 0,\ 0\right)$. Neutral-current scattering contributes a term which is equal for all flavor eigenstates, and thus a negligible multiple of the identity matrix. Following [46], the MSW effect modifies Eq. 2.13 to:

$$\begin{aligned} P\left(\nu_\mu \to \nu_e\right) &= \sin^2 2\theta_{13} s_{23}^2 \sin^2 \Delta_{13} \left(1 + \frac{2a}{\Delta m_{31}^2}\left(1 - 2s_{13}^2\right)\right) \\ &+ 8c_{13}^2 s_{12} s_{13} s_{23} c_{12} c_{23} \cos\delta_{CP} \cos\Delta_{23} \sin\Delta_{31} \sin\Delta_{21} \\ &- 2\sin^2 2\theta_{13} s_{12}^2 s_{23}^2 \cos\Delta_{23} \sin\Delta_{31} \sin\Delta_{21} \\ &- 2c_{13}^2 \sin 2\theta_{12} \sin 2\theta_{23} s_{13} \sin\delta_{CP} \sin\Delta_{32} \sin\Delta_{31} \sin\Delta_{21} \\ &+ 4c_{13}^2 s_{12}^2 \left(c_{12}^2 c_{23}^2 + s_{12}^2 s_{23}^2 s_{13}^2 - 2c_{12} c_{23} s_{12} s_{23} s_{13} \cos\delta_{CP}\right) \sin^2 \Delta_{12} \\ &- 2\sin^2 2\theta_{13} s_{23}^2 \cos\Delta_{32} \sin\Delta_{31} \frac{aL}{4E}\left(1 - 2s_{13}^2\right) \end{aligned} \tag{2.16}$$

where $a = 2\sqrt{2}G_F N_e$ is small and $\Delta_{ij} \equiv 1.27\Delta m_{ij}^2 L/E$. In adapting Eq. 2.16 to antineutrinos, we must take $\delta_{CP} \to -\delta_{CP}$ as before, but must also take $a \to -a$. Thus, there are additional two terms in Eq. 2.16 (as compared to Eq. 2.13) which act as if they are CP-odd. In matter, $\Delta P_{\mu e}$ becomes:

$$\begin{aligned} \Delta P_{\mu e} &= -4c_{13}^2 \sin 2\theta_{12} \sin 2\theta_{23} s_{13} \sin\delta_{CP} \sin\Delta_{32} \sin\Delta_{31} \sin\Delta_{21} \\ &+ 4a \sin^2 \theta_{13} s_{23}^2 \sin\Delta_{13} \left(1 - 2s_{13}^2\right) \left(\frac{\sin\Delta_{13}}{\Delta m_{31}^2} - \frac{\cos\Delta_{32} L}{4E}\right) \end{aligned} \tag{2.17}$$

Depending on the experimental parameters, matter effects can mimic a CP-violating signal. This effect also depends on the ordering of the neutrino masses, or the mass hierarchy, due to the $\sin\Delta_{13}$ dependence of the last term of Eq. 2.17. For a "normal hierarchy" with $m_{1,2} < m_3$ the MSW effect will increase $\Delta P_{\mu e}$ by enhancing $P\left(\nu_\mu \to \nu_e\right)$ and suppressing $P\left(\bar{\nu}_\mu \to \bar{\nu}_e\right)$, while an "inverted hierarchy" with $m_{1,2} > m_3$ will have the opposite effect. Since the absolute hierarchy has not yet been established, this variable can affect an experiment's sensitivity to measuring δ_{CP}.

2.3 Possible Mechanisms for Neutrino Masses

As described in Sec. 2.1, neutrinos are considered massless in the Standard Model; this fits the historical data of ν ($\bar{\nu}$) always having left-handed (right-handed) helicity. However, the

flavor oscillations described in Sec. 2.2.2 require at least one of the neutrino masses to be nonzero, and at least two to be nondegenerate. Current experimental evidence, described in Chapter 3, supports that at least two neutrinos are massive, and all three are nondegenerate. Thus, an extension to the Standard Model is warranted in which neutrinos are given nonzero masses, but the exclusive helicities of observed relativistic neutrinos and antineutrinos are maintained.

The Standard Model Lagrangian in Eq. 2.2 does allow for neutrinos to be massive Dirac fermions with the setting of a nonzero mass in the first term,

$$L_F \propto m_n u \left(\bar{\nu_L}\nu_R + \bar{\nu_R}\nu_L\right) \tag{2.18}$$

though this would warrant right-handed neutrinos with $\bar{\nu_L}$ independent of ν_R. It is also possible to extend the Lagrangian with Majorana mass terms, thereby rendering each of the neutrinos its own antiparticle $(\nu_L)^C = (\nu^C)_R$ [36]. One common theoretical framework to accommodate this is the so-called "Seesaw Mechanism" which arises out of superstring-based Grand Unification Theories [53, 54]. This mechanism introduces both Majorana and Dirac mass terms into the Lagrangian yielding heavy right-handed neutrinos with masses near the Grand Unification scale, and left-handed neutrinos with appropriately small masses. Exactly how these fields are constructed leads to three different types of seesaw mechanism: type-I [53, 54], type-II [55, 56], and type-III [57]. In many cases, the theory also implies the existence of Majorana neutrinos and neutrinoless double beta decay [58]. All allow for neutrino flavor oscillations. The exact mass of such right-handed neutrinos could have implications for the observed matter-antimatter asymmetry in the universe [59, 60, 61], though direct searches have so far provided no evidence [62, 63, 64, 65].

Chapter 3

Neutrino Oscillation Experiments

3.1 Past Experimental Oscillation Results

The first evidence for anomalous neutrino behavior came from measurements of the solar neutrino flux by the Homestake Mine experiment beginning in the late 1960's [66, 67]. Their underground chemical-based neutrino detector registered a deficit of observed events as compared to flux predicted by the Standard Solar Model by nearly a factor of three. The mechanism for this deficit was not immediately understood. Confirming measurements of the deficit from the GALLEX [68, 69] and SAGE [70] experiments helped rule out detector-related systematics as a cause, and prompted further precision measurements of solar neutrinos, and neutrinos from other sources.

Measurements of atmospheric neutrinos in the 1980's and 1990's by the IMB [71], Kamiokande [72] and Super-Kamiokande [73] experiments gave strong evidence in support of flavor oscillations between neutrinos even before the solar anomaly was resolved. Each measured the ratio ν_μ/ν_e in GeV-energy neutrinos to be smaller than expected, and to vary with incoming neutrino angle. This indicated that neutrinos originating from cosmic ray interactions in the Earth's atmosphere were oscillating between flavors as they passed through the planet. Similar measurements would eventually be conducted by the MINOS [74], MACRO [75], and Soudan-2 [76] experiments.

Concurrent with the atmospheric measurements, further data taken by the Kamiokande [77] and subsequent Super-Kamiokande [78] experiments also confirmed the deficit of solar neu-

trinos. However, it would not be until the 2000's when the SNO experiment would measure neutral-current interactions from all flavors of solar neutrinos and definitively show that solar electron neutrinos were oscillating to other types [79].

Following the success of neutrino beams in producing ν_μ [25] and as probes in deep-inelastic scattering (*e.g.* [80]), searches for oscillations were also conducted by placing detectors at distances from sources of accelerator-produced neutrinos. At the time of this writing, recent results from accelerator-based neutrino experiments include the observation of $\nu_\mu \to \nu_\tau$ oscillations by the OPERA experiment [81], tests of sterile neutrinos by the ICARUS experiment [82], and long-baseline measurements of $\nu_\mu \to \nu_X$ oscillations by the MINOS [83, 5] and K2K [84] experiments. Most recently, the T2K experiment [85] has begun operation, as discussed later.

A global summary of all exclusion and acceptance regions from a plethora of oscillation searches are shown in Fig. 3.1, including data up to 2011. When results from all experiments are combined, the acceptance regions allowed in the parameter space of 3-neutrino mixing become very small, as illustrated in Figure 3.2. This level of precision hints at the maturity of the field, and the wealth of data accumulated since the discovery of neutrino flavor oscillations. The combined solar data of SNO [4, 86] and Super-Kamiokande [78], and the long-baseline reactor data of KamLAND [87], constrain the "solar" mixing angle $\sin^2(2\theta_{12}) = 0.857 \pm 0.024$ and mass splitting $\Delta m^2_{21} = (7.50 \pm 0.20) \times 10^{-5}$ eV^2. Super-Kamiokande [88] and MINOS [21, 83, 5] combine to provide the best constraints on the "atmospheric" mixing angle $\sin^2(2\theta_{23}) > 0.95$ and mass splitting $\Delta m^2_{32} = \left(2.32^{+0.12}_{-0.08}\right) \times 10^{-3}$ eV^2.

The global data are not without anomalies. Most striking is the result of the LSND experiment [89], which found evidence for $\bar{\nu}_\mu \to \bar{\nu}_e$ oscillations consistent with a mass splitting of $\Delta m^2 \sim 1$ eV^2, a value which is inconsistent with atmospheric or solar oscillation modes. This result has been tested in both $\bar{\nu}_\mu \to \bar{\nu}_e$ and $\nu_\mu \to \nu_e$ modes by the MiniBooNE experiment [90, 91], with the $\bar{\nu}$ results showing consistency with the LSND result. However, MiniBooNE itself has provided another anomaly in an excess of events over background at low neutrino energy, which is not explained by LSND-like mixing [92]. These anomalies are often attributed to mechanisms mediated by one or more "sterile" neutrinos which interact via flavor mixing with the known flavors of neutrinos, but do not couple to the Z and avoid

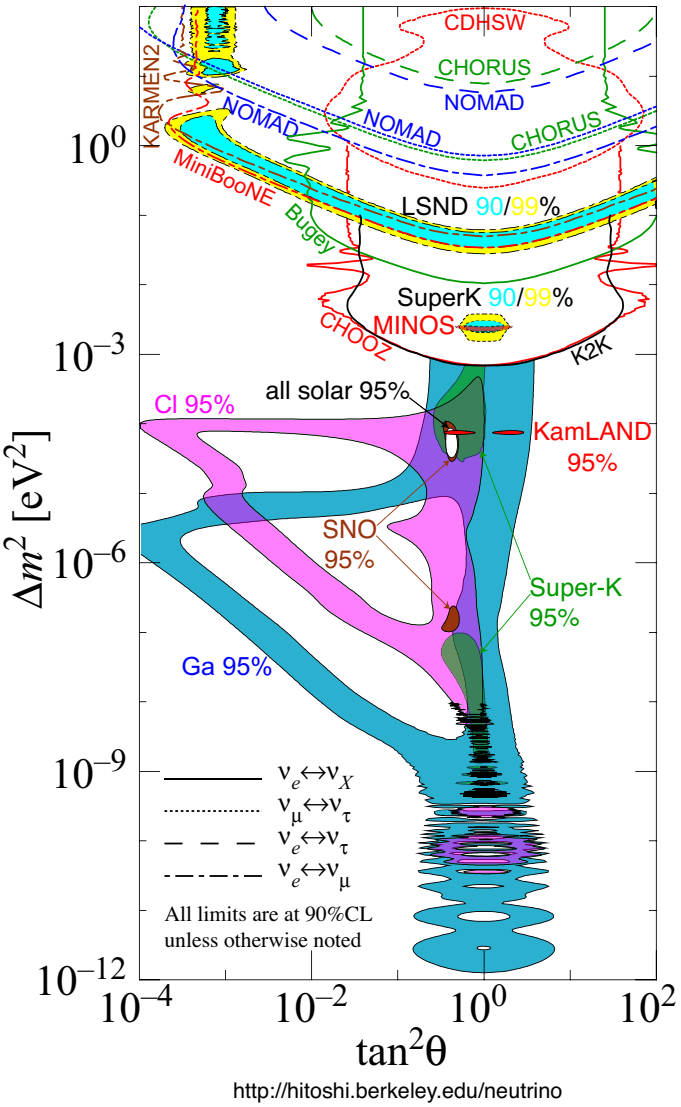

Figure 3.1: Regions of allowed squared-mass splittings and mixing angles allowed or excluded by various experimental results, as of 2011. Figure created by H. Murayama [3]. References for data shown are listed at `http://hitoshi.berkeley.edu/neutrino/ref2011.html`.

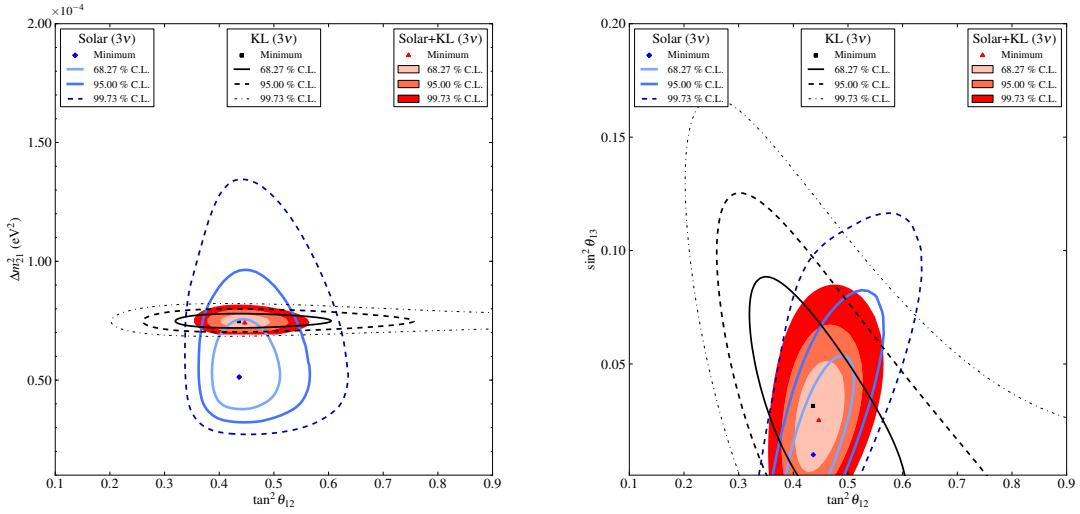

(a) SNO+KamLAND θ_{12} & Δm^2_{12}

(b) SNO+KamLAND θ_{12} & θ_{13}

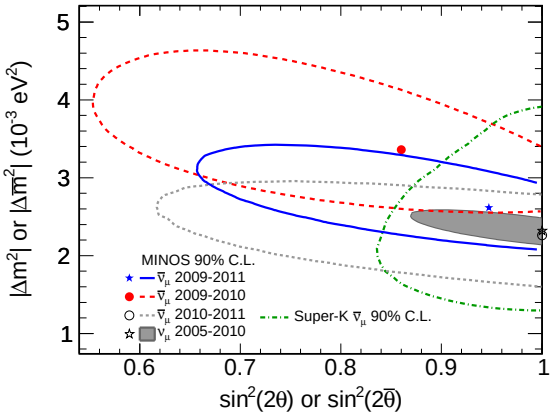

(c) MINOS+SuperK

Figure 3.2: Detailed plots of the best-fit values of oscillation parameters in a 3-neutrino mixing model, according to combined or best experimental data. Plots do not take into account results from $\sin^2(2\theta_{13})$ measurements described in Chapter 8. Figures 3.2(a) and 3.2(b) from [4]. Figure 3.2(c) from [5].

contributing to the width of the Z resonance (*e.g.* [93], [94], and [95]). Other experiments have begun complementary tests of the parameter space, but have so far provided only exclusion limits [82]. More recently, re-analysis of predicted reactor fluxes [13, 96] and a global fit to all $\bar{\nu}_e$ disappearance data have similarly given the suggestion of mixing to a sterile neutrino at $\Delta m^2 > 0.5$ eV^2 in what has been deemed the "Reactor $\bar{\nu}$ Anomaly" [97].

As of mid-2011, the only remaining unmeasured parameters in the PMNS matrix were θ_{13} and δ_{CP}. The most stringent constraints on θ_{13} come from reactor-based experiments, particularly the Palo Verde [6] and Chooz [7] collaborations. Each utilized a single liquid scintillator detector at a baseline of between 750 and 1100 m, with varying degrees of overburden. Having only one detector each, the experiments compared their observed IBD candidate rates to predictions based on reactor data (though Chooz did employ an "anchor point" on their predicted flux based on the measurement of the very-short baseline Bugey4 experiment [98], a technique also used by Double Chooz and described in Sec. 6.3). In the cases of both experiments, degradation of the Gd-doped liquid scintillator halted the period of useful data-taking. The results of both experiments are shown in Fig. 3.3. The final result of the Chooz experiment gave an upper bound of $\sin^2(2\theta_{13}) \lesssim 0.14$ [7] at the central value of $\Delta m^2_{31} = 2.32 \times 10^{-3}$ eV^2 measured by MINOS [83, 5], providing the most stringent constraint on θ_{13} until the middle of 2011. Measurements after that time, leading to the observation of a nonzero θ_{13}, are described later in Chapter 8.

3.2 Modern Searches for θ_{13}-Driven Oscillations

Modern experiments attempting to measure θ_{13}-driven oscillations generally employ one of two approaches: 1.) attempting to measure $\bar{\nu}_e \to \bar{\nu}_X$ disappearance using reactor-produced $\bar{\nu}_e$ flux; or 2.) attempting to measure $\nu_\mu \to \nu_e$ appearance in an accelerator-produced beam of mostly ν_μ. Each style of experiment has their own unique advantages, challenges, and systematic uncertainties.

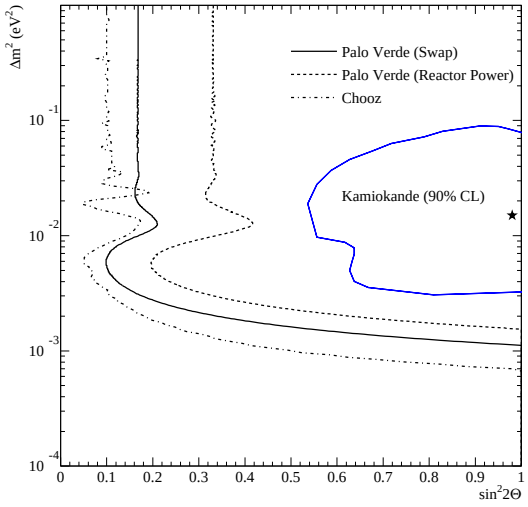

Figure 3.3: Exclusion limits on oscillations of reactor $\bar{\nu}_e$ at 90% C.L., given in a plot from [6]. Palo Verde results are from that reference, while Chooz results are from [7].

3.2.1 Accelerator-Based Searches

Accelerator-based neutrino oscillation experiments observe neutrinos created by a fixed-target particle beam at some distance from the target. The beam of neutrinos is typically created by impinging protons on a target to produce $\pi^{\pm}$ and $K^{\pm}$ mesons, then allowing those mesons to decay and emit neutrinos in the highly-boosted direction of the initial beam. Sufficient neutrino beam intensities are achieved by focusing the mesons with one or more magnetic horns, as well as providing a long, empty decay region in which the hadrons are free to decay before interacting with matter. The beams are typically rich in ν_μ and $\bar{\nu}_\mu$, with a non-negligible ν_e and $\bar{\nu}_e$ contamination.

Oscillations driven by θ_{13} are observable in accelerator-created neutrino beams by measuring the rate of ν_e appearance some distance from the beam production point. The probability for a ν_μ to oscillate into a ν_e in vacuum is given by the lengthy Eq. 2.13. While this equation gives opportunity to measure a large number of physical parameters, this opportunity also complicates precision measurements of any single parameter. Further, neutrino beam energies of 1-10 GeV require a baseline $L \sim 1,000$ km to provide experi-

mental sensitivity to oscillation effects. If both the neutrino beam production site and the detector are to be located within the Earth's crust, this length of baseline is only achievable by sending the beam along a chord line through the Earth, further complicating the form of Eq. 2.13 by requiring that matter effects be taken into account, yielding Eq. 2.16.

Two accelerator-based experiments are currently taking data in order to measure $P(\nu_\mu \rightarrow \nu_e)$. The MINOS experiment [99] has been in operation since 2005, measuring neutrinos produced by the NuMI beam [100] at Fermilab, outside of Batavia, IL, USA. MINOS observes neutrinos interacting in a pair of detectors of similar segmented iron-and-plastic-scintillator design: a 980 ton near detector a few hundred meters from the neutrino production site; and a 5,400 ton far detector at a baseline of $L = 735$ km.

The T2K (Tokai-to-Kamioka) experiment [85, 49] is located in Japan, and began operation in early 2010. It observes neutrinos created at the J-PARC laboratory near Tokai, using the Super-Kamiokande water Cherenkov detector to measure potential oscillations at a baseline of $L = 295$ km. A suite of different near detectors [101, 102, 103, 104] is used to characterize the beam at short baselines. The beam is directed such that the Super-K far detector is located off-axis, yielding a neutrino flux of lower average energy, but with a more sharply-peaked spectrum than the on-axis flux.

Recent results from each of these experiments are discussed in Chapter 8.

In addition to MINOS and T2K, the NOνA experiment [105] will also attempt to measure θ_{13}-driven oscillations once it is fully constructed. NOνA also observes neutrinos from the NuMI beam, but does so at positions off the central beam axis where the neutrinos are of generally lower energy, but the peaked neutrino spectrum is narrower. The NOνA near and far detectors are situated a few hundred meters and 810 km from the neutrino production site, respectively. Both detectors are of the same segmented design, constructed of extruded segments of PVC which are filled with liquid scintillator and read out by avalanche photodiodes.

3.2.2 Reactor-Based Searches

Nuclear fission reactions produce many $\bar{\nu}_e$ as the fragments of fissioned fuel nuclei shed neutrons in order to reach an energetically-stable nuclear configuration. The few-MeV

energies at which these reactions occur aren't capable of creating the partner leptons of $\bar{\nu}_\mu$ and $\bar{\nu}_\tau$, so the flux of neutrinos emanating from the reactors is very pure. This pure flux provides a route to measuring θ_{13} by searching for a disappearance in the expected number of $\bar{\nu}_e$. A combination of the $\bar{\nu}_e$ spectrum emitted by the fission products with the energy-dependent Inverse Beta Decay cross-section gives rise to a singly-peaked interaction spectrum, with interactions most probable at around $E_{\bar{\nu}} = 3$ MeV (see Figure 6.5). The probability of an $\bar{\nu}_e$ disappearing is governed by the formula given in Eq. 2.11. Because the mass splittings $\Delta m^2_{31} \approx \Delta m^2_{23}$ and Δm^2_{12} are different by orders of magnitude, experiments measuring $\sin^2(2\theta_{13})$ at baselines of ~ 1 km from reactors may neglect oscillations driven by the mixing angle θ_{12}. This is shown in the simplification of Eq. 2.11 down to the much more manageable Eq. 2.12, and illustrated in Figure 2.2. Thus, reactor $\bar{\nu}_e$ disappearance measurements can allow a very precise and straight-forward measurement of $\sin^2(2\theta_{13})$ without dependencies on other oscillation parameters.

3.2.2.1 Multi-Detector Design of Modern Experiments

Modern reactor $\bar{\nu}_e$ oscillation experiments are based on a multi-detector, multi-baseline principle that employs (at least) a "near" detector to precisely measure an un-oscillated flux close to the neutrino source, and a "far" detector to measure the effects of potential oscillations on the spectrum after some distance [106, 107]. While it is possible to make a measurement of $\sin^2(2\theta_{13})$ based on the predicted flux of $\bar{\nu}_e$, *a la* Palo Verde [6] or Chooz [7], this approach is limited by systematic uncertainties on the reactor flux prediction and signal detection efficiency. However, if the near and far detectors of a multiple-baseline experiment are built to identical specifications, the effects of these systematics are greatly diminished. This is why each of the experiments described in the next few subsections utilizes multiple, identically-constructed detectors. With this approach, the limiting systematics are the relative efficiencies of the two detectors, and knowledge of irreducible backgrounds in each detector.

3.2.2.2 Double Chooz

Double Chooz [9] is located in the Ardennes region in northeastern France, near the Franco-Belgian border. The power plant site is the same location as where the CHOOZ experiment [7] was constructed. The reactor complex houses a pair of 4.25 GW_{th} pressurized water reactors. Double Chooz is being constructed in a phased manner: first a Far detector will be built at an average baseline of 1,050 m; later a Near detector will be constructed at an average baseline of ∼450 m. Both detectors are of identical construction, and contain an 8.3 ton antineutrino target fiducial mass. As of this writing, the Far detector has been constructed and has been taking physics data since April 2011; the Near detector is under construction.

As it is the focus of this thesis, the Double Chooz experiment, especially in its Far Detector-only first phase, is described in much greater detail in Chapter 4. Results from Double Chooz oscillation analyses are described in-depth in Chapters A and 7, and discussed in the context of other measurements of θ_{13} in Chapter 8.

3.2.2.3 Daya Bay

The Daya Bay experiment [108] is located in southeastern China, outside of Hong Kong. Three reactor complexes on the site, called Daya Bay, Ling Ao I, and Ling Ao II, each host two reactors. The six reactors all produce 2.9 GW_{th} nominal power. When fully constructed, Daya Bay will be comprised of eight identically-designed Antineutrino Detector (AD) units. Two AD's will be located at a site near to the Daya Bay reactors, two AD's will be located at a site near each of the Ling Ao reactor sites, and the final four AD's will be installed at a Far site around 1.7 km from all of the reactors. At time of writing, Daya Bay has been running in an initial reduced configuration, with only three AD's at the Far site and one AD at the Ling Ao near site, and are in process of installing all AD's. Daya Bay began taking data in this reduced configuration in late December 2011.

Recent results from Daya Bay are discussed in Chapter 8.

3.2.2.4 RENO

The RENO experiment [109] is located in South Korea, 250 km south of Seoul at the Yonggwang nuclear power plant. The power plant hosts six reactors arranged in a line, approximately evenly spaced with 1.3 km between the first and last core. The total combined thermal power of the six reactors is 16.4 GW_{th}. RENO's identical detectors are placed at distances of 292 m and 1380 m from the centroid of the reactors. RENO began taking physics data with both of its detectors in August 2011.

Recent results from RENO are discussed in Chapter 8.

Part II

The Double Chooz Experiment

Chapter 4

The Double Chooz Experiment

The main goal of the Double Chooz experiment is a measurement of flavor oscillations due to $\sin^2(2\theta_{13})$ in the $\bar{\nu}_e$ flux emanating from a pair of nuclear reactors, using two identical liquid-scintillator detectors. This chapter describes the Double Chooz experimental apparatus in general terms, and covers the operation of the Inner Detector (ID) in detail. Detailed description of the Outer Veto (OV), the Columbia University group's principle hardare contribution to the experiment, is delayed to Chapter 5 so that it may be covered in greater detail.

The Double Chooz experiment is designed on the principle of using identical detectors at different baselines from the antineutrino-emitting reactors to precisely measure any effects of $\sin^2(2\theta_{13})$-driven oscillations. Section 4.1 of this chapter will describe the general layout of the detectors and reactor factility. The design of each detector will be further described in Section 4.2, with emphasis on the Inner Detector (Sec. 4.2.1). Descriptions of the detector's calibration system, which are integral to performing an oscillation analysis based on observed neutrino spectrum, follow in Section 4.2.5. Finally, description of the Data Acquisition System, electronics, and software used to process detector data is found in Section 4.3. Since the Far and Near detectors are intended to be operationally identical with near identical design, and accounting for the fact that the analyses described in Chapters A and 7 utilize only the far detector, this chapter will not contain separate discussions of each detector.

4.1 Experiment Site & Layout

The Double Chooz experiment [9] is situated in the Ardennes region of France, at the site of the Centrale Nucléaire de Chooz, near the eponymous village. The power plant hosts two N4-type pressurized water reactors (PWRs) for generating electrical power. Each reactor has a nominal thermal power of 4.25 GW_{th} and produces around 1.49 GW of electrical power [110]. Double Chooz will employ a multiple-detector approach to measure $\bar{\nu}_e$ oscillations in the flux from both reactors: a near detector will measure the flux before oscillations become significant, while a far detector will measure the flux at a distance of ∼1050m from the two-reactor barycenter. Illustrations of the expected final configuration with both Near and Far detectors may be seen in Figures 4.1 and 4.2. To minimize relative differences between detectors and systematics in the two-detector phase, both the Near and Far detectors will be built to the same design. For similar reasons, the detectors are constructed at locations where the ratio of the flux from each reactor will be the same in each detector.

Figure 4.1: Aerial photograph of the Double Chooz site in Ardennes, France, showing the general layout of the detectors around the reactor complex. Reactors are the gray, domed cylindrical buildings near center. Note that 'East' and 'West' reactors are named erroneously in this photograph: the labels should be swapped.

Double Chooz will make use of the existing experimental hall previously occupied by the CHOOZ experiment [7]. This reduces civil construction time and costs, and allows Double Chooz to be constructed in a phased manner: the Far detector is completed first,

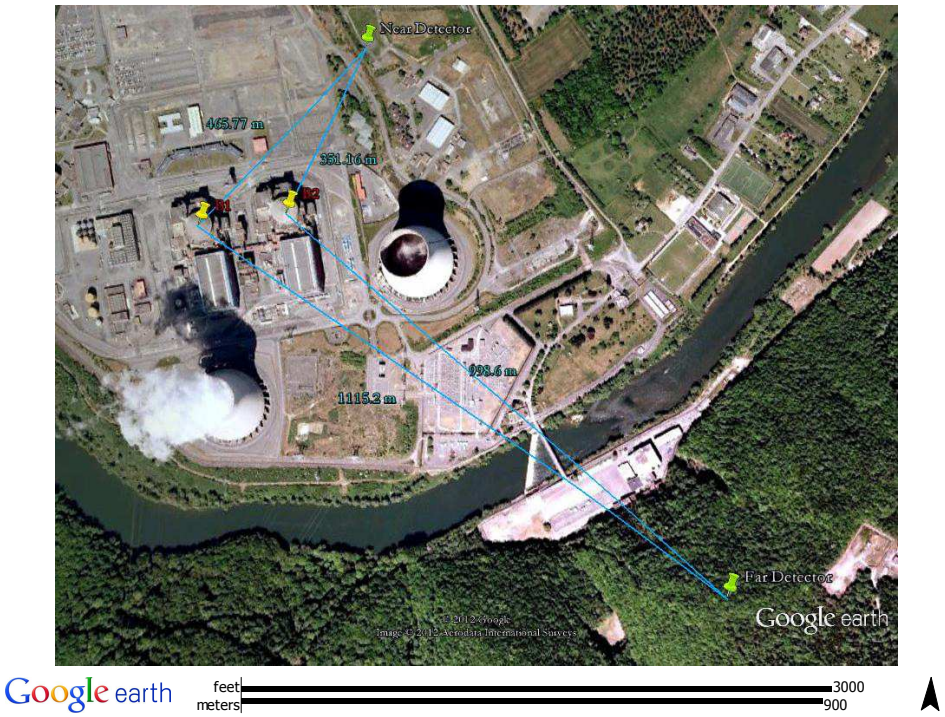

Figure 4.2: Overhead photograph of the Double Chooz site in Ardennes, France. Reactors B1 and B2 are marked with yellow pushpins and red labels. Near and Far detector locations are marked with green pushpins and white labels. Blue lines and measurements indicate baselines between each reactor and detector. Produced with Google Earth.

and can perform a single-detector measurement of θ_{13} while the Near detector is being constructed. Once the Near detector is on-line, the Far detector will have already accrued significantly more data than if it were simultaneously started with the Near, improving the initial Near-Far measurements.

4.2 Detector Design

The Double Chooz detector employs a multiple-volume detector design to reduce systematic uncertainties and the rates of irreducible backgrounds. A schematic of the detector is shown in Figure 4.3. The detector is generally divided into three regions: the Inner Detector (ID), Inner Veto (IV), and Outer Veto (OV). The ID is further divided into three volumes: the $\bar{\nu}$ Target, γ-catcher, and Buffer, and surrounded by passive steel shielding. Mounted at a number of locations on the detector are various calibration systems.

4.2.1 Inner Detector

The Inner Detector (ID) is defined by a steel vessel vessel (also called the Buffer Vessel) 5516 mm in diameter, 5674 mm in radius, and 3 mm thick. On the wall of this vessel are mounted 390 Hamamatsu R7081 10"-diameter photomultiplier tubes (PMTs) [111]. This model was chosen in part for its low-background glass construction. The ID PMTs face inwards towards the center of the detector, and provide the main basis for calorimetric measurements of particle interactions inside the ID. Each PMT is surrounded by a Mu-metal cylindrical shield to suppress the effects of ambient magnetic fields [112]. The PMTs are supplied with high voltage power ($\sim$1.3 kV from a CAEN A1535P mainframe) by a single cable which also carries away the PMT signal (5 mV/PE). Signal and HV are decoupled by a splitter, with the signal being routed to the data acquisition electronics (see Sec. 4.3).

A set of 800 PMTs were characterized for use in both the Far and Near Double Chooz detectors [113, 114, 115], with a subset selected for the Far detector. Characteristics such as single-photoelectron signal shape, single-PE/pedestal ratio, combined quantum and collection efficiency, pulse transit time spread, and after-pulse probability, charge output linearity, and dark hit rate were measured for each PMT. Following installation of the PMTs

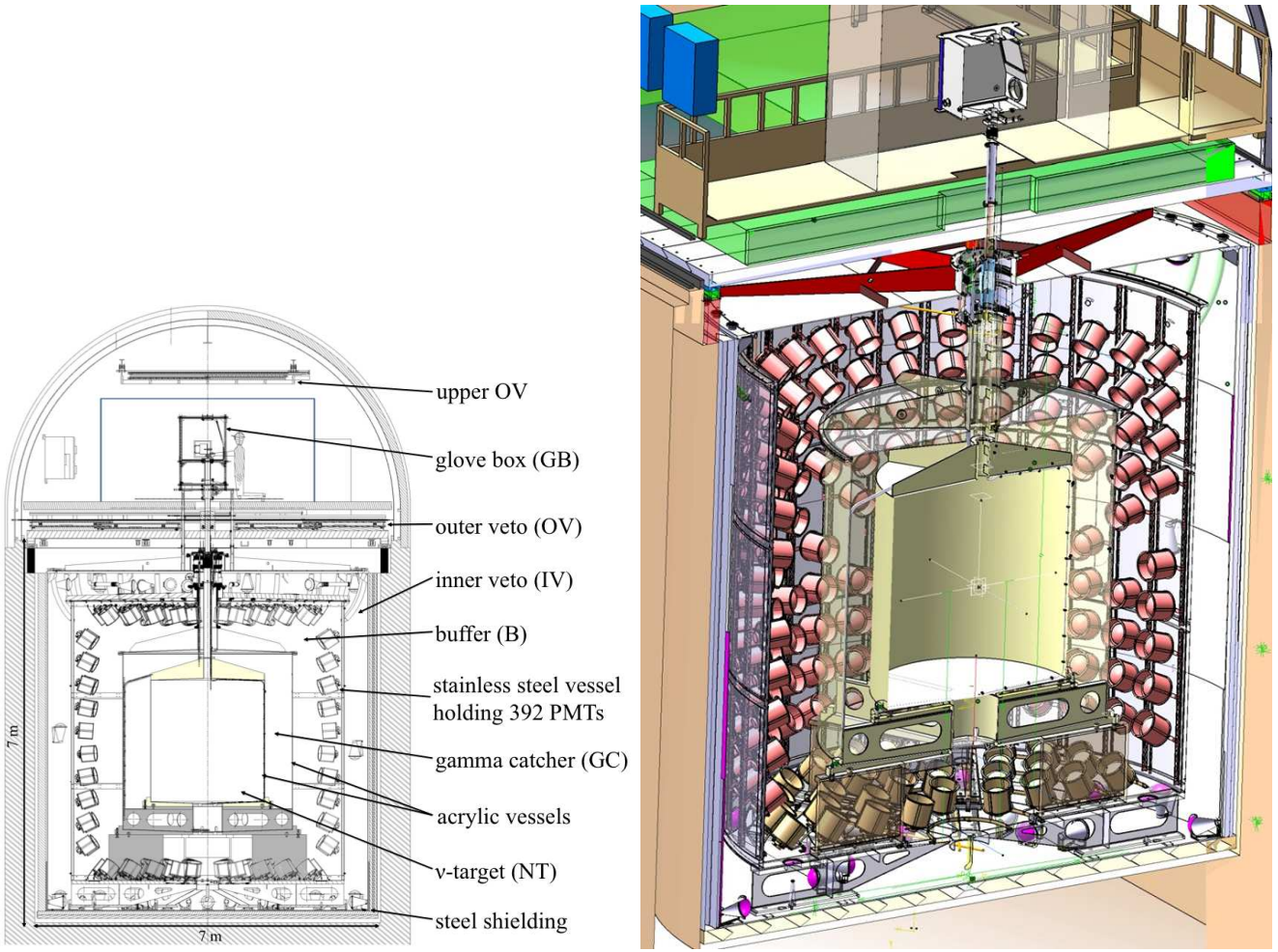

(a) Cross-Section Schematic

(b) CAD Cutaway View

Figure 4.3: A cross-sectional schematic of the Double Chooz detector (Fig. 4.3(a)), and a CAD cutaway view (Fig. 4.3(b)). Figure 4.3(a) from [8].

in the Far Detector, some were found to generate flashes of light due to sparking in the circuitry located in the epoxy base. Reduction of false triggers caused by this spontaneous light emission was achieved by a combination of turning off the High-Voltage power to 14 PMTs, and through software-based signal discrimination methods (see Sec. A).

4.2.1.1 $\bar{\nu}$ Target

The $\bar{\nu}$ Target contains the Gd-doped liquid scintillator which defines the fiducial volume of the Gd-capture-driven Double Chooz neutrino analysis. This volume is contained by an acrylic vessel of cylindrical shape, 2458 mm in height and 1150 mm in radius, with a thickness of 8 mm.

The target scintillator has been newly-developed for Double Chooz, with design emphasis on long-term chemical stability [116]. The CHOOZ experiment was limited in its physics reach by the gradual optical degradation of its scintillator [7], motivating this design emphasis for Double Chooz.

The base solvent mixture is composed of ortho-phenylxylylethane (o-PXE) and n-dodecane mixed at a ratio of 20/80. The chosen scintillation fluor is PPO (2,5-diphenyloxazole), with bis-MSB (4-bis-(2-methylstyryl)benzene) used as a wavelength-shifter to shift scintillation light to wavelengths where the detector liquids are more transparent. Doping with Gadolinium is achieved by use of a meta-β-diketone, $Gd(thd)_3$, or Gd(III)-tris-(2,2,6,6-tetramethyl-heptane-3,5-dionate), at a concentration of 0.123% by weight, or $\sim$1 gram/liter. This complex metalorgnanic compound has been found to exhibit higher solubility in organic solvents, lending itself to long-term chemical stability. The high vapor pressure of the molecule also allowed purification by sublimation, reducing radioimpurities due to U, Th, and K chains.

Precise knowledge of the total number of free Hydrogen nuclei in the fiducial volume is integral to the $\bar{\nu}$ oscillation measurement, on account of the detection process $\bar{\nu}_e + p \rightarrow e^+ + n$ rate scaling with the number of target protons in the detector's fiducial volume. In the single-detector phase, the "proton number" is essential to predicting the expected number of detected IBD interactions in the $\bar{\nu}$ Target. The two-detector phase of the experiment relies on direct comparison of the proton numbers in each of the detectors in order to establish the

expected near/far ratio of events. The proton number uncertainty is minimized through accurate mass measurements of the $\bar{\nu}$ Target fluid, and by use of scintillator ingredients which have been well-characterized by precision chemical analysis. For the Double Chooz far detector, a weight measurement of the $\bar{\nu}$ Target scintillator was made during the filling of the detector, determining the mass to a precision of 0.04%. The free hydrogen fraction of the Target liquids has been found to be 13.6%, with a relative precision of 0.3% [117]. These uncertainties are included in the IBD detection efficiency uncertainty, described later in Chapters A and 7.

4.2.1.2 γ-catcher

The γ-catcher serves to increase photon conversion efficiency while maintaining the definition of the fiducial volume by the Gd-doped target. It is contained by an acrylic vessel of cylindrical shape with a thickness of 12 mm. In each dimension, it provides 55 cm of fluid thickness around the $\bar{\nu}$ Target. This provides a total volume of scintillator of 22.5 m^3. The γ-catcher scintillator is composed of the same o-PXE and n-dodecane as the $\bar{\nu}$ Target, but with medicinal white oil also added in order to match the light yield and density to that of the Gd-doped target scintillator [117]. The same PPO fluor and bis-MSB wavelength shifter are used, as in the $\bar{\nu}$ target.

The γ-catcher ensures conversion of emitted γ's from processes near the edge of the $\bar{\nu}$ Target into scintillation light. This allows the Gd-doped region of the $\bar{\nu}$ Target to fully define the fiducial volume of the detector without loss of calorimetric precision near the edge of the fiducial volume.

4.2.1.3 Buffer

The Buffer is a layer of mineral oil which serves to shield the scintillating regions of the detector from radioactivity naturally present in the photomultiplier tubes, steel detector vessel, and surrounding rock. This layer is 105 cm thick, or 110 m^3 of fluid. The liquid is a mixture of 53% medicinal white oil and 47% n-alkane, by volume, chosen for its transparency, low aromaticity, and minimal scintillation light yield. Use of the buffer is one of the significant improvements of the Double Chooz detector over the previous design of

CHOOZ.

4.2.2 Inner Veto

The Inner Veto (IV) is the outermost layer of the main detector, and serves to tag and track through-going cosmic ray muons, and tag fast neutrons. The IV consists of 90 m^3 of liquid scintillator monitored by 78 Hamamatsu R1408 8" PMTs arranged around the sides (12 PMTs), bottom (48 PMTs), and top (24 PMTs) of the cylinder. These PMTs were previously used in the IMB and Super-Kamiokande experiments [118]. The scintillator used in the IV is a mixture of linear alkyl benzene (LAB) and n-alkanes, with 2 g/l PPO fluor and 20 mg/l bis-MSB wavelength shifter added. The stainless steel vessel has dimensions of 6.8 m height and 3.3 m radius, holding a fluid layer 50 cm thick around all sides of the ID, except for a small break for the detector chimney at the top, ensuring high muon tagging efficiency. The inside of the vessel was painted with a highly-reflective white AR100/CLX coating from MaxPerles. Similarly, the outer sides of the buffer vessel, which face into the IV, are coated with reflective VM2000 sheets. This design was optimized for muon detection efficiency by maximizing the number of produced photoelectrons per MeV of MIP energy deposition using MC simulation of the detector [119]. The resulting muon rejection efficiency of the IV as configured is above 99.9% for muons which cross the IV volume [8].

4.2.3 Steel Shielding

The main detector is surrounded outside of the IV by 15 cm of passive, demagnetized steel shielding. This layer shields against naturally-occurring γ-radiation in the rock and cavern surrounding the detector.

4.2.4 Outer Veto

The Outer Veto (OV) sits atop the layer of steel shielding above the main detector. Described more in Chapter 5, the OV provides additional muon veto coverage, especially over the chimney of the main detector where IV coverage is lacking. The OV is constructed of segmented plastic scintillator modules. One bi-layer of modules sits atop the surface

of the steel shielding, while another smaller bi-layer is suspended from the ceiling of the experimental hall.

4.2.5 Calibration Systems

The Double Chooz detector is equipped with a variety of calibration systems used to characterize detector response and measure long-term detector performance stability. Not all systems described here are in full use at the time of this writing. Hardware systems include light sources and deployed radioactive sources. Radioactive sources available include ^{137}Cs (0.662 MeV γ emitter), ^{68}Ge (2×0.511 MeV positron annihilation γ emitter), ^{60}Co (1.173 MeV and 1.333 MeV γ emitter), and ^{252}Cf (fission neutron emitter); all sources are encapsulated to preserve scintillator chemical integrity.

4.2.5.1 ID & IV Light Injection

The Inner Detector and Inner Veto are each equipped with a multi-wavelength light-injection system (LI). Light from blue and UV LEDs (λ =385, 425, and 470 nm for the ID, and λ =365 and 475 nm for the IV) is conveyed into the detector by optical fibers, with the end points of the fibers located on the covers of the PMTs. Some end points are also equipped with light diffuser plates to provide broad beams. LED properties like flash rate, intensity, and duration are remotely controllable. Calibration data using the LI system are taken at regular intervals, from which PMT gain, PMT time offset, and detector readout stability can be measured.

4.2.5.2 z-Axis Deployment System

The z-Axis deployment system allows light sources and radioactive sources to be deployed directly into the $\bar{\nu}$ Target. Sources are deployed via a motorized pulley-and-line system down through the chimney of the detector to a vertical position known to a precision of 1 mm. A glove box mounted at the top of the detector chimney, shown in Figure 4.4, is used as a source deployment interface. The interior of the glovebox is pressurized with nitrogen above ambient pressure in order to maintain clean and radiopure detector conditions while in use.

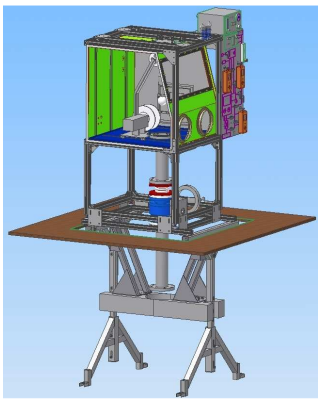

Figure 4.4: CAD schematic of the glovebox which serves as an interface for deploying calibration sources into the detector. The cylindrical flange near the bottom of the figure attaches to the detector chimney via a flexible manifold to minimize mechanical stress on the acrylic vessels. The blue square at the middle of the figure is a ball valve which is typically kept closed during normal detector operation, but opened in order to allow source deployment. White disks inside the green glove box (gloves not shown) are the pulley used by the z-axis deployment system. Panel to the right of the glove box ports is the nitrogen gas control system.

4.2.5.3 Guide Tube

Encapsulated radioactive sources may be deployed into the GC by means of a rigid, hermetic, looped, stainless steel guide tube (GT). Sources are driven through the length of the tube on the end of a wire, driven by an electric motor. This system allows sources to be deployed just outside of the $\bar{\nu}$ Target vessel wall or just inside the GC wall, *e.g.* a ^{252}Cf source to measure neutron capture at the edge of the detector's fiducial volume. Within the tube, the position of sources is known to 1 cm.

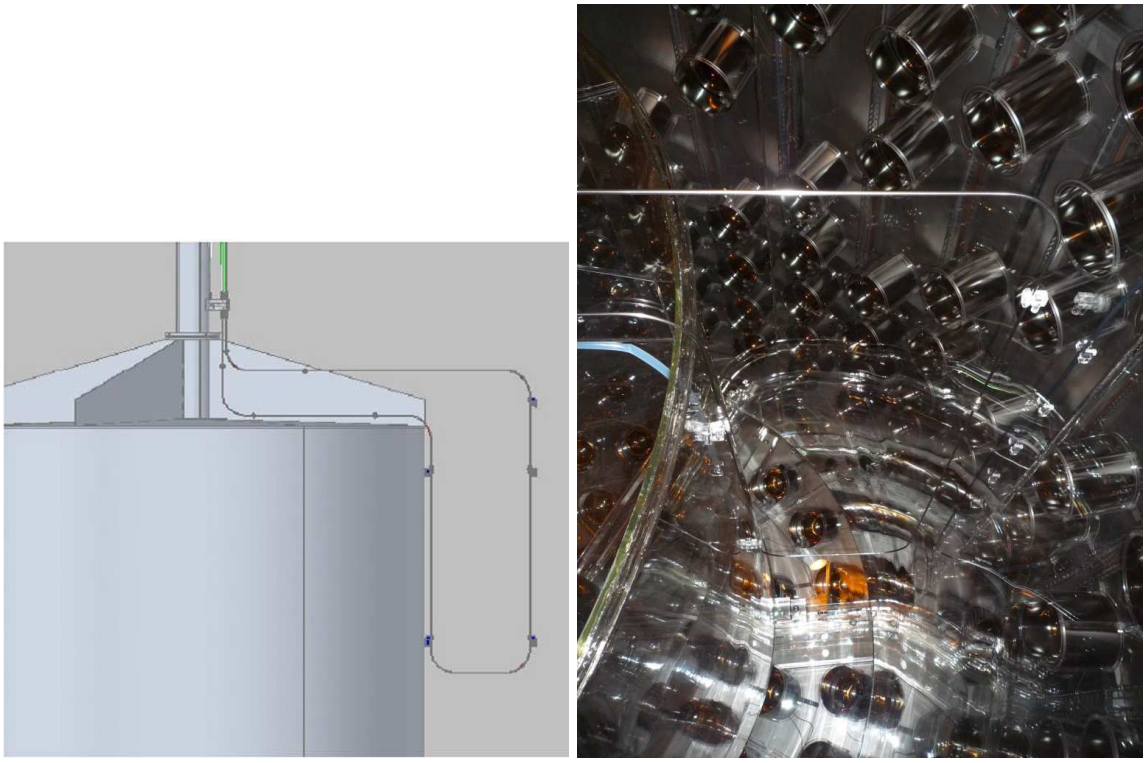

(a) Guide Tube CAD Schematic (b) Installed Guide Tube

Figure 4.5: Fig. 4.5(a): CAD schematic of Guide Tube, shown mounted against edge of $\bar{\nu}$ target vessel (GC and buffer vessels not shown). Fig. 4.5(b): Photograph of Guide Tube installed in Far Detector, showing photomultipliers in background.

4.2.5.4 Buffer Tube

A hermetic deployment tube is located in the buffer, allowing source deployment just outside of the GC vessel wall. As with the GT, the glovebox is used as a deployment interface, and a wire driver moves the source capsule through the tube to a position with precision ∼1 cm.

4.2.5.5 Articulated Arm

The articulated arm system will allow radioactive sources to be deployed throughout the $\bar{\nu}$ Target region. As depicted in Figure 4.6, teh arm would deploy down the chimney of the $\bar{\nu}$ target, and the atriculation woudl allow a calibration source to be placed anywhere within that vessel with high spatial precision. This form of calibration would allow full mapping of detector response as a function of position within the $\bar{\nu}$ Target, energy, and particle species. At the time of this writing, the articulated arm has not yet been installed in the Far Detector laboratory.

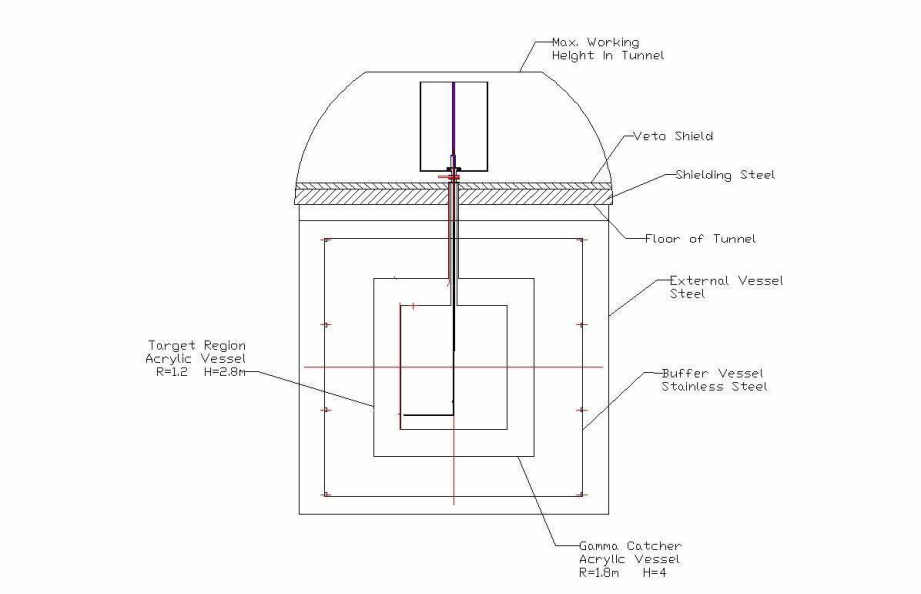

Figure 4.6: Depiction of the Articulated Arm being deployed along the central axis of the $\bar{\nu}$ target, and articulating near the bottom of the acrylic vessel. Detector vessels are shown in the surrounding, along with the glovebox at the top of the detector. From [9].

4.3 Main Detector Data Acquisition Systems

Signals from the PMTs of the ID and IV are read out by a single Data Acquisition System (DAQ) based on digitization of PMT waveforms by flash-ADC electronics [120]. The DAQ processes data split from the PMT signal/HV cables, and handles it until written to disk as digitized waveforms.

PMT signals from the splitters enter into custom Front-End Electronics (FEE) where the signals are amplified, clipped, baseline-restored, and filtered for coherent noise. These steps prepare the signal pulses for digitization. The FEE also sums sets of 8 PMT channels and feeds the summed charge signals to a custom trigger system. To prevent overshoot in the trigger system, the summed signal is truncated after 100 ns by re-adding a delayed signal; this also has the effect of suppressing signals of larger frequency than ∼1MHz.

The trigger system [121, 122] is designed to be deadtime-free. PMT signals from the ID and IV are divided into three groups: two groups of 195 PMTs each distributed uniformly around the ID, denoted A and B; and one grouping of the IV PMTs. If the sum of any group is above a specified threshold, all waveforms of all PMTs in the ID and IV are recorded for 256 ns. This threshold is approximately 0.35 MeV of visible energy for the ID, and 10 MeV for the IV. This low threshold of the ID trigger yields an efficiency of 100% with negligible uncertainty at the analysis threshold of 0.7 MeV. Discussion of the trigger efficiency as it effects the oscillation analysis may be found in Sections A.3.2.2 and 7.3.2.2.

Waveform digitization is carried out by 64 CAEN-Vx1721 (VME64x) waveform digitizers. Each unit reads eight channels with 8-bit flash-ADCs at a sampling rate of 500 MS/s. Internal memory in each unit allows for caching of up to 1024 waveforms of 4 μsec each without external readout. The 256 ns readout length for each waveform was chosen based on MC studies to sample at least ∼90% of the scintillation light from the single energy deposition. The dynamic range of the flash-ADC units leads to nonlinear response above 100 MeV visible energy, with significant (∼40%) non-linearity estimated above 500 MeV. Periodic monitoring of FADC baselines shows them to be stable to within a single ADC unit, though power-cycling of the units has been observed to induce instabilities in the baselines. This instability induces nonlinearities in single-channel response at low energies, below 2 PEs. However, the effect has been measured using LI calibration data, and is corrected for

in offline processing.

4.3.1 Performance

All waveform data from the FADC units are read out to commodity computer hardware, where it is written to disk for caching until transmission to an off-site data center. Examples of waveforms for Inner Detector and muon events are shown in Figure 4.7. Data from the OV are written to disk via a separate DAQ chain (as described in Sec. 5) with merging of the data streams occurring offline. All sources of energy deposition in the Innder Detector provides a trigger rate of nearly 200Hz. At this trigger rate, in total, nearly 50TB of data per year are generated by the Double Chooz Far detector. Since the Near Detector will be covered by less overburden, the incidence of muons will be much higher, prompting an even higher data rate.

Later, during offline processing, the waveform data are integrated to yield the total amount of charge deposited q_l deposited on each PMT l. Conversion of these data to a measure of the visible energy deposited in the ID is often referred to as the "Energy Scale" of the detector. Methods and evaluations of the uncertainties on the energy scale, which was treated differently for each analysis iteration, may be found in Sections A.5 and 7.5.

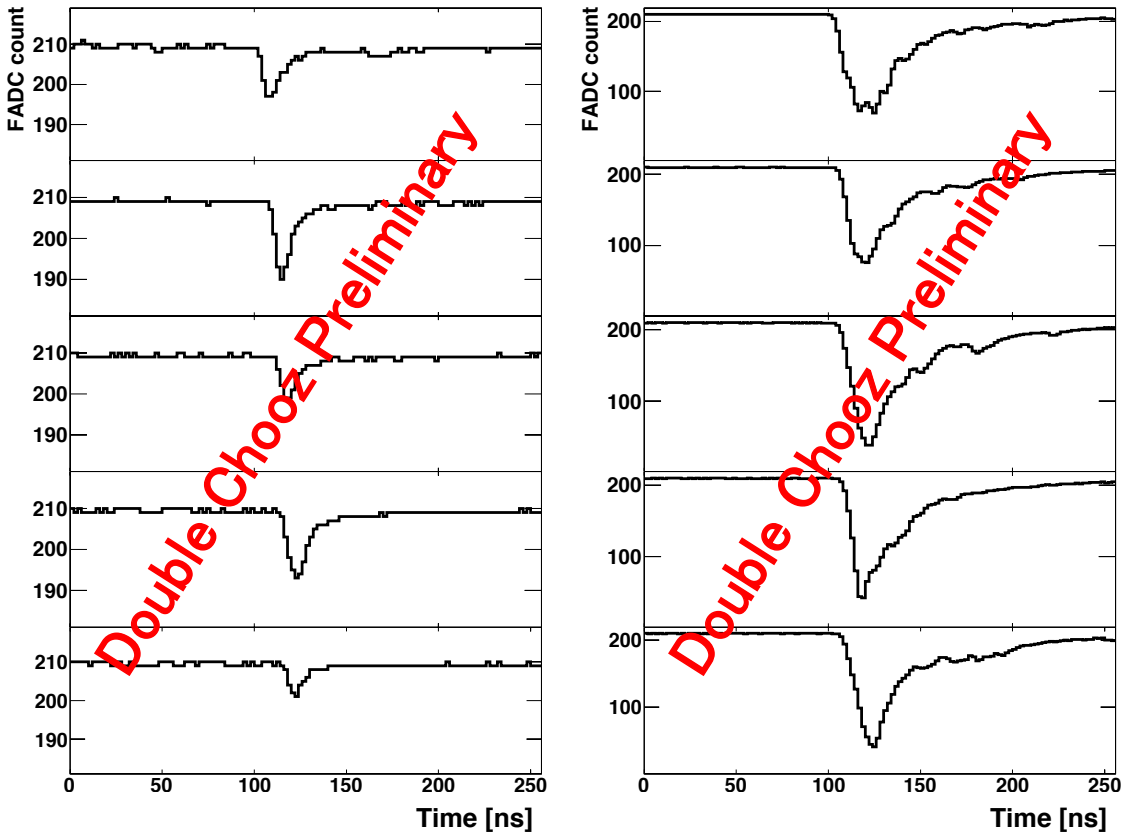

(a) ID Event Waveforms

(b) Muon DAQ Waveforms

Figure 4.7: Sample data wave forms from the Double Chooz DAQ. Fig. 4.7(a) is an energy depostion within the Inner Detector, while Fig. 4.7(b) is a muon passing through the detector.

Chapter 5

The Double Chooz Outer Veto

The Double Chooz Outer Veto (OV) is a plastic scintillator large-area veto designed to tag cosmic ray muons passing through and near the main detector. Cosmic ray muons are the progenitors of most of Double Chooz's backgrounds, with some backgrounds being irreducible by use of the Inner Veto alone. The OV allows reduction of backgrounds caused by muons which miss the Inner Veto, and enables characterization of some of these backgrounds through additional veto coverage and muon tracking. This chapter begins by describing the design concept (Sec. 5.1) of the OV and the design of the modules of which it is comprised (Sec 5.2. The principal hardware contribution by Columbia University to the Double Chooz experiment was the electronics and Data Acquisition System of the OV, which are described in Sections 5.3 and 5.3.1, with further descriptions of software components in Sections 5.4 through 5.5.2. An evaluation of overall OV performance is summarized in Section 5.6.

5.1 Design

The design of the Outer Veto varies slightly between the Double Chooz Near and Far detectors, though the concepts and general construction scheme are the same. The Outer Veto consists of multiple planes of high-efficiency muon detectors, arranged such that the planes cover the entire top of the Inner Detector, with additional coverage out to the sides of the ID. A cartoon representation of this can be seen in Figure 5.1. One plane rests on top of the steel shielding directly above the lid of the Inner Detector, with an opening in

the middle of the plane to accommodate the chimney. A second plane, the "Upper OV", is placed above the chimney and glove box, and extends horizontally to provide a veto against any muons which might enter the ID through the chimney. The OV extends past the horizontal extent of the ID in order to provide veto power against "near-miss" muons, which miss the IV but can still contribute backgrounds via spallation products.

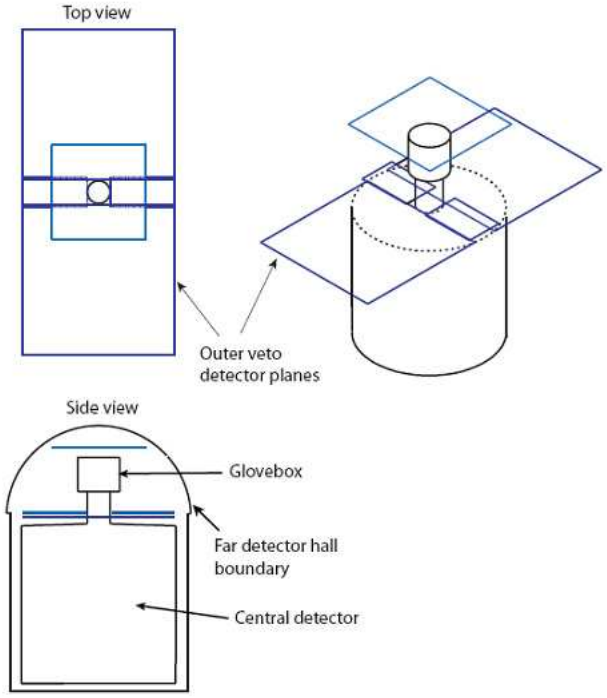

Figure 5.1: A cartoon of the Upper and Lower Outer Veto planes, relative to the Inner Detector, chimney, and glove box.

Each plane of the OV is comprised of multiple layers of overlapping segmented plastic scintillator modules. A total of 44 modules are used in the Far Detector's OV, while the Near OV will be comprised of up to 70 modules. The segmentation is due to construction of the modules from long plastic scintillator strips (see Sec. 5.2). The modules in different layers are rotated orthogonal to each other to allow the segmented nature of the modules to enable localization of muon tracks (and subsequently denoted x and y layers). While most modules are places atop the steel shielding located on top of each detector, some modules (8 for the Far OV, and up to 16 for the Near OV) are suspended from the ceiling of each

experimental hall to provide veto coverage over the dead "chimney" region of the detector. The extent of the OV is larger than the vertical cross-section of the detector to enable the tracking of "near-miss" muons which can act as progenitors to fast-neutron backgrounds.

The Outer Veto was employed for its designed purpose beginning with the second published Double Chooz analysis, as described in Sec. 7. Details on its use in characterizing and vetoing the fast neutron and stopping muon backgrounds may be found in Sec. 7.4.3.

5.2 Module Design

Each OV module is constructed from 64 rectangular-profile (1 cm $\times$ 5 cm) extruded plastic scintillator strips, as illustrated in Figure 5.2. The scintillator strips are coated during extrusion with a thin layer of opaque white plastic to assist in light containment. Also during extrusion, a hole is left along the center line of the strip to allow placement of a wavelength-shifting optical fiber; the fiber collects scintillation light generated within the plastic and conveys it to either end of the strip with less attenuation than traveling in the plastic alone. The strips are arranged into two layers of 32 strips each in a 2-over-1 overlapping fashion to reduce uninstrumented area. Two sizes of module have been produced, defined by the lengths of their constituent strips: "long" modules of strips 3625 mm in length, and "short" modules of strips 3225 mm in length. The other dimensions of each module are dictated by the profile dimensions of the strips, being 1625 mm in width and $\sim$ 50 mm height.

The optical fibers strung through each strip read out the light generated by through-going muons. One end of the fiber is glued to a mirrored surface, while the other end is fed to a fiber holder. The fiber holder, shown in Figure 5.4, acts as an interface to a 64-channel multi-anode PMT, which measures the light collected by the fiber. An example of such a PMT can be seen in Figure 5.3. The PMTs used on the Outer Veto are Hamamatsu H8804, and are mounted externally to the module against the fiber holder, with precision-placed pins ensuring alignment between the grid of polished fiber ends and the grid of photocathodes.

Structurally, the modules have been designed to rest on a flat surface during operation.

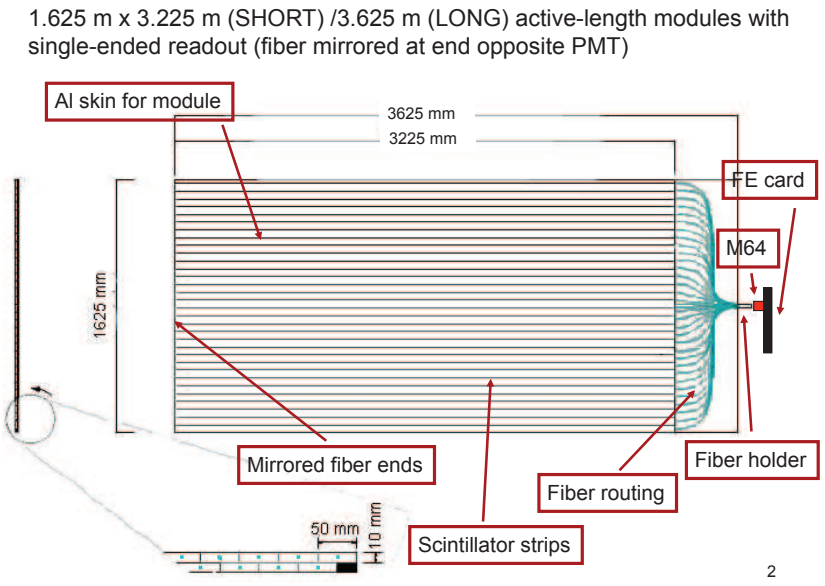

Figure 5.2: Illustration of an Outer Veto Module, showing overlapping-strip construction.

Figure 5.3: Photograph of a Hamamatsu 64-channel multi-anode PMT, similar to those used on the Double Chooz Outer Veto. Note that component labeled "FE Board" is referred to as a PMT Board in the text.

Figure 5.4: Photograph of a module during construction showing the Fiber Holder with wavelength-shifting fibers inserted. Note structure of fibers fanning out to double layer of 2-over-1 offset plastic scintillator strips.

Some structural integrity is provided by the aluminum C-beams around the edges of the modules. The exterior of the modules is thin sheet aluminum, with RTV adhesive used to ensure light-tightness at seams. Mounting points at the corners of the modules ensure precision placement within the experimental hall and position stability. Alignment pins for optical photogrammetry targets are also positioned at points on the top surface of the module.

5.3 DAQ Design

The OV Data Acquisition System (OVDAQ) is responsible for receiving light from the ends of the module fibers, converting it to electrical impulses with the 64-channel multi-anode PMTs, digitizing the pulse heights, and writing the data to disk in a portable format.

5.3.1 Electronics Hardware Design

The OVDAQ electronics have been developed around a token-ring readout design. Each link of the token-ring daisy chain is a custom PMT readout board ("PMT Board") designed around the Maroc2 ASIC [123, 124] and a programmable flash-ADC. Signal data packets which have made their way around the token ring are conveyed to a computer via a USB interface board ("USB Board"), shown in Figure 5.5. The USB board is also responsible for sending control and diagnostic commands to the PMT boards on the chain.

Figure 5.5: Photograph of a Double Chooz Outer Veto USB readout board. USB connection is made at grey socket at left. Power may be received via USB connection, or by black power socket at lower-left. CAT6 cables to daisy chain of PMT boards attach at square metallic sockets on upper- and lower-right of board. LEMO clock connection attaches to cylindrical metallic connector at right.

The PMT readout board ("PMT Board" or "Front-End (FE) Board") attaches directly via a socket to the back of an M64 PMT. A schematic of this board's layout is shown in Figure 5.6. Signals from the PMT enter directly into the Maroc2 ASIC. The first stage of processing involves a pre-amplifier, where a set of programmable gain constants are applied. The signals from each channel are then split and processed along two parallel paths. One path utilizes a fast-acting unipolar pulse shaper and fast threshold comparator to quickly prepare signals for logical processing by an FPGA. The other path uses a more accurate slow shaper and buffer to temporarily hold signals until a trigger decision is rendered by the FADC. Depending on the programmed trigger conditions, the FADC can allow the delayed slow signals to be passed to an ADC and output to the rest of the readout chain.

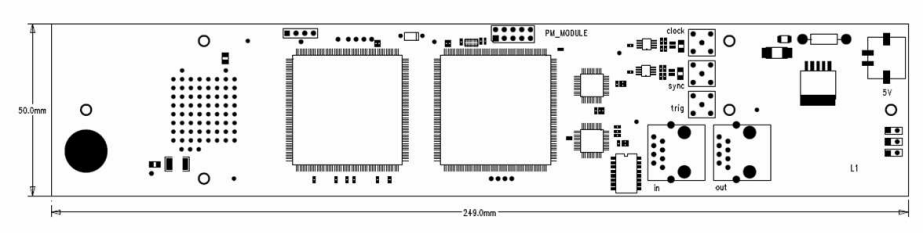

Figure 5.6: Schematic layout of an Outer Veto PMT Readout board. From left to right: large black circle is HV input socket; grid of 64 black dots is socket for attaching M64 photomultiplier tube; large chip on left is Maroc2; large chip on right is FPGA; trio of 5-pin connectors labeled 'clock', 'sync', and 'trig' are LEMO sockets; pair of 8-pin connectors labeled 'in' and 'out' are CAT6 sockets for data daisy chain; 2-pin terminal labeled '5V' is low-voltage power socket; trio of objects at bottom-right are LED status indicators.

The FPGA trigger conditions have been developed to allow high single-module muon veto efficiency while managing the output data rate of the OV as a whole. Tests within the Double Chooz experimental hall showed a high degree of background radiation. Compton scatters by natural gamma rays inside the OV module strips created a prohibitively-high data rate if data were to be read out following each single-strip trigger. Thus, the FPGA was configured to allow data readout only in cases of geometrically-overlapping strips being simultaneously hit. This reduced the trigger rate to a manageable level without diminishing muon detection efficiency.

5.3.2 Maroc2 Crosstalk Testing

Preparation for Outer Veto operation involved characterization and testing of the PMT board and Maroc2's functional properties. One particular measured property was the amount of inter-channel signal crosstalk. Inter-channel crosstalk on the Maroc2 chip could contribute spurious triggers to OV operation. Characterization of this effect was carried out with two complementary methods: an optical mask illuminating isolated pixes of an M64 PMT; and injection of charge into single channels of the PMT board socket. The methods are complimentary in that the optical model measures a combination of dynode chain crosstalk in the PMT and electronic crosstalk in the PMT board and Maroc2, while the charge injection method measures only the electronic component of any crosstalk.

5.3.2.1 Optical Crosstalk Measurements

Optical crosstalk measurements were made at a test stand at Barnard College, utilizing a prototype Microsoft Windows-native OVDAQ. The test stand was comprised of a dark box with an aluminum PMT mounting plate on one end, and a Picoquant LED light source mounted at the other. Illumination of the LED was synchronized with a gate trigger on the DAQ. Inside the aluminum PMT base plate, an opaque mask was slid parallel to and in front of the PMT photocathodes. The mask was drilled with a series of holes spaced so as to allow light from the LED to fall on crosstalk-isolated channels of the PMT. A ten-second-long data run was taken to acquire gated data. The mask was then slid in incremental positions to allow the next set of pixels on the PMT face to be evaluated, and another data run taken. This process was repeated nine times to allow all pixels on the PMT face to be tested. The data were then analyzed to measure the pulse heights in pixels neighboring those being illuminated.

A sample of 50 PMTs were tested in order to characterize tube quality control parameters. Results from this sample are shown in Fig. 5.7. No serious deviations were detected. While this test was a measure of the full tube and electronics crosstalk response, the opaque mask setup precluded accurately quantifying the expected crosstalk. Since the mask was separated from the face of the PMT by a few millimeters, alignment of the mask and dispersion of the LED light after passing through the mask was found to be non-negligible

in measuring the absolute amount of crosstalk. The LED-based test bench measurements were nevertheless a valuable quality assurance exercise.

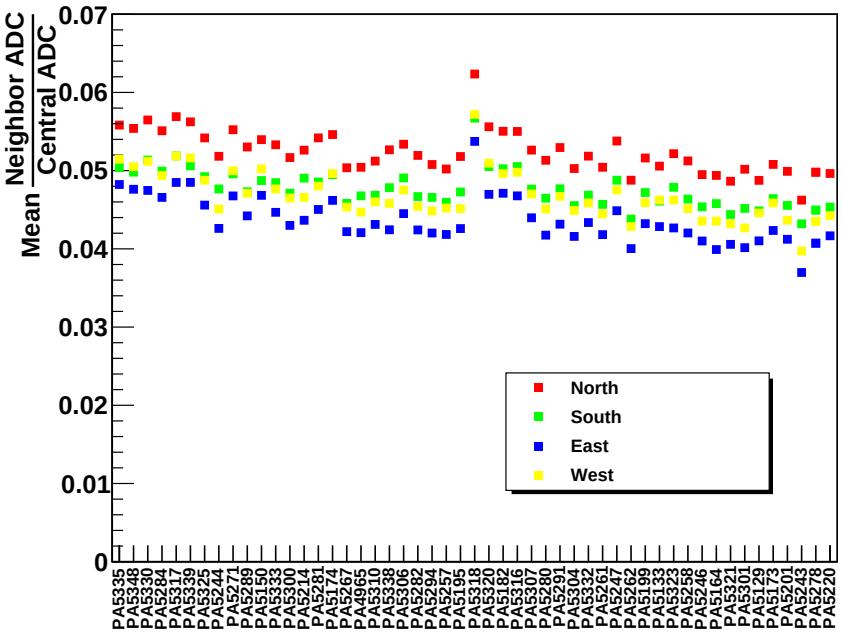

Figure 5.7: Results of optical crosstalk measurements for 50 M64 PMTs.

5.3.2.2 Electronic Crosstalk Measurements

In this testing scenario, the PMT board was examined without a PMT mounted to its 64-channel socket. Instead, the socket was fitted with a breadboard consisting of a LEMO connector and loose lead with a single-pin tip. The single pin allowed charge to be injected into any of the 64 channels of the socket by manual placement of the pin in that socket. A negative square pulse 8ns wide was fed into the LEMO connector, where a 10kΩ resistor

converting the pulsed voltage to an excess of charge on the lead tip. The height of the pulse was varied to allow the crosstalk at different amounts of injected charge to be measured. Short runs of the Windows DAQ took data while a 10kHz pulse rate triggered the PMT. Studies were carried out investigating how crosstalk effects changes as a function of injected charge and board DAC trigger threshold.

To investigate how crosstalk levels are affected by the DAQ threshold, data runs were carried out with a pulse height of 1V over a range of DAC thresholds from 600 to 1200 in steps of 100. Results are shown in Figures 5.8 and 5.9. The data clearly show that for DAC values of 800 and above, no crosstalk was seen in any of the 64 channels. At thresholds of 700 and above, no crosstalk is seen farther than one channel away from the injection channel. In cases where crosstalk was observed, all levels are below 1% of the signal measured in the injection channel. As the pulse height studies farther down will show, crosstalk is higher for lower pulse heights, so it may be presumed that increasing the pulse height for these trials would have resulted only in lesser measured values. Early results from PMT characterization studies have indicated that operational DAC thresholds will likely be in a range near 1000. This should serve to suppress most crosstalk during the experiment's running.

Main Results

Following the strange results described above, and in better agreement with the predicted amounts of charge which would be observed due to PMT usage, any further tests were carried out on a range of pulse heights between 0.5V and 2.5V in increments of 0.5V. Pulse heights of between 1.0 and 1.5V were measured to produce a mean ADC count of approximately 350, the equivalent of 10 photoelectrons. Measurements were carried out with two different PMT boards to allow possible levels of variation between chips to be investigated.

Preliminary results revealed a counter-intuitive relationship between the relative crosstalk and pulse height: increases in pulse height reduced the relative crosstalk. One hypothesis to explain this behavior suggests that the amount of signal induced in nearby channels does not scale with voltage as quickly as the main signal does. As a result, the ratio of the

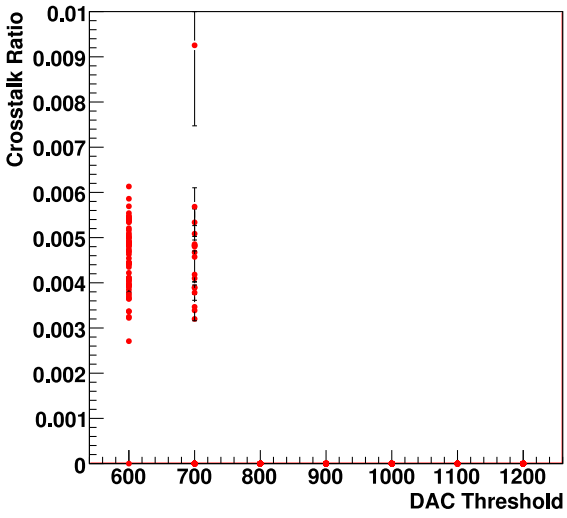

(a) Left Channel $(n-1)$

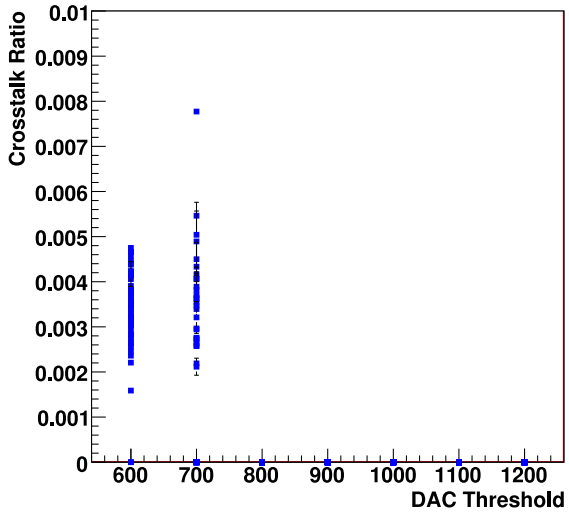

(b) Right Channel $(n+1)$

Figure 5.8: Crosstalk as a function of DAC threshold for the neighboring channels closest to the injected channel.

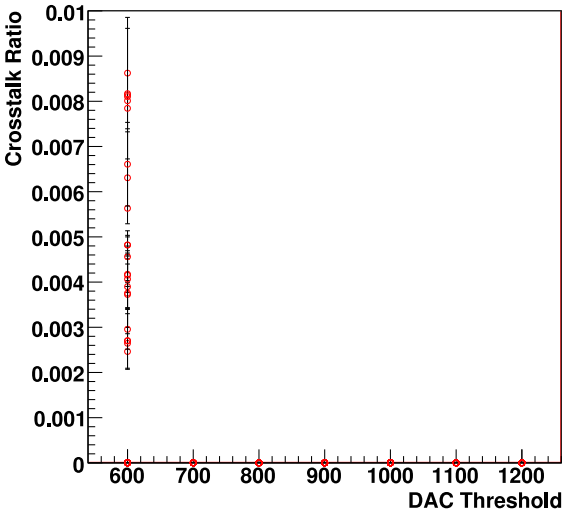

(a) Left Channel $(n-2)$

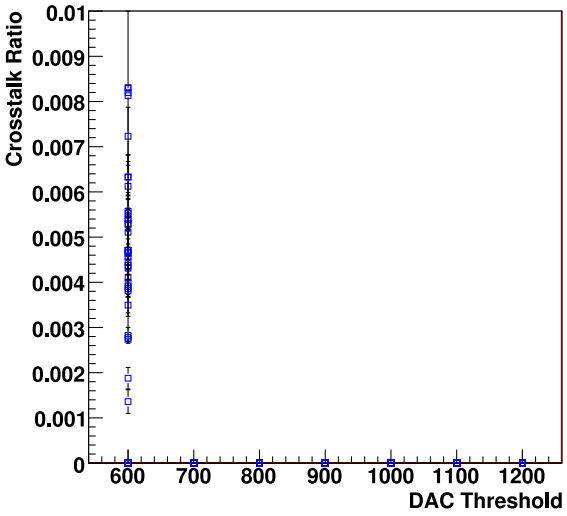

(b) Right Channel $(n+2)$

Figure 5.9: Crosstalk as a function of DAC threshold for the second-closest neighbors to the injected channel.

two decreases with as the pulse height is raised. Another theory attributes the crosstalk to the fast shaper in the Maroc2 chip creating a constant amount of crosstalk in neighboring channels whenever it triggers. Reprocessing data to measure the absolute magnitude of the crosstalk instead of the relative ratio supported this theory, showing that the magnitude of crosstalk did not change as a function of injected charge. These data quickly allowed the scale of electronic crosstalk affects to be placed at the sub-percent level.

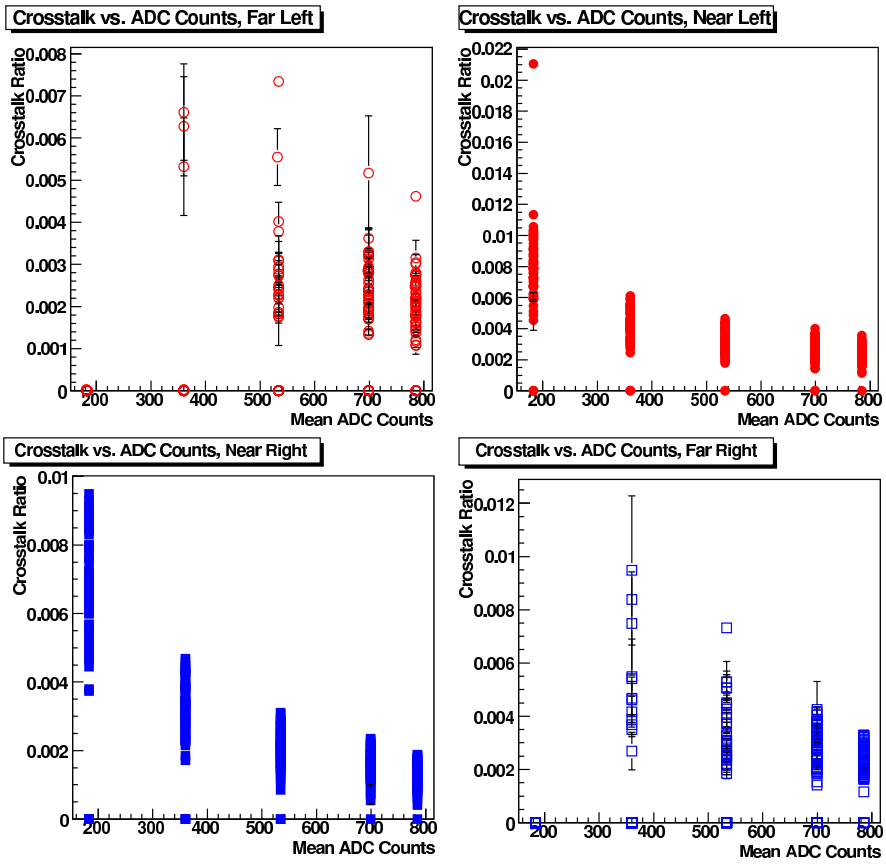

Figure 5.10: Crosstalk as a function of injected charge, parametrized by the measured mean ADC count.

Further investigation revealed some subtle properties of the crosstalk. A number of channel pairs were observed to have zero mutual crosstalk for many (sometimes all) values of the injected pulse height. Upon consulting a schematic of the Maroc2 pin layout (shown in Fig. 5.3.2.2), these channels were verified as being those whose input and output terminals

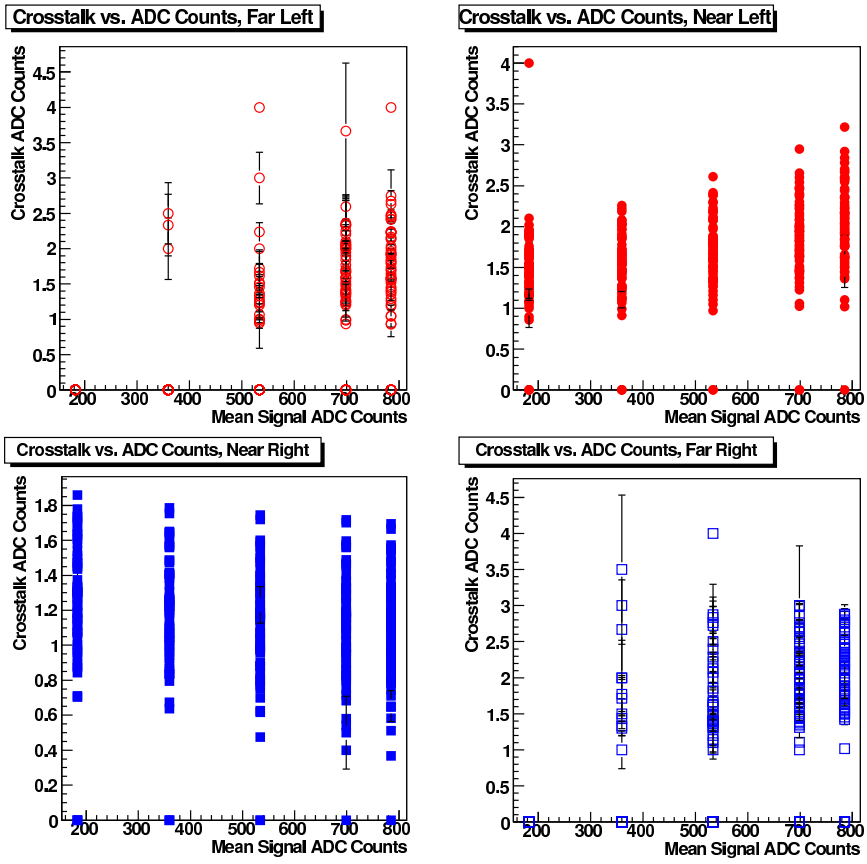

Figure 5.11: Absolute crosstalk magnitude, in ADC counts, as a function of injected charge, parametrized by the measured mean ADC count.

were located around the corners of the Maroc2 chip from each other, and are thus well-isolated. In other cases, a grounding pin separated two sequential channels, providing a similar isolation effect.

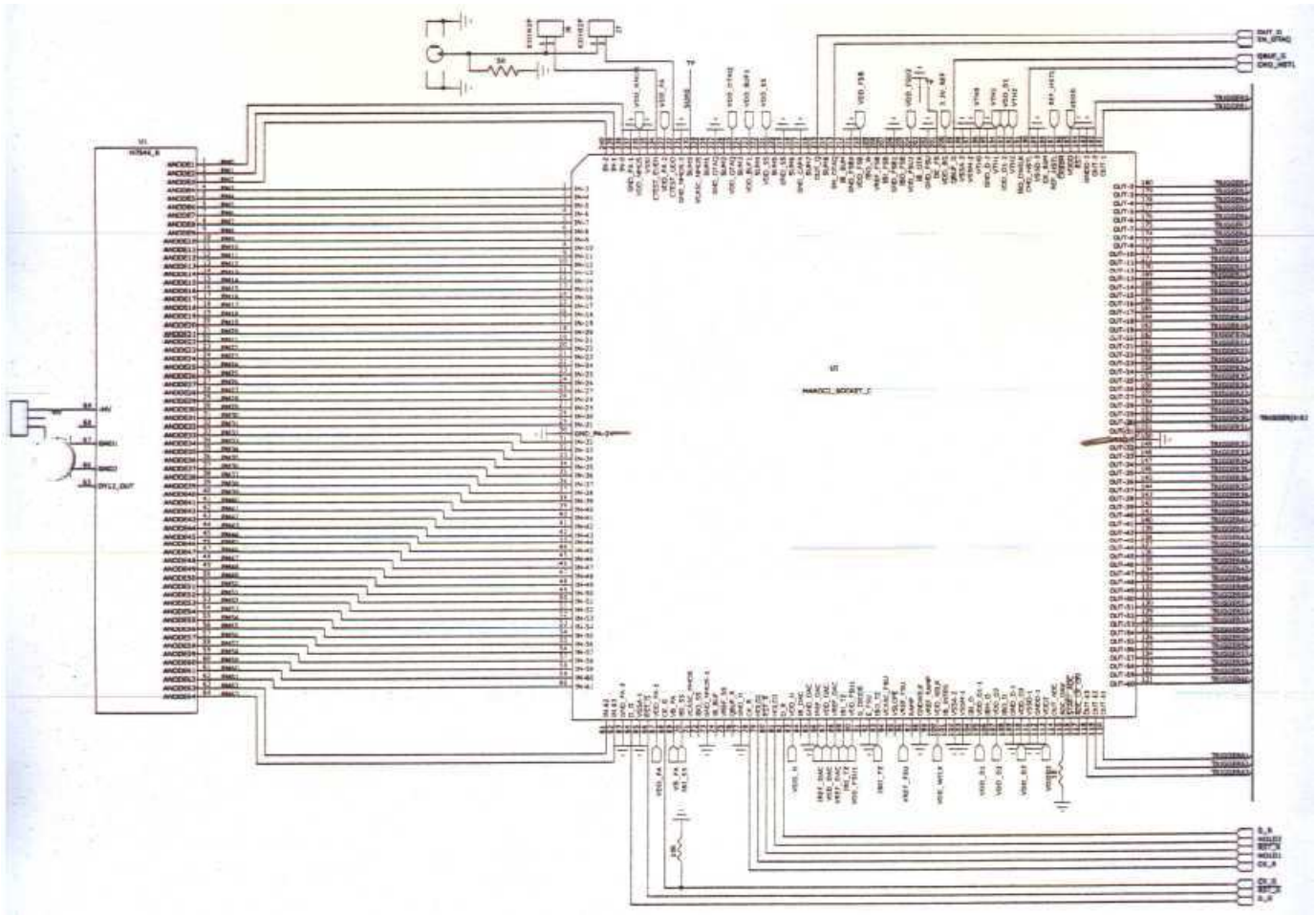

Figure 5.12: Diagram of the Maroc2's pin layout. Features to note include the ordered positioning of input and output channels from top to bottom, corner separation between channels 1 and 2, and 61 and 62, as well as ground pin separation between channels 31 and 32.

Also, there was evidence that crosstalk between channels increased in a linear fashion with channel number. This trend was present at all pulse heights, and for both first and second neighbors. The cause of this is unknown, and can most likely be attributed to some

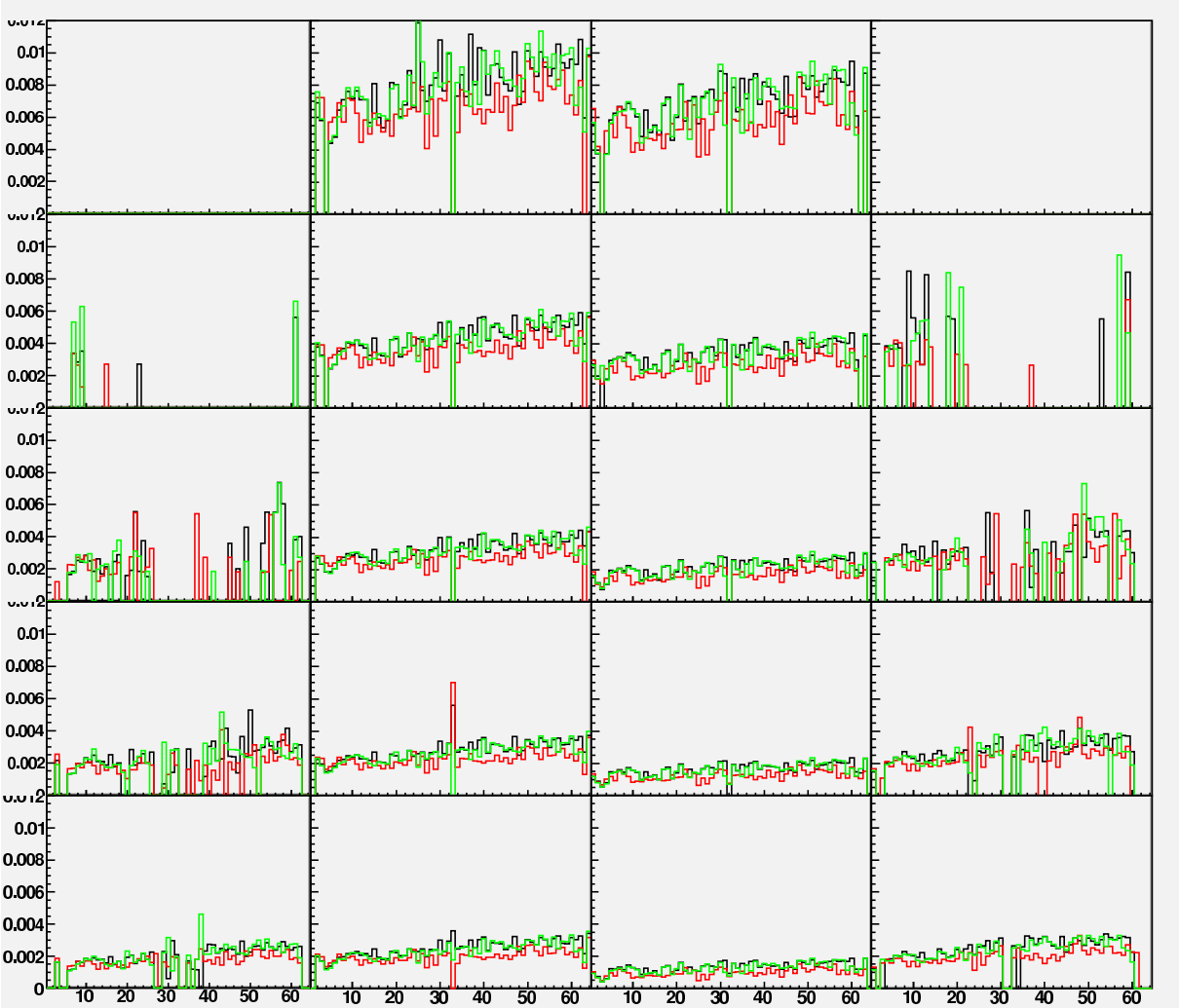

Figure 5.13: A set of plots showing crosstalk ratios as a function of channel number from zero to 64 for three different PMT boards (in red, black, and green). Leftmost column shows far-left neighbors, rightmost shows far-right neighbors, while the two central columns show left and right near neighbors. Rows show data sets for a common pulse height (mean ADC count) starting with the lowest at the top. Each subplot is on a scale from zero to 0.0012 for the crosstalk ratio. Of note are the 'linearity in channel number' trend, as well as the 'left-right asymmetry.' Zero-crosstalk channels can be clearly seen which channel numbers corresponding to well-isolated neighbors.

Pulse Height [V]	ADC Counts
0.5	183
1.0	360
1.5	534
2.0	699
2.5	785

Table 5.1: Table of corresponding pulse heights and measured signal ADC counts. For reference, 350 ADC counts is equivalent to approximately 10 PE.

aspect of the internal chip design. During data-taking, the order of channel testing did not follow the numbering convention, with the raster-like method of testing starting in an arbitrary direction. The trend was also seen in both chips tested, with the order of channel testing different between the two chips. Thus, it is unlikely that this was a time-dependent affect. Consulting the pin layout of the Maroc2, it appears that higher-numbered channels enter and exit the chip on the opposite side as lower-numbered channels. There may be some aspect of the chip architecture or environment which changes from one side to the other, producing this linear dependence. Finally, there was a noticeable asymmetry in the amount of crosstalk depending on whether the neighboring channel was of a lower or higher number than the injected channel. Again, there is no obvious cause of this, so it can only be attributed to some aspect of the Maroc2 internal architecture. The level of asymmetry was not large enough compared to the scale of the crosstalk to warrant any further consideration.

Correction for Crosstalk

The desired end result of these analyses is a set of correction factors which may be applied during normal operation of the Outer Veto in the case of simultaneous hits on two neighboring scintillator channels. A subtractive correction would allow errant signals from crosstalk to be removed, allowing physicists to check if the signals came from a single particle traversing both scintillator strips, or from crosstalk. Since the amount of crosstalk does vary channel-by-channel for any given pulse height, the simplest approach is to apply a

correction based on the mean crosstalk for that pulse height. However, since the total level of crosstalk, including fluctuations, is at or below those of optical crosstalk and temporal baseline variations, a correction for such a small effect would be superfluous.

The results of these studies deemed it unlikely that electronic crosstalk would contribute large numbers of errant hits to the operation of the OV. The 350 ADC counts measured in a typical muon hit could be expected to generate sub-percent-level crosstalk in the nearest neighbors to the hit channel. This level of fluctuation is on the same order as time-varying fluctuations in the baseline of the readout channels, a factor considered negligible. Due to this similarity, applying any correction for crosstalk in analysis or simulation was deemed impractical. Other characterizations of the PMTS suggested that operating DAC thresholds for the experiment would be in a range near 1000, a value where crosstalk in both near and far neighbors was greatly suppressed. Thus, electronic crosstalk on the PMT board and within the Maroc2 chip was considered a negligible source of errant hits in OV operation.

5.4 OV EventBuilder and DOGSifier

After being written to disk in a binary format, data from each of the USB readout streams must be merged together into coincident events and subsequently converted to a standardized Double Chooz data format. These steps are carried out by programs labeled the EventBuilder and DOGSifier, respectively, both of which were developed by M. Toups [125].

5.5 Monitoring Software

Diagnostic monitoring of the OVDAQ is implemented at two timescales: real-time monitoring with no logging via the Online Monitor and DAQ exception handling; and logged long-term monitoring via the Offline Monitor.

5.5.1 OV Online Monitor

The OV Online Monitor provides real-time monitoring of the OV data stream. Decoding of binary data files from the OV DAQ occurs in parallel to, and independent from, the OV Event Builder. Data are filled into a moving-time-window buffer, and a number of diagnostic

metrics are measured. These metrics include per-channel average ADC, per-channel average hit rate, per-channel pedestal, average board rate, and average board ADC. Data from the OV trigger boxes are also monitored, including trigger box hit rate per input, and trigger box sync packet arrival offset. Finally, a number of system health parameters are measured, including the rate of packets which fail parity checks, and DOGSifier lag behind EBuilder processing. Additionally, monitoring of OV High Voltage systems is implemented through the querying of a time-history database. An alarm notification system performs checks on all metrics, triggering notifications to shifters or experts depending on the observed severity of the warning.

The OV Online Monitor is integrated with other Double Chooz Online systems. Alarms notifications are sent to shifters by way of the Gaibu notification system and its GUI and email capabilities. The OV Online Monitor is fully integrated with the Double Chooz Online Monitor Framework [126], making use of its histogram and plotting libraries and conveying graphical data using its Server/Client system.

The OV Online Monitor is written in C++, with use of ROOT and Double Chooz Online Monitor Framework libraries. Additional detail about the OV Online Monitor implementation, as well as some code, can be found in Appendix E.

5.5.2 OV Offline Monitor

After the OV data have been event-built and DOGSified, they are periodically examined by the OV Offline Monitor. The Offline Monitor is designed to provide diagnostic data from periodic high-statistics samples of OV data, which are then logged in a database for long-term stability monitoring. As currently configured, the Offline Monitor examines all data from a day's worth of physics data-taking. Constituent hits of events are categorized by type (singles as crosstalk, mu-like doubles and xy-overlaps as muons) and counted. The rates of each type of event are stored on a per-channel basis in a MySQL database for later reference. Diagnostic plots of these data may be generated using ROOT macros for specified periods of time as studies warrant.

5.6 Performance

The Far Detector Outer Veto was installed in two stages between the Summers of 2011 and 2012. During the first phase between June 2011 and July 2011, the 36 modules of the lower OV were installed and commissioned. These modules began contributing to the experiment data stream later that Summer. The second stage occurred between June 2012 and July 2012, during which the upper OV was installed, commissioned, and fully integrated into detector operation.

In general operation, the Outer Veto is used as a "binary" veto: if a candidate IBD event is coincident with a valid trigger in the Outer Veto, it may be considered a background, depending on the analysis being performed. In most cases, a valid trigger is defined as a single "μ-like" double hit in a single module, where two physically-overlapping strips in a single module have triggered above threshold. This condition does not provide a reconstructable track for every OV event, but does provide the best possible efficiency as a veto at a sustainable trigger rate. Figure 5.14 shows example hit patters of OV triggers which are coincident with different cases of Inner Detector and Inner Veto triggers. The hit patterns show a marked "shadow" of the inner detector as expected. Hits in the OV which coincide with an ID hit but are *not* located directly over the ID outline may be random coincidences, or may be due to the progenitor near-miss muons of correlated backgrounds. Veto coverage of these types of near-miss muons provides additional veto power that the IV cannot provide, and in the future may allow tagging of pure samples of these types of backgrounds.

It is possible to estimate the efficiency of the Outer Veto at detecting muons which pass through it by cross-referencing with reconstructed muon tracks in the Inner Detector. Muon tracks within the ID and IV are reconstructed using a software tool called FIDO. If a muon track within the Inner Detector or Inner Veto points back at the OV, but the OV hasn't registered a trigger, that would be indicative of a hit lost to inefficiency. The result of this study is the inefficiency map shown in Figure 5.15, where a lower number indicates better performance. These results indicate that the OV offers muon detection efficiency of no worse than 98.5% for muons passing through OV away from its boundaries.

Data from the Outer Veto were not used in main analysis presented in the first Double

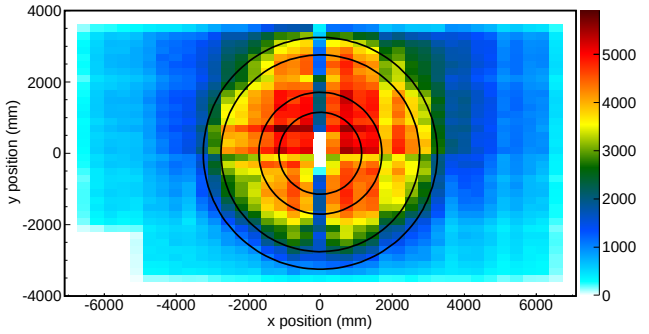

(a) ID-Coincident

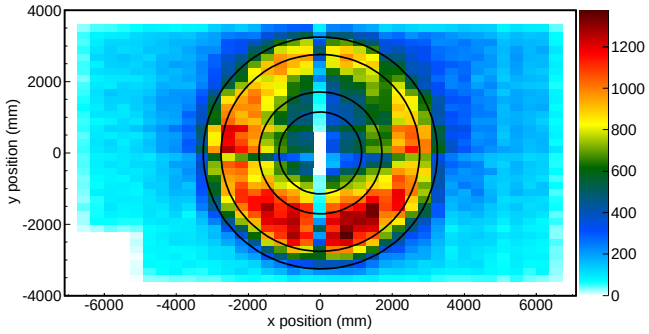

(b) No ID Energy, IV Coincident

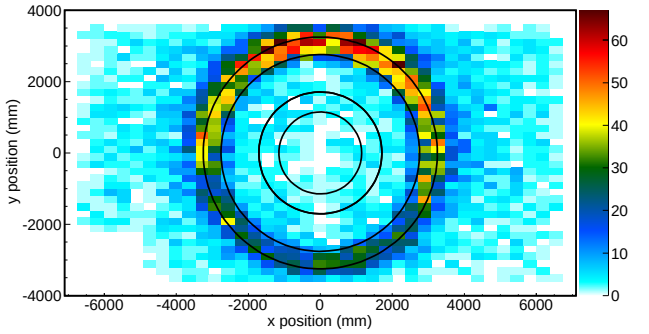

(c) IV Coincident, Large IV Energy

Figure 5.14: Plots of the locations of triggers in the Outer Veto which are coincident with triggers in either the Inner Detector or Inner Veto. Top figure shows events which are coincident with a trigger in the Inner Detector. Middle figure shows events which are coincident with a trigger in the Inner Veto, where no energy is deposited in the Inner Detector. Bottom figure shows events which are coincident with an event in the Inner Veto where a large amount of energy was deposited, indicative of a downward-going muon passing down the vertical length of the Inner Veto. Plots created by M. Strait.

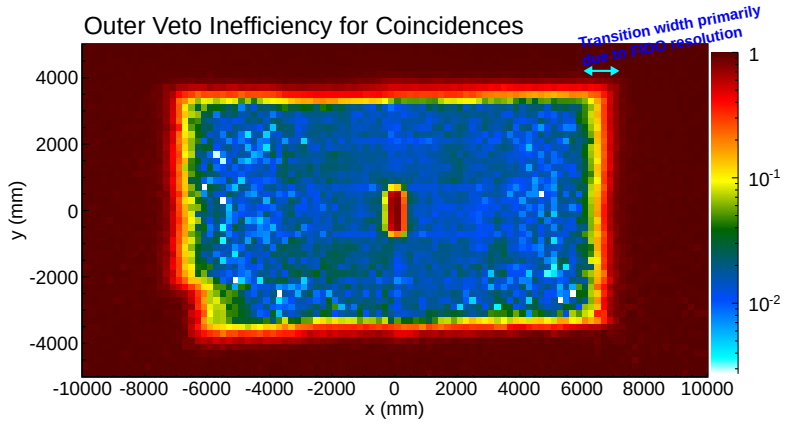

Figure 5.15: Map of measured inefficiency of the Outer Veto, using muon tracks reconstructed within the Inner Detector and Inner Veto using the FIDO reconstruction tool. An inefficiency of unity means that muons in that region of the plane of coverage are not detected by the OV. A lower number indicates better veto efficiency. Plot by M. Strait.

Chooz publication (see Sec. A). While the OV was taking data during much of the detector operating time included in that analysis, OV data was only used to further scrutinize data taken during a short period of two-reactors-off time (see Sec. A.4.4.2), and not as a general veto condition for physics data. The Outer Veto was included as a veto condition in the oscillation analysis of the second Double Chooz publication (see Sec. 7). It was further used in measuring the rate and shape of the fast neutron and stopping muon backgrounds (Sec. 7.4.3) as well as examination of a second period of two-reactors-off data (Sec. 7.8).

Part III

Double Chooz Analyses

Chapter 6

Neutrino Signal Flux Estimation & Uncertainties

Due to the phased construction schedule of Double Chooz, the far detector was commissioned before the beginning of near detector construction. As evidenced by previous experiments [6, 7], it is possible to make a measurement of θ_{13} using a single detector combined with an accurate prediction of the $\bar{\nu}_e$ flux emitted from the reactors. Additionally, the predicted flux can be constrained using data from other experiments as a "virtual" near detector. This chapter describes the signal estimation method used by the Double Chooz experiment, and the associated uncertainty calculation methods. The expected instantaneous neutrino rate and its inputs are described in Sec. 6.1, and this formalism is adapted to a prediction binned in neutrino energy and time in Sec. 6.2. In Sec. 6.3, the binned prediction formalism is adapted to accomodate an "anchor point" on its normalization based on the Bugey4 experimental results. Finally, in Sec. 6.4, methods for propagating the systematic uncertainties on the time- and energy-binned prediction are described in detail.

6.1 Instantaneous $\bar{\nu}_e$ Rate from a Single Reactor

Reactor antineutrino experiments detect $\bar{\nu}_e$ by observing the "Inverse β-decay" (IBD) interaction $\bar{\nu}_e + p \rightarrow e^+ + n$ as a flux of $\bar{\nu}_e$ from the critical reactor passes through the detector. The expected rate $\frac{dN^R(t)}{dt}$ of $\bar{\nu}_e$-induced IBD interactions from reactor R inside a detector

at time t is:

$$\frac{dN^R(t)}{dt} = \frac{\epsilon N_p}{4\pi} \frac{P_{th}^R(t)}{L_R^2 \langle E_f \rangle^R(t)} \langle \sigma_f \rangle^R(t) \tag{6.1}$$

In this equation, N_p denotes the number of free protons constituting the detector, ϵ denotes the detection efficiency of the detector, and L_R denotes the distance between the detector and each reactor. Other quantities depend on the state of the reactor at the time t: the thermal power P_{th}^R, the mean energy per fission $\langle E_f \rangle^R(t)$, and the mean cross-section per fission $\langle \sigma_f \rangle^R(t)$. Except for P_{th}^R, each of these time-dependent quantities is a function of the reactor fuel composition.

The following paragraphs will further describe the inputs to Eq. 6.1 in detail, as well as extend the formalism to one which considers the shape of the interaction spectrum. The order of explanation will follow the physical path of the neutrino from fissions in the reactor, to interaction in the detector. Each input to Eq. 6.1 also contributes some systematic uncertainty to $\frac{dN^R(t)}{dt}$, the effects of which will be discussed in Sec. 6.4.

6.1.1 Reactor Fission Rate Calculation

The two N4-type pressurized water reactors (PWRs) at the Centrale Nucléaire de Chooz produce heat through sustained fission of four principal fuel nuclides: ^{235}U, ^{238}U, ^{239}Pu, and ^{241}Pu. In addition to energy, each fission produces neutron-heavy daughter nuclides and fast neutrons. These daughter nuclides undergo β-decay in order to reach a stable nuclear state, and in doing so, release $\bar{\nu}_e$.

The first step to predicting the number of $\bar{\nu}_e$ released by each reactor is calculating the time-dependent rate of fissions $f_k^R(t)$ of the four fuel nuclides $k = \{^{235}\text{U},^{238}\text{U},^{239}\text{Pu},^{241}\text{Pu}\}$ inside the reactor core R. The $f_k^R(t)$ are heavily dependent upon the amount of each fuel nuclide within the reactor's instantaneous fuel inventory, as well as the instantaneous thermal power $P_{th}^R(t)$ of the critical reactor. This calculation is carried out using one of two reactor simulation packages: MNCP Utilities for Reactor Evolution (MURE), a 3-dimensional Monte Carlo-based simulation [11, 12]; or DRAGON, a 2-dimensional neutron transport model [127]. Example results from the MURE calculations may be seen in Figure 6.1. Validation of these codes [128] was carried out by comparisons of simulation results to destructive fuel assay data from a cycle of the Japanese Takahama-3 reactor [129], and to

the results of simulations using the same data by other code packages.

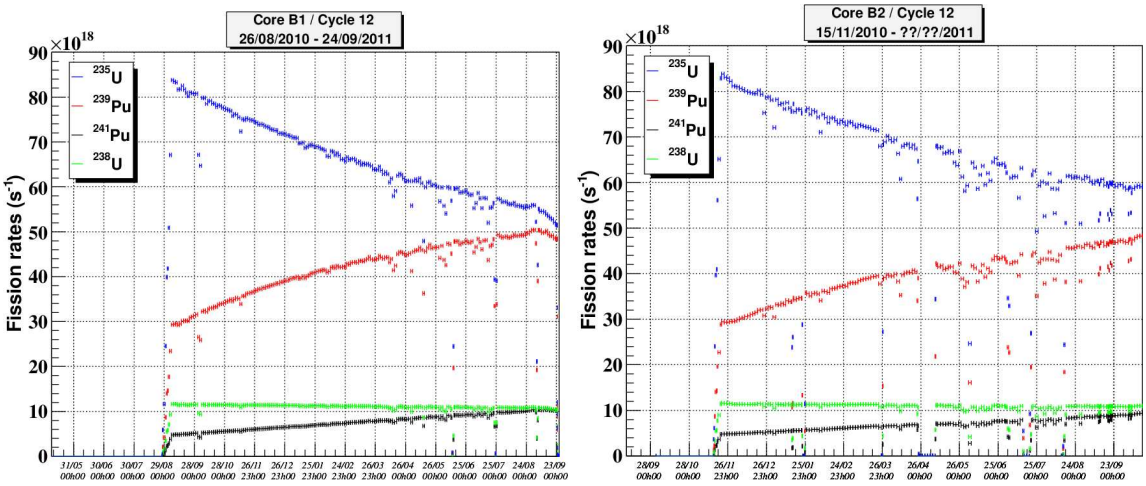

(a) Reactor B1 (b) Reactor B2

Figure 6.1: Fission rates for the Chooz reactors, as calculated by simulations with MURE, for each of the four main fuel nuclides. The lack of smooth evolution in time is due to fluctuations of the thermal power in each reactor. Note the decrease of ^{235}U due to burn-up over time, and the increase of ^{239}Pu and ^{241}Pu as those isotopes are bred from fertile fuel. From [10].

In practice, the MURE simulation calculates the fission rates $f_k^R(t)$ at 48-hour steps in the reactor fuel cycle based data acquired from the reactor management company, Electricite et Gaz de France (EdF). The data include reactor operating parameters such as thermal power $P_{th}^R(t)$ (see Fig. 6.11), concentration of boron in the moderator water, and control rod positions within the core. The simulation uses these parameters to determine the mass inventory of each fuel nuclide at the beginning of each time step. With the mass inventory known, the number of fissions of each nuclide is determined using the mean energy per fission $\langle E_f \rangle_k$ from each nuclide k and its subsequent daughters. The $\langle E_f \rangle_k$ are calculated from nuclear theory [130].

For our purposes, in addition to the fission rates $f_k^R(t)$ we also define the fuel fraction

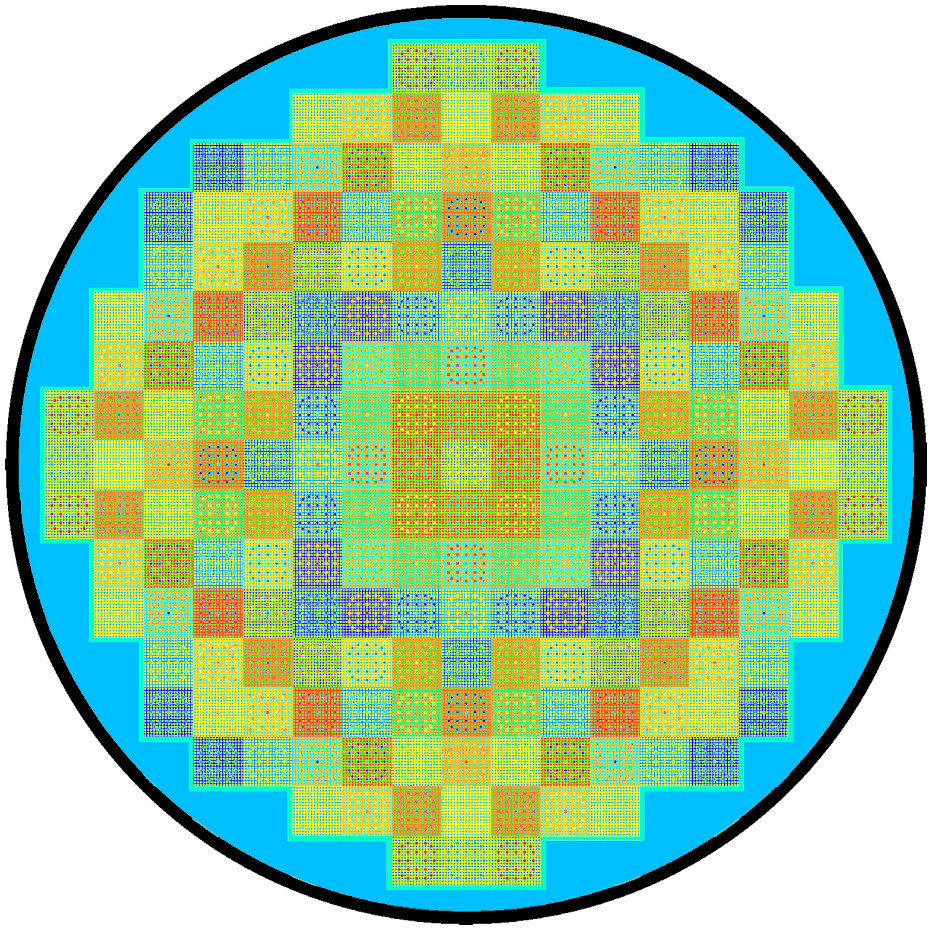

Figure 6.2: Top-down view diagram of reactor geometry, as used in the MURE [11, 12] simulations of the Chooz reactors. Outer black ring is steel pressure vessel; light blue is pressurized water moderator. Colored squares represent reactor fuel assemblies, with colors indicating fuel inventory and control rod type. From [10].

$\alpha_k^R(t)$ of each fuel nuclide within the reactor R at time t:

$$\alpha_k^R(t) = \frac{f_k^R(t)}{\sum_{k=1}^{4} f_k^R(t)} \tag{6.2}$$

where the index k runs over the four principle fuel nuclides ^{235}U, ^{238}U, ^{239}Pu, and ^{241}Pu. This fractional fuel composition allows other quantities in Eq. 6.1 to be parametrized in time, but independently of $P_{th}^R(t)$. Plots of these quantities are shown in Figure 6.3 for all three reactor fuel cycles considered in the Double Chooz analyses. The $\alpha_k^R(t)$ for a single fuel cycle are shown in Figure 6.4 along with representative error bars. Uncertainties on the $\alpha_k^R(t)$ stem from metrology of simulation inputs, as well as potential biases of the simulation algorithms.

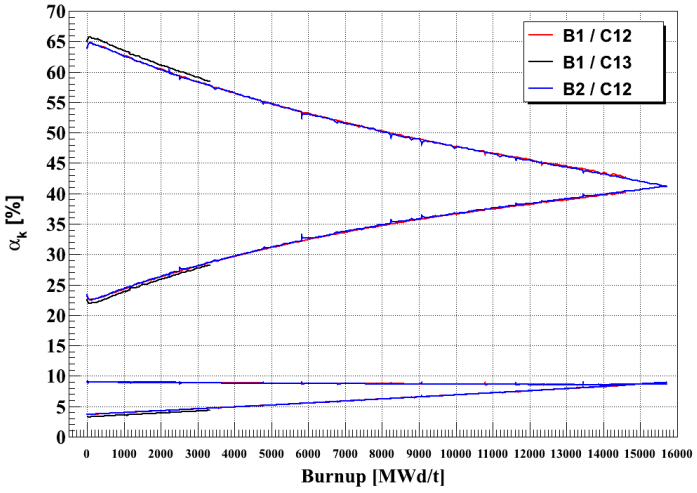

Figure 6.3: Fractional fission rates as a function of fuel burnup as calculated by simulations of the Chooz reactors using MURE. Inventories for three different fuel cycles are shown. Uppermost line represents ^{235}U, which is burned up over time; middleline represents ^{239}Pu, which increases over time; nearly-hoizontal line represents ^{238}U; increasing line at the bottom represents ^{241}Pu. From [10].

One other such quantity is the mean energy per fission $\langle E_f \rangle^R(t)$ of reactor R at time t, which is a weighted average of the $\langle E_f \rangle_k$ according to the time-dependent fractional fuel

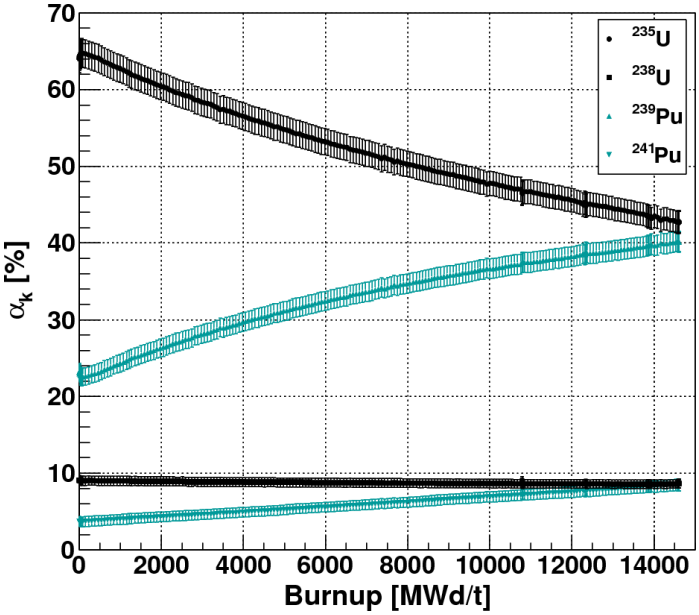

Figure 6.4: Fractional fission rates as a function of fuel burnup as calculated by simulations of the Chooz reactors using MURE, for a single fuel cycle of a reactor at Chooz. Uppermost line represents ^{235}U, which is burned up over time; middleline represents ^{239}Pu, which increases over time; nearly-hoizontal line represents ^{238}U; increasing line at the bottom represents ^{241}Pu. From [10].

composition $\alpha_k^R(t)$:

$$\langle E_f \rangle^R(t) = \sum_{k=1}^{4} \alpha_k^R(t) \langle E_f \rangle_k . \tag{6.3}$$

This quantity evolves in time slowly during the reactor fuel cycle as ^{235}U burns up and more of the thermal power is generated by the breeding and fissioning of ^{239}Pu and ^{241}Pu.

6.1.2 Mean Cross-Section per Fission

The mean cross-section per fission $\langle \sigma_f \rangle^R(t)$ of reactor R at time t in Eq. 6.1 is derived from the fuel composition (via the $\alpha_k^R(t)$) and the mean cross-section per fission $\langle \sigma_f \rangle_k$ of each principal fuel nuclide:

$$\langle \sigma_f \rangle^R(t) = \sum_{k=1}^{4} \alpha_k^R(t) \langle \sigma_f \rangle_k \tag{6.4}$$

The cross-sections per fission $\langle \sigma_f \rangle_k$ of each nuclide k are constructed by integrating the product of the emitted neutrino spectrum $S_k(E_{\bar{\nu}})$ with the inverse β-decay cross section $\sigma_{IBD}(E_{\bar{\nu}})$ over the full range of neutrino energies $E_{\bar{\nu}}$:

$$\langle \sigma_f \rangle_k = \int_0^\infty S_k(E_{\bar{\nu}}) \sigma_{IBD}(E_{\bar{\nu}}) dE_{\bar{\nu}} \tag{6.5}$$

An example of the resulting spectral shape may be seen in Figure 6.5. One notable feature of $\langle \sigma_f \rangle^R(t)$ is its time evolution, since it is a weighted average of the time-dependent fuel nuclide inventory $\alpha_k^R(t)$. Along with the time-dependence of the mean energy per fission $\langle E_f \rangle^R(t)$ of Eq. 6.3, this leads to a natural decreasing trend in time of the number of expected neutrinos even with the reactor held at constant power. This effect is illustrated in Figures 6.6 and 6.7, which are generated from the prediction of Eq. 6.1.

The neutrino spectra S_k have been developed from the emitted β spectra of neutron-activated foils of uranium and plutonium. Experiments carried out at the ILL research reactor in Grenoble, France, exposed thin films of ^{235}U [131, 14, 132], ^{239}Pu [14, 133], and ^{241}Pu [133] to a flux of neutrons from the critical reactor for short periods of 12 to 24 hours. The foils were then placed inside a high-resolution β spectrometer [134] and their emitted spectra measured. The measured spectra have then been fit to existing nuclear decay data and virtual β-decay branches to predict the emitted $\bar{\nu}_e$ spectra [96, 13]. Examples of the

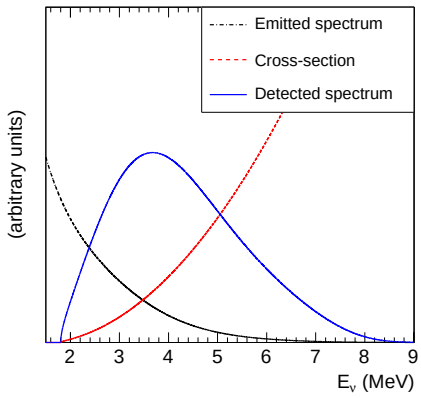

Figure 6.5: Illustration of the emitted neutrino spectrum from ^{235}U, the Inverse β-decay cross-section on free protons, and the resulting interaction spectrum shape when the two are multiplied together. The integral over the full spectral shape for all energies yields the $\langle\sigma_f\rangle_k$ for $k = {}^{235}$U, as mentioned in the text. From [13].

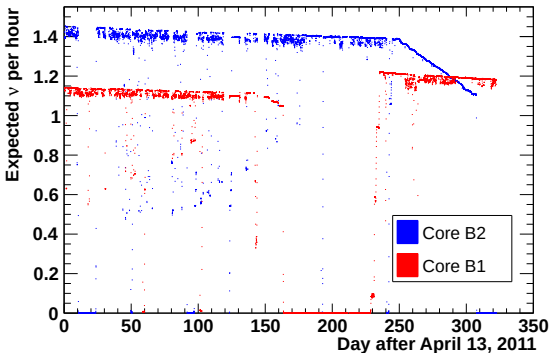

Figure 6.6: Expected neutrino rate as calculated by Eq. 6.1 for each of the Chooz reactors B1 and B2, versus calendar date. Notable features are the sharp fluctuations following reactor power, and the slow decline in time as the fuel inventory and mean energy per fission evolve with fuel burn-up. Figure by D. Lhuillier.

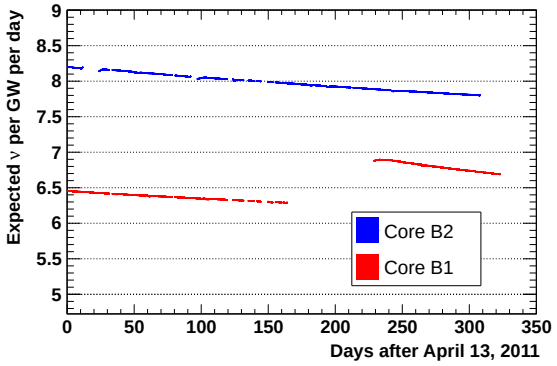

Figure 6.7: Expected neutrino rate as calculated by Eq. 6.1 and normalized for reactor power, for each of the Chooz reactors B1 and B2, versus calendar date. Especially notable is the slow decline in time of predicted neutrino rate as the fuel inventory and mean energy per fission evolve with fuel burn-up. Figure by D. Lhuillier.

β-decay data and fits may be found in Figure 6.8. Some theoretical corrections must be applied to these predicted neutrino spectra, due to the finite irradiation time used in the β spectrum measurements at ILL, as discussed in [13]. The magnitude of these corrections is small, as shown in Figure 6.10, but important due to their proximity to the area of highest oscillation probability for an experiment at a baseline of $L_R \sim 1000$m.

The only exception to this method is for the fuel nuclide ^{238}U, for which no β spectrum data yet exist. The reference spectrum for this nuclide has been constructed by theoretical means [15], or predicted based on the same *ab initio* method used to fit other spectra using known decay paths of ^{238}U [13]. In regimes of $E_{\bar{\nu}}$ where no data are available, a funtional fit to the data (or existing theory) with a sixth-order exponential-polynomial is made, as shown in Figure 6.9. While this provides a prediction for the number of neutrinos at all energies, the functional fits are considered inaccurate and used only when no alternative (*e.g.* interpolated data) exists.

The IBD cross-section $\sigma_{IBD}(E_{\bar{\nu}})$ is calculated from the charged-current interaction $\bar{\nu}_e + p \rightarrow n + e^+$. After integrating over all possible e^+ recoil directions, the simplified formula is given in [135] as:

$$\sigma_{IBD}\left(E_{\bar{\nu}}\right) = K E_{e^+} \sqrt{{E_{e^+}}^2 - m_e^2} \tag{6.6}$$

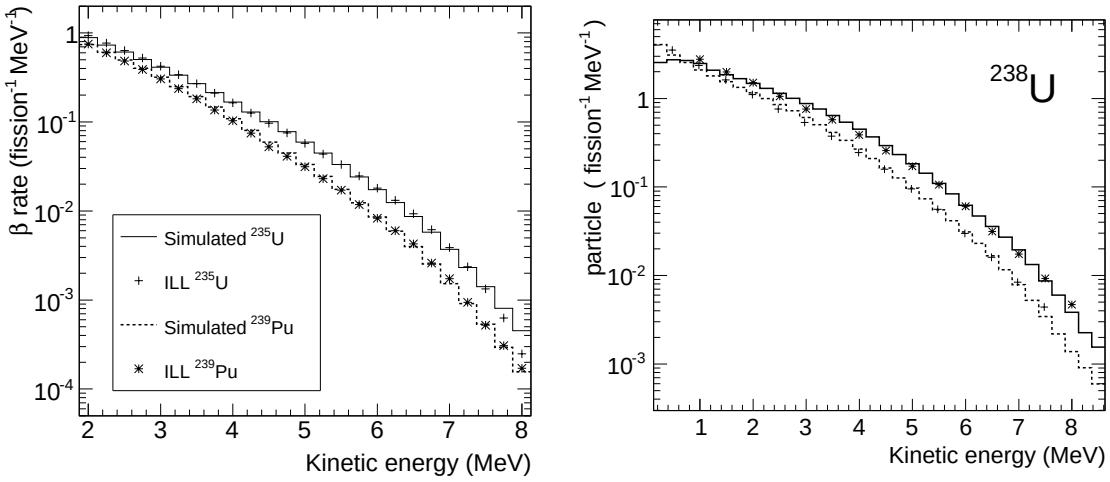

(a) ^{235}U and ^{239}Pu Spectra and Data

(b) ^{238}U Spectra

Figure 6.8: Beta spectra predicted by the *ab initio* method of [13] as compared to data for ^{235}U and ^{239}Pu, or to other theoretical predictions for ^{238}U. ILL Data in Fig. 6.8(a) are from [14]. In Fig. 6.8(b), dashed and solid histograms are for β and $\bar{\nu}$ spectra, respectively; points are from [15]. Both figures from [13].

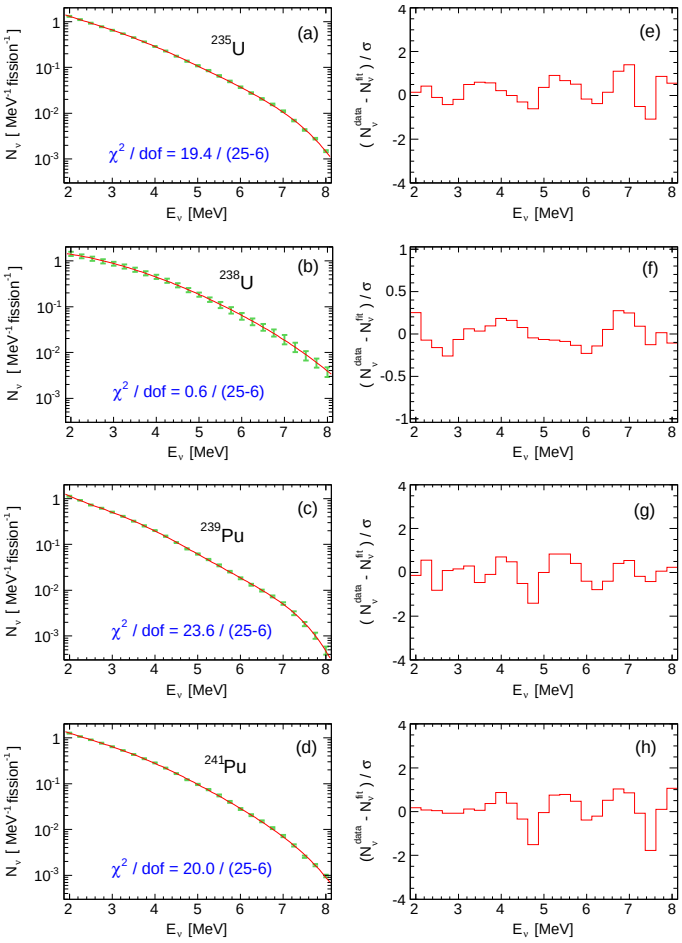

Figure 6.9: Predictions of neutrino spectra using the *ab initio* method of [13], along with exponential-polynomial fit to each. Plots from [13].

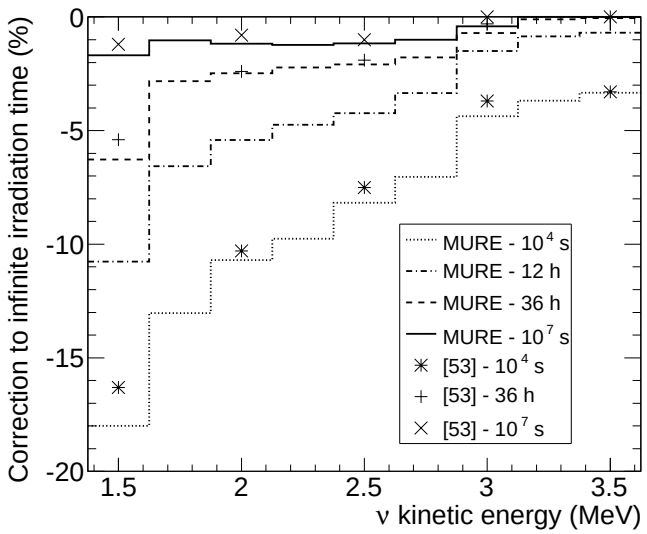

Figure 6.10: Estimated corrections to binned neutrino reference spectra, due to conversion from finite irradiation time in measurement of beta spectra to long irradiation time of fuel nuclides in reactor operation. Plot from [13].

where E_{e^+} is:

$$E_{e^+} = \frac{1}{2}\left(\sqrt{M_n^2 - 4M_p\left(-E_\nu + \Delta + \frac{\Delta^2 - m_e^2}{2M_p}\right)} - M_n\right) \tag{6.7}$$

where $\Delta = M_n - M_p$. The prefactor K is depends inversely on measurements of the neutron lifetime; a value of $K = 0.961 \times 10^{-43}$ cm^2 MeV^{-2} from the recent MAMBO-II experiment [136] is used. To add further precision to this cross-section, radiative corrections from [137] are included via numerical calculation.

6.2 Binned Expected Neutrino Count

For a study of neutrinos which are binned in time t and reconstructed energy E_{e^+} it is useful to rephrase Eq. 6.1 to allow for this style of binning, as well. The number of expected IBD interactions will be determined for a detector running period period T between times t_T and $t_T + \Delta t_T$, during which the parameters of Eq. 6.1 can be considered constant. Pragmatically, this assumption of constant parameters stems from the time granularity

of input data: the thermal power $P_{th}^R(t)$ is measured every minute during stable reactor operation. Sample thermal power data for each of the reactors are shown in Figure 6.11. Other parameters which evolve in time, often calculated via simulation with a more coarse time granularity than the power measurements, may also be considered constant during the period T, thus: $P_{th}^R(t) \to P_{th}^R(T)$; $f_k^R(t) \to f_k^R(T)$; $\alpha_k^R(t) \to \alpha_k^R(T)$; $\langle\sigma_f\rangle^R(t) \to \langle\sigma_f\rangle^R(T)$; $\langle E_f\rangle^R(t) \to \langle E_f\rangle^R(T)$. Next, we consider the energy bin i between $E_{\bar{\nu}} = [E_i, E_i + \Delta E_i]$, which limits the range of the integral in Eq. 6.5 and defines the mean cross-section per fission $\langle\sigma_f\rangle_k^i$ for nuclide k and energy bin i:

$$\langle\sigma_f\rangle_k^i = \int_{E_i}^{E_i+\Delta E_i} S_k(E_{\bar{\nu}})\sigma_{IBD}(E_{\bar{\nu}})dE_{\bar{\nu}}. \tag{6.8}$$

For the rest of this document, the time-dependent mean cross-section per fission for a reactor will be denoted $\langle\sigma_f\rangle^R(t)$ with a superscript capital R, while the time-independent mean cross-section per fission for nuclide k (and energy bin i) will be denoted $\langle\sigma_f\rangle_k$ ($\langle\sigma_f\rangle_k^i$) with lower case sub (sub and super) scripts. The prediction of IBD events $N_{i,T}^R$ in time period T and energy bin i is thus found by integrating Eq. 6.1 in time and limiting the energy range as in Eq. 6.8:

$$\begin{aligned} N_{i,T}^R &= \frac{\epsilon N_p}{4\pi} \int_{t_T}^{t_T+\Delta t_T} \frac{P_{th}^R(t)}{L_R^2 \langle E_f\rangle^R(t)} \sum_{k=1}^{4} \alpha_k^R(t) \langle\sigma_f\rangle_k^i \, dt \\ &= \frac{\epsilon N_p}{4\pi} \frac{P_{th}^R(T)}{L_R^2 \langle E_f\rangle^R(T)} \Delta t_T \sum_{k=1}^{4} \alpha_k^R(T) \langle\sigma_f\rangle_k^i \end{aligned} \tag{6.9}$$

where we have invoked the constant nature of most parameters during the considered time period T, as described above. In the case where the detector is exposed to n_R multiple reactors, the total number of expected neutrinos $N_{i,T}$ in bin i during period T is the sum of each reactor's contribution:

$$N_{i,T} = \sum_{R=1}^{n_R} N_{i,T}^R. \tag{6.10}$$

For Double Chooz, R is summed over the two reactors B1 and B2.

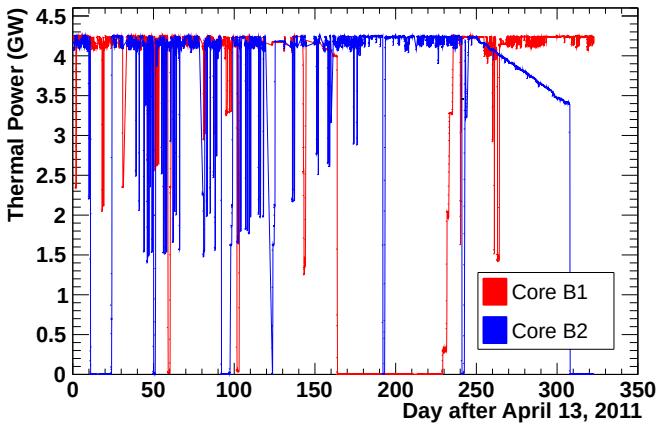

Figure 6.11: Thermal power measurements with 1-minute granularity for the two reactor cores at Chooz, B1 and B2, plotted versus calendar time. Notable features include: 1.) the near-binary nature of reactor power during operation, for economic reasons; and 2.) the downward-sloping trends in thermal power at the end of each fuel cycle (starting at 140 days for B1 and 250 days for B2) where the reactor is nearing sub-criticality. From [10].

6.3 Bugey4 Anchor Point

Even with recent recalculation, the neutrino reference spectra of [96] and [13] carry an uncertainty on their normalization of ∼2.5%. Measurements of the total cross-section per fission from a nuclear reactor have been made to better degrees of precision. In particular, the Bugey4 experiment measured $\langle\sigma_f\rangle^{\text{Bugey4}} = (5.752 \pm 0.081) \times 10^{-43}$ cm^2 per fission from a PWR with a nominal fractional fuel composition of $\alpha_{^{235}\text{U}} = 0.538$, $\alpha_{^{238}\text{U}} = 0.078$, $\alpha_{^{239}\text{Pu}} = 0.328$, $\alpha_{^{241}\text{Pu}} = 0.056$ [98]. This measurement provides a constraint of ∼1.4% on the expected flux from an identical reactor. The measurement may be used as an "Anchor Point" to constrain fluxes from other reactors by redefining $\langle\sigma_f\rangle^R$ in Eq. 6.1 to account for differences in fuel composition with respect to that of the Bugey4 reactor, termed α_k^{Bugey4}:

$$\langle\sigma_f\rangle^R(t) = \langle\sigma_f\rangle^{\text{Bugey4}} + \sum_{k=1}^{4}\left(\alpha_k^R(t) - \alpha_k^{\text{Bugey4}}\right)\langle\sigma_f\rangle_k . \tag{6.11}$$

In practice, the difference $\left(\alpha_k^R(t) - \alpha_k^{\text{Bugey4}}\right)$ in the second term of Eq. 6.11 is $\lesssim 0.05$, thereby suppressing the susceptibility of $\langle\sigma_f\rangle^R(t)$ to systematic uncertainties from the $\langle\sigma_f\rangle_k$.

Extending this formalism to the prediction of neutrino count binned in energy and time, we modify Eq. 6.9:

$$\begin{aligned} N^R_{i,T} &= \frac{\epsilon N_p}{4\pi} \int_{t_T}^{t_T+\Delta t_T} \frac{P^R_{th}(t)}{L^2_R \langle E_f \rangle^R (t)} \frac{\langle \sigma_f \rangle^R (t)}{\left(\sum_{k=1}^{4} \alpha^R_k(t) \langle \sigma_f \rangle_k \right)} \sum_{k=1}^{4} \alpha^R_k(t) \langle \sigma_f \rangle^i_k \\ dt &= \frac{\epsilon N_p}{4\pi} \frac{P^R_{th}(T)}{L^2_R \langle E_f \rangle^R (T)} \frac{\langle \sigma_f \rangle^R (T)}{\left(\sum_{k=1}^{4} \alpha^R_k(T) \langle \sigma_f \rangle_k \right)} \Delta t_T \sum_{k=1}^{4} \alpha^R_k(T) \langle \sigma_f \rangle^i_k . \end{aligned} \tag{6.12}$$

Here the $\langle \sigma_f \rangle^i_k$ and $\langle \sigma_f \rangle_k$ are defined as in Eq. 6.8, and $\langle \sigma_f \rangle^R (t)$ is as defined in Eq.6.11; all other symbols hold the same meanings as in Eq. 6.1.

The effect of this normalization anchor may be characterized in the following manner. Since the Bugey4 experiment was located at $L = 17$ m from its reactor, oscillations due to a sterile neutrino with $\Delta m^2_{41} \approx 0.5$ eV^2 would essentially effect a change in the normalization of the neutrino flux observed by Bugey4, of magnitude $P_{surv}(\bar{\nu}_e \rightarrow \bar{\nu}_e) = 1 - \frac{1}{2}\sin^2(2\theta_{14})$. This is effect is included in the measured value of $\langle \sigma_f \rangle^{\text{Bugey4}}$. Thus, the effect of sterile oscillations as observable by Double Chooz would manifest as a change on the normalization of the weighted-summed $\langle \sigma_f \rangle_k$ in Eq. 6.11. Since these "fuel composition correction terms" account for only $\sim 1\%$ of $\langle \sigma_f \rangle^R (t)$ on average, even a maximally-mixing sterile neutrino would effect a very small change in the total observed spectrum of Double Chooz, which is indistinguishable from systematic shift of the signal normalization within the $\sim$1.8% estimated uncertainty. Thus, the effect of any sterile oscillations on Double Chooz's sensitivity to measuring $\sin^2(2\theta_{13})$ is minimal.

As discussed in Sec. 6.4.5, the use of Bugey4 as a "virtual" near detector has the effect of reducing the total systematic uncertainty contributed by the reactor flux to the final oscillation analysis. This anchor point on the normalization has been adopted for use by Double Chooz for its first [16] and second [8] results.

6.4 Binned Expectation Uncertainty Propagation

Nearly all components of Eq. 6.9 contribute some systematic uncertainty to the expected number of IBD events. In anticipation of an oscillation analysis utilizing a binned fit, these

uncertainties are propagated using a covariance matrix M_{ij} relating the predictions in energy bins i and j, where the binning is in true neutrino energy E_ν. As described in Sections A.3.1.1 and 7.3.1.1, this matrix will be converted to a covariance matrix binned in reconstructed visible energy (E_{reco} or E_{vis}, depending on the analysis iteration) using a MultiSim method (see Appendix C.3). That matrix is then summed with matrix contributions from other sources of systenatic uncertainty, and used to calculate the goodness-of-fit of the data to oscillation models with different values of $\sin^2(2\theta_{13})$, as described in Sections A.6.1 and 7.7.1. Rigorous construction of the covariance matrix M_{ij} is thus vital to performing a neutrino oscillation analysis.

The matrix M_{ij} representing the total systematic uncertainty on the signal prediction can be built as a sum of uncorrelated components M_{ij}^U from different uncertainty contributors U:

$$\begin{aligned} M_{ij} &= \sum_U M_{ij}^U \\ &= M_{ij}^\epsilon + M_{ij}^L + M_{ij}^{N_p} + M_{ij}^{P_{th}} + M_{ij}^{\langle E_f \rangle} + M_{ij}^{\langle \sigma_f \rangle} + M_{ij}^{\alpha_k} \end{aligned} \tag{6.13}$$

Each independent matrix M_{ij}^U is constructed using a "Jacobian" formalism based on partial derivatives. For uncertainty contributors governed by one parameter σ_U (*e.g.* N_p, ϵ, $\langle \sigma_f \rangle^{\text{Bugey4}}$ if it is used, the L_R, and the P_{th}^R), the M_{ij}^U is constructed as:

$$M_{ij}^U = J_i^U \left(\sigma_U\right)^2 J_j^U \tag{6.14}$$

where J_i^U is the Jacobian:

$$J_i^U = \frac{\partial N^{i,T}}{\partial U}. \tag{6.15}$$

For uncertainty contributors governed by a number of correlated parameters $\{U\} = U_\beta$ (*e.g.* the $\langle \sigma_f \rangle_k^i$ and the $\alpha_k^R(t)$) the M_{ij}^U construction requires summing over the potential cross-terms of those parameters:

$$M_{ij}^{\{U\}} = \sum_{\beta,\gamma} J_i^{U,\beta} m_{\beta\gamma}^{\{U\}} J_j^{U,\gamma} \tag{6.16}$$

where $m_{\beta\gamma}^{\{U\}}$ is the covariance matrix relating the parameters U_β.

6.4.1 Multiple Integration Periods

As later described in Sec. 7.6, the power of an oscillation analysis is enhanced by dividing the data into n_τ integration periods τ_I based on reactor power levels. This sorting has implications for the handling of uncertainties; the matrix M_{ij} of Eq. 6.13 must be expanded to M_{ab}, where the indexes a and b run over the $n_E \times n_I$ bins of all integration periods: $a = i + n_E I$. The matrix M_{ab} is again separable into a set of component matrices M^U_{ab}, with some modification to the indexing of the binned neutrino prediciton. The following modifications are warranted, when combining Equations 6.9 or 6.12 with Equation 6.10 and the new binning convention:

$$\text{Eq. 6.9} \rightarrow N_a = \frac{\epsilon N_p}{4\pi} \sum_{T\in\tau_I} \sum_R \Delta t_T \frac{P^R_{th}(T)}{L^2_R \langle E_f \rangle^R (T)} \sum_{k=1}^{4} \alpha^R_k(T) \langle \sigma_f \rangle^i_k \tag{6.17}$$

$$\text{Eq. 6.12} \rightarrow N_a = \frac{\epsilon N_p}{4\pi} \sum_{T\in\tau_I} \sum_R \Delta t_T \frac{P^R_{th}(T)}{L^2_R \langle E_f \rangle^R (T)} \frac{\langle \sigma_f \rangle^R (T)}{\left(\sum_{k=1}^{4} \alpha^R_k(T) \langle \sigma_f \rangle_k \right)} \sum_{k=1}^{4} \alpha^R_k(T) \langle \sigma_f \rangle^i_k \tag{6.18}$$

where in both cases the period τ_I is the non-contiguous set of detector runs associated with bin a. The Jacobian formalism is still applicable, swapping $i \rightarrow a$ in Eq. 6.15 to produce:

$$J^U_a = \frac{\partial N^a}{\partial U}. \tag{6.19}$$

The time-correlated natures of many dominant sources of uncertainty demand that the list of "runs" and integration period sorting scheme be established prior to calculation of M_{ab}. Once this has taken place, calculation of M_{ab} is straight-forward.

6.4.2 Covariance Matrix Components of Prediction Anchored to ILL Spectra

If the normalization of the predicted spectrum is determined using the normalization of the converted ILL spectra described in Sec. 6.1.2, N^a is given by Eq. 6.19. Full forms of the resulting M^U_{ab} are given below. In this section, since the Bugey4 measurement is not used, all references to $\langle \sigma_f \rangle^R (T)$ refer to the definition in Eq. 6.4.

Number of Target Protons N_p

While it is not strictly a reactor-associated uncertainty, the uncertainty on N_p can be treated as part of this ensemble of systematics. In this thesis, like most Double Chooz publications, it is considered to be part of the detection efficiency systematics, and divorced from the "reactor" systematics. By inspection, it is correlated between reactors.

$$M_{ab}^{N_p} = \left(\sum_{T\in\tau_I,R} N_{i,T}^R\right) \frac{\sigma_{N_p}^2}{N_p^2} \left(\sum_{T\in\tau_J,R} N_{j,T}^R\right) \tag{6.20}$$

Detector Efficiency ϵ

While it is not strictly a reactor-associated uncertainty, the uncertainty on ϵ can be treated as part of this ensemble of systematics. In this thesis, like most Double Chooz publications, it is considered to be part of the detection efficiency systematics, and divorced from the "reactor" systematics. By inspection, it is correlated between reactors.

$$M_{ab}^{\epsilon} = \left(\sum_{T\in\tau_I,R} N_{i,T}^R\right) \frac{\sigma_{\epsilon}^2}{\epsilon^2} \left(\sum_{T\in\tau_J,R} N_{j,T}^R\right) \tag{6.21}$$

Mean energy per Fission $\langle E_f\rangle_k$

This uncertainty is correlated between reactors, since the $\langle E_f\rangle_k$ are common physical parameters.

$$M_{ab}^{\langle E_f\rangle_k} = \left(\sum_{T\in\tau_I,R} N_{i,T}^R \frac{\alpha_{k,T}^R}{\langle E_f\rangle^R(T)}\right) \sigma^2_{\langle E_f\rangle_k} \left(\sum_{T\in\tau_J,R} N_{j,T}^R \frac{\alpha_{k,T}^R}{\langle E_f\rangle^R(T)}\right) \tag{6.22}$$

Binned Cross-Section per Fission $\langle\sigma_f\rangle_k^i$

This uncertainty is correlated between reactors, since the $\langle\sigma_f\rangle_k^i$ are common physical parameters.

$$M_{ab}^{\langle\sigma_f\rangle} = \sum_{k,l}^{4}\sum_{\gamma,\beta}^{N_{bins}}\left(\sum_{T\in\tau_I}\sum_{R} N_{i,T}^{R}\left(\frac{\alpha_k^R(T)}{\langle\sigma_f\rangle^R(T)}\right)\right) \times\left(\sum_{T\in\tau_J}\sum_{R} N_{j,T}^{R}\left(\frac{\alpha_l^R(T)}{\langle\sigma_f\rangle^R(T)}\right)\right)\delta\langle\sigma_f\rangle_k^{\gamma}\,\delta\langle\sigma_f\rangle_l^{\beta} \tag{6.23}$$

As mentioned above, the use of $\langle\sigma_f\rangle_{R,t}$ here refers to the definition in Eq. 6.5. The covariance matrix representing $\delta\langle\sigma_f\rangle_k^{\gamma}\,\delta\langle\sigma_f\rangle_l^{\beta}$ is determined from the converted beta spectrum datamentioned in Sec. 6.1.2. Since the $\langle\sigma_f\rangle_k^i$ carry significtant measurement uncertainty, this $M_{ab}^{\langle\sigma_f\rangle}$ contributes a 2.5% uncertainty to the final signal covariance matrix.

Baseline L_R

The primary contribution to this source of uncertainty is metrology errors from the survey of the tunnel leading to the Double Chooz Far Laboratory. Because that survey is common between the measurements of each reactor's baseline L_R, this source of uncertainty is treated as correlated between the two reactors.

$$M_{ab}^{L_R} = \left(\sum_{T\in\tau_I} N_{i,T}^{R}\right)\frac{4}{L_R^2}\sigma_{L_R}^2\left(\sum_{T\in\tau_J} N_{j,T}^{R}\right) \tag{6.24}$$

Past surveys of the Chooz reactor site and Double Chooz experimental hall allow for each of the L_R to be known to within ∼20 cm, yielding an uncertainty contribution to the total signal covariance matrix from the L_R of 0.04%.

Fuel Abundance α_k^R

Since the same MURE simulation is used to determine the α_k^R for each reactor, there is the potential for a systematic bias which is common to both sets of numbers. Thus, this uncertainty is treated as correlated between both reactors.

$$M_{ab}^{\alpha_k^R} = \sum_{k,l=1}^{4} \left(\sum_{T\in\tau_I} N_{i,T}^R \left(\frac{\langle\sigma_f\rangle_k}{\langle\sigma_f\rangle^R(T)} - \frac{\langle E_f\rangle_k}{\langle E_f\rangle^R(T)} \right) \right) \times \left(\sum_{T\in\tau_J} N_{j,T}^R \left(\frac{\langle\sigma_f\rangle_l}{\langle\sigma_f\rangle^R(T)} - \frac{\langle E_f\rangle_l}{\langle E_f\rangle^R(T)} \right) \right) m_{k,l}^{\alpha,R} \quad (6.25)$$

The matrix $m_{k,l}^{\alpha,R}$ is determined by multiple runnings of the MURE simulation.

Thermal Power P_{th}^R

The potential for common metrology biases warrants that this uncertainty be treated as correlated between reactors.

$$M_{ab}^{P_{th}^R} = \sum_{T\in\tau_I} \left(N_{i,T}^R \frac{\sigma_{P_{th}}(T)}{P_{th}^R(T)} \right) \sum_{T\in\tau_J} \left(N_{j,T}^R \frac{\sigma_{P_{th}}(T)}{P_{th}^R(T)} \right) \quad (6.26)$$

The time-dependence and magnitude of this uncertainty are described in more detail in Sections A.3.1 and 7.3.1.

6.4.3 Covariance Matrix Components of Prediction Anchored to Bugey4 Rate

If the normalization of the predicted spectrum is established using the Bugey4 measurement, $N^{,a}$ in is given by Eq. 6.18. After this change, the forms of Equations 6.20, 6.21, 6.22, 6.24, and 6.26 remain unchanged. The matrix contributions given in Equations 6.23 and 6.25 must be replaced by new matrices given below, and an additional contribution representing the uncertainty on the Bugey4 measurement must be included. In the following subsections, all references to $\langle\sigma_f\rangle_{R,t}$ refer to the definition found in Eq. 6.11.

This method was used in the first [16] and second [8] Double Chooz publications with one and two integration periods, respectively. It was also used in Double Chooz's studies of Lorentz Violation [138] with 24 integration periods.

Bugey4 Rate Measurement σ_{Bugey}

This uncertainty is correlated between reactors, since the Bugey4 measurement is presumed to be a common constraint on the fluxes of each.

$$M_{ab}^{\sigma_{\text{Bugey4}}} = \left(\sum_{T\in\tau_I,R} N_{i,T}^{R}\frac{1}{\langle\sigma_f\rangle^{R}(T)}\right)\sigma^2_{\sigma_{\text{Bugey4}}}\left(\sum_{T\in\tau_J,R} N_{j,T}^{R}\frac{1}{\langle\sigma_f\rangle^{R}(T)}\right) \quad (6.27)$$

Binned Cross-Section per Fission $\langle\sigma_f\rangle_k^i$

This uncertainty is correlated between reactors, since the $\langle\sigma_f\rangle_k^i$ are common physical parameters.

$$\begin{aligned} M_{ab}^{\langle\sigma_f\rangle} = & \sum_{k,l}^{4}\sum_{\gamma,\beta}^{N_{bins}}\left(\sum_{T\in\tau_I,R} N_{i,T}^{R}\left(\frac{\alpha_k^R(T)-\alpha_k^{Bugey}}{\langle\sigma_f\rangle^{R}(T)}+\frac{\alpha_k^R(T)\delta_{i\gamma}}{\sum_m \alpha_m^R(T)\langle\sigma_f\rangle_m^{\gamma}}-\frac{\alpha_k^R(T)}{\sum_m \alpha_m^R(T)\langle\sigma_f\rangle_m}\right)\right) \\ & \times\left(\sum_{T\in\tau_J,R} N_{j,T}^{R}\left(\frac{\alpha_l^R(T)-\alpha_l^{Bugey}}{\langle\sigma_f\rangle^{R}(T)}+\frac{\alpha_l^R(T)\delta_{j\beta}}{\sum_m \alpha_m^R(T)\langle\sigma_f\rangle_m^{\beta}}-\frac{\alpha_l^R(T)}{\sum_m \alpha_m^R(T)\langle\sigma_f\rangle_m}\right)\right)\delta\langle\sigma_f\rangle_k^{\gamma}\,\delta\langle\sigma_f\rangle_l^{\beta} \end{aligned} \quad (6.28)$$

Here, $\langle\sigma_f\rangle^{R}(t)$ is defined as in Eq. 6.11. The covariance matrix representing $\delta\langle\sigma_f\rangle_k^{\gamma}\,\delta\langle\sigma_f\rangle_l^{\beta}$ is determined from the converted beta spectrum datamentioned in Sec. 6.1.2. AS described in Section 6.3, the Bugey4 anchor point has the effect of suppressing this uncertainty contribution from the 2.5% value of the unanchored Eq. 6.23, down to 0.17% of the total signal.

Fuel Abundance α_k^R

Since the same MURE simulation is used to determine the $\alpha_k^R(t)$ for each reactor, there is the potential for a systematic bias which is common to both sets of numbers. Thus, this uncertainty is treated as correlated between both reactors.

$$M_{ab}^{\alpha_k^R} = \sum_{k,l}\left(\sum_{T\in\tau_I} N_{i,T}^R\left(\frac{\langle\sigma_f\rangle_k}{\langle\sigma_f\rangle^R(T)} - \frac{\langle E_f\rangle_k}{\langle E_f\rangle^R(T)} - \frac{\langle\sigma_f\rangle_k}{\sum_m \alpha_m^R(T)\langle\sigma_f\rangle_m} + \frac{\langle\sigma_f\rangle_k^i}{\sum_m \alpha_m^R(T)\langle\sigma_f\rangle_m^i}\right)\right) \times\left(\sum_{T\in\tau_J} N_{j,T}^R\left(\frac{\langle\sigma_f\rangle_l}{\langle\sigma_f\rangle^R(T)} - \frac{\langle E_f\rangle_l}{\langle E_f\rangle^R(T)} - \frac{\langle\sigma_f\rangle_l}{\sum_m \alpha_m^R(T)\langle\sigma_f\rangle_m} + \frac{\langle\sigma_f\rangle_l^j}{\sum_m \alpha_m^R(T)\langle\sigma_f\rangle_m^j}\right)\right) m_{k,l}^{\alpha,R} \tag{6.29}$$

The matrix $m_{k,l}^{\alpha,R}$ is determined by multiple runnings of the MURE simulation.

6.4.4 Covariance Matrix Components of Prediction Anchored to Measured Near Detector Spectrum

The crux of the multi-detector approach is the use of a near detector to measure the emitted reactor flux while the flux is as close to unoscillated as possible. While the Double Chooz Near detector is not yet available to make this measurement, there are other experiments which could stand-in as a "virtual" near detector and provide a measured unoscillated reference spectrum, similar to how the Bugey4 measurement provided a reference neutrino rate[1]. Current data fitting this bill exist from the Rovno [139], Bugey3 [140], and Daya Bay [141] experiments, with future data anticipated from very-near-baseline experiments like Nucifer [142].

As with use of the Bugey4 anchor, it would be necessary to apply corrections to the spectra to account for differences in fuel composition between the Chooz reactors and the reactor used in the reference experiment. In addition, consideration of systematics such as energy resolution, energy scale, and background spectra would be required. This method has not yet been put into practice, but may allow the Double Chooz Far-only analysis to circumvent the 1.4% limiting uncertainty of the Bugey4 Anchor Point, and lend greater power to oscillation analyses involving spectral shape considerations.

[1]The author is grateful to V. Sinev who first proposed the use of this method with the Rovno data.

Source	Uncertainty without Bugey4 Anchor	Uncertainty with Bugey4 Anchor
Bugey4 Rate	–	1.42
$\langle E_f \rangle$	0.16	0.16
$\langle \sigma_f \rangle_k$ & σ_{IBD}	2.50	0.17
L_R	0.04	0.04
P_{th}^R	0.48	0.48
α_k^R	0.80	0.88
Total	2.68	1.76

Table 6.1: Reactor uncertainty components with and without use of the Bugey4 measurement as an anchor on the total normalization. Uncertaintiees are quoted as percentages of the total predicted signal rate.

6.4.5 Comparison of Uncertainty Contributions

As described in Section 6.3, use of the Bugey4 anchor not only has the effect of reducing sensitivity to sterile neutrino oscillations, but also reduces the total uncertainty on the rate of IBD interactions predicted as a result of the reactor flux. Qualitatively comparing the matrices of Section 6.4.2 with those of Section 6.4.3 hints that the biggest effects of using the Bugey4 anchor point will manifest in through the fuel composition matrix $M_{ab}^{\alpha_k^R}$ and the reference spectra matrix $M_{ab}^{\langle \sigma_f \rangle}$, though the additional matrix $M_{ab}^{\sigma_{\text{Bugey4}}}$ representing the uncertainty of the Bugey4 measurement comes into play. The uncertainties contributed by each component both with and without use of the Bugey4 anchor point are listed in Table 6.1. The reduction of the uncertainty due to the reference spectrum is marked, from 2.5% of the signal to 0.17%. This effect outweights the acquired uncertainty contribution of 1.42% from the Bugey4 measurement itself.

Table 6.1 also reveals which uncertainties are dominant for single-detector reactor experiments. Without a near detector, or a "virtual" near detector or anchor point, uncertainties due to the reference spectra are serverely limiting. This in and of itself is the motivation for

the two-detector concept described in Section 3.2.2. Beyond that, the next-dominant uncertainty comes from simulation of the reactor fuel composition, though those uncertainties are constrainable with a measured flux spectrum provided by a near detector. A similar statement can be made for the third dominant uncertainty, reactor thermal power.

Chapter 7

Second Double Chooz Publication

The oscillation analysis iteration using data from the Double Chooz Far Detector was published as Ref. [8] in late July, 2012. In this chapter, this analysis iteration and publication is often referred to as "DC2ndPub" for brevity. A facsimile of the of the publication may be found in Appendix K.2.

7.1 Data Set

Data for this analysis were taken between April 13, 2011, and March 15, 2012. Most of the data from the data-taking period of the first Double Chooz analysis were included, in addition to detector data previously excluded from the analysis from the same period. In all, physics data from 251.27 days of detector run time were included, out of 338 calendar days. One notable enhancement to this analysis was the inclusion of data from the Outer Veto in the analysis, which had been present but not used during the first analysis.

7.2 Candidate Selection Cuts

7.2.1 Second Publication Analysis

The following cuts were applied to data to define a set of Inverse Beta Decay candidates:

- Prompt signal energy: $E_{\text{vis}} \in [0.7,\ 12.2]$ MeV. (Distribution shown vs. delayed signal energy in Figure 7.1).

- Delayed signal energy: $E_{\text{vis}} \in [6.0,\ 12.0]$ MeV. (Distribution shown in Figure 7.2, and shown vs. prompt signal energy in Figure 7.1).
- Time difference Δt between prompt and delayed: $\Delta t \in [2,\ 100]$ μsec. (Distribution shown in Figure 7.3).
- Time between prompt signal and the preceding muon: $\Delta t_\mu > 1$ msec. A muon is defined as any event having charge in the IV $Q_{IV} > 10000$ DUQ, or inner detector energy $E_{\text{vis}} > 30$ MeV.
- Spontaneous light noise rejection cuts.
  - PMT hits approximately homogeneous based on maximum charge on any single PMT Q_{max} and total charge Q_{tot} of all PMTs: $Q_{max}/Q_{tot} < 0.09$ for all events, and $Q_{max}/Q_{tot} < 0.055$ for delayed event. (Distributions shown in Figure 7.4).
  - PMT hits approximately simultaneous based on pulse start times T_{start} of each PMT: RMS(T_{start}) < 40 nsec. (Distributions shown in Figure 7.5).
- Multiplicity rejection cut: no valid trigger ($E_{\text{vis}} > 0.5$ MeV, and passes light noise cuts) in the 100 μsec before the prompt candidate, only one valid trigger in the $[2,\ 100]$ μsec window following the prompt event, and no valid trigger in a $[100,\ 400]$ μsec window following the prompt event.
- Outer Veto Anticoincidence: no hit in Outer Veto within 224 nsec.
- ^{9}Li reduction cut following high-energy muons: if $E_\mu > 600$ MeV, then require $\Delta t_\mu > 1$ msec.

The cuts used to select IBD candidates were modified from those described in Sec. A.2 in two notable ways: the rejection of events whose prompt signal is coincident with (within 224 ns) a trigger in the Outer Veto; and rejection of candidates following within 0.5 seconds after a muon that deposits more than 600 MeV in the ID.

The goal of using an OV-based veto cut is suppression of the fast neutron and stopping μ backgrounds. Prompt signals quickly following an OV trigger have a high likelihood of originating from proton recoils from fast neutrons. Adding this veto condition contributes

a small amount of dead time to the detector operation, but reduces the overall fast-n and stopping μ rates significantly. This cut is taken into account in the measurement of the total fast neutron and stopping μ rate, as described in Sec. 7.4.3.

Cutting events within 0.5 seconds following a large muon energy deposition is done with the intent of reducing the total rate of cosmogenic ^{9}Li events. Muons depositing more than 600 MeV in the inner detector have a high likelihood of producing showers of spallation products, including ^{9}Li. Vetoing for a short amount of time after these muons has the effect of reducing the ^{9}Li background population in the IBD candidate sample, but at the trade-off of a significant amount of detector live time. Sensitivity studies to null-oscillation results were used optimize these cuts.

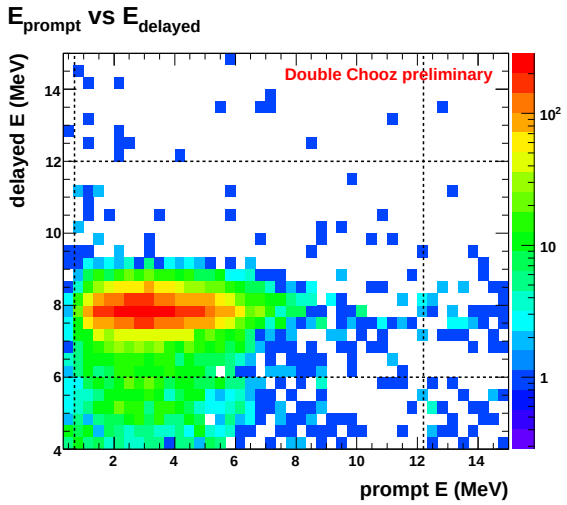

Figure 7.1: Plot of prompt coincidence visible energy vs. delayed coincidence visible energy for the main "^{9}Li-reduced" IBD candidate selection. Prompt and delayed signal windows are indicated by dashed black lines. From [8].

While neither the spatial position of the prompt nor of delayed events was used as a selection cut, these reconstructed positions were examined as cross-checks to show that most selected IBD candidates were localized within the Gd-doped neutrino target fiducial volume. Projections of these distributions are shown in Figure 7.6 for the prompt and Figure 7.7 for the delayed events.

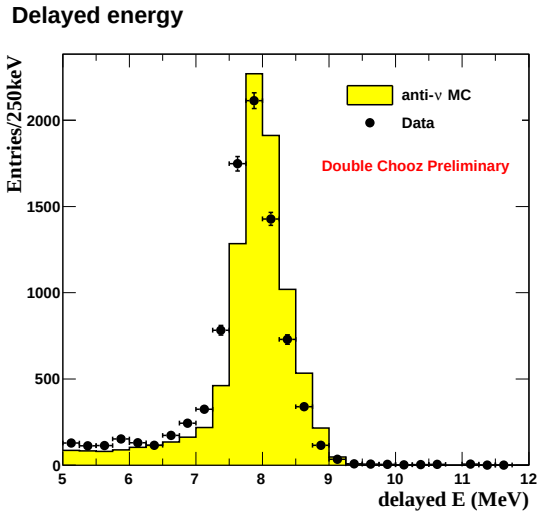

Figure 7.2: Delayed signal visible energy distribution for the main "^{9}Li-reduced" IBD candidate selection. Data are black points, with IBD Monte Carlo shown by yellow region. Delayed candidate energy window is $6 < E_{\text{vis}} < 12$ MeV. From [8].

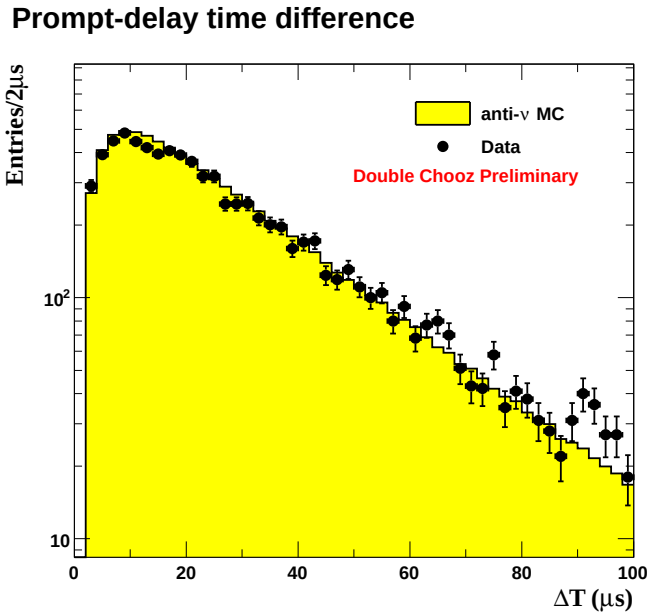

Figure 7.3: Time Difference between prompt and delayed signal of the "^{9}Li-reduced" IBD candidates. Data are black points with statistical errors; yellow region is IBD Monte Carlo. From [8].

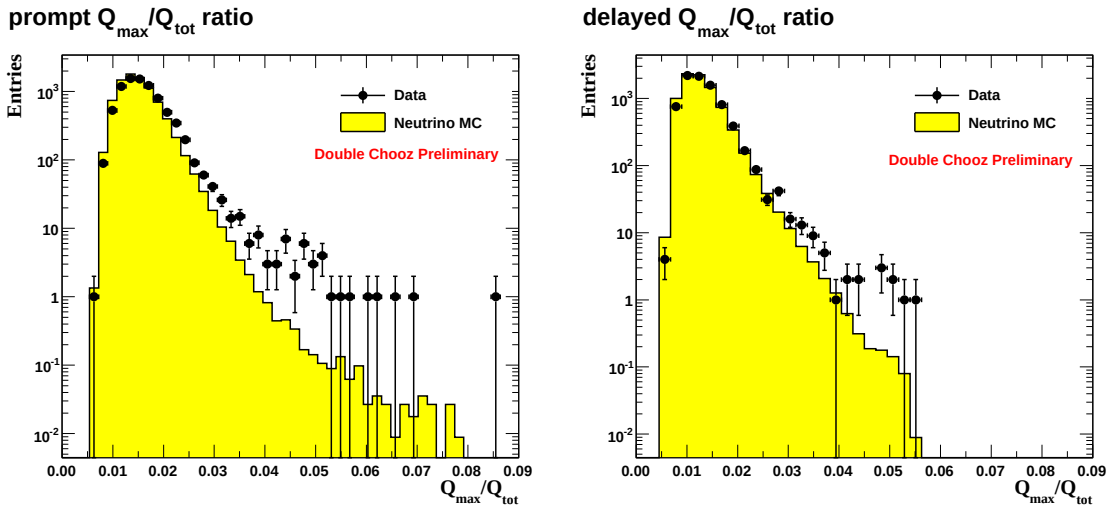

(a) Prompt Event Q_{max}/Q_{tot}

(b) Delayed Event Q_{max}/Q_{tot}

Figure 7.4: Distributions of Q_{max}/Q_{tot} for prompt and delayed components of the "^{9}Li-reduced" IBD candidates. Black points with statistical error bars are data; yellow region is IBD Monte Carlo. Both from [8].

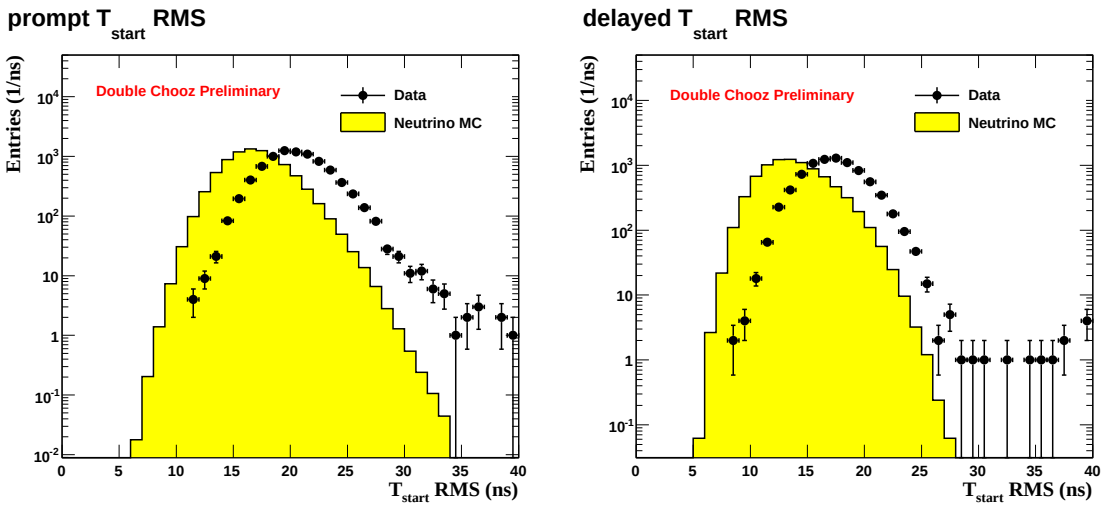

(a) Prompt Event RMS(T_{start}) (b) Delayed Event RMS(T_{start})

Figure 7.5: Distributions of RMS(T_{start}) for prompt and delayed components of the "^{9}Li-reduced" IBD candidates. Black points with statistical error bars are data; yellow region is IBD Monte Carlo. Both from [8].

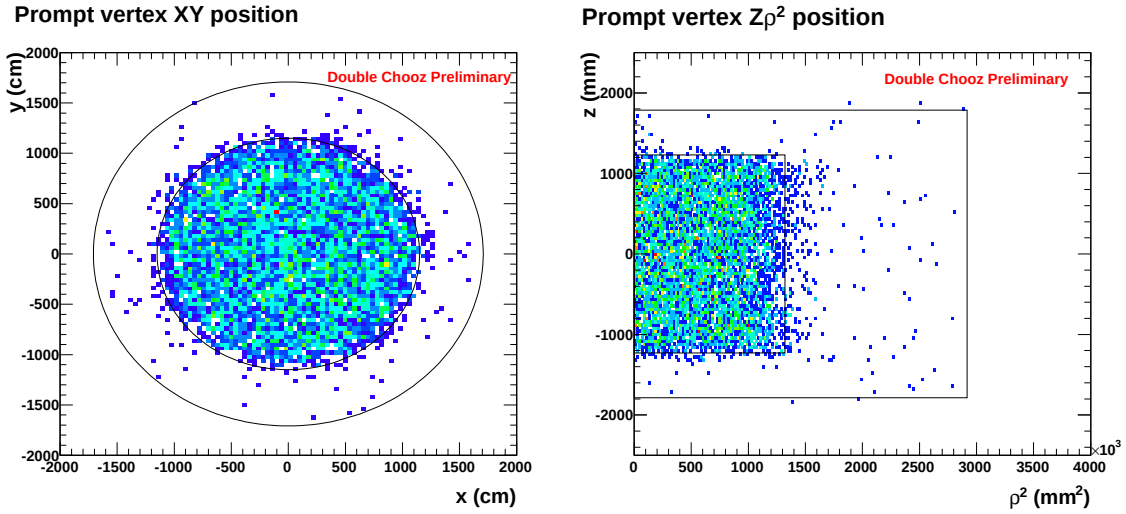

(a) Prompt Events in xy Plane

(b) Prompt Events in $z\rho^2$ Plane

Figure 7.6: Reconstructed positions of the prompt events of the IBD candidates selected with the main "^{9}Li-reduced" selection cuts, projected in the xy- (Fig. 7.6(a)) and $x\rho^2$-planes (Fig. 7.6(b)). Black circles/rectangles represent the extent of the target and gamma catcher volumes.

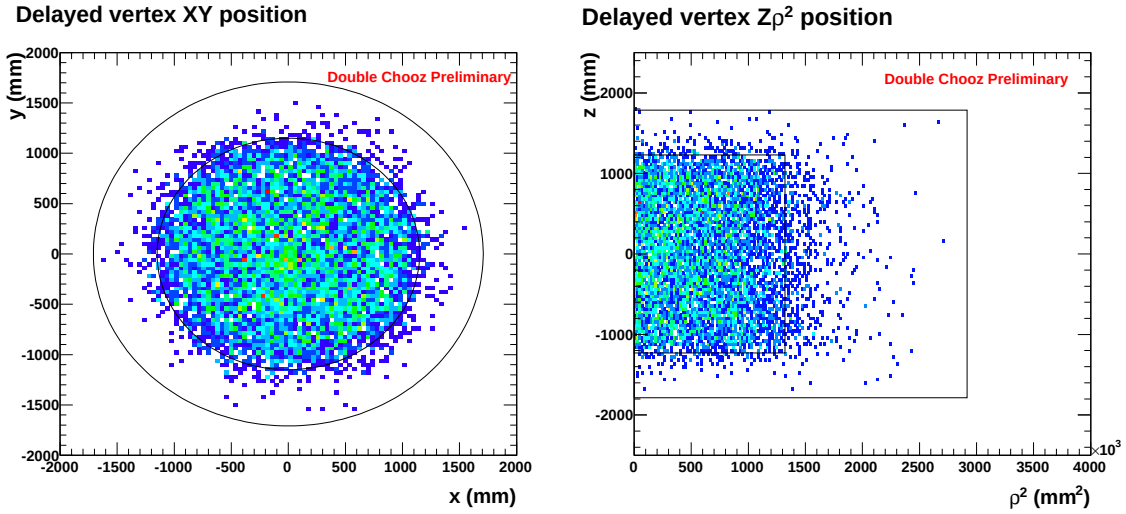

(a) Delayed Events in xy Plane

(b) Delayed Events in $z\rho^2$ Plane

Figure 7.7: Reconstructed positions of the delayed events of the IBD candidates selected with the main "^{9}Li-reduced" selection cuts, projected in the xy- (Fig. 7.7(a)) and $x\rho^2$-planes (Fig. 7.7(b)). Black circles/rectangles represent the extent of the target and gamma catcher volumes.

Additional Dead Time Incurred	^{9}Li Rate [1/day]	Rate-Only, 1 IP	Rate+Shape, 1 IP	Rate-Only, 2 IP's	Rate+Shape, 2 IP's
0%	2.3	0.05730	0.04205	0.05595	0.04195
5%	2.3 - 1.03 = 1.027	0.05635	0.04175	0.05520	0.04165
20%	2.3 - 1.47 = 0.85	0.05705	0.04280	0.05605	0.04270
50%	2.3 - 1.65 = 0.65	0.05990	0.04670	0.05930	0.04665

Table 7.1: Null-oscillation sensitivity intervals for different candidate selection cut ensembles, quoted at 68% confidence level. Systematics and statistics are approximately those of DC2ndPub. Column headings refer to the χ^2 statistics described in Sec. 7.7.2, and the use of multiple integration periods as described in Sec. 7.6.

7.2.2 Peripheral Analyses

In the lead-up to performing the second Double Chooz analysis, three different analyses were considered in parallel, with each using slightly different sets of candidate selection cuts. The collaboration decided on a set of selction cuts before "opening the box", based on the results of null-oscillation sensitivity studies. The results of these studies are shown in Table 7.1. Using these results, the set of selection cuts described in Sec. 7.2.1 was chosen as the main analysis; in Table 7.1, results labeled as "5% Additional Dead Time Incurred" are representative of this analysis. However, the other two analyses were carried out in parallel as "cross-checks" of the main-line result. The selection cuts for each peripheral analysis are described in the following subsections.

7.2.2.1 No ^{9}Li Reduction Cuts

The first peripheral ensemble of cuts was comprised of all cuts described above, but dropping the condition rejecting candidates following within 0.5 seconds after a muon that deposits more than 600 MeV in the ID. Said another way, this ensemble was the set of cuts used in the first Double Chooz publication (Sec. A.2) with the OV-based veto added. This analysis was maintained to allow some level of comparison to results obtained during the first Double Chooz analysis iteration. This particular set of cuts provided more live time

than the DC2ndPub cut ensemble, as can be seen by comparing the contents of Tables 7.2 and 7.3, but allowed significantly more ^{9}Li events to be accepted as IBD candidates. This analysis is colloquially referred to as the "non-^{9}Li-reduced" analysis, or somewhat confusingly as the "standard analysis" in documents which precede the publication of [8]. In this document, any references to a "standard" or "main" analysis refer to the analysis using the cuts described in Sec. 7.2.1.

7.2.2.2 "^{9}Li-free" Reduction Cuts

The second peripheral ensemble of cuts was comprised of all cuts described above, but changing the condition rejecting candidates following high-energy muons for a more stringent two-part cut:

- If the IBD candidate followed within $\Delta t_\mu < 600$ msec and $E_\mu > 550$ MeV, then the IBD candidate is rejected.
- Else, if the IBD candidate followed within $\Delta t_\mu < 600$ and $E_\mu > 400$ MeV and the reconstructed vertex of the IBD candidate is within 800 mm of the reconstructed muon track (by distance of closest approach), then the IBD candidate is rejected.
- Else, the IBD candidate is accepted.

The lower threshold on E_μ for this cut imposes significant ($\sim$50%) dead time on the detector, but has the effect of reducing the ^{9}Li content of the IBD candidate sample to less than one expected count per day. Thus, it is colloquially referred to as the "^{9}Li-Free" analysis.

7.2.3 Effects of IBD Selection on Detector Livetime

Each selection cut which imposes a vetoed time period decreases the amount of detector livetime, down from a maximum possible live time equal to the run time of the detector. The resulting live time is used to calculate the number of expected background events in the IBD candidate sample (used in Sec. 7.4), as well as to determine the normalization of the IBD signal expectation (described in Sec. 7.3.2). Cuts which factor into the determination of the live time include:

- Muon Veto: rejection of candidates within 1 msec after any muon.
- OV-based Veto: rejection of candidates within 224 ns of an OV trigger.
- ^{9}Li reduction cut: rejection of events within 500 msec after a high-energy muon.
- Second-order muon veto effect: due to "overlapping" muons which arrive sooner than 1 msec after another muon[1].

For the non-^{9}Li-reduced and ^{9}Li-free analyses, the dead time contribution of the ^{9}Li reduction cut is eliminated or enhanced, respectively. Tables 7.2, 7.3, and 7.4 list live time numbers for the main and peripheral analyses, along with comparisons of the live time as a fraction of detector run time. In these tables, "Run Time" is the recorded length of all physics runs which comprise the data set, and "First-Order Live Time" is the run time minus the dead time effected by all cuts except for the second-order muon veto effect. The "Second-Order Live Time" includes the second-order muon veto effect, and is calculated as 99.9% of the First-Order Live Time based on the Poisson statistics of overlapping muons. The second-order live time numbers are used to determine the background expectations in Sec. 7.4, while the (2^{nd}-Order live)/(run time) ratio is used to determine the signal normalization in Sec. 7.3.2.

7.3 Signal Prediction

Prediction of the IBD signal component of all IBD candidates is achieved in two general steps: prediction of the number of IBD interactions in the detector by $\bar{\nu}_e$; and the prediction of the selection efficiency when the detector response and selection cuts are applied to those events. This process utilizes the Double Chooz Monte Carlo, with corrections applied only when discrepancies between data and MC are measured. For this analysis, the only

[1]In practice, dead time due to muons is calculated as (number of muon triggers)×(1 ms veto window). However, it is possible for a second muon to arrive within that 1 ms window and start a new 1 ms veto window; the veto windows of each muon "overlap." This correction is calculated by using Poisson statistics and the rate of muon triggers in the detector to determine the average rate of overlapping muons, and the average additoinal deadtime incurred. A similar, but even more rare, effect can occur with triplets of overlapping muons; this is also accounted for.

	Reactors Both On	**One Reactor $P_{th} <$ 20%**	**Total**
Run Time [days]	153.6115	97.6623	251.2737
First-Order Live Time [days]	139.41	88.7476	228.1576
Second-Order Live Time [days]	139.2706	88.6589	227.9294
(2^{nd}-Order Live)/Run Time Ratio	0.90664	0.90781	0.90709

Table 7.2: Run time, and corrected live time numbers for the second Double Chooz analysis (cuts described in Sec. 7.2.1). Described in detail in Sec. 7.2.3. For discussion of integration periods based on reactor power, see Sec. 7.6.

	Reactors Both On	**One Reactor $P_{th} <$ 20%**	**Total**
Run Time [days]	153.6115	97.6623	251.2737
First-Order Live Time [days]	146.7610	93.3035	240.0645
Second-Order Live Time [days]	146.6142	93.2102	239.8244
(2^{nd}-Order Live)/Run Time Ratio	0.95445	0.95441	0.95443

Table 7.3: Run time, and corrected live time numbers for the second Double Chooz analysis data with no ^{9}Li reduction cuts (cuts described in Sec. 7.2.2.1). Described in detail in Sec. 7.2.3. For discussion of integration periods based on reactor power, see Sec. 7.6.

	Reactors Both On	**One Reactor $P_{th} <$ 20%**	**Total**
Run Time [days]	153.6115	97.6623	251.2737
First-Order Live Time [days]	72.0597	45.8120	117.872
Second-Order Live Time [days]	71.9876	45.7662	117.7538
(2^{nd}-Order Live)/Run Time Ratio	0.46863	0.46861	0.46862

Table 7.4: Run time, and corrected live time numbers for the second Double Chooz analysis data with "^{9}Li-free" cuts used (cuts described in Sec. 7.2.2.2). Described in detail in Sec. 7.2.3. For discussion of integration periods based on reactor power, see Sec. 7.6.

corrections necessary were to account for the multiplicity cut (see Sec. 7.3.2.7) and the gadolinium capture fraction (see Sec. 7.3.2.4) as represented by the non-unity correction coefficients in Table 7.6.

7.3.1 Reactor Prediction

The reactor neutrino prediction and its accompanying uncertainties were generated using the prescription described in Chapter 6. Two significant changes were implemented as compared to the reactor flux prediction used in the first publication: the reactor power uncertainty was assigned as a function of the time-dependent power; and the periods of data integration were split into two time periods based on the reactor power. The latter change is described in detail in Sec. 7.6.

While the degree of the uncertainty $\sigma_{P_{th}}$ on the thermal power $P_{th}^R(t)$ of reactor R was considered to be constant in time for the first analysis iteration, subsequent study indicated that the fractional power uncertainty $\sigma_{P_{th}}/P_{th}^R$ increased as a function of P_{th}^R. Particularly, the fractional uncertainty on the thermal power, and thus on the normalization of the expected number IBD events, was found to increase at low values of P_{th}^R. Data acquired from EDF allowed for a regression fit and subsequent analytical form for $\sigma_{P_{th}}\left(P_{th}^R(t)\right)$ to be constructed. The increase in the total signal uncertainty was small ($\sim$0.02%), due to

two key factors. First, due to economic reasons, the reactors are typically kept at near-full power when in operation at all. Second, operation at lower power produces a smaller rate of expected IBD events, so the additional absolute uncertainty on the total integrated number of expected IBD events is reduced.

For this data set, a total exposure of 33.71 GW-ton-years was collected after taking into account livetime considerations (see Sec. 7.2.3). Data from the same period as the first analysis iteration comprised 15.34 GW-ton-years, with the remaining 18.37 GW-ton-years taken after Nov. 11, 2011. The total number of expected IBD candidates from each reactor are listed in Table 7.13 (and in Tables 7.15 and 7.14 for the non-^{9}Li-reduced and ^{9}Li-free analyses). It is worth noting that the average rate of expected IBD events was lower for this analysis than for the first iteration, due to the sizable amount of one-reactor-off data accrued since November 2011.

7.3.1.1 Reactor Uncertainty Propagation

Uncertainty contributions to the $\bar{\nu}_e$ signal were treated as described in Sec. 6.4.3. As in the first Double Chooz analysis iteration, a MultiSim method using the selected signal Monte Carlo events of Eq. 7.5 was used to convert the matrix M^{rxt}_{ab} from a binning in $E_{\bar{\nu}}$ to a matrix M^{rxt}_{ij} binned in E_{vis} (see Appendix C.3):

$$M^{\text{rxt}}_{ab} \xrightarrow[N_i^{\text{exp}}\ \text{MC Events}]{\text{MultiSim}} M^{\text{rxt}}_{ij} \tag{7.1}$$

The use of multiple integration periods (see Sec. 7.6) was accounted for in this conversion, with simulated neutrinos being properly binned according to which run and integration period they were associated with.

The resulting matrix M^{rxt}_{ij} represented a total uncertainty on the $\bar{\nu}_e$ signal rate of 1.76%. A breakout of the components of M^{rxt}_{ij} may be found in Table 7.5. This number corresponds to 1.66% of the total expected IBD candidate rate, including signal and backgrounds.

7.3.2 Signal Selection Efficiency

As in the first DC publication, the detector simulation is used to model all IBD candidate selection efficiencies at first order, with corrections applied only when deemed necessary.

Source	Uncertainty [%]
Bugey4 Rate	1.42
$\langle E_f \rangle$	0.16
$\langle \sigma_f \rangle_k$ & σ_{IBD}	0.17
L_R	0.04
P_{th}^R	0.5
α_k^R	0.88
Total	1.76

Table 7.5: Reactor uncertainty components, quoted as percentages of the total predicted signal rate.

The first correction applied is to account for the signal IBD sample having been generated according to detector run time, while the analysis is performed using detector live time. Described in greater detail in Sec. 7.2.3, this correction takes slightly different values for each integration period, based on the average muon rate and OV usage in each period.

Further corrections are applied to account for differences in selection efficiency between the Monte Carlo simulation, and similar metrics measured from calibration data. In some cases a correction is not deemed necessary, but the a comparison between data and Monte Carlo simulation must still be made in order to establish uncertainty intervals on each effect. These effects are described in the following subsections, and include: target proton number (Sec. 7.3.2.1); DAQ trigger efficiency (Sec. 7.3.2.2); spill-in/spill-out effects (Sec. 7.3.2.3); Gadolinium capture fraction (Sec. 7.3.2.4); delayed coincidence Δt cut (Sec. 7.3.2.5); delayed energy containment efficiency (Sec. 7.3.2.6); and multiplicity cut (Sec. 7.3.2.7). A full accounting of the corrections due to each effect, and their associated uncertainty contributions, can be found in Table 7.6. Combining the numbers in Table 7.6 with the (live time)/(run time) ratios of Table 7.2.3 yields the normalization correction coefficients, shown in Table 7.7 which are to be applied to the reactor prediction described in Sec. 7.3.1.

Source	**Uncertainty**	**MC Correction Coeff.**
Target Proton Number	0.3%	1.000
Electronics & Trigger & DAQ	Negligible	1.000
Spill-In/Spill-Out	0.3%	1.000
$\frac{\text{Gd}}{\text{Gd+H}}$	0.3%	0.985
Δt Cut	0.5%	1.000
Delayed window n Capture Fraction	0.7%	1.000
Multiplicity Cut	Negligible	0.99455
Signal Total	1.005%	0.97963

Table 7.6: Monte Carlo signal selection efficiency corrections. Described in 7.3.2. Uncertainties are quoted with relative to the total signal normalization. Total correction coefficient is applied to the reactor prediction to account for discrepancies between data and simulation.

	Reactors Both On	**One Reactor $P_{th} <$ 20%**	**Total**
DC2ndPub Cuts	0.88818	0.88932	0.88862
No ^{9}Li Reduction Cuts	0.93501	0.93497	0.93499
"^{9}Li-Free" Cuts	0.45909	0.45907	0.45908

Table 7.7: Signal normalization coefficients for each ensemble of analysis cuts described in Sec. 7.2. Numbers are products of the "(2^{nd}-Order Live)/Run Time Ratio" numbers of Tables 7.2, 7.3, and 7.4, multiplied against the "Signal Total" number of Tab. 7.6.

7.3.2.1 Target Proton Number

The number of free hydrogen nuclei in the neutrino target N_p, also called the target proton number, is needed to drive the prediction of the number of observed IBD signal events, as shown in Eq. 6.17.

Measurement of N_p is achieved by combining measurements of the neutrino target scintillator's chemical composition, with an accurate measurement of the mass of scintillator filled into the neutrino target vessel during filling of the Far Detector. As previously mentioned in Sec. 4.2.1.1, the free hydrogen fraction of the Target liquids was found to be 13.6%, with a relative precision of 0.3% [117]. The mass measurement executed during filling established the mass to be (8,287±2) kg, resulting in a proton number of $(6.738 \pm 0.020) \times 10^{29}$ for the scintillator in the target vessel, excluding the chimney. With an internal diameter of 150 mm, the scintillator in the chimney contributes an additional 1.16×10^{25} protons per centimeter of filled liquid. The Monte Carlo simulation accurately models the 127.15 cm of liquid inside the target chimney. Temperature measurements indicated an average target temperature of 14.6 degrees C, versus the a measured temperature of 13.6 degrees C when the mass measurement was made. Adding corrections for thermal expansion of the liquid imposes a change of 0.08% in the target proton number. Thus, the final proton number after accounting for the chimney region and temperature corrections was found to be $N_p = 6.7473 \times 10^{29}$ protons. The uncertainty on the total corrected mass measurement is 0.04%. The relative uncertainties on the chemical composition and target mass combine to give the 0.3% uncertainty quoted in Table 7.6.

While mentioned in Sec. 6.4.2 as contributing to the "reactor signal" uncertainty, the uncertainty on N_p is bundled with other "detector efficiency" uncertainties by collaboration convention, as it is a quantity describing a property of the detector itself. It is *not* included in the reactor uncertainty numbers quoted in Sec. 7.3.1.1.

7.3.2.2 DAQ Trigger Efficiency

As described in Sec. 4.3, the Inner Detector DAQ reads out the pulse waveforms of all PMT's whenever the total integrated charge in either of two trigger groups is above 0.35 MeV. The summed integrated charge at low visible energies has some uncertainty, which

gives rise to and uncertainty on the trigger efficiency at a given visible energy E_{vis}.

Each read-out DAQ event is assigned a descriptor called a "trigger word". A measurement of the trigger efficiency is performed by operating the DAQ at a trigger threshold far below the standard physics data threshold. These low-threshold data are then examined offline, and the fraction of properly-assigned trigger words as a function of E_{vis} is measured, using additional electronics diagnostic data and a close correlation between those diagnostics and E_{vis}. The results of this measurement are shown in Fig. 7.8 for a range of E_{vis}.

By this method, the trigger efficiency at the physics trigger threshold is 50% at 400 keV. The prompt E_{vis} range for oscillation analysis purposes begins at 0.7 MeV, where the quoted efficiency is $100\%^{+0.0\%}_{-0.1\%}$. The $\bar{\nu}_e$ interaction threshold is at $E_{\text{vis}} = 1.0$ MeV, where the quoted efficiency is $100\% \pm 0.0\%$. Thus, the trigger efficiency is found to be a negligible source of signal uncertainty, and is listed as such in Table 7.6.

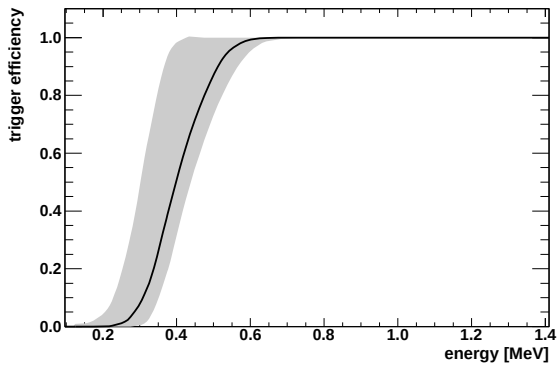

Figure 7.8: Trigger efficiency as a function of reconstructed visible energy. Grey band indicates total uncertainty due to statistical and systematic effects. Efficiency at trigger threshold is 50% at 400 MeV. Analysis prompt energy range begins at 0.7 MeV, where the quoted efficiency is $100\%^{+0.0\%}_{-0.1\%}$. The $\bar{\nu}_e$ interaction threshold is at 1.0 MeV, where the quoted efficiency is $100\% \pm 0.0\%$. From [8].

7.3.2.3 Spill-In/Spill-Out

Spill-In and Spill-Out are jargon describing two classes of IBD events which occur close to the NT/GC interface. Spill-In events occur when the neutrino has interacted in the GC but the resulting neutron came into the NT to capture on Gadolinium, thus registering the interaction as a valid IBD candidate even though it did not originate inside the NT. Spill-out events involve a neutrino interaction which occurs inside the NT, but the resulting neutron has gone into the GC and cannot capture on Gadolinium, thus invalidating the interaction as an IBD candidate even though it did originate from a proton inside the NT. Due to geometric considerations, the number of spill-in events exceeds the number of spill-out events by 1.35% ± 0.30% as a percentage of the total number of expected IBD interactions in the NT.

Spill-in/spill-out effects are modeled in the detector simulation, but four parameters affect the behavior and accuracy of the model:

- Neutron thermalization and transport modeling.
- Gadolinium concentration of the NT scintillator.
- Free Hydrogen concentration in the GC scintillator.
- Neutrino target acrylic vessel geometry.

All factors were deemed to be modeled accurately, so no modification to the signal normalization due to spill-in/spill-out was necessary. Studies were performed with IBD Monte Carlo events and variations of the parameters of each of the four above factors. From these studies, a symmetric systematic uncertainty of 0.3% on the total signal normalization was established.

7.3.2.4 Gadolinium Capture Fraction

Neutrons produced by IBD interactions in the $\bar{\nu}_e$ target capture on either Gadolinium or Hydrogen in the vast majority of occurrences. The fraction of captures which occur on Gadolinium ϵ_{Gd} directly factors into the number of detected IBD candidates, and is defined:

$$\epsilon_{Gd} = \frac{C_{n-Gd}}{C_{n-Gd} + C_{n-H}} \tag{7.2}$$

where C_{n-Gd} and C_{n-H} are the numbers of neutrons which capture on Gadolinium and Hydrogen, respectively, in a particular period of time.

A measurement of ϵ_{Gd} in data is performed by examining calibration data produced by using a tagged ^{252}Cf radioactive source, which produces neutrons by fission. The spectrum of the neutron captures is fit to a series of Gaussian peaks at known energies of H and Gd neutron captures, and the integrals of the peaks are compared to the predicted yield ϵ_{Gd} for the data. This measurement is then compared to Monte Carlo events generated by a simulated ^{252}Cf source, and the relative difference $(\epsilon_{Gd}^{data} - \epsilon_{Gd}^{sim})/\epsilon_{Gd}^{data}$ determines whether or not a correction must be applied to the signal prediction.

For this analysis iteration, a relative difference of ∼1.5% was measured, mandating that a correction factor of 0.985 be applied to the signal prediction. The uncertainty associated with this measurement was 0.3%, calculated from the degree of variation in ϵ_{Gd}^{data} and ϵ_{Gd}^{sim} observed between the center and edges of the fiducial volume.

7.3.2.5 Delayed Coincidence Δt Cut

Following an IBD interaction, the neutron captures on either Gadolinium or Hydrogen with a characteristic time determined by the relative concentrations of the two elements in the target scintillator. This characteristic time can be predicted from the chemical properties of the scintillator and implemented in the detector simulation.

The validity of this detector property is evaluated by comparing ^{252}Cf calibration data in the detector with simulation Monte Caro ^{252}Cf events. The relevant containment efficiency $\epsilon_{\Delta t}$ is the ratio:

$$\epsilon_{\Delta t} = \frac{C_{[2,100]}}{C_{[0,200]}} \tag{7.3}$$

where $C_{[a,b]}$ is the number of delayed energy depositions with (a μsec)$<$ Δt $<$(b μsec), following a tagged ^{252}Cf fission, with Δt measured following the energy deposition of the fission. This quantity was measured along the z-axis of the detector using a ^{252}Cf source deployed down the chimney, as well as for various positions along the outer edge of the $\bar{\nu}_e$ target using the guide tube.

No correction factor was applied to the signal normalization based on these studies. The uncertainty on the signal normalization due to a possible systematic effect in the Δt

distribution was found to be 0.5% relative to the total signal prediction, calculated from the degree of relative variation in $\epsilon_{\Delta t}$ for data and MC observed between the center and edges of the fiducial volume.

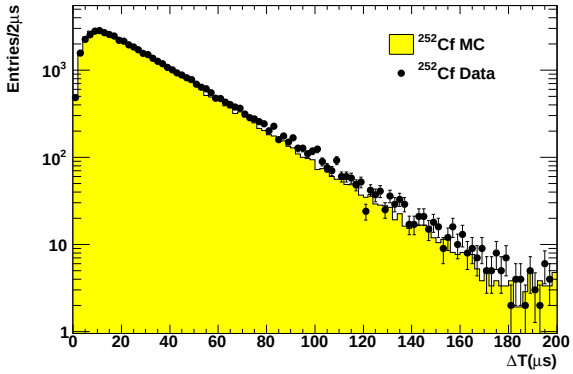

Figure 7.9: Delayed neutron capture time from ^{252}Cf calibration source deployment data. Black points are data; yellow region is from calibration source Monte Carlo. From [8].

7.3.2.6 Delayed Energy Containment Efficiency

Even with the design feature of the γ-catcher to maximize energy containment, it is still possible for γ rays emitted from n-Gd captures to escape conversion into visible light, *i.e.* from absorption in material. This lack of complete containment has a higher probability of occurrence at high values of ρ and z, near the edges of the $\bar{\nu}_e$ target. This effect is modeled in the detector simulation, but is highly dependent on geometric, optical, and particle transport properties of the simulation.

The relevant containment efficiency $\epsilon_{\Delta E}$ is measured by the ratio taken from ^{252}Cf data:

$$\epsilon_{\Delta E} = \frac{C_{[6,12]}}{C_{[4,12]}} \tag{7.4}$$

where $C_{[a,b]}$ is the number of delayed energy depositions with (a MeV)$< E_{\rm vis} <$(b MeV), following a tagged ^{252}Cf fission. This quantity was measured along the z-axis of the detector using a ^{252}Cf source deployed down the chimney, as well as for various positions along the outer edge of the $\bar{\nu}_e$ target using the guide tube.

While no modification to the simulation was employed to account for relative measured

differences between data and simulation, an uncertainty on the total signal normalization was estimated conservatively at 0.7% of the total signal rate based on these measurements, calculated from the degree of relative variation in $\epsilon_{\Delta E}$ for data and MC observed between the center and edges of the fiducial volume.

7.3.2.7 Multiplicity Cut

Recalling from Section 7.2.1, the multiplicity cut requires that no valid trigger ($E_{\text{vis}} > 0.5$ MeV, and passes light noise cuts) occur in the 100 μsec window before the prompt event, and that there exist only one only one valid trigger in the [2, 100] μsec window following the prompt event, and no valid trigger in a [100, 400] μsec window following the prompt event. This cut does not reduce any background, but eliminates ambiguious cases where two prompt events of different energies could "share" a delayed event.

The multiplicity cut imposes a correction on the normalization of the predicted IBD signal selection of 0.99455, due to the lack of interleaved singles events in the Monte Carlo. This correction factor is based on the Poisson probability of a single event with the proper energy appearing within the 500 μsec isolation window imposed by the multiplicity cut. The rate of single events is a well-measured 10.87 Hz, leading to a probability of 0.005435. This probability is subtracted from unity to get the correction factor to be applied to the predicted signal. This correction has negligible uncertainty, due to the precise measurement of the single event rate.

7.3.3 Signal Prediction Summary

Following the considerations mentioned in Sec. 7.3.1, the expected number of $\bar{\nu}_e$-induced IBD interactions in the detector N_a is calculated as given in Eq. 6.17, where the index a runs over the 72 bins in $E_{\bar{\nu}}$ and integration period.

In practice, the number of protons N_{prot} used in calculating the N_a includes the neutrino target scintillator, target tank, gamma catcher, GC tank, and buffer oil. According to the N_a, Monte Carlo events are generated in these volumes according to the expected proton density and reactor power. In addition to the IBD kinematic quantities from the detector, each Monte Carlo event contains the true energy $E_{\bar{\nu}}$ and originating reactor R of, and

the baseline L traveled by the progenitor $\bar{\nu}_e$. These Monte Carlo events are generated at 100-times expected statistics in order to limit any statistical fluctuations; their weights are scaled down when used in the final oscillation fit.

The Monte Carlo events are then processed through the GEANT4-based [143] detector simulation package, DCGLG4sim [144]. DCGLG4sim simulates how the scintillation and Cerenkov photons created following the IBD interactions propagate throughout the detector. The resulting simulation data are then used as input to the Double Chooz Read-out System Simulation (DCRoSS), which simulates the detector and electronics responses to the simulated photons collected by the PMTs. A suite of reconstruction algorithms are then applied, culminating in the final quantity of measured visible energy E_{vis} for each energy deposition.

The reconstructed Monte Carlo events then have the set of IBD candidate selection cuts from Sec. 7.2.1 applied to them (or, in the cases of the peripheral analyses, the amended selection cuts from Sec. 7.2.2.1 or 7.2.2.2). Thus, the only modifications to the event weights which need to be applied are due to those effects which are not modeled properly in the simulation chain, as described in Sec. 7.3.2. This is accomplished by applying the signal normalization factor as given in Table 7.7. The chain of processing from the calculated number of expected IBD events to an expected number of IBD candidates in the detector N_i^{exp} is as follows:

$$N_a^R \begin{pmatrix} E_{\bar{\nu}} \\ L \end{pmatrix} \xrightarrow[\text{CT}]{\text{GLG4sim, RoSS}} N_i^R \begin{pmatrix} E_{\bar{\nu}} \\ L \\ E_{\text{vis}} \end{pmatrix} \xrightarrow[\text{Sig. Norm. Factor}]{\text{IBD Cand. Sel.}} N_i^{\text{exp},R} \begin{pmatrix} E_{\bar{\nu}} \\ L \\ E_{\text{vis}} \end{pmatrix} \tag{7.5}$$

where the final index i runs over bins in reconstructed energy E_{vis} and integration period. The selected Monte Carlo IBD candidates represented as $N_i^{\text{exp},R}$ will be used as inputs to the final oscillation fit in Sec. 7.7.

7.3.3.1 Efficiency Uncertainty Propagation

The effect of an error on the selection efficiency can act as a bias in the signal normalization. Thus, the uncertainties listed in Table 7.6 are added in quadrature and propagated to the oscillation analysis as a covariance matrix derived from the shape of the predicted signal.

This matrix is implemented as a normalization uncertainty with a total relative magnitude of:

$$\frac{\sigma_{\text{eff}}}{\sum_{i=1}^{36}\sum_{R=1,2} N_i^{\text{exp},R}} = 1.005\% \tag{7.6}$$

of the signal prediction. The same degree of normalization uncertainty is presumed to apply to both integration periods, and is fully correlated between them:

$$M_{ij}^{\text{eff}} = \left(\sum_{R=1,2} N_i^{\text{exp},R}\right)\left(\frac{\sigma_{\text{eff}}}{\sum_{i=1}^{36}\sum_{R=1,2} N_i^{\text{exp},R}}\right)^2\left(\sum_{R=1,2} N_j^{\text{exp},R}\right). \tag{7.7}$$

7.4 Background Measurements

Three main backgrounds were included in the oscillation fit, and constrained by measurements using the data. The background from accidental coincidences is described in Sec. 7.4.1, the cosmogenic ^{9}Li background is described in Sec. 7.4.2, and the combined fast-neutron/stopping-muon correlated background is described in Sec. 7.4.3. The final part of each of those sections describes how the uncertainty on each measurement is propagated into the final oscillation fit (Sec. 7.7) as a covariance matrix, a fit parameter and pull term in the fit statistic, or a combination. It is worthwhile to note that the final measurements of the ^{9}Li and fast-neutron/stopping-muon backgrounds will be output parameters from the oscillation fit itself. Finally, a set of cross-checks of the background measurements is described in Sec. 7.4.4.

7.4.1 Accidental Background

The accidental background contribution was measured by applying the neutrino selection cuts described in Sec. 7.2 to data, but using a coincidence window separated by 1 second. This "off-time" window effectively measures the rate of random coincidences passing the neutrino selection cuts without the correlated events from real n-Gd captures of IBD-generated neutrons. A total of 198 off-time windows, each separated by 500 μs, were used to increase the statistics of the measurement, thereby improving its precision. The

total rate for accidental background events in the prompt spectrum was measured to be $R_{\text{acc.}} = (0.261 \pm 0.002)$ events per day. The spectrum, shown in Fig. 7.10, is found to be in agreement with an estimated spectrum of events produced by natural radioactivity. Any light noise remaining after the cuts described in Sec. 7.2 is included in this measurement, and is estimated to contribute 1% of the total accidentals rate.

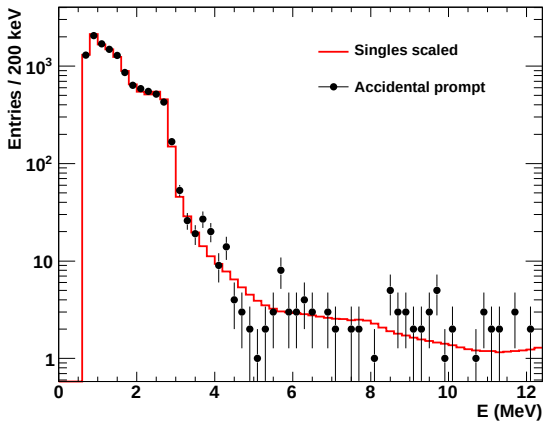

Figure 7.10: Accidental background spectrum measurement from the second Double Chooz oscillation analysis. Black points are data, red line is a scaled estimation of the singles spectrum derived from measurements of natural radioactivity in the detector. From [8].

7.4.1.1 Uncertainty Propagation

Since this measurement is from data, uncertainties on the binned accidental background spectrum are considered to be uncorrelated between bins. For the measured background rate of $R_{\text{acc.}} = 0.261$ events per day and uncertainty $\sigma_{R_{\text{acc.}}} = 0.002$ events per day, the covariance matrix associated with the accidental background population $N_i^{\text{acc.}}$ is:

$$M_{ij}^{\text{acc.}} = \delta_{ij} \sqrt{\frac{N_i^{\text{acc.}}}{\sum_k N_k^{\text{acc.}}}} \left(\frac{\sigma_{R_{\text{acc.}}}}{R_{\text{acc.}}} \right)^2 \sqrt{\frac{N_j^{\text{acc.}}}{\sum_k N_k^{\text{acc.}}}}. \tag{7.8}$$

7.4.2 Cosmogenic Lithium-9

The rate of ^{9}Li in the IBD candidate sample is constrained and estimated by observing the distribution in time Δt_μ of IBD-like interactions since the closest preceding muon in a 20-second time window. The distribution of Δt_μ is fit to a combination of an exponential and a constant background:

$$f\left(\Delta t_\mu\right) = \left(\frac{A}{\tau_9}\exp\left(-\frac{\Delta t_\mu}{\tau_9}\right) + C\right)\left(1 - \frac{\Delta t_\mu}{T}\right) \tag{7.9}$$

where τ_9 is the 257 msec lifetime of ^{9}Li, A is proportional to the rate of ^{9}Li, C represents the constant background, and the term containing $T = 3600$ seconds is a correction factor accounting for the finite lengths of physics runs. The fit value for A and its uncertainty are converted into a rate for ^{9}Li using the total live time of the data used to construct the fit.

This exponential fit is repeated for muon-IBD events where the muon energy E_μ falls into one of three energy ranges:

1. $E_\mu > 600$ MeV (HE): Classified as showering muons; the probability of these muons having produced a cosmogenic isotope is enhanced by their showering property. The exponential fit of Eq. 7.9 yields a rate of cosmogenic events from muons in this energy range of 0.95 ± 0.11 day^{-1}.

2. 250 MeV $< E_\mu <$ 600 MeV (ME): Classified as muons which have passed through the $\bar{\nu}_e$ target and GC, but may not have generated a shower of particles. These muons do contribute to the population of cosmogenic events. The sample is purified by requiring a maximum distance between the muon track and the IBD-like event of $d_{\mu\nu} < 80$ cm. Uncertainty on the efficiency of this cut is estimated from the lateral distance profile of the $E_\mu > 600$ MeV sample. From the subsequent exponential fit of Eq. 7.9 to this sample, a rate of cosmogenic events from muons in this energy range of 1.08 ± 0.44 day^{-1} is found.

3. $E_\mu <$ 250 MeV (LE): Classified as muons which pass through the buffer or clip an edge of the GC. The same distance cut as the 250 MeV $< E_\mu <$ 600 MeV sample is applied. A fit to Eq. 7.9 places an upper limit on the number of cosmogenic events from this muon sample of < 0.3 day^{-1}.

The total measured rate of cosmogenic isotopes is then $2.05^{+0.62}_{-0.52}$ events per day. The uncertainties on this measurement are dominated by the low statistics involved in acquiring a clean sample of middle-energy ^{9}Li events.

It should be noted that contamination from ^{12}B, another cosmogenic isotope with a life time of $\tau_{12} = 29$ ms, is removed from the measured cosmogenic rate in this analysis by requiring a maximum distance between prompt and delayed events of the IBD-like event of 90 cm. This cut has a small inefficiency of $\sim 1\%$.

The ^{9}Li-reduction cut mentioned in Sec. 7.2.1 has the effect of vetoing cosmogenic events within 0.5 sec following a muon with $E_\mu > 600$ MeV, reducing the total cosmogenic rate by 0.89 ± 0.10 events per day. Thus, the remaining cosmogenic ^{9}Li rate in the DC2ndPub analysis is found to be 1.25 ± 0.54 events per day, where the central value has been modified slightly to symmetrize the error bars while maintaining the same uncertainty interval.

Cosmogenic event rates for the peripheral analyses were also determined by similar fits to their Δt_μ distributions. A rate of 2.10 ± 0.57 events per day was measured for the non-^{9}Li-reduced analysis. The ^{9}Li-free analysis' stringent cuts reduce its cosmogenic rate to 0.60 ± 0.54 events per day. For both of these numbers, the central values have been modified to produce symmetric error bars while maintaining the absolute uncertainty interval.

As an aside from the main rate measurement, a spectrum of cosmogenic events was produced by selecting events with $E_\mu > 620$ MeV and $d_{\mu\nu} < 70$ cm, with $\Delta t_\mu < 600$ ms. Random coincidences were also subtracted, producing the measured spectrum shown in Figure 7.11.

7.4.2.1 Uncertainty Propagation

The ^{9}Li background is propagated to the final fit by combining a Monte Carlo-generated spectrum of events with the measured background rate. The spectrum is created by using a nuclear model to simulate ^{9}Li decays in the Inner Detector. This generator, dubbed DC-GenSpec, is based on nuclear decay data [145, 146], and allows for some nuclear parameters to be adjusted in order to evaluate potential effects on the end spectrum. The generated MC events are then processed through the detector response simulation and reconstruction, similar to the sequence of Eq. 7.5. Following application of the IBD candidate selection

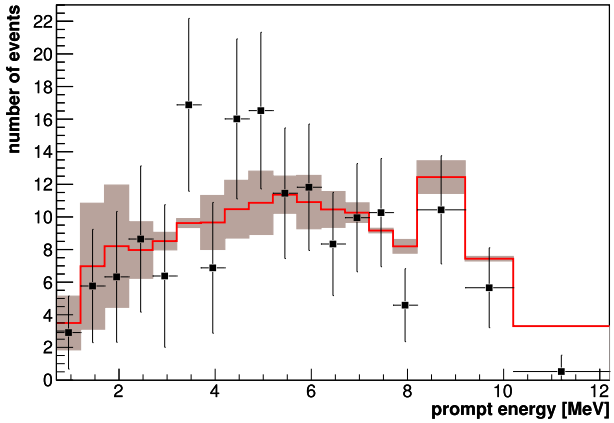

Figure 7.11: Spectrum of cosmogenic candidate events, with $E_\mu > 620$ and $d_{\mu\nu} < 70$ cm, with $\Delta t_\mu < 600$ ms. Random coincidences have been subtracted from the spectrum. Red line is Monte Carlo prediction, with shaded region representing uncertainty on the Monte Carlo spectral shape from nuclear decay model uncertainties. From [8].

cuts, the product is a high-statistics set of ^{9}Li events which would fit IBD candidate criteria. These events are re-weighted in order to make the integral of the spectrum fit the central-value expectation of ^{9}Li rate times detector live time. When binned, this normalized spectrum gives the central-valued prediction for the ^{9}Li background population $N_i^{\mathrm{Li,CV}}$.

Uncertainties on the ^{9}Li prediction are treated as two orthogonal components: a normalization component based on the uncertainty of the measured rate; and a spectral shape component.

For the measured background rate of $R_{\mathrm{Li}} = 1.25$ events per day and uncertainty $\sigma_{R_{\mathrm{Li}}} = 0.54$ events per day, the covariance matrix associated with the ^{9}Li background population $N_i^{\mathrm{Li,CV}}$ is:

$$M_{ij}^{\text{Li rate}} = N_i^{\mathrm{Li,CV}} \left(\frac{\sigma_{R_{\mathrm{Li}}}}{R_{\mathrm{Li}}} \right)^2 N_j^{\mathrm{Li,CV}} \tag{7.10}$$

This formalism is also easily applied to the "Li-Free" or non-Li-reduced cases by using the corresponding rates and uncertainties. Since the spectral shape is based on nuclear decay properties of ^{9}Li, it is not expected to change with the use of different timing cuts.

In practice, the uncertainty on the ^{9}Li rate is implemented with a fit parameter $\epsilon_{^9\mathrm{Li}}$ and corresponding pull term in the fit statistic, as described in Sec. 7.7.2.1. Thus, in the fit

implementation, the ^{9}Li spectrum enters as a dynamic set of values N_i^{Li} calculated as:

$$N_i^{\mathrm{Li}} = \epsilon_{^9\mathrm{Li}} N_i^{\mathrm{Li,CV}} \tag{7.11}$$

In cases where the matrix $M_{ij}^{\text{Li rate}}$ is used to represent the ^{9}Li rate uncertainty, the parameter $\epsilon_{^9\mathrm{Li}}$ is fixed to its null-effect value of 1.

The uncertainty on the spectral shape is determined by comparing the output of two Monte Carlo event sets with different nuclear decay parameters. The central-value ^{9}Li spectrum $N_i^{\mathrm{Li,CV}}$ is compared to a spectrum $N_i^{\mathrm{Li,Max}}$ with the endpoint energies of the nuclear decay states all set to the limits of their uncertainty intervals. The matrix is then constructed:

$$M_{ij}^{\text{Li shape}} = \left(N_i^{\mathrm{Li,Max}} - N_i^{\mathrm{Li,CV}}\right) \times \left(N_j^{\mathrm{Li,Max}} - N_j^{\mathrm{Li,CV}}\right) \tag{7.12}$$

Since this uncertainty component is close to, but not exactly, a "spectral shape only" uncertainty, the sum of the elements $\sum_{i,j} M_{ij}^{\text{Li shape}}$ is near zero. The elements of this matrix are recalculated as a function of the rate pull parameter $\epsilon_{^9\mathrm{Li}}$ in cases where it is used, as described in Sec. 7.7.1.

7.4.3 Fast Neutron & Stopping μ Backgrounds

Two irreducible correlated backgrounds are known to affect Double Chooz:

- Fast Neutron Recoils (FN): A muon passing near the detector creates a spallation neutron which enters the ID without triggering the IV. The neutron interacts with a proton, with the scintillation of the recoiling proton providing the prompt component of the delayed coincidence. The neutron the captures on Gd to provide the delayed component.

- Stopping muons (SM): A muon enters the ID undetected through the dead region of the detector surrounding the chimney, and stops. The short scintillation track of the muon provides the prompt component of the delayed coincidence, while the muon decay and Michel electron provides the delayed component. Because the stopping muon must enter the detector through dead (noninstrumented or nonscintillating) regions, which only exist around the chimney, these events are known to concentrate

towards the top and radial center of the detector. around the chimney of the detector, These events have a prompt-delayed time distribution following the 2.2 μsec lifetime of the muon.

Study of this combined set of backgrounds is accomplished by examining IBD candidates in the energy region 12 MeV $< E_{\rm vis} <$ 30 MeV where no IBD signal events are expected. The spectrum is then extrapolated down into the IBD signal region 0.7 MeV $< E_{\rm vis} <$ 12.2 MeV. In order to allow independent study of each, the components of this background are divided using a cut on the time difference δt between the prompt and delayed parts of the events in this high-$E_{\rm vis}$ sample. As shown in Figure 7.12, the Δt profile of stopping muons is driven by capture of the μ, with a characteristic time of 2.2μsec, while fast neutron events follow a Δt profile with the same $\sim 30\mu$sec characteristic time as IBD events. Thus, stopping muon events are selected as having $\Delta t < 10\mu$sec, while fast neutron recoils are those events with $\Delta t > 10\mu$sec. In combination with independent measurements of tagged samples of each background component, these two rate measurements allow for a measurement of the fast-neutron and stopping muon background energy spectral shape without making prior assumptions regarding combined spectral shape. It is similar to the method described in Sec. A.4.3, except that the previously-used method presumed a flat distribution for the combined background.

7.4.3.1 Stopping Muon Tagging

A pure sample of stopping muon events is tagged by selecting events where the delayed component of the coincidence is certainly from the Michel electron produced in muon decay. This is achieved by using a delayed energy window of 20 MeV $< E_{\rm vis} <$ 60 MeV. In this energy regime, the largest background is from high-energy spontaneous light noise. The light noise events are subtracted from the measured stopping muon spectrum by use of a large off-time window: 1000 μsec $< \Delta t <$ 1100μsec, with the measured off-time spectrum scaled down to the 10 μsec window of the stopping muon selection. The background-subtracted prompt spectrum of the stopping muon population is then fit to a linear hypothesis.

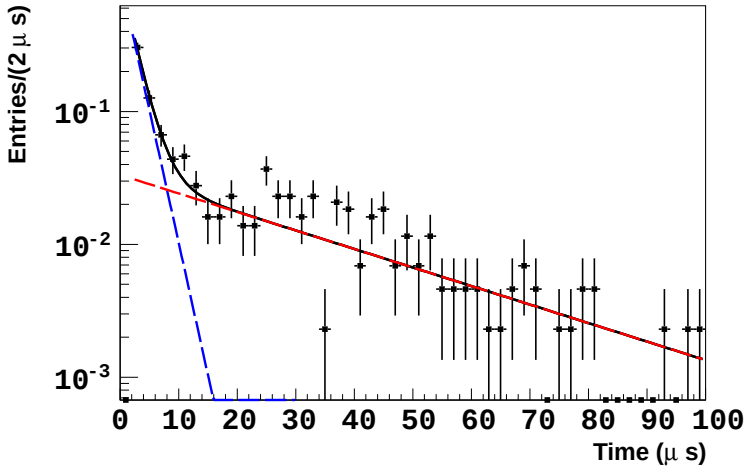

Figure 7.12: Distribution of time separation Δt between prompt and delayed signal components of background events with 12 MeV $< E_{\text{vis}} <$ 30 MeV. Two-exponential fit represents populations of stopping muons (blue dashed) with 2.2μsec time constant, and fast neutron recoils (dashed red) with $\sim 30\mu$sec time constant.

7.4.3.2 Fast Neutron Tagging

A pure sample of fast neutron recoil events is isolated by selecting events which are coincident with a low-E_{vis} energy deposition in the IV. This strategy is based on the assumption that fast neutron recoils are often produced by neutrons from showering muons, where the multiplicity of neutrons produced by the muon is high. Neutrons other than the IBD candidate-producing one interact within the IV by proton recoil, or capture on hydrogen. However, this type of event has large "background" contributions due to: true IBD interactions in the inner detector, coincident with a neutron capture in the IV; IV interactions by gamma rays from natural radioactivity; or dark noise in the IV PMTs. The dark noise background is suppressed by requiring that at least two IV PMTs produce charge as part of the tagged event. The other backgrounds are tagged by use of spatial criteria: a requirement that the prompt and delayed components of the IBD-like signal occur within 150 cm of each other rejects interactions by gamma rays in the IV; a requirement that the IV and ID PMT signals occur within a [-2, 95] ns window of each other rejects coincidental antineutrino events. The remaining background-subtracted spectrum is then fit to a linear hypothesis to determine the final background estimate.

Component	Rate [day^{-1}]	Unc. [day^{-1}]
Fast Neutron	0.33	0.16
Stopping Muon	0.60	0.22
Total	0.93	0.26

Table 7.8: Fast neutron and stopping muon population break-out, before use of OV-based veto condition. Rate measurements described in Sections 7.4.3.1 and 7.4.3.2.

7.4.3.3 Background Combination

The total fast-neutron/stopping-muon background spectrum is found by summing the final spectra produced by the methods described in Sections 7.4.3.1 and 7.4.3.2. The background-subtracted spectra produced in each section are summed, and fit to a linear hypothesis. The fit spectrum is extrapolated into the IBD signal region, and scaled to the summed measured rates of each background component. The total expected background rate from fast neutrons and stopping muons is 0.93 ± 0.26 per day, before any OV-based veto is imposed. The break-out of fast neutron and stopping muon populations and their uncertainties is given in Table 7.8.

7.4.3.4 Inclusion of OV-based Veto Condition

As described in Sec. 7.2.1, IBD candidate selection criteria for this analysis require an anticoincidence of the prompt event with the Outer Veto. This measure was found to decrease the rate of fast neutron and stopping muon events by 9% and 43%, respectively, as shown in Table 7.9. As shown in Figure 7.14, most of the vetoed events were reconstructed near the center top of the detector, consistent with the majority coming from stopping muons entering near the chimney. Similarly, Figure 7.15 shows most of the OV events of the anti-coincident events having come from the area of OV coverage near the chimney of the Inner Detector. The prompt spectrum of the anticoincident events is shown in Figure 7.16, and displays a distribution that is consistent with a flat spectrum.

The final combined rate for the background was found to be 0.67 ± 0.20 d^{-1}, including the OV anticoincidence. The OV anticoincidence condition was also used to establish the

Component	OV Not Used	OV Anticoincidence Used	Reduction $\frac{N_{\text{w/o OV}}-N_{\text{with OV}}}{N_{\text{with OV}}+N_{\text{w/o OV}}}$
Fast Neutron	0.33 ± 0.16 d^{-1}	0.30 ± 0.14 d^{-1}	9 ± 6 %
Stopping Muon	0.60 ± 0.22 d^{-1}	0.34 ± 0.18 d^{-1}	43 ± 28%
Total	0.93 ± 0.26 d^{-1}	0.67 ± 0.20 d^{-1}	28 ± 11%

Table 7.9: Fast neutron and stopping muon population break-out, before and after use of OV-based veto condition. Rate measurements described in Sections 7.4.3.1 and 7.4.3.2, with OV veto described in Section 7.4.3.4.

propagated uncertainty on the slope of the fast neutron/stopping muon spectrum: a rescaled version of the spectrum without the anticoincidence requirement was used to define the 1σ deviation for the spectral shape.

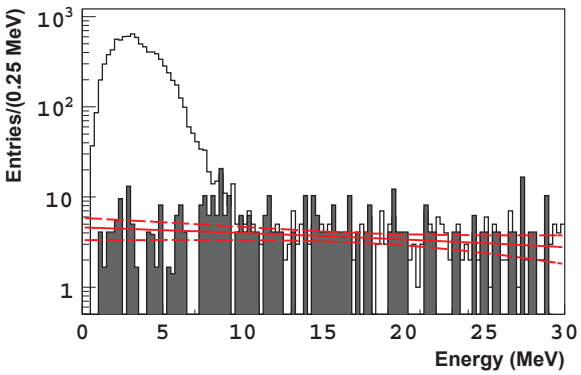

Figure 7.13: Fast Neutron and Stopping Muon combined spectral model best fit (solid red line) with $\pm 1\sigma$ error band (dashed red), energy distribution of tagged FN and SM population (gray histogram), and IBD spectrum. From [8].

7.4.3.5 Uncertainty Propagation

Uncertainties on the FN/SM prediction are treated as two orthogonal components: a normalization component based on the uncertainty of the measured rate; and a spectral shape

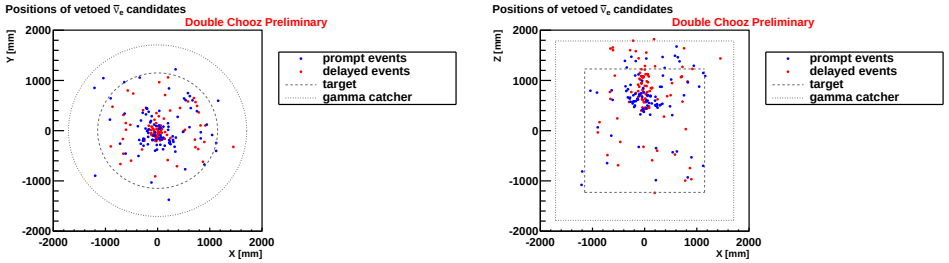

(a) xy View (b) xz View

Figure 7.14: Reconstructed positions of selected IBD candidates projected in the $xy-$ (Fig. 7.14(a)) and $xz-$planes (Fig. 7.14(b)).

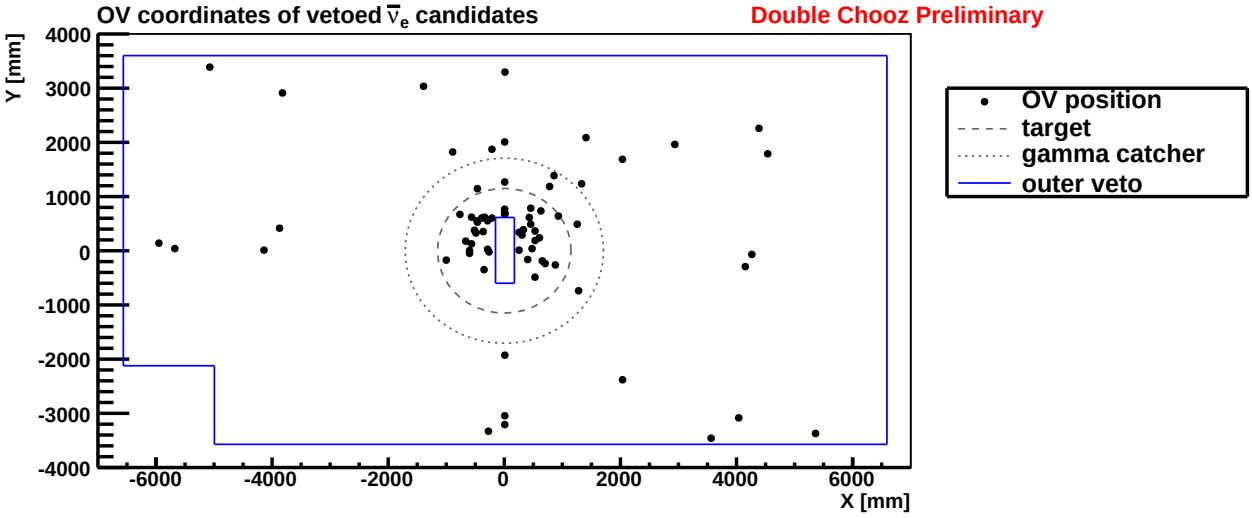

Figure 7.15: Reconstructed XY positions in the Outer Veto of events rejected by the OV-based anticoincidence (black dots). Solid blue outline shows the extent of Outer Veto coverage; dashed and dotted circles show extent of target and gamma catcher volumes.

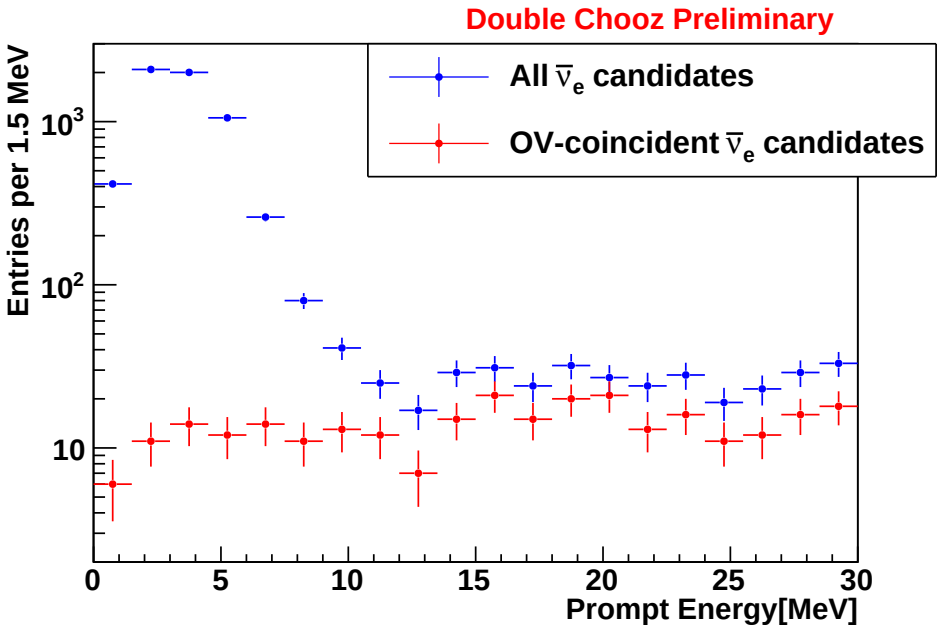

Figure 7.16: Prompt spectra of all selected IBD candidates using the "^{9}Li-reduced" cuts (blue points) and spectrum of IBD candidates coincident with a signal in the Outer Veto (red points).

component.

For the measured background rate of $R_{\rm fn} = 0.67$ events per day and uncertainty $\sigma_{R_{\rm fn}} = 0.20$ events per day, the covariance matrix associated with the FN/SM background population $N_i^{\rm fn,CV}$ is:

$$M_{ij}^{\text{fn rate}} = N_i^{\rm fn,CV} \left(\frac{\sigma_{R_{\rm fn}}}{R_{\rm fn}} \right)^2 N_j^{\rm fn,CV} \tag{7.13}$$

In practice, the uncertainty on the FN/SM rate is implemented with a fit parameter $\epsilon_{\rm fn}$ and a corresponding pull term in the fit statistic, as described in Sec. 7.7.2.1. Thus, in the fit implementation, the FN/SM spectrum enters as a dynamic set of values $N_i^{\rm fn}$ calculated as:

$$N_i^{\rm fn} = \epsilon_{\rm fn} N_i^{\rm fn,CV} \tag{7.14}$$

In cases where the matrix $M_{ij}^{\text{fn rate}}$ is used to represent the FN/SM rate uncertainty, the parameter $\epsilon_{\rm fn}$ is fixed to its null-effect value of 1.

As mentioned in Sec. 7.4.3.4, the uncertainty on the spectral shape is determined by comparing the fit combined spectra $N_i^{\rm fn,CV}$ to the spectrum without the OV anticoincidence requirement $N_i^{\text{fn,No OV}}$, with the $N_i^{\text{fn,No OV}}$ scaled to the same normalization as the $N_i^{\rm fn,CV}$. The covariance matrix is then constructed:

$$M_{ij}^{\text{fn shape}} = \left(N_i^{\text{fn,No OV}} - N_i^{\rm fn,CV} \right) \times \left(N_j^{\text{fn,No OV}} - N_j^{\rm fn,CV} \right). \tag{7.15}$$

Since this uncertainty component is implemented as a "spectral shape only" uncertainty, with $N_i^{\rm fn,CV}$ and $N_i^{\text{fn,No OV}}$ having the same total normalization the sum of the elements $\sum_{i,j} M_{ij}^{\text{fn shape}}$ is zero. The elements of this matrix are recalculated as a function of the rate pull parameter $\epsilon_{\rm fn}$ in cases where it is used, as described in Sec. 7.7.1.

7.4.4 Cross-checks of Background Measurements

Two cross-checks of the measured background rates were made by independent means: an extrapolation of background rates from the measured rate of observed events as a function of reactor power, and a measurement of the observed rate during periods of time where both reactors were at near-zero thermal power.

7.4.4.1 Observed Candidate Rate vs. Expected $\bar{\nu}_e$ Rate

Plotting the observed IBD candidate rate versus expected event rate, as is done in Figure 7.17, is loosely equivalent to plotting the IBD candidate rate versus average reactor power. At the minimal expected rate, where both reactors are at or near zero thermal power, the irreducible backgrounds dominate the observed IBD candidate rate. Thus, a linear fit to these data allows a measurement of the sum of all irreducible backgrounds to be made by extrapolation. This is the linear fit depicted on Figure 7.17, and gives a best-fit value for the background rate of 2.9 ± 1.1 events per day, consistent within uncertainties with the combined background estimate of 2.18 ± 0.58 events per day. This linear fit also allows for a measurement of $\sin^2(2\theta_{13})$ based on the slope of the line; in essence, a "rate+time"-style fit. The linear best-fit shown in Figure 7.17 corresponds to a value of $\sin^2(2\theta_{13}) = 0.19 \pm 0.06$ at the MINOS value for Δm^2_{31} [83]. This value is in agreement within uncertainties with those values found by the fitting methods described in Sec. 7.7.

7.4.4.2 Measured Candidate Rate with Both Reactors Off

Soon after the Nov. 2011 end of the data-taking period for the first Double Chooz analysis iteration, both reactors B1 and B2 were shut down for a period of ∼24 hours. This period yielded a physics data livetime of 0.84 days (22.5 hours) during which the dominant sources of expected IBD candidates are the irreducible backgrounds. Fewer than 0.3 residual $\bar{\nu}_e$ events are expected during this time period with the reactor cores idle from residual radioactive decays. Three events were found which passed the first four IBD candidate selection cuts listed in Sec. 7.2.1, compared to a background prediction of about 2.18. Two of these events were found to have prompt energies of 4.8 MeV and 9.4 MeV, and were reconstructed within 30 cm and 240 cm of the closest energetic muon. The second candidate was found to be rejected by the "^{9}Li-reduction" showering muon veto. These factors suggest that these IBD candidates were cosmogenic ^{9}Li background events. The third candidate was found to have a prompt energy of 0.8 MeV, with its prompt and delayed components reconstructed 3.5 m distance from each other. This is suggestive of an accidental coincidence.

While the second publication analysis was in progress, another 8 days of data with both

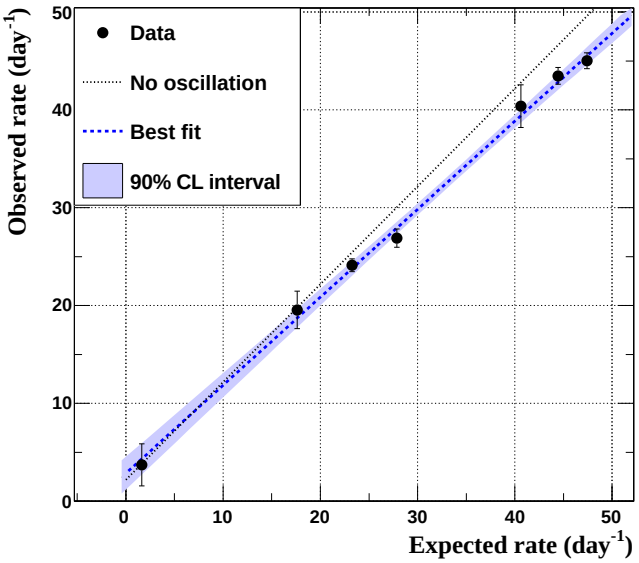

Figure 7.17: Daily number of observed IBD candidate events plotted versus the expected number of $\bar{\nu}_e$ events. Dashed blue line shows the best fit to the data, with blue region giving the 90% confidence level band. Dotted line shows the expectation from the no-oscillation scenario. Best-fit parameters described in text of Sec. 7.4.4. From [8].

reactors off were taken. While these data were not included in the analysis of the second publication, they are described in more detail in Sec. 7.8, and in [147].

7.5 Energy Scale

The energy scale of DC2ndPub was revised from that of the first analysis iteration in a number of ways. The definition of the visible energy E_{vis} for an energy deposition in the Inner Detector is found by summing the charge q_l in all channels l and applying a set of corrections:

$$E_{\text{vis}} = \left(\sum_l \frac{q_l}{\text{gain}_l(q_l)} \right) \times f_u^m(\rho, z) \times f_s^m(t) \times f_{\text{MeV}}^m \tag{7.16}$$

where $f_u^m(\rho, z)$ is a correction taking into account the spatial dependencies in the detector response, $f_s(t)$ is a correction taking into account time dependence of the detector response, and f_{MeV} sets the correspondence between detector response and absolute measured energy. These corrections carry indices m to show that in practice they take different numerical values if this methodology is applied to detector data or Monte Carlo. Each component of this equation is explained in the subsequent subsections, with treatment of the total uncertainty described in Sec. 7.5.5.

7.5.1 Per-channel Gain vs. Charge

Studies of the per-channel gain $\text{gain}_l(q_l)$ showed measurable non-linearities at low values of q_l. An illustration of this effect based on data taken during LED light-injection calibration runs is shown in Fig. 7.18. At the average light level of the Inner Detector ($\sim 230 PE/\text{MeV}$), this effect could bias the reconstructed charge of a given energy deposition by up to 10%. To correct for this effect, a fit was made to gain measurements below 200 units of charge for each channel, with the fitted function used for applied gain in those regions. This gain function was found to change following a power-cycle of the electronics, warranting calibration data to be taken and fits performed following each such event. Similar fits are made to the Monte Carlo simulated gain, following with the analysis paradigm of applying identical methodologies to both detector data and simulation events, though no such nonlinearity is modeled in the Monte Carlo.

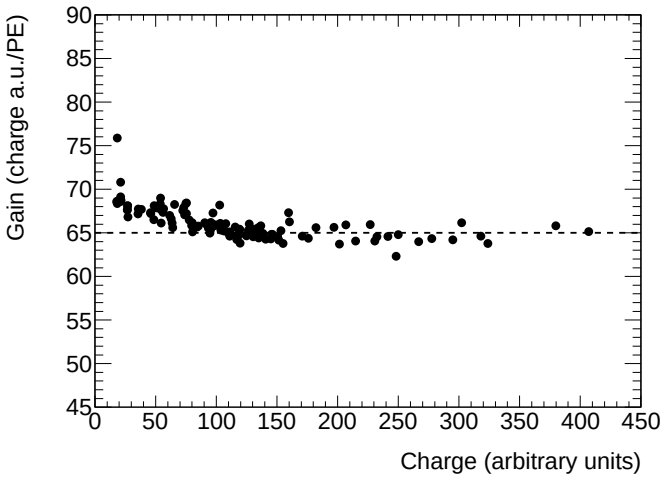

Figure 7.18: Illustration of the dependence of gain for a single channel at low values of integrated pulse charge. Dashed line indicates an ideal behavior of the gain for all values of charge. From [8].

7.5.2 Detector Response Spatial Correction

The spatial correction $f_u^m(\rho, z)$ is constructed by measuring differences in the location of the n-H capture peak using cosmogenic spallation neutrons. These measurements are characterized in a number of voxels of the detector, creating a "map" of the detector's energy response in cylindrical coordinates ρ and z as compared to the response in the center. A graphical representation of this map is shown in Fig. 7.19. The largest deviations found within the Neutrino Target were found to be of order 5%. A 2D interpolation method provided a smooth behavior to the function at all values of ρ and z within the ID. A similar map was generated with, and applied to, Monte Carlo events.

7.5.3 Detector Response Time Dependence Correction

Changes in detector response as a function of time were driven by two principal effects: changes in readout gain or scintillator response; and the elimination of some PMT/electronics channels from calorimetric use due to failure of certain operational diagnostic metrics. These effects were corrected for using a measurements of the n-Gd capture peak using cosmogenic spallation neutrons; a plot of this peak position can be seen in Figure 7.20. The refer-

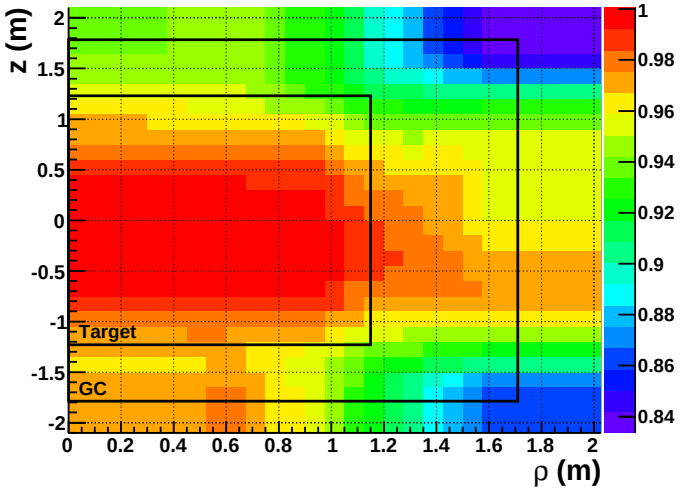

Figure 7.19: Detector calibration map in cylindrical coordinates ρ and z, as sampled with spallation neutrons capturing on Hydrogen within the Inner Detector. Solid black lines denote the boundaries of the Target and Gamma Catcher regions. Response variations are quantified as the fractional response with respect to that at the detector center. A similar map is constructed with the Monte Carlo simulation to similarly account for its slightly different spatial response dependence. From [8].

ence time t_0 of this calibration was taken to the a ^{252}Cf deployment at the center of the detector during the August 2011 calibration campaign. A measure of the remaining instability was made by observing the location of the spallation n-H capture peak following the time-dependent correction, shown in Figure 7.21, and found to be 0.61%.

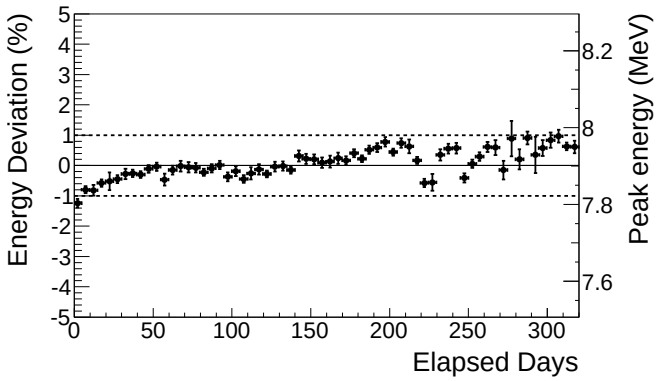

Figure 7.20: Measured E_{vis} of the spallation n-Gd capture peak, used to characterize detector response stability in time. From [8].

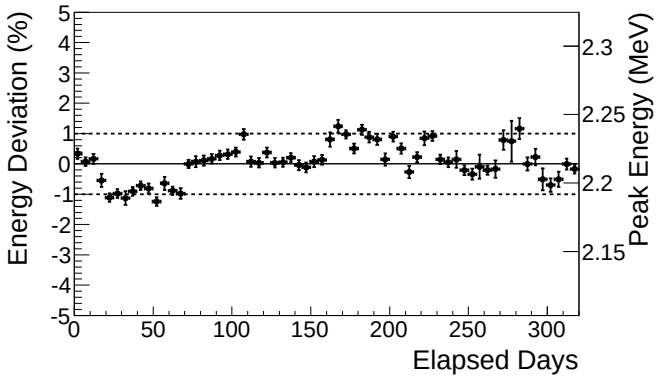

Figure 7.21: Plot of the reconstructed spallation n-H capture peak as a function of time during data taking. Observed step-like behavior is correlated with cycles of the electronics power. From these data, the systematic uncertainty on the energy response stability is estimated to be 0.61%. From [8].

Source	Error (%)
Spatial Non-uniformity	0.43
Time Instability	0.61
Non-linearity	0.85
Total σ_{P_E}/P_E	1.13

Table 7.10: Components of the total energy scale uncertainty interval.

7.5.4 Absolute Energy Scale

The absolute energy calibration is established with radioactive source deployments along the z-axis of the Inner Detector during the August 2011 calibration campaign. Monte Carlo simulation of the same sources was also used to determine the energy scale of the MC. From these methods, the absolute energy scale was found to be $f_{\text{MeV}}^{\text{data}} = 229.9\ PE/\text{MeV}$ for detector data, and $f_{\text{MeV}}^{\text{MC}} = 227.7\ PE/\text{MeV}$ for simulation, at the center of the detector at t_0.

7.5.5 Uncertainty Propagation

Uncertainties on the energy scale are propagated to the oscillation fit by complimentary methods of either a covariance matrix, or a pull parameter shifting the bins of the affected populations. Energy scale uncertainties only affect those event types which rely on the Monte Carlo for energy reconstruction: the $\bar{\nu}_e$ signal prediction, and the ^{9}Li prediction. The uncertainty prescription combines contributions from three sources: non-uniformity of detector response, instability of detector response, and relative non-linearity. While one of the contributions is due to non-linearity, all contributions are presumed to effect a linear shift in the energy scale.

Traditionally, the energy scale is modulated in the final oscillation fit as a parameter P_E which scales the energy E_{vis}^0 of some events comprising the Monte Carlo prediction:

$$E_{\text{vis}} = P_E E_{\text{vis}}^0. \tag{7.17}$$

This scaling is only applied to events whose energies E_{vis}^0 are determined by the Monte Carlo

reconstruction, and not by measurement in data (*e.g.* IBD signal events and ^{9}Li events, but not fast neutrons/stopping muons or accidentals). As tabulated in Table 7.10, three sources of uncertainty combine to give a relative interval $\sigma_{P_E}/P_E = 1.13\%$.

In practice, it was found that allowing P_E to float as a pull parameter in the χ^2 minimization fit led to instabilities of the minimizing software, MINUIT [148]. A pull parameter was desired in order to quantify the best-fit result, so a new approach was adopted based on a covariance matrix and a set of bin shifts derived from the matrix. These bin shifts were then associated with a new parameter α_E (to be more fully described below), allowing nearly-full functionality of the energy scale pull term without the previously-seen minimizer instabilities.

The energy scale covariance matrix was constructed using a MultiSim method (see Appendix C.4 for more detail). Sets of $u = [1, ..., U]$ random Gaussian throws $\{P_E\}_u$ are made on the energy scale parameter P_E and the correlated-random bin deviations $\{\delta N_i^{\text{pred}}\}_u = \{N_i^{\text{pred}}\}_u - \{N_i^{\text{pred}}\}_{P_E=1}$ are used to construct an average covariance matrix M_{ij}^{escale}:

$$M_{ij}^{\text{escale}} = \frac{1}{U}\sum_{u=1}^{U}\left(\{\delta N_i^{\text{pred}}\}_u \times \{\delta N_j^{\text{pred}}\}_u\right) \tag{7.18}$$

The matrix M_{ij}^{escale} is then converted to a set of fractional bin shifts S_i.

$$S_i = \sqrt{\frac{M_{ii}^{\text{escale}}}{N_i^{\text{pred}}}} \times \begin{pmatrix} -1 \text{ if } M_{ii}^{\text{escale}} < 0 \\ 1 \text{ if } M_{ii}^{\text{escale}} > 0 \end{pmatrix}. \tag{7.19}$$

The S_i represent the standard deviation of the fractional amount by which each bin should change for a 1σ deviation of the parameter P_E. The binary condition in the exponent evaluates to 0 or 1, and determines the overall sign of the bin shift. These shifts are propagated into the fit as being proportional to a new parameter α_E, and applied to the reweighted N_i^{pred} as shifts proportional to α_E:

$$N_i^{\text{pred}} = \left(N_i^{\text{pred}}\right)_{P_E=1} \times (1 + (\alpha_E - 1)\, S_i) \tag{7.20}$$

This presumes that the bin shifts effected by the energy scale are linear in nature, which is known to be an approximation similar to that which is presumed when constructing a covariance matrix. By construction, the effect is very similar to 1σ changes in P_E, as

illustrated in Figure 7.22. While the bin shifts are used for the majority of the analyses, the covariance matrix M_{ij}^{escale} is employed in the frequentist approach (see Sec. 7.7.4) with α_E fixed to 1.

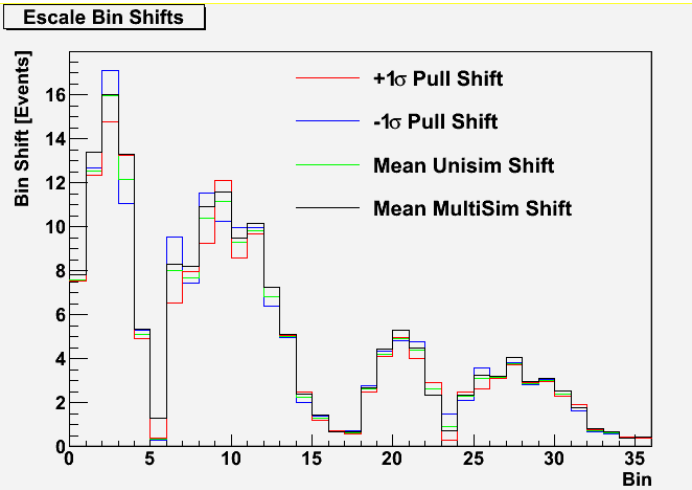

Figure 7.22: Magnitude of the shift of a bin's population for the main analysis, if different energy scale undertainty implementations are used. Red and blue lines indicate the shifts due to a $\pm 1\sigma$ shift of the parameter P_E as defined in Eq. 7.17. Green line represents the average shift due to $1sigma$ fluctuations in P_E in either direction. Black line represents the shift calculated with the MultiSim method as described by Eq. 7.19.

7.6 Multiple Integration Periods

Due to annual refueling shutdowns of the reactors, a significant portion of the data taken following the first Double Chooz publication was during periods of one-reactor-off time. During these periods, the signal/background ratio of the expected IBD candidate set is reduced by a factor of $\sim$2. In a rate-only analysis, this reduction of the relative amount of signal can actually *decrease* the sensitivity of the experiment as more data are taken, due to the absolute uncertainties of the backgrounds remaining constant. This fact motivated investigations into dividing the data into different integration periods based on the reactor power levels and performing a simultaneous fit to both periods.

The working premise of a multiple integration period (multi-IP) analysis is that dividing

data into n_τ integration periods based on reactor power will allow a high signal/background period (when both reactors are on) to drive the sensitivity of fit to oscillations, while a period of low signal/background (when one reactor is off/both are at low power) can be potentially be used to constrain background rates through fitting. Said another way, a multi-IP fit is a "rate+shape+time" fit where the temporal information contributes to background fitting while periods of high signal/background remain unhindered by additional backgrounds, though the range of the "time" variable may not correspond one-to-one with sequentially-taken data.

During the lead-in to the second Double Chooz publication, the quantity of one-reactor-off data and legacy binning choices allowed for an analysis with two integration periods ($n_\tau = 2$) to be considered. In this scenario, one integration period would contain data where both reactors were near full power, while the other would contain data where one or both reactors were at reduced power. A scenario with three integration periods ($n_\tau = 3$: both reactors near full power; reactor B1 reduced; reactor B2 reduced) was considered, but ruled impractical since it would have required the use of different binnings between integration periods in order to maintain sufficient statistics per bin. A three-IP analysis[2] should be reconsidered in the future, as Double Chooz continues to accrue data.

An analysis with two integration periods ($n_\tau = 2$) requires a set of sorting rules for determining which data are put in which period. These sorting rules were chosen based on which scheme would produce the best sensitivity to a null-oscillation measurement. The two sets of sorting rules considered were as follows, for integration periods numbered 0 and

[2]For example, a hypothetical $n_\tau = 3$ analysis could use the following sorting rules, for integration periods enumerated 0, 1, and 2:

- If the minimum power of either reactor is less than 20% during a particular detector run, then:
  - If reactor B1's minimum power is less than or equal to that of Reactor 2, the detector run is placed in IP 1.
  - If reactor B2's minimum power is less than that of Reactor 1, the detector run is placed in IP 2.
- Otherwise, the detector run is placed in IP 0.

Fit χ^2 Method	Single IP	"90-Plus" Rules	"20-minus" Rules
Rate-Only	0.05624	0.05418	0.05279
Shape-Only	0.08129	0.08114	0.08099
Rate+Shape	0.03949	0.03936	0.03925

Table 7.11: Null-oscillation sensitivity results from hypothetical analyses using different integration period sorting rules based on reactor power with the number of integration periods $n_\tau = 2$. Sensitivities are 1σ upper limits on $\sin^2(2\theta_{13})$. Detector systematics for these studies were a close approximation to what was used in the second DC publication, based on the state of studies at the time. As mentioned in 7.7.2, all χ^2 statistics with $n_\tau > 1$ include a time component, by definition.

1:

1. The "90-plus" sorting scheme
   - If the minimum power of either reactor is less than 90% during a particular detector run, then that detector run is placed in IP 1.
   - Otherwise, the detector run is placed in IP 0.
2. The "20-minus" sorting scheme
   - If the minimum power of either reactor is less than 20% during a particular detector run, then that detector run is placed in IP 1.
   - Otherwise, the detector run is placed in IP 0.

Results of sensitivity studies using each set of sorting rules are shown in Table 7.11. While both two-IP scenarios show improvement over a single integration period, the "20-minus" scheme shows optimal sensitivity to a null-oscillation measurement. Based on these results, the "20-minus" sorting rules were used for the oscillation analysis of the second Double Chooz publication.

7.7 Oscillation Fit & Results

The oscillation fit was performed using the CUfits statistics toolkit (see Appendix B). CUfits is designed to re-weight an ensemble of Monte Carlo event populations, all of which are tabulated in Table 7.12 according to a set of fit parameters. These re-weighted events are filled into a histogram representing the total signal-plus-background prediction $N_i^{\rm pred}$ for the IBD candidates observed in the Double Chooz Far Detector:

$$N_i^{\rm pred} = \sum_{R=1,2} N_i^{\bar{\nu},R}\left(\sin^2(2\theta_{13}), \Delta m^2_{31}, \alpha_E\right) + N_i^{\rm Li}\left(\epsilon_{^9{\rm Li}}, \alpha_E\right) + N_i^{\rm fn}\left(\epsilon_{textfn}\right) + N_i^{\rm acc} \quad (7.21)$$

where the index i runs over bins in visible energy $E_{\rm vis}$ and integration period. The predicted number of signal antineutrino events $N_i^{\bar{\nu},R}$ from each reactor R is calculated from the reactor expectation $N_i^{{\rm exp},R}$ of Eq. 7.5 by reweighting each event according to the effective two-neutrino survival probability:

$$\begin{aligned} N_i^{\bar{\nu},R} &= P\left(\bar{\nu}_e \to \bar{\nu}_e\right) N_i^{{\rm exp},R} \\ &= \left(1 - \sin^2(2\theta_{13}) \sin^2\left(\frac{1.27 L_R \Delta m^2_{31}}{E_{\bar{\nu}}}\right)\right) N_i^{{\rm exp},R} \qquad (7.22) \\ & \qquad (7.23) \end{aligned}$$

A summary of each initial event population at null-oscillation and with initial-valued fit parameters is given in Table 7.13 for the main "^{9}Li-reduced" analysis, and in Tables 7.14 and 7.15 for the peripheral analyses.

Population	Original Population	Fit Parameters
$N_i^{\bar{\nu},R}$	$N_i^{{\rm exp},R}$	$\sin^2(2\theta_{13}),\ \Delta m^2_{31},\ \alpha_E$
$N_i^{\rm Li}$	$N_i^{\rm Li,CV}$	$\epsilon_{^9{\rm Li}},\ \alpha_E$
$N_i^{\rm fn}$	$N_i^{\rm fn,CV}$	$\epsilon_{\rm fn}$
$N_i^{\rm acc}$	–	–

Table 7.12: Summary of final oscillation fit input event species, and their parametric dependencies.

The oscillation analysis fit proceeds by comparing to the observed number of IBD candidates in each bin N_i to the prediction $N_i^{\rm pred}$ and calculating a goodness-of-fit using one

	Reactors Both On	**One Reactor $P_{th} < 20\%$**	**Total**
Live Time [days]	139.27	88.66	227.93
IBD Candidates	6088	2161	8249
$\bar{\nu}$ Reactor B1	2910.9	774.6	3685.5
$\bar{\nu}$ Reactor B2	3422.4	1331.7	4754.1
Total $\bar{\nu}$	6333.3	2106.4	8439.7
Lithium-9	174.1	110.8	284.9
Fast-n & Stopping μ	93.3	59.4	152.7
Accidentals	36.4	23.1	59.5
Total Backgrounds	303.8	193.4	497.1
Total Prediction	6637.1	2299.7	8936.8

Table 7.13: Summary of observed IBD candidates for the main "^{9}Li-reduced" analysis, with corresponding signal and background predictions for each integration period. No oscillation fit parameter results have been applied.

of the statistics described in Sec. 7.7.2. By collaboration agreement made before "opening the box" and fitting to data, the Rate+Shape statistic of Eq. 7.30 is used as the main-line analysis, with the Rate-only and Shape-only statistics of Eq. 7.31 and 7.33 used in complimentary analyses. This decision was based on null oscillation sensitivity studies not unlike those shown in Table 7.1, which showed the Rate+Shape fit to provide an optimally-sensitive measurement. The studies were performed with the actual systematic uncertainties used in the final oscillation analysis; these are summarized in Tale 7.16 for all analyses.

The statistic is minimized numerically using MINUIT [148]. At each iteration of the minimization, N_i^{pred} is recalculated based on the values of the fit parameters listed in Table 7.12. Subsequently, the covariance matrix M_{ij} is also recalculated based on the reweighted components of N_i^{pred} as described in Sec. 7.7.1. Following recalculation of N_i^{pred} and M_{ij}, the fit statistic is evaluated for that iteration. A combination of MINUIT's

	Reactors Both On	**One Reactor $P_{th} <$ 20%**	**Total**
Live Time [days]	146.6142	93.2102	239.8244
IBD Candidates	6563	2358	8921
$\bar{\nu}$ Reactor B1	3064.4	814.4	3878.8
$\bar{\nu}$ Reactor B2	3602.8	1400.1	5002.9
Total $\bar{\nu}$	6667.3	2214.5	8881.8
Lithium-9	307.9	195.7	503.6
Fast-n & Stopping μ	98.2	62.5	160.7
Accidentals	48.6	30.9	79.5
Total Backgrounds	454.7	289.1	743.8
Total Prediction	7122.1	2503.7	9625.8

Table 7.14: Summary of observed IBD candidates for the peripheral "non-^{9}Li-reduced" analysis, with corresponding signal and background predictions for each integration period. No oscillation fit parameter results have been applied.

SIMPLEX, HESSE, and MIGRAD minimization algorithms [3] is employed until a set of best-fit parameters is established. The multi-dimensional uncertainty intervals on each parameter are then evaluated by using the HESSE algorithm to calculate the parameter covariance matrix. The results of this oscillation fit are described in detail in Sec. 7.7.3.

In practice, uncertainty intervals are determined by evaluating the behavior of the fit statistic, generically called χ^2 for the purposes of this paragraph (the actual fit statistics used are described in Sec. 7.7.2). At best-fit, the statistic takes a minimum value χ^2_{bf}. Uncertainty intervals are then evaluated in the multi-dimensional space of all floating fit parameters. The 1σ interval of a parameter is defined by the boundary where $\Delta\chi^2 = \chi^2 - \chi^2_{bf} = 1$ in the case of one unbounded parameter (see the "Statistics" section of [36]). With a proper error definition, these intervals are calculated by MINUIT's HESSE algorithm.

A break-out of the uncertainty interval on $\sin^2(2\theta_{13})$ into "statistical" and "system-

[3] Consult the MINUIT manual [148] for more details on each algorithm.

	Reactors Both On	**One Reactor $P_{th} <$ 20%**	**Total**
Live Time [days]	71.9876	45.7662	117.7538
IBD Candidates	3120	1136	4256
$\bar{\nu}$ Reactor B1	1504.6	399.9	1904.5
$\bar{\nu}$ Reactor B2	1769.0	687.4	2456.4
Total $\bar{\nu}$	3273.6	1087.3	4360.9
Lithium-9	43.2	27.5	70.7
Fast-n & Stopping μ	48.2	30.7	78.9
Accidentals	15.83	10.1	25.93
Total Backgrounds	107.23	68.3	175.53
Total Prediction	3380.9	1155.5	4536.4

Table 7.15: Summary of observed IBD candidates for the peripheral "^{9}Li-free" analysis, with corresponding signal and background predictions for each integration period. No oscillation fit parameter results have been applied.

atic" parts is achieved by running a null-oscillation sensitivity study at 100-times expected statistics, and considering the resulting 68% C.L. sensitivity as the "purely systematic" component of the total uncertainty. A null-oscillation sensitivity is chosen over boosting the statistics of the observed data in order to prevent lending improper weight to statistical fluctuations found in the data. This systematic part is subtracted in quadrature from the total uncertainty to yield the "statistical" component.

7.7.1 Parameter-Dependent Covariance Matrix

One notable change of the fit procedure as compared to the first Double Chooz analysis (Sec. A.6) was the use of a covariance matrix that was recomputed as a function of the fit parameters. This technique allowed the proper implementation of the Pearson χ^2 fit statistic, as well as rigorous implementation of parameter-dependent systematics.

The uncertainty on the signal and background predictions is initially defined by a co-

Source	"Non-^{9}Li-reduced"	"^{9}Li-reduced"	"^{9}Li-free"
Statistics	1.0150%	1.0564%	1.4803%
Selection Efficiency	0.9195%	0.9470%	0.9604%
Reactor	1.6144%	1.6626%	1.6862%
Detector	0.3555%	0.2823%	0.2463%
^{9}Li Background	1.5318%	1.5266%	1.4450%
Fast-n/Stopping-μ Background	0.4941%	0.5089%	0.5161%
Accidental Background	0.0074%	0.0051%	0.0077%
Total	2.6831%	2.7288%	2.8934%

Table 7.16: Uncertainties from all sources for both the main "^{9}Li-reduced" analysis, and the peripheral analyses. Numbers quoted are the relative uncertainty contributed to the rate of events, as a percentage of the number of observed IBD candidates in each analysis.

variance matrix M_{ij}. If no pull parameters are used to represent any uncertainties, the matrix has the form:

$$M_{ij}^{\text{No Pulls}} = M_{ij}^{\text{stat}} + M_{ij}^{\text{rxt}} + M_{ij}^{\text{eff}} + M_{ij}^{\text{Li rate}} + M_{ij}^{\text{Li shape}} + M_{ij}^{\text{fn rate}} + M_{ij}^{\text{fn shape}} + M_{ij}^{\text{escale}} \quad (7.24)$$

In practice, pull parameters and pull terms are used to represent some uncertainties, in which case the components of the covaraince matrix corresponding to those systematics must be omitted from the summed matrix. Thus, if the list of pull parameters described in Sec. 7.7.2.1 is used, the matrix has the form:

$$M_{ij} = M_{ij}^{\text{stat}} + M_{ij}^{\text{rxt}} + M_{ij}^{\text{eff}} + M_{ij}^{\text{Li shape}} + M_{ij}^{\text{fn shape}} \quad (7.25)$$

The matrix in Eq. 7.25 is used in the main oscillation analysis. The M_{ij} of Eq. 7.25 is similar to the matrix used in the first analysis (see Sec. A.6.1) with two major exceptions. First, the covariance matrix is now 36-by-36 in dimension to account for bins in both integration periods. Second, the statistical uncertainty component is defined by the Pearson χ^2 convention:

$$M_{ij}^{\text{stat}} = \delta_{ij}\sqrt{N_i^{\text{pred}} N_j^{\text{pred}}}. \quad (7.26)$$

Since N_i^{pred} is a function of the oscillation parameters Δm^2_{31} and θ_{13}, as well as the pulled background and energy scale parameters (see Table 7.12 for a listing of parameters), it follows that M_{ij}^{stat} is also dependent on those fit parameters. Thus, this component of the matrix must be re-calculated at each iteration of the fit minimization. This is done following the re-weighting of all constituent events populations of N_i^{pred} according to the applicable parameters (See Eq. 7.21 and Table 7.12).

The same re-weighting technology required by this statistical uncertainty prescription can also be utilized with the systematic uncertainty components of M_{ij}. At the beginning of the minimization algorithm, fractional covariance matrices are created from each component of the total covariance matrix. This is done by dividing each matrix component by the relevant event population. For example, to create a fractional version m_{ij}^{rxt} of the reactor covariance matrix contribution M_{ij}^{rxt}, which depends on the signal population $\sum_{R=1,2} N_i^{\bar{\nu},R}$:

$$m_{ij}^{\text{rxt}} = \frac{M_{ij}^{\text{rxt}}}{\left(\sum_{R=1,2} N_i^{\bar{\nu},R}\left(\sin^2(2\theta_{13}), \Delta m^2_{31}, \alpha_E\right)\right)\left(\sum_{R=1,2} N_j^{\bar{\nu},R}\left(\sin^2(2\theta_{13}), \Delta m^2_{31}, \alpha_E\right)\right)}. \tag{7.27}$$

This "fractionalization" first takes place at the beginning of the fit process, when all fit parameters are at their null-oscillation values and the related event populations are at their initial values. At each iteration u of the numerical minimization, the event populations are recalculated and the covariance matrices are "de-fractionalized", *e.g.* for the reactor matrix:

$$M_{ij}^{\text{rxt}}|_u = \left(\sum_{R=1,2} N_i^{\bar{\nu},R}\left(\sin^2(2\theta_{13})|_u, \Delta m^2_{31}|_u, \alpha_E|_u\right)\right) m_{ij}^{\text{rxt}} \left(\sum_{R=1,2} N_j^{\bar{\nu},R}\left(\sin^2(2\theta_{13})|_u, \Delta m^2_{31}|_u, \alpha_E|_u\right)\right) \tag{7.28}$$

These de-fractionalized matrices are then summed, and used to calculate the fit statistic at iteration u of the minimization.

7.7.2 Definitions of χ^2 Statistics

Oscillation analyses were performed using three different χ^2 statistics. Each statistic contains a set of floating fit parameters in addition to the oscillation amplitude, called "pull

Matrix	Associated Populations
M_{ij}^{stat}	N_{ij}^{pred}
M_{ij}^{rxt}	$\sum_{R=1,2} N_i^{\bar{\nu},R}$
M_{ij}^{eff}	$\sum_{R=1,2} N_i^{\bar{\nu},R}$
$M_{ij}^{\text{Li shape}}$	N_i^{Li}
$M_{ij}^{\text{fn shape}}$	N_i^{fn}
M_{ij}^{escale}	$N_i^{\text{Li}} + \sum_{R=1,2} N_i^{\bar{\nu},R}$

Table 7.17: Covariance matrices that are reweighted during the fit process, uncertainty contribution of each, and the associated event populations by which they are reweighted. Note that M_{ij}^{escale} is often deprecated in favor of a using α_E as a fit parameter, with a pull term in the fit statistic.

parameters", which are constrained by externally-specified data. While naming conventions of the below equations are similar to those used in Sec. A.6.2, it is worthwhile to note that the use of multiple integration periods ($n_\tau > 1$) effectively adds a time component to each statistic, *i.e.* the "rate plus shape" statistic is actually a "rate plus shape plus time" statistic.

While analyses were performed using each of these statistics, an agreement among the collaboration made in advance of the analysis stipulated that χ^2_{RS} would be used to determine the official oscillation measurement. This decision was based upon continued confidence in the energy scale and its associated systematics, as well as continued demonstration of the superior sensitivity of χ^2_{RS} to that of χ^2_{RO} in null-oscillation hypothesis studies.

7.7.2.1 Pull Term Contribution

All of the statistics contained "pull terms" constraining the behavior of some fit parameters. As described in previous sections, the fit parameters affect the values of the N_i^{pred}. In particular, a multiplier $\epsilon_{^9\text{Li}}$ on the ^{9}Li rate (Sec. 7.4.2.1), a multiplier ϵ_{fn} on the FN/SM rate (Sec. 7.4.3.5), the oscillation parameters $\sin^2(2\theta_{13})$ and Δm^2_{31}, and the energy scale α_E (Sec. 7.5) were included as pull parameters. For each parameter, a "pull term" or

constraint term is added to the fit statistic. The pull term constrains the value of each parameter towards its central value while still allowing it to vary within the prescribed external uncertainty interval. This accounts for uncertainty on the parameter in the fit in a way that is roughly[4] equivalent to a contribution to the covariance matrix [149, 150].

To keep later equations concise, we collect all pull terms into a separable term χ^2_{pulls} which will be included in other, later-described fit statistics. This portion of the statistics is denoted:

$$\chi^2_{\text{pulls}} = \frac{(\epsilon_{\text{fn}} - 1)^2}{\sigma^2_{\text{fn}}} + \frac{(\epsilon_{^9\text{Li}} - 1)^2}{\sigma^2_{^9\text{Li}}} + \frac{(\alpha_E - 1)^2}{\sigma^2_{\alpha_E}} + \frac{\left(\Delta m^2_{31} - \left(\Delta m^2_{31}\right)_{\text{MINOS}}\right)^2}{\sigma^2_{\text{MINOS}}} \tag{7.29}$$

Each statistic is minimized with respect to all of these parameters during the fitting process. The parameters ϵ_{fn}, $\epsilon_{^9\text{Li}}$, and α_E are bounded by uncertainty intervals determined as described in the above text. The mass splitting Δm^2_{31} is constrained to the central value as measured by MINOS [83]. The uncertainty on Δm^2_{31} has been symmetrized and expanded to account for effects in converting the measurement of a ν_μ disappearance experiment to a quantity relevant for $\bar{\nu}_e$ disappearance experiments, including ambiguity of the mass hierarchy [151].

It is worthwhile to note that while the pulled parameters must be minimized as part of the fit, they do not contribute a new degree of freedom if they are accompanied by a pull term in the statistic. In essence, a free parameter is added, but a data point is also added, with no net change in the number of degrees of freedom.

[4]The author doubts this assertion. The equivalence shown in [149] and [150] presumes that each pull term or contribution to the covariance matrix are independent, and known precisely at the beginning of the minimization procedure. This does not rigorously allow for the technique of re-calculating the values of other covariance matrix contributions based on the values of the pull paramters, as is described in Sec. 7.7.1. However, an argument can be made that the technique of Sec. 7.7.1 is appropriate to the situation at hand, and correct in that context. See Appendix G for more discourse on the requirements for complete equivalence in different uncertainty scenarios.

7.7.2.2 Rate + Shape Fit Statistic

The "rate + shape" chi-squared statistic was defined as:

$$\chi^2_{RS} = \sum_{i,j=1}^{36} \left(N_i - N_i^{\text{pred}}\right) (M_{ij})^{-1} \left(N_j - N_j^{\text{pred}}\right)^{\text{T}} + \chi^2_{\text{pulls}} \tag{7.30}$$

This statistic takes into account all potential spectral and temporal information contained in the binned data and the correlated uncertainties of the prediciton. Except for the increase in the number of bins due to the use of multiple integration periods, and the use of a different set of pulled parameters, it is identical in general form to Eq. A.27.

7.7.2.3 Rate-Only Fit Statistic

The rate-only statistic compares the measured rate of IBD candidates to the predicted rate in each integration period by summing over all energy bins in each integration period. For an integration period τ_I indexed by I, we define:

$$\begin{aligned} N_I &= \sum_{i \in \tau_I} N_i \\ N_A^{\text{pred}} &= \sum_{i \in \tau_I} N_i^{\text{pred}} \end{aligned}$$

Also, we compactify the covariance matrix into a smaller $n_\tau \times n_\tau$ matrix:

$$M_{IJ} = \sum_{i \in \tau_I} \sum_{j \in \tau_J} M_{ij}$$

The "rate-only" chi-squared statistic is then defined as:

$$\chi^2_{RO} = \sum_{I,J=1}^{n_\tau} (N_I) (M_{IJ})^{-1} (N_J)^{\text{T}} + \chi^2_{\text{pulls}} \tag{7.31}$$

As previously mentioned, $n_\tau = 2$ for this analysis. As mentioned above, use of this statistic in fact gives a "rate plus time" fit. Since the number of integration periods is more than one, the number of degrees of freedom is nonzero, and thus this style of fit does not give a minimum χ^2 value of zero.

7.7.2.4 Shape-Only Fit Statistic

The shape-only goodness-of-fit statistic used for DC2ndPub was suggested by G. Mention, and is subtly different from that used in the first Double Chooz analysis (described in Sec. A.6.2.4).

The "shape-only" chi-squared statistic is designed to neglect any normalization information associated with the signal prediction. In effect, it renders the normalization of the signal as a free parameter ξ. If all uncertainties are contained in the covariance matrix M_{ij}, it is possible to analytically solve for ξ using the background-subtracted observed IBD candidates $\left(N_j - \sum_b^{\text{Bkgnds.}} N_j^b\right)$ and the signal prediction $\left(\sum_{R=1,2}^{\text{Reactors}} N_i^{\nu,R}\right)$:

$$\xi = \frac{\left(\sum_{R=1,2}^{\text{Reactors}} N_i^{\nu,R}\right)(M_{ij})^{-1}\left(N_j - \sum_b^{\text{Bkgnds.}} N_j^b\right)^{\text{T}}}{\left(\sum_{R=1,2}^{\text{Reactors}} N_i^{\nu,R}\right)(M_{ij})^{-1}\left(\sum_{R=1,2}^{\text{Reactors}} N_j^{\nu,R}\right)^{\text{T}}} \tag{7.32}$$

The "shape-only" chi-squared statistic is then defined using ξ to renormalize the predicted signal, as:

$$\begin{aligned}\chi^2_{SO} &= \sum_{i,j=1}^{36}\left[\left(N_i - \left(\xi\sum_{R=1,2}^{\text{Reac.}} N_i^{\nu,R} + \sum_b^{\text{Bkgnds.}} N_i^b\right)\right)\right. \\ &\left.\times (M_{ij})^{-1}\left(N_j - \left(\xi\sum_{R=1,2}^{\text{Reac.}} N_j^{\nu,R} + \sum_b^{\text{Bkgnds.}} N_j^b\right)\right)^{\text{T}}\right] + \chi^2_{\text{pulls}}\end{aligned} \tag{7.33}$$

Because the signal normalization is treated as a free parameter, this statistic has one fewer degree of freedom than χ^2_{RS} of Eq. 7.30.

7.7.3 Results

Using the main "^{9}Li-reduced" cuts to select IBD candidates, and minimizing χ^2_{RS} of Eq. 7.30 as the fit statistic, the best fit of the prediction to the data is found at $\sin^2(2\theta_{13}) = 0.109 \pm 0.030\ (\text{stat.}) \pm 0.025\ (\text{syst.})$ at $\Delta m^2_{31} = 2.32 \times 10^{-3}\ \text{eV}^2$, with $\chi^2_{RS}/\text{d.o.f.} = 42.1/35$. A full tabulation of the best-fit parameters can be found in Table 7.18. The measured prompt spectrum from this analysis is shown in Figure 7.23 (split into the two reactor-

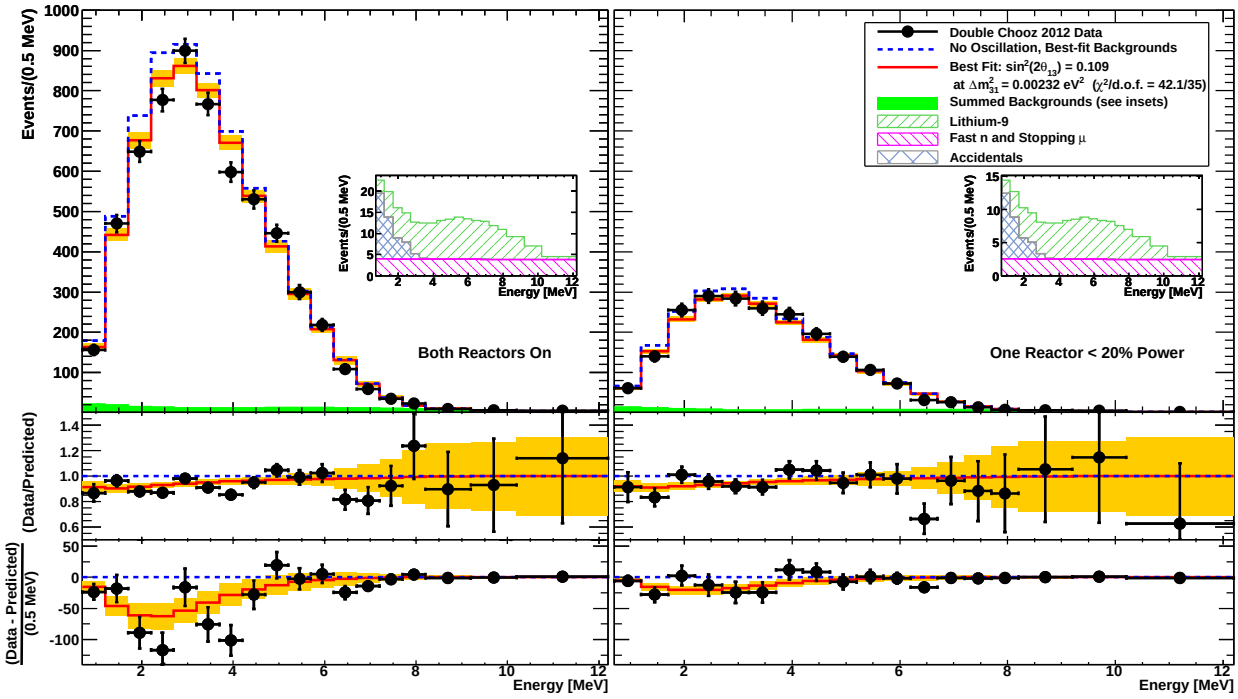

Figure 7.23: Measured prompt energy spectrum for each integration period (data points) superimposed on the expected prompt energy spectrum, including backgrounds (green region), for the no-oscillation (blue dotted curve) and best-fit (red solid curve) at $\sin^2(2\theta_{13}) = 0.109$ and $\Delta m^2_{31} = 2.32 \times 10^{-3}$ eV^2. Orange region indicates systematic uncertainties on prediction. Inset: stacked spectra of backgrounds. Bottom: differences between data and no-oscillation prediction (data points), and differences between best fit prediction and no-oscillation prediction (red curve). From [8].

defined integration periods) and Figure 7.24 (as one integration period). In these plots, the fit parameters have been set to their best-fit values as given in Table 7.18 (or Table 7.19).

Further information can be gained from examining the output fit parameters and their output uncertainty intervals in Table 7.19. In the main fit employing χ^2_{RS}, both the $\epsilon_{^9\mathrm{Li}}$ and α_E parameters have output uncertainty intervals much smaller than the input uncertainties, indicating that they are constrained by the fit to a more strict degree than the initial uncertainty in the pull term alone allows. Conversely, the fit results show the lack of Double Chooz's ability to provide a measurement of Δm^2_{31} near the MINOS central value.

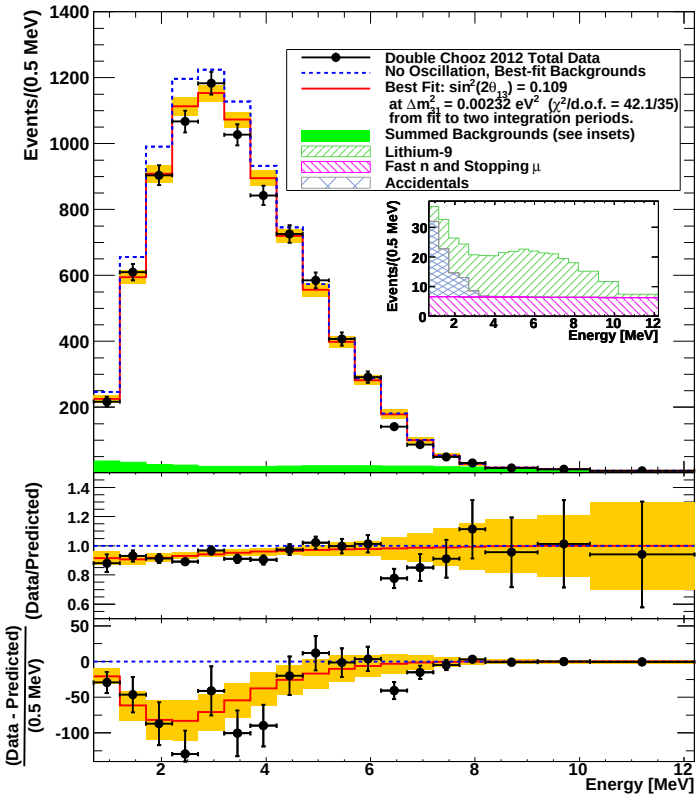

Figure 7.24: Measured prompt energy spectrum from both integration periods (data points) superimposed on the expected prompt energy spectrum, including backgrounds (green region), for the no-oscillation (blue dotted curve) and best-fit (red solid curve) at $\sin^2(2\theta_{13}) = 0.109$ and $\Delta m^2_{31} = 2.32 \times 10^{-3}$ eV^2. Orange region indicates systematic uncertainties on prediction. Inset: stacked spectra of backgrounds. Bottom: differences between data and no-oscillation prediction (data points), and differences between best fit prediction and no-oscillation prediction (red curve). Note that best-fit parameters were obtained using a fit to two integration periods. From [8].

7.7.3.1 Data From First Publication Period, and Data Since

The data set was also split into two sets and fit independently: one set corresponding to the same data used in the first Double Chooz publication (see Figure 7.25(a)); and one set of all data taken since November 2011 (see Figure 7.25(b)). Only a single integration period was used for the fit out of statistical considerations, to ensure no bins with zero population. Results from performing fits with different goodness-of-fit statistics are given in Table 7.20. Comparable to the main analysis discussed above, a fit of only data from the first publication using a Rate+Shape statistic (equivalent to χ^2_{RS} of Eq. 7.30 but with only 18 total bins) yielded a best-fit value of $\sin^2(2\theta_{13}) = 0.0744 \pm 0.046$ with $\chi^2/\text{NDF} = 18.3/17$. The uncertainty interval of this measurement shows improvement over the value of $\sin^2(2\theta_{13}) = 0.086 \pm 0.041(\text{stat.}) \pm 0.030(\text{syst.})$ reported in the first Double Chooz publication [16]. For comparison, the prompt spectra of the same data set as processed in each analysis are shown side-by-side in Figure 7.26. Analysis of only the data taken since the first publication yielded a best-fit of $\sin^2(2\theta_{13}) = 0.143 \pm 0.043$ with $\chi^2/\text{NDF} = 9.54/17$. Comparison of these numbers and their uncertainty intervals is not straight-forward, due to the number of systematics potentially correlated between each analysis.

7.7.3.2 Peripheral Analyses

As has been mentioned throughout this section, two peripheral analyses were performed in parallel: a "non-^{9}Li-reduced" analysis, and a "^{9}Li-free" analysis. Fit results for all statistic variants and these peripheral selection sets can be seen in Tables 7.21 and 7.22. In general, the results are in agreement with the main analysis.

7.7.4 Frequentist Confidence Intervals

In addition to the uncertainty intervals on θ_{13} established by the behavior of $\Delta\chi^2_{RS}$, confidence intervals were established for the oscillation analysis using a frequentist methodology, based off the techniques of [152]. The frequentist method utilizes the prediction N_i^{pred} and the covariance matrix M_{ij} representing all sources of uncertainty to simulate an ensemble of pseudoexperiments for each of a set of "true" values of $\sin^2(2\theta_{13})$. Confidence intervals are drawn by comparing the $\Delta\chi^2_{RS}$ value for the true experimental data to the distribution

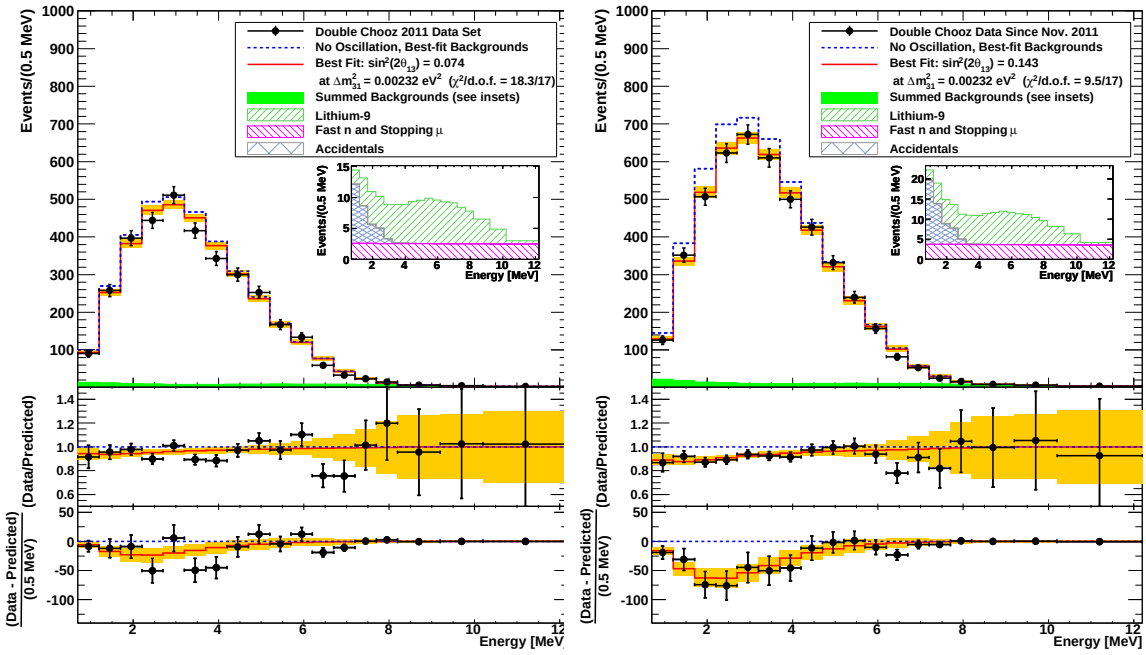

(a) First Publication Data Set

(b) Data Since First Publication

Figure 7.25: Data and best-fit spectra from applying current analysis techniques to the data set used to produce the first Double Chooz publication (Fig. 7.25(a)), and data taken since that publication (Fig. 7.25(b)). Measured prompt energy spectra (data points) are superimposed on the expected prompt energy spectrum, including backgrounds (green region), for the no-oscillation (blue dotted curve) and best-fit (red solid curve) of each data set. Orange region indicates systematic uncertainties on prediction. Inset: stacked spectra of best-fit backgrounds for each data set. Bottom: differences between data and no-oscillation prediction (data points), and differences between best fit prediction and no-oscillation prediction (red curve). Both from [8].

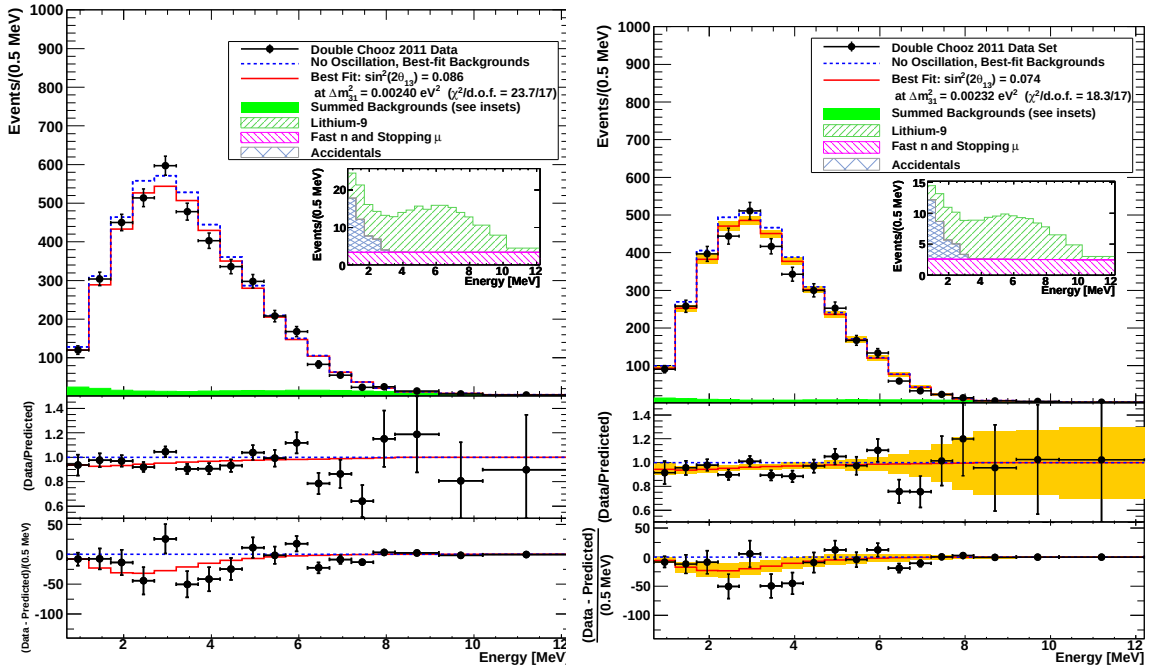

(a) Original First Publication Analysis (b) First Publication Data, This Analysis

Figure 7.26: A comparison of oscillation fits to the DC1stPub data set using the analysis methods of DC1stPub (Fig. 7.26(a)) and the analysis methods of DC2ndPub (Fig. 7.26(b)). Each fit was done with a single integration period. Measured prompt energy spectra (data points) are superimposed on the expected prompt energy spectrum, including backgrounds (green region), for the no-oscillation (blue dotted curve) and best-fit (red solid curve) of each data set. Orange region (not shown in Fig. 7.26(a)) indicates systematic uncertainties on prediction. Inset: stacked spectra of best-fit backgrounds for each data set. Bottom: differences between data and no-oscillation prediction (data points), and differences between best fit prediction and no-oscillation prediction (red curve). Fig. 7.26(a) adapted from [16]; Fig. 7.26(b) from [8].

of $\Delta\chi^2_{RS}$ values from the pseudoexperiments. This method is described in more detail in Appendix F.

A set of 21 "true" values of $\sin^2(2\theta_{13})$ were tested along the range $0. \leq \sin^2(2\theta_{13}) \leq 0.25$. The allowed region for the data was determined at 68% C.L. to be $0.067 < \sin^2(2\theta_{13}) < 0.15$, or at 90% C.L. to be $0.043 < \sin^2(2\theta_{13}) < 0.18$. Using the test point at $\sin^2(2\theta_{13}) = 0$, the null-oscillation hypothesis was ruled out at 99.8% C.L., or 2.9σ. It is expected that these 1σ confidence intervals differ slightly from those presented in Section 7.7.3, since the frequentist method correctly covers intervals where the behavior of the χ^2 becomes nonlinear close to unphysical regions of parameter space.

7.7.5 Fit Without MINOS Δm^2_{31} Constraint

Since the oscillation analysis utilizes a binned spectrum, there is a possibility that the Double Chooz data can provide a weak measurement of Δm^2_{31} by localizing the "dip" of the signal spectrum distortion caused by flavor oscillation. Since Double Chooz sits at an average baseline of $L = 1050$ meters, the location of "oscillation max" in the spectrum is close to the lower bound of the IBD signal region. Thus, any constraint on Δm^2_{31} is expected to be weak.

To perform a simultaneous measurement of $\sin^2(2\theta_{13})$ and Δm^2_{31}, the pull term in Eq. 7.29 related to Δm^2_{31} is omitted from the fit statistic, leaving that parameter free of any initial constraints. The fit statistic is minimized as described in Sec. 7.7, though the error definitions are modified to account for the change in the number of unconstrained parameters: the 1σ interval is now defined by the hyperellipse in fit parameter space where $\Delta\chi^2 = 2.3$ for the chosen fit statistic [36].

Results for a simultaneous fit to $\sin^2(2\theta_{13})$ and an unconstrained Δm^2_{31} are shown in Figure 7.27, for each of the goodness-of-fit statistics described in Section 7.7.2. Examining the Rate+Shape fit, the best-fit point from DC2ndPub is allowed within 3σ, though that point is near a local minimum. The global minimum is at $\sin^2(2\theta_{13}) = 0.167$ and $\Delta m^2_{31} = 2.64 \times 10^{-2}$ eV^2, with χ^2_{RS}/d.o.f. $= 31.9/34$, compared to the best fit at $\sin^2(2\theta_{13}) = 0.109$ and $\Delta m^2_{31} = 2.32 \times 10^{-3}$ eV^2, at χ^2_{RS}/d.o.f. $= 42.1/35$ when the MINOS constraint is included. This best-fit point is at tension with the measurements of MINOS, Super-K,

and the other reactor experiments, and is likely due to a statistical fluctuation. When the range of the fit paramters is limited to $\Delta m^2_{31} < 10^{-2}$ eV^2, the best-fit is consistent with the MINOS measurement within errors, as stated in [8].

7.8 More Two-Reactor-Off Data

While the second publication analysis was being prepared, a maintenance shut-down of reactor B1 between May 27 and June 4, 2012, occurred during the scheduled refueling shutdown of reactor B2. Both reactors were stopped for 7.73 days during this period, bringing the total both-reactors-off exposure of the Far Detector to 8.71 days when combined with the 2011 data described in Sec. A.4.4.2. Analysis of these data are presented in [147].

Beyond inclusion of these data in the binned observation and prediction, it is possible to include the measured number of events from the off-off period as a constraint on the summed background rates in the oscillation analysis. The χ^2 may be modified by adding an extra term comparing the summed predicted rate of the backgrounds $R^{\text{bkg.}}_{\text{pred.}} = R^{^9\text{Li}}_{\text{pred.}} + R^{\text{Acc.}}_{\text{pred.}} + R^{\text{fn/s}\mu}_{\text{pred.}}$ and the measured rate of events from the off-off period R_{OffOff}:

$$\chi^2 = \chi^2_{RS} + \left(\frac{R^{\text{bkg.}}_{\text{pred.}} - R_{\text{OffOff}}}{\sqrt{R_{\text{OffOff}}/L_{\text{OffOff}}}} \right)^2 \tag{7.34}$$

where L_{OffOff} is the total amount of off-off detector live time. Unfortunately, the amount of off-off data accrued during both periods has a total statistical uncertainty of comparable magnitude to the systematic uncertainties from other background measurement methods, and therefore does not contribute a very powerful constraint to the χ^2. The effect of including this constraint at this level of statistics is a slight improvement in experimental sensitivity, as shown in Fig. 7.28 for varying amounts of off-off data with other systematics and data statistics comparable to the second DC publication.

Due to when the data were taken, this augmentation to the analysis was not used in the second Double Chooz publication.

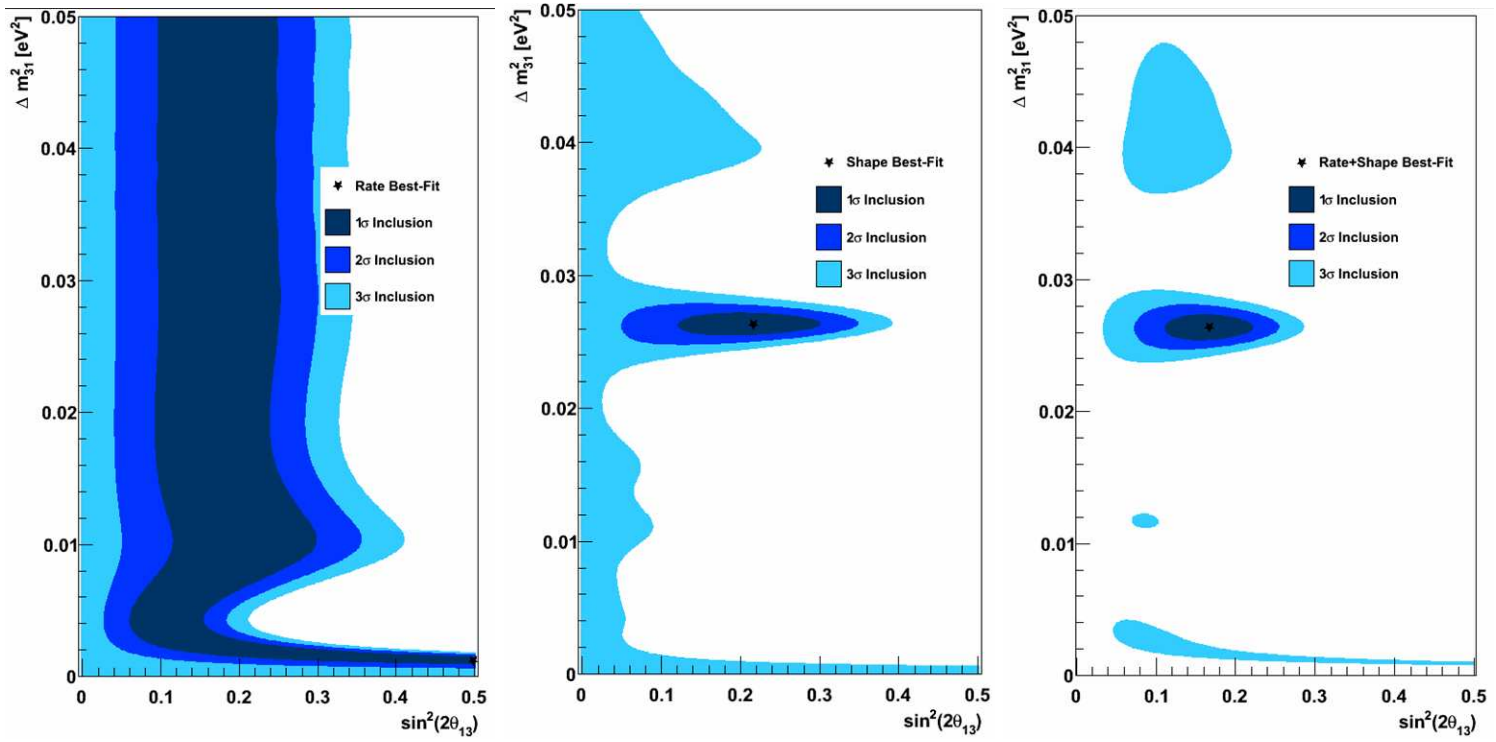

(a) Rate-Only Fit (b) Shape-Only Fit (c) Rate+Shape Fit

Figure 7.27: Oscillation parameter inclusion regions for fits without any constraint on Δm^2_{31}, for three different goodness-of-fit statistics. Star indicates best-fit point.

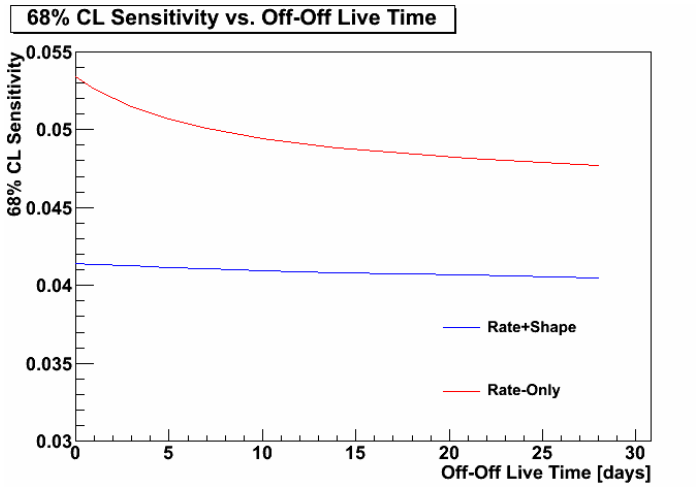

Figure 7.28: Sensitivity to null-oscillation measurement for Double Chooz as a function of accrued two-reactors-off data. Statistics of all other data and systematics are at the values of the second Double Chooz publication.

Fit Statistic	$\sin^2(2\theta_{13})$	$\sin^2(2\theta_{13})$ Stat. Error	$\sin^2(2\theta_{13})$ Syst. Error	Δm^2_{31} [$\times 10^{-3}$ eV^2]	$\epsilon_{\rm fn}$	$\epsilon_{^9\rm Li}$	α_E	P_E	χ^2_{bf}/d.o.f.
Inputs	0.0	–	–	2.32 ±0.12	1.000 ±0.299	1.000 ±0.432	1.0 ±1.0	1.000 ±0.0113	–
Rate+Shape χ^2_{RS}	0.10929 ±0.03899	0.02958	0.02540	2.32 ±0.12	0.959 ±0.200	0.799 ±0.228	−0.269 ±0.580	0.986 ±0.007	42.13/35
Rate-Only χ^2_{RO}	0.17025 ±0.05228	0.05228	0.03464	2.32 ±0.12	1.031 ±0.295	1.122 ±0.395	1.028 ±0.997	1.000 ±0.0112	0.503/1
Shape-Only χ^2_{SO}	−0.07274 ±0.07716	0.07716	0.07236	2.32 ±0.12	0.950 ±0.203	0.696 ±0.194	1.436 ±0.970	1.005 ±0.011	40.52/34

Table 7.18: Oscillation fit results obtained using two integration periods and the "^{9}Li-reduced" selection cuts, for three fit statistics. Fit parameters were $\sin^2(2\theta_{13})$, Δm^2_{31}, $\epsilon_{\rm fn}$, $\epsilon_{^9\rm Li}$, and α_E. The parameters α_E and P_E are equivalent in effect, with a shift in units. Parameters with uncertainty intervals significantly less than those of the input values show that the fit provides constraint on those parameters. Some values are converted to event rates in Table 7.19.

Fit Parameter	**Initial Value**	**Best-Fit Value**
^{9}Li Bkg. $\epsilon_{^9\mathrm{Li}}$	(1.25 ± 0.54) d^{-1}	(1.00 ± 0.29) d^{-1}
FN/SM Bkg. $\epsilon_{FN/SM}$	(0.67 ± 0.20) d^{-1}	(0.64 ± 0.13) d^{-1}
Energy Scale P_E	1.000 ± 0.011	0.986 ± 0.007
Δm^2_{31} (10^{-3} eV^2)	2.32 ± 0.12	2.32 ± 0.12

Table 7.19: Parameters in the oscillation fit. Initial values are determined by measurements of background rates or detector calibration data. Best-fit values are outputs of the minimization procedure. From [8].

First Publication Data Set		
Fit Statistic	Best-fit $\sin^2(2\theta_{13})$	χ^2/d.o.f.
Rate+Shape χ^2_{RS}	0.0744 ± 0.04584	18.30/17
Rate-Only χ^2_{RO}	0.10996 ± 0.05781	–
Shape-Only χ^2_{SO}	-0.07594 ± 0.14997	16.68/16
Data Set Since Nov. 2011		
Fit Statistic	Best-fit $\sin^2(2\theta_{13})$	χ^2/d.o.f.
Rate+Shape χ^2_{RS}	0.14258 ± 0.04259	9.54/17
Rate-Only χ^2_{RO}	0.19599 ± 0.05828	–
Shape-Only χ^2_{SO}	0.08283 ± 0.10765	9.10/16

Table 7.20: Fit results from applying various fit statistics to the data set used in the first Double Chooz analysis, and to all data taken since Nov. 2011. Fits used a single integration period, reducing the number of degrees of freedom as compared to the fits summarized in Table 7.18.

Fit Statistic	$\sin^2(2\theta_{13})$	Δm^2_{31} [$\times 10^{-3}$ eV^2]	ϵ_{fn}	$\epsilon_{^9\text{Li}}$	χ^2_{bf}/d.o.f.
Inputs	0.0	2.32 ± 0.12	1.000 ± 0.299	1.000 ± 0.271	–
Rate+Shape χ^2_{RS}	0.11502 ± 0.03978	2.32 ± 0.12	0.942 ± 0.213	0.897 ± 0.149	45.50/35
Rate-Only χ^2_{RO}	0.16532 ± 0.05269	2.32 ± 0.12	1.027 ± 0.295	1.070 ± 0.246	0.373/1
Shape-Only χ^2_{SO}	0.03951 ± 0.10304	2.32 ± 0.12	0.933 ± 0.211	0.872 ± 0.148	44.72/34

Table 7.21: Oscillation fit results obtained using two integration periods and the "non-^{9}Li-reduced" selection cuts, for three fit statistics. Fit parameters were $\sin^2(2\theta_{13})$, Δm^2_{31}, ϵ_{fn}, and $\epsilon_{^9\text{Li}}$. Parameters with uncertainty intervals significantly less than those of the input values show that the fit provides constraint on those parameters.

Fit Statistic	$\sin^2(2\theta_{13})$	Δm^2_{31} [$\times 10^{-3}$ eV^2]	ϵ_{fn}	$\epsilon_{^9\text{Li}}$	χ^2_{bf}/d.o.f.
Inputs	0.0	2.32 ± 0.12	1.000 ± 0.299	1.000 ± 0.900	–
Rate+Shape χ^2_{RS}	0.10875 ± 0.04356	2.32 ± 0.12	1.074 ± 0.231	1.307 ± 0.522	38.01/35
Rate-Only χ^2_{RO}	0.14322 ± 0.05695	2.32 ± 0.12	1.055 ± 0.296	1.452 ± 0.849	2.37/1
Shape-Only χ^2_{SO}	0.00698 ± 0.12939	2.32 ± 0.12	1.061 ± 0.230	1.280 ± 0.512	37.09/34

Table 7.22: Oscillation fit results obtained using two integration periods and the "^{9}Li-free" selection cuts, for three fit statistics. Fit parameters were $\sin^2(2\theta_{13})$, Δm^2_{31}, ϵ_{fn}, and $\epsilon_{^9\text{Li}}$. Parameters with uncertainty intervals significantly less than those of the input values show that the fit provides constraint on those parameters.

Part IV

Context & Conclusions

Chapter 8

Double Chooz Measurements in Context

8.1 Winter 2011/Spring 2012: First Oscillation Results

As Double Chooz was commissioning and taking data with its Far Detector in preparation for a first pscillation analysis, there were many hints that a measurement of nonzero $\sin^2(2\theta_{13})$ was imminent. During 2010, best-fit values for $\sin^2(2\theta_{13})$ were released by the accelerator experiments MINOS [153] (April 9, 2010) and T2K [20] (June 15, 2010). Additionally, three-neutrino fits to atmospheric neutrino data by the Super-Kamiokande collaboration [154] (February 2010) and and to long-baseline reactor neutrino data by the KamLAND collaboration [87] (Sept. 24, 2010) would each give best-fit values at $\sin^2(2\theta_{13}) > 0$ with weak confidence intervals. MINOS would again update its result on July 20, 2011, showing nonzero $\sin^2(2\theta_{13})$ for all values of δ_{CP} at 89% confidence level [21] and eclipsing CHOOZ's result [7] as the most stringent upper bound on $\sin^2(2\theta_{13})$. While these results were suggestive, none on its own was statistically conclusive.

In late-summer 2011, it was known within the community that all three of Double Chooz, RENO, and Daya Bay were either in late commissioning stages, or already taking physics data. With the many hints of nonzero $\sin^2(2\theta_{13})$, and θ_{13} best-fit values within evidence/discovery reach for all three reactor experiments, a proverbial horse race was on.

Preliminary results from the first Double Chooz analysis (as described in Appendix A)

were first presented at the LowNu2011 conference in Seoul, South Korea, held during November, 2011. These results were later published as Ref. [16], a facsimile of which is contained in Appendix K.1. (In an entertaining turn of events, the results also appeared as "physics jargon" on the whiteboards of the CBS Network television comedy "The Big Bang Theory" as shown in Figure 8.1.) "Indications" for a nonzero θ_{13} were claimed in this result, with a best-fit value of $\sin^2(2\theta_{13}) = 0.086 \pm 0.041$ (stat.) ± 0.030 (0.030), and the null-oscillation hypothesis rejected at 94.6% C.L. with the use of a frequentist method. While not statistically significant enough for a discovery claim, a combination of this result with the previous MINOS and T2K results gave a combined 3σ inclusion region of $0.003 < \sin^2(2\theta_{13}) < 0.219$. This indication likely prompted the other reactor experiments to hasten their searches, as this confidence interval suggested that the true value of θ_{13} would be measurable with only a few months' data by Daya Bay or RENO [22].

In March 2012, the Daya Bay experiment published its first oscillation results [18], shortly following a paper [141] detailing the uniform operation of their many detectors. Daya Bay had been taking data with a reduced experimental configuration, moving up their multiple-baseline data-taking timetable: two detectors at the DYB near site, one near detector at the Ling Ao site, and three detectors at the Far site. The first Daya Bay result utilized 55 days of physics data taken with all six detectors. The result claimed a reactor model-independent neutrino rate measurement of $\sin^2(2\theta_{13}) = 0.092 \pm 0.016(\text{stat.}) \pm 0.005(\text{syst.})$, with θ_{13} nonzero at a 5.2σ level of confidence.

The next month, the RENO experiment published its first results [19], settling on a rate-only measurement with two detectors and six reactors of $\theta_{13} = 0.113 \pm 0.013(\text{stat}) \pm 0.019(\text{syst.})$, with $\sin^2(2\theta_{13})$ nonzero at a 4.9σ level of confidence. While consistent with the Daya Bay result, anomalies in RENO's fit spectrum versus expected behavior were noted by some in the community [155].

8.2 Summer 2012: Updated Results

During the following Summer, Double Chooz and Daya Bay both released updated results at the Neutrino 2012 conference, held in Kyoto, Japan, during June of 2012. Double

(a) Detector Cartoon

(b) Nuclides & Background

(c) Oscillation Fit Results

Figure 8.1: Still frames from the CBS Network comedy "The Big Bang Theory" (Season 5 Episode 11, "The Speckerman Recurrance") depicting Double Chooz-related material on whiteboards around the set. Fig. 8.1(a) partially shows a sideview drawing of the Inner Detector, with concentric vessels and PMTs depicted (note the omission of the Gamma Catcher Vessel; this may in fact be a depiction of the CHOOZ detector [7]). Fig. 8.1(b) depicts a table of reactor fuel nuclides and the average number of $\bar{\nu}_e$ and energy released by a fission of each (likely from [9]), and a cartoon of a cosmogenic background. Fig. 8.1(c) shows a summary of the Double Chooz results presented at the LowNu 2011 conference, which were a preliminary version of those published in [16]. All images from [17].

Chooz's results, which would later be published as Ref. [8] and are the principal focus of this thesis, gave a new measured value of $\sin^2(2\theta_{13}) = 0.086 \pm 0.041(\text{stat.}) \pm 0.030(\text{syst.})$ and disfavored the null-oscillation hypothesis at 2.9σ using frequentist methods. This result can be seen compared to all preceding measurements of $\sin^2(2\theta_{13})$ in Figure 8.2. Daya Bay's results [156, 157] gave an updated rate-only measurement of $\sin^2(2\theta_{13}) = 0.089 \pm 0.010(\text{stat.}) \pm 0.005(\text{syst.})$, inconsistent with the null-oscillatino hypothesis at $> 8\sigma$. Additionally, T2K gave updated results with additional data [158], in which they claim a measurement of $\sin^2(2\theta_{13}) = 0.104^{+0.060}_{-0.045}$, for associated mixing parameters $\Delta m^2_{32} = 2.4 \times 10^{-3}$ eV^2, $\delta_{CP} = 0$, and $\theta_{23} = \pi/4$. This accelerator-based measurement is inconsistent with the null hypothesis at 3.2σ. Following these results, it is now well-accepted that θ_{13} is nonzero and "large" when considered in terms of CP-violation searches.

8.3 The Post-θ_{13} Era

Within one year since the current generation of reactor experiments began taking data, the state of the θ_{13} field has changed drastically. These measurements have taken θ_{13} from being the last unknown mixing angle to one of the most precisely measured neutrino parameters. Indeed, it is unlikely that any future accelerator-based experiment will better the precision provided by the current generation of reactor experiments without the completion of a full-scale neutrino factory [159]. This sea change has greater implications for the field of neutrino physics, with bearing on future measurements of quantities in the PMNS matrix, as well as on what other measurements can be achieved with reactor $\bar{\nu}_e$ experiments now that returns on efforts to measure θ_{13} are diminishing.

8.3.1 Outlook on the PMNS Matrix

It can be said that neutrino oscillation physics now has only a few quantities left to measure, with the only completely-unknown quantities remaining in the PMNS matrix being the CP-violating Dirac phase δ_{CP}, and the ordering of the mass hierarchy. However, the nonzero value of θ_{13} allows for the possibility that δ_{CP} *can* be measured. Some quantities still remain ambiguous: the mass hierarchy, and the precise value of θ_{23} being above or below

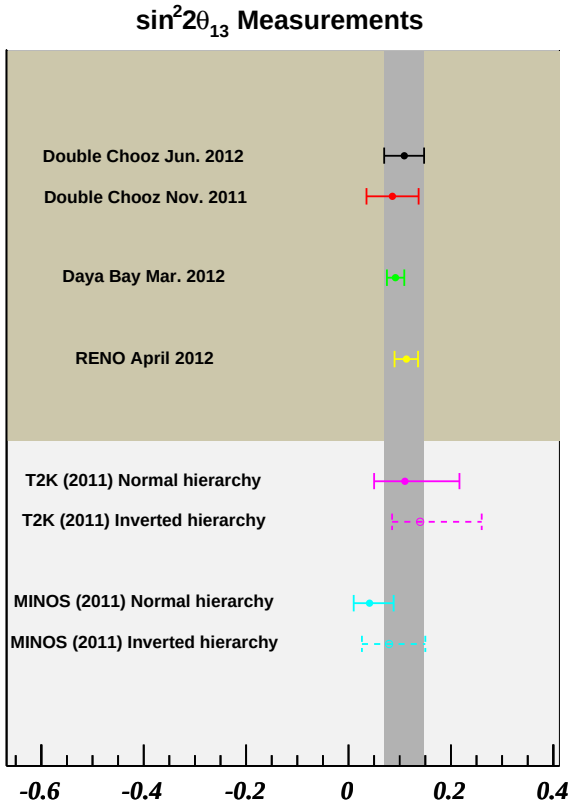

Figure 8.2: Plot of measurements of $\sin^2(2\theta_{13})$ from accelerator and reactor experiments up to and including the Double Chooz results presented at the Neutrino 2012 conference in June 2012. Results in order are from the second Double Chooz publication [8], the first Double Chooz publication [16], Daya Bay [18], RENO [19], T2K [20], and MINOS [21]. Error bars correspond to 1σ. For T2K and MINOS, the CP-violating Dirac phase δ_{CP} has been arbitrarily fixed to $\delta_{CP} = 0$. Plot from [8].

$\frac{\pi}{4}$.

Fits to global data [160, 161, 162] (which include the results presented at the Neutrino 2012 conference) already give some hints of a potential best parameter fit around $\delta_{CP} \sim \pi$, though they are not very statistically significant. The next measurement attempts of the remaining mixing parameters will come from the accelerator-based T2K [85, 49] and NOνA [105] experiments, which are running and under construction, respectively. These experiments may be able to conclusively resolve the mass hierarchy at the 2σ confidence level, but only for a certain range of δ_{CP} [163]. The combination of the data from both T2K and NOνA, along with tuning of the event selection parameters of each based on knowledge of $\sin^2(2\theta_{13})$, can increase this range [164]. However, with currently-planned facilities, it is unlikely that δ_{CP} will be measured with significance greater than 3σ for all possible values of δ_{CP} [165, 166]. Future measurements of mixing parameters may be made by experiments which are still in the proposal stages, such as INO [167], DAEδALUS [168], LBNE [169], Hyper-Kamiokande [170, 171], and CERN-MEMPHYS [172, 173]. To independently and conclusively probe all values of δ_{CP}, a functional neutrino factor my be required [166].

8.3.2 Outlook on Reactor $\bar{\nu}_e$ Experiments

Now that $\sin^2(2\theta_{13})$ is known to be large, the current generation of reactor experiments will likely be faced with diminishing returns on the precision of their measurements with further data taking. The current generation of reactor experiments were designed to eventually be limited in their precision of measurement by systematic uncertainties, in particular those which govern the relative signal normalizations and background rates between the multiple detectors of each experiment. Without being statistics-limited, the experiments will quickly reach a regime where their measurement precision asymptotically approaches the systematic limit. An illustration of this effect may be seen in Figure 8.3, adapted from [22], where the null-oscillation sensitivities of each experiment are shown for best-estimate uncertainty paramters from Winter 2011/2012. Once in this systematically-limited regime, further data taking is of diminishing benefit, and the experiment with the most optimal configuration will inevitably provide the most precise measurement of $\sin^2(2\theta_{13})$, which is undoubtedly Daya Bay.

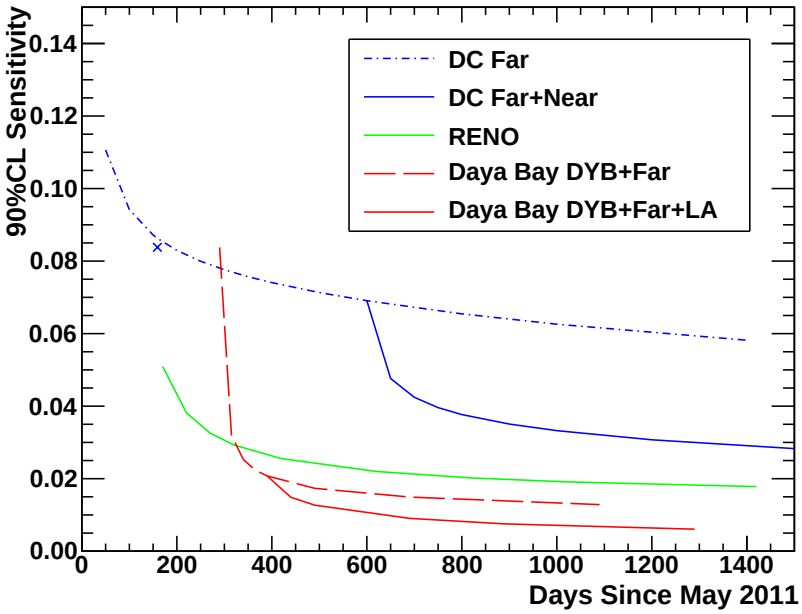

Figure 8.3: 90% C.L. sensitivity estimates for null-oscillation measurements in each of the three current-generation reactor experiments, adapted from [22]. Presumed background rates, signal rates, and systematic parameters may be found in that reference. Note the asymptotic behavior of each experiment towards a systematically-limited precision after reaching a stable experimental configuration.

Having measured θ_{13} very precisely, reactor $\bar{\nu}_e$ experiments may be able to provide measurements of other observables. Of particular interest is updated data relevant to the "Reactor Anomaly" [97]: while the current generation of experiments lacks sensitivity to Δm^2_{Ster}, a precise comparison of a measured flux at a near detector to a reactor-based prediction could provide an allowed range for $\sin^2(2\theta_{\text{Ster}})$ [95]. At the time of this writing, no experimental collaboration has released such an analysis, though fits to global data [174, 175] continue to show support for the heavy-sterile neutrino hypothesis. Recently-published recalculations of neutrino reference spectra [176], which are thought to be significantly more precise than those of [13] or [96] may give additional power to experiments weighing in on this anomaly. However, there has been a recent realization that the sterile mixing parameters can be tightly constrained using data from the IceCube [177, 178] experiment and its DeepCore [179] extension. The data do not show any obvious signs of supporting the sterile hypothesis [180]. The most conclusive test of the anomaly may soon come from very-near baseline reactor experiments such as Nucifer [142], or from deployments of intense radioactive sources inside liquid scintillator detectors [181, 182].

Concurrently-operating reactor experiments with different baselines also presents the unique opportunity to measure Δm^2_{31} without relying upon accelerator experiments [183]. Also recently demonstrated for the first time is the ability for a multiple-detector reactor $\bar{\nu}_e$ experiment to test for Lorentz violation in neutrino oscillations by using the flux from each reactor as the arms of a quantum interferometer, rotating with sidereal time [138].

The next generation of reactor $\bar{\nu}_e$ experiments may be focused on measuring effects of the mass hierarchy, and a precision measurement of θ_{12}. This experimental concept involves a kton-scale liquid scintillator detector at a baseline of $\sim$60 km from a large reactor complex [184, 185, 186, 187]. The proposed Daya Bay-II experiment [188] would perform this measurement by placing a detector inland from the Daya Bay reactor site, with an expected exposure schedule of 60 to 120 kton-years with either multiple detectors, or a single $>$ 20 kton detector (compared to an expected exposure of 0.8 kton-years for the current Daya Bay configuration [108]). A similar experiment dubbed RENO-50 has also been proposed to be built in South Korea [189]. This approach may be severely limited by the ability for reconstruction algorithms to provide sufficient energy resolution [190],

requiring knowledge of any nonlinearities in detector response to the $\sim 0.1\%$ level.

Chapter 9

Conclusions

The Double Chooz experiment has completed its first year of measuring the $\bar{\nu}_e$ flux from a pair of nuclear reactors, in the search for effects of flavor oscillations. This dissertation has presented the motivation for this search, a description of the experimental methods of the search, and the results from the first improved analysis. Additional focus has been given to the Outer Veto, which was the Columbia University group's principal hardware contribution to the experiment and the author's greatest service contribution to the experiment. Further, the statistical methods of the $\bar{\nu}_e$ signal prediction and the oscillation analysis have been described in detail.

The current measurement of $\sin^2(2\theta_{13})$ from Double Chooz, $\sin^2(2\theta_{13}) = 0.109 \pm 0.030\ (\text{stat.}) \pm 0.025\ (\text{syst.})$ at $\Delta m^2_{31} = 2.32 \times 10^{-3}$ eV^2, is on the cusp of providing definite evidence for a nonzero value. It is inevitable that further data and improvement of systematics through analytical effort will increase this confidence level in the future. The completion of the Double Chooz Near Detector will contribute greatly to this effort, effectively suppressing the signal systematics which currently limit the Far Detector-only measurement. However, it may be difficult for Double Chooz to reach similar levels of sensitivity as the other reactor $\bar{\nu}_e$ experiments. Nevertheless, Double Chooz's unique situation of being able to measure backgrounds *in situ* and the analysis methods which it has pioneered should continue to contribute to the progress of the field. While not statistically significant at the discovery level, the results of Double Chooz's search for reactor $\bar{\nu}_e$ flavor oscillations and a nonzero θ_{13} have provided evidence and motivation for the field.

Part V

Bibliography

Bibliography

[1] Koichiro Nishikawa. Recent status of accelerator neutrino experiments. *Nucl.Instrum.Meth.*, A623:17–22, 2010.

[2] Double Chooz Collaboration Web Site, 2006.

[3] H. Murayama, 2011.

[4] B. Aharmim et al. Combined Analysis of all Three Phases of Solar Neutrino Data from the Sudbury Neutrino Observatory. 2011, 1109.0763.

[5] P. Adamson et al. An improved measurement of muon antineutrino disappearance in MINOS. *Phys.Rev.Lett.*, 108:191801, 2012, 1202.2772.

[6] F. Boehm, J. Busenitz, B. Cook, G. Gratta, H. Henrikson, et al. Final results from the Palo Verde neutrino oscillation experiment. *Phys.Rev.*, D64:112001, 2001, hep-ex/0107009.

[7] M. Apollonio et al. Search for neutrino oscillations on a long baseline at the CHOOZ nuclear power station. *Eur.Phys.J.*, C27:331–374, 2003, hep-ex/0301017.

[8] Y. Abe, C. Aberle, J.C.dos Anjos, J.C. Barriere, M. Bergevin, et al. Reactor electron antineutrino disappearance in the Double Chooz experiment. 2012, 1207.6632.

[9] F. Ardellier et al. Double Chooz: A Search for the neutrino mixing angle theta(13). 2006, hep-ex/0606025.

[10] A. Onillon and C. Jones. Reactor and $\bar{\nu}_e$ spectrum prediction for the double chooz experiment. `http://neu2012.kek.jp/neu2012/programme.html`, june 2012. "Poster #495 presented at the Neutrino 2012 Conference at Kyoto, Japan".

[11] O. Meplan et al. *ENC 2005: European Nuclear Conference ; Nuclear power for the XXIst century: from basic research to high-tech industry.* 2005.

[12] *NEA-1845/01*, 2009. documentation for MURE.

[13] Th.A. Mueller, D. Lhuillier, M. Fallot, A. Letourneau, S. Cormon, et al. Improved Predictions of Reactor Antineutrino Spectra. *Phys.Rev.*, C83:054615, 2011, 1101.2663.

[14] F. Von Feilitzsch, A.A. Hahn, and K. Schreckenbach. EXPERIMENTAL BETA SPECTRA FROM PU-239 AND U-235 THERMAL NEUTRON FISSION PRODUCTS AND THEIR CORRELATED ANTI-NEUTRINOS SPECTRA. *Phys.Lett.*, B118:162–166, 1982.

[15] P. Vogel, G.K. Schenter, F.M. Mann, and R.E. Schenter. REACTOR ANTINEUTRINO SPECTRA AND THEIR APPLICATION TO ANTI-NEUTRINO INDUCED REACTIONS. 2. *Phys.Rev.*, C24:1543–1553, 1981.

[16] Y. Abe et al. Indication for the disappearance of reactor electron antineutrinos in the Double Chooz experiment. *Phys.Rev.Lett.*, 108:131801, 2012, 1112.6353.

[17] CBS Network. The Big Bang Theory, Season 5 Episode 11, The Speckerman Recurrence. Netowrk Television Program, December 2011.

[18] F.P. An et al. Observation of electron-antineutrino disappearance at Daya Bay. *Phys.Rev.Lett.*, 108:171803, 2012, 1203.1669.

[19] J.K. Ahn et al. Observation of Reactor Electron Antineutrino Disappearance in the RENO Experiment. *Phys.Rev.Lett.*, 108:191802, 2012, 1204.0626.

[20] K. Abe et al. Indication of Electron Neutrino Appearance from an Accelerator-produced Off-axis Muon Neutrino Beam. *Phys.Rev.Lett.*, 107:041801, 2011, 1106.2822.

[21] P. Adamson et al. Improved search for muon-neutrino to electron-neutrino oscillations in MINOS. *Phys.Rev.Lett.*, 107:181802, 2011, 1108.0015.

[22] C. Mariani. Review of Reactor Neutrino Oscillation Experiments. *Mod.Phys.Lett.*, A27:1230010, 2012, 1201.6665.

[23] E. Fermi. Trends to a Theory of beta Radiation. (In Italian). *Nuovo Cim.*, 11:1–19, 1934.

[24] F. Reines. The neutrino: From poltergeist to particle. *Rev.Mod.Phys.*, 68:317–327, 1996.

[25] G. Danby, J.M. Gaillard, Konstantin A. Goulianos, L.M. Lederman, Nari B. Mistry, et al. Observation of High-Energy Neutrino Reactions and the Existence of Two Kinds of Neutrinos. *Phys.Rev.Lett.*, 9:36–44, 1962.

[26] K. Kodama et al. Observation of tau neutrino interactions. *Phys.Lett.*, B504:218–224, 2001, hep-ex/0012035.

[27] M. Goldhaber, L. Grodzins, and A.W. Sunyar. HELICITY OF NEUTRINOS. *Phys.Rev.*, 109:1015–1017, 1958.

[28] Boris Kayser, G.T. Garvey, E. Fischbach, and Simon Peter Rosen. Are Neutrinos Always Lefthanded? *Phys.Lett.*, B52:385, 1974.

[29] J.A. Formaggio et al. Search for the lepton number violating process anti-neutrino(muon) e- → muon- anti-neutrino(e). *Phys.Rev.Lett.*, 87:071803, 2001, hep-ex/0104029.

[30] S.R. Mishra, K.T. Bachmann, R.H. Bernstein, R.E. Blair, C. Foudas, et al. MEASUREMENT OF INVERSE MUON DECAY MUON-NEUTRINO + E → MU- + ELECTRON-NEUTRINO AT FERMILAB TEVATRON ENERGIES 15-GEV - 600-GEV. *Phys.Rev.Lett.*, 63:132–135, 1989.

[31] F.J. Hasert et al. Observation of Neutrino Like Interactions Without Muon Or Electron in the Gargamelle Neutrino Experiment. *Phys.Lett.*, B46:138–140, 1973.

[32] A.C. Benvenuti and et al. Observation of Muonless Neutrino Induced Inelastic Interactions. *Phys.Rev.Lett.*, 32:800–803, 1974.

[33] S.L. Glashow, J. Iliopoulos, and L. Maiani. Weak Interactions with Lepton-Hadron Symmetry. *Phys.Rev.*, D2:1285–1292, 1970.

[34] Steven Weinberg. A Model of Leptons. *Phys.Rev.Lett.*, 19:1264–1266, 1967.

[35] Abdus Salam. page 367. Almquist and Wiksells, Stockholm, 1969.

[36] J. Beringer et al. Review of Particle Physics (RPP). *Phys.Rev.*, D86:010001, 2012.

[37] Peter W. Higgs. Broken symmetries, massless particles and gauge fields. *Phys.Lett.*, 12:132–133, 1964.

[38] Ziro Maki, Masami Nakagawa, and Shoichi Sakata. Remarks on the unified model of elementary particles. *Prog.Theor.Phys.*, 28:870–880, 1962.

[39] B. Pontecorvo. Neutrino Experiments and the Problem of Conservation of Leptonic Charge. *Sov.Phys.JETP*, 26:984–988, 1968.

[40] Hiroshi Nunokawa, Stephen J. Parke, and Jose W.F. Valle. CP Violation and Neutrino Oscillations. *Prog.Part.Nucl.Phys.*, 60:338–402, 2008, 0710.0554.

[41] Makoto Kobayashi and Toshihide Maskawa. CP Violation in the Renormalizable Theory of Weak Interaction. *Prog.Theor.Phys.*, 49:652–657, 1973.

[42] J. Schechter and J.W.F. Valle. Neutrino Masses in SU(2) x U(1) Theories. *Phys.Rev.*, D22:2227, 1980.

[43] the SLD electroweak. Precision electroweak measurements on the Z resonance. *Phys.Rept.*, 427:257–454, 2006, hep-ex/0509008.

[44] Andre de Gouvea, Boris Kayser, and Rabindra N. Mohapatra. Manifest CP violation from Majorana phases. *Phys.Rev.*, D67:053004, 2003, hep-ph/0211394.

[45] Harry J. Lipkin. Quantum theory of neutrino oscillations for pedestrians: Simple answers to confusing questions. *Phys.Lett.*, B642:366–371, 2006, hep-ph/0505141.

[46] Burton Richter. Conventional beams or neutrino factories: The Next generation of accelerator based neutrino experiments. 2000, hep-ph/0008222.

[47] Vernon D. Barger, K. Whisnant, and R.J.N. Phillips. CP Violation in Three Neutrino Oscillations. *Phys.Rev.Lett.*, 45:2084, 1980.

[48] Sandip Pakvasa. LOW-ENERGY WEAK INTERACTIONS: THEORY. *AIP Conf.Proc.*, 68:1164, 1980.

[49] Y. Itow et al. The JHF-Kamioka neutrino project. pages 239–248, 2001, hep-ex/0106019.

[50] S.P. Mikheev and A. Yu. Smirnov. Resonance Amplification of Oscillations in Matter and Spectroscopy of Solar Neutrinos. *Sov.J.Nucl.Phys.*, 42:913–917, 1985.

[51] L. Wolfenstein. Neutrino Oscillations in Matter. *Phys.Rev.*, D17:2369–2374, 1978.

[52] A. De Rujula, M.B. Gavela, and P. Hernandez. The atmospheric neutrino anomaly without maximal mixing? *Phys.Rev.*, D63:033001, 2001, hep-ph/0001124.

[53] Murray Gell-Mann, Pierre Ramond, and Richard Slansky. COMPLEX SPINORS AND UNIFIED THEORIES. *Conf.Proc.*, C790927:315–321, 1979.

[54] Tsutomu Yanagida. HORIZONTAL SYMMETRY AND MASSES OF NEUTRINOS. *Conf.Proc.*, C7902131:95, 1979.

[55] Rabindra N. Mohapatra and Goran Senjanovic. Neutrino Masses and Mixings in Gauge Models with Spontaneous Parity Violation. *Phys.Rev.*, D23:165, 1981.

[56] George Lazarides, Q. Shafi, and C. Wetterich. Proton Lifetime and Fermion Masses in an SO(10) Model. *Nucl.Phys.*, B181:287, 1981.

[57] S. M. Barr. New type of seesaw mechanism for neutrino masses. *Phys. Rev. Lett.*, 92:101601, Mar 2004.

[58] Rabindra N. Mohapatra and Goran Senjanovic. Neutrino Mass and Spontaneous Parity Violation. *Phys.Rev.Lett.*, 44:912, 1980.

[59] Laura Covi, Esteban Roulet, and Francesco Vissani. CP violating decays in leptogenesis scenarios. *Phys.Lett.*, B384:169–174, 1996, hep-ph/9605319.

[60] M.A. Luty. Baryogenesis via leptogenesis. *Phys.Rev.*, D45:455–465, 1992.

[61] G.F. Giudice, A. Notari, M. Raidal, A. Riotto, and A. Strumia. Towards a complete theory of thermal leptogenesis in the SM and MSSM. *Nucl.Phys.*, B685:89–149, 2004, hep-ph/0310123.

[62] Georges Aad et al. Search for heavy neutrinos and right-handed W bosons in events with two leptons and jets in pp collisions at sqrt(s) = 7 TeV with the ATLAS detector. *Eur.Phys.J.*, C72:2056, 2012, 1203.5420.

[63] R. Aaij et al. Searches for Majorana neutrinos in B^- decays. *Phys.Rev.*, D85:112004, 2012, 1201.5600.

[64] Serguei Chatrchyan et al. Search for heavy neutrinos and W bosons with right-handed couplings in a left-right symmetric model in pp collisions at 7 TeV. 2012, 1210.2402.

[65] Serguei Chatrchyan et al. Search for heavy lepton partners of neutrinos in proton-proton collisions in the context of the type III seesaw mechanism. 2012, 1210.1797.

[66] B.T. Cleveland, Timothy Daily, Jr. Davis, Raymond, James R. Distel, Kenneth Lande, et al. Measurement of the solar electron neutrino flux with the Homestake chlorine detector. *Astrophys.J.*, 496:505–526, 1998.

[67] K. Lande, B.T. Cleveland, R. Davis, J. Distel, P. Wildenhain, et al. The Homestake solar neutrino program. *Nucl.Phys.Proc.Suppl.*, 77:13–19, 1999.

[68] A.I. Abazov, O.L. Anosov, E.L. Faizov, V.N. Gavrin, A.V. Kalikhov, et al. Search for neutrinos from sun using the reaction Ga-71 (electron-neutrino e-) Ge-71. *Phys.Rev.Lett.*, 67:3332–3335, 1991.

[69] P. Anselmann et al. GALLEX results from the first 30 solar neutrino runs. *Phys.Lett.*, B327:377–385, 1994.

[70] Dzh.N. Abdurashitov, E.L. Faizon, V.N. Gavrin, A.O. Gusev, A.V. Kalikhov, et al. Results from SAGE. *Phys.Lett.*, B328:234–248, 1994.

[71] D. Casper et al. Measurement of atmospheric neutrino composition with the imb-3 detector. *Phys. Rev. Lett.*, 66:2561–2564, May 1991.

[72] Y. Fukuda et al. Atmospheric muon-neutrino / electron-neutrino ratio in the multi-GeV energy range. *Phys.Lett.*, B335:237–245, 1994.

[73] Y. Fukuda et al. Evidence for oscillation of atmospheric neutrinos. *Phys.Rev.Lett.*, 81:1562–1567, 1998, hep-ex/9807003.

[74] P. Adamson et al. Measurements of atmospheric neutrinos and antineutrinos in the MINOS Far Detector. *Phys.Rev.*, D86:052007, 2012, 1208.2915.

[75] M. Ambrosio et al. Measurement of the atmospheric neutrino induced upgoing muon flux using MACRO. *Phys.Lett.*, B434:451–457, 1998, hep-ex/9807005.

[76] W.W.M. Allison et al. Neutrino oscillation effects in Soudan-2 upward-stopping muons. *Phys.Rev.*, D72:052005, 2005, hep-ex/0507068.

[77] K.S. Hirata et al. Real time, directional measurement of B-8 solar neutrinos in the Kamiokande-II detector. *Phys.Rev.*, D44:2241, 1991.

[78] S. Fukuda et al. Solar B-8 and hep neutrino measurements from 1258 days of Super-Kamiokande data. *Phys.Rev.Lett.*, 86:5651–5655, 2001, hep-ex/0103032.

[79] Q.R. Ahmad et al. Direct evidence for neutrino flavor transformation from neutral current interactions in the Sudbury Neutrino Observatory. *Phys.Rev.Lett.*, 89:011301, 2002, nucl-ex/0204008.

[80] W.G. Seligman, C.G. Arroyo, L. de Barbaro, P. de Barbaro, A.O. Bazarko, et al. Improved determination of alpha(s) from neutrino nucleon scattering. *Phys.Rev.Lett.*, 79:1213–1216, 1997, hep-ex/9701017.

[81] N. Agafonova et al. Observation of a first ν_τ candidate in the OPERA experiment in the CNGS beam. *Phys.Lett.*, B691:138–145, 2010, 1006.1623.

[82] M Antonello, B Baibussinov, P Benetti, E Calligarich, N Canci, et al. Experimental search for the LSND anomaly with the ICARUS LAr TPC detector in the CNGS beam. 2012, 1209.0122.

[83] P. Adamson et al. Measurement of the neutrino mass splitting and flavor mixing by MINOS. *Phys.Rev.Lett.*, 106:181801, 2011, 1103.0340.

[84] M.H. Ahn et al. Indications of neutrino oscillation in a 250 km long baseline experiment. *Phys.Rev.Lett.*, 90:041801, 2003, hep-ex/0212007.

[85] K. Abe et al. The T2K Experiment. *Nucl.Instrum.Meth.*, A659:106–135, 2011, 1106.1238.

[86] B. Aharmim et al. Low Energy Threshold Analysis of the Phase I and Phase II Data Sets of the Sudbury Neutrino Observatory. *Phys.Rev.*, C81:055504, 2010, 0910.2984.

[87] A. Gando et al. Constraints on θ_{13} from A Three-Flavor Oscillation Analysis of Reactor Antineutrinos at KamLAND. *Phys.Rev.*, D83:052002, 2011, 1009.4771.

[88] K. Abe et al. Search for Differences in Oscillation Parameters for Atmospheric Neutrinos and Antineutrinos at Super-Kamiokande. *Phys.Rev.Lett.*, 107:241801, 2011, 1109.1621.

[89] A. Aguilar-Arevalo et al. Evidence for neutrino oscillations from the observation of anti-neutrino(electron) appearance in a anti-neutrino(muon) beam. *Phys.Rev.*, D64:112007, 2001, hep-ex/0104049.

[90] A.A. Aguilar-Arevalo et al. A Search for electron neutrino appearance at the $\Delta m^2 \sim 1\text{eV}^2$ scale. *Phys.Rev.Lett.*, 98:231801, 2007, 0704.1500.

[91] A.A. Aguilar-Arevalo et al. Event Excess in the MiniBooNE Search for $\bar{\nu}_\mu \to \bar{\nu}_e$ Oscillations. *Phys.Rev.Lett.*, 105:181801, 2010, 1007.1150.

[92] A.A. Aguilar-Arevalo et al. Unexplained Excess of Electron-Like Events From a 1-GeV Neutrino Beam. *Phys.Rev.Lett.*, 102:101802, 2009, 0812.2243.

[93] Michel Sorel, Janet M. Conrad, and Michael Shaevitz. A Combined analysis of short baseline neutrino experiments in the (3+1) and (3+2) sterile neutrino oscillation hypotheses. *Phys.Rev.*, D70:073004, 2004, hep-ph/0305255.

[94] G. Karagiorgi, Z. Djurcic, J.M. Conrad, M.H. Shaevitz, and M. Sorel. Viability of Delta m**2 1- eV**2 sterile neutrino mixing models in light of MiniBooNE electron neutrino and antineutrino data from the Booster and NuMI beamlines. *Phys.Rev.*, D80:073001, 2009, 0906.1997.

[95] K.N. Abazajian, M.A. Acero, S.K. Agarwalla, A.A. Aguilar-Arevalo, C.H. Albright, et al. Light Sterile Neutrinos: A White Paper. 2012, 1204.5379.

[96] Patrick Huber. On the determination of anti-neutrino spectra from nuclear reactors. *Phys.Rev.*, C84:024617, 2011, 1106.0687.

[97] G. Mention, M. Fechner, Th. Lasserre, Th.A. Mueller, D. Lhuillier, et al. The Reactor Antineutrino Anomaly. *Phys.Rev.*, D83:073006, 2011, 1101.2755.

[98] Y. Declais, H. de Kerret, B. Lefievre, M. Obolensky, A. Etenko, et al. Study of reactor anti-neutrino interaction with proton at Bugey nuclear power plant. *Phys.Lett.*, B338:383–389, 1994.

[99] D.G. Michael et al. The Magnetized steel and scintillator calorimeters of the MINOS experiment. *Nucl.Instrum.Meth.*, A596:190–228, 2008, 0805.3170.

[100] K. Anderson, B. Bernstein, D. Boehnlein, Kenneth R. Bourkland, S. Childress, et al. The NuMI Facility Technical Design Report. 1998.

[101] N. Abgrall, B. Andrieu, P. Baron, P. Bene, V. Berardi, et al. Time Projection Chambers for the T2K Near Detectors. *Nucl.Instrum.Meth.*, A637:25–46, 2011, 1012.0865.

[102] The T2K Fine-Grained Detectors. 2012, 1204.3666.

[103] K. Abe, N. Abgrall, Y. Ajima, H. Aihara, J.B. Albert, et al. Measurements of the T2K neutrino beam properties using the INGRID on-axis near detector. 2011, 1111.3119.

[104] K. Matsuoka, A.K. Ichikawa, H. Kubo, K. Maeda, T. Maruyama, et al. Design and performance of the muon monitor for the T2K neutrino oscillation experiment. *Nucl.Instrum.Meth.*, A624:591–600, 2010, 1008.4077.

[105] D.S. Ayres et al. NOvA: Proposal to build a 30 kiloton off-axis detector to study nu(mu) —¿ nu(e) oscillations in the NuMI beamline. 2004, hep-ex/0503053.

[106] V. Martemyanov, L. Mikaelyan, V. Sinev, V. Kopeikin, and Yu. Kozlov. The Kr2Det project: Search for mass 3 state contribution —U(e3)—**2 to the electron neutrino using a one reactor - two detector oscillation experiment at Krasnoyarsk underground site. *Phys.Atom.Nucl.*, 66:1934–1939, 2003, hep-ex/0211070.

[107] L.A. Mikaelyan and V.V. Sinev. Neutrino oscillations at reactors: What next? *Phys.Atom.Nucl.*, 63:1002–1006, 2000, hep-ex/9908047.

[108] Xinheng Guo et al. A Precision measurement of the neutrino mixing angle theta(13) using reactor antineutrinos at Daya-Bay. 2007, hep-ex/0701029.

[109] J.K. Ahn et al. RENO: An Experiment for Neutrino Oscillation Parameter θ_{13} Using Reactor Neutrinos at Yonggwang. 2010, 1003.1391.

[110] Reseau de Transport d'Electricite. `http://clients.rte-france.com/lang/an/visiteurs/vie/prod/PMD_hebdo.jsp`, August 2012.

[111] Hamamatsu Corp., 2009.

[112] E. Calvo, M. Cerrada, C. Fernandez-Bedoya, Ines Gil-Botella, C. Palomares, et al. Characterization of large area photomutipliers under low magnetic fields: Design and performances of the magnetic shielding for the Double Chooz neutrino experiment. *Nucl.Instrum.Meth.*, A621:222–230, 2010, 0905.3246.

[113] T. Matsubara, T. Haruna, T. Konno, Y. Endo, M. Bongrand, et al. Development and evaluation of 10-inch Photo-Multiplier Tubes for the Double Chooz experiment. *Nucl.Instrum.Meth.A*, 2011, 1104.0786.

[114] C. Bauer, E. Borger, R. Hofacker, K. Janner, F. Kaether, et al. Qualification Tests of 474 Photomultiplier Tubes for the Inner Detector of the Double Chooz Experiment. *JINST*, 6:P06008, 2011, 1104.0758.

[115] F. Kaether and C. Langbrandtner. Transit Time and Charge Correlations of Single Photoelectron Events in R7081 PMTs. *ArXiv e-prints*, July 2012, 1207.0378.

[116] C. Aberle, C. Buck, B. Gramlich, F. X. Hartmann, M. Lindner, S. Schönert, U. Schwan, S. Wagner, and H. Watanabe. Large scale Gd-beta-diketonate based organic liquid scintillator production for antineutrino detection. *Journal of Instrumentation*, 7:6008, June 2012, 1112.5941.

[117] C. Aberle, C. Buck, F.X. Hartmann, and S. Schnert. Light yield and energy transfer in a new gd-loaded liquid scintillator. 516(4 - 6):257 – 262, 2011.

[118] K. Zbiri. Note on Drexel tests of the IMB R1408 PMTs used in the inner veto of both far and near detectors of the Double Chooz experiment. *ArXiv e-prints*, April 2011, 1104.4045.

[119] D. Dietrich, D. Greiner, J. Jochum, T. Lachenmaier, L. F. F. Stokes, and M. Röhling. Monte Carlo aided design of the inner muon veto detectors for the Double Chooz experiment. *ArXiv e-prints*, July 2012, 1207.1623.

[120] A. Cabrera. The Double Chooz detector. *Nucl.Instrum.Meth.*, A617:473–477, 2010.

[121] S. Roth, A. Stahl, C. Wiebusch, A. Cucoanes, B. Reinhold, and F. Beissel. A Trigger for the Double Chooz Reactor Neutrino Experiment. *Astronomische Nachrichten*, 328:686, September 2007.

[122] F. Beissel, A. Cabrera, A. Cucuanes, J. V. Dawson, D. Kryn, C. Kuhnt, S. Lucht, B. Reinhold, M. Rosenthal, S. Roth, A. Stahl, A. Stüken, and C. Wiebusch. The Trigger and Timing System of the Double Chooz Experiment. *ArXiv e-prints*, September 2012, 1209.5607.

[123] Pierre Barrillon. MAROC: Multi Anode Readout Chip. page 26, 2007.

[124] Pierre Barrillon et al. *64-channel Front-End readout chip, MAROC2 data sheet*, 2007.

[125] Matthew Henry Toups. *A Search For Electron Antineutrino Disappearance with the Double Chooz Far Detector*. Phd thesis, Columbia University, 2012.

[126] T. Konno, A. Cabarera, M. Ishitsuka, M. Kuze, and Y. Sakamoto. Online data monitoring framework based on histogram packaging in network distributed data acquisition systems. *J.Phys.Conf.Ser.*, 331:022014, 2011.

[127] G. Marleau et al. *Report IGE-157*, 1994.

[128] C.L. Jones, A. Bernstein, J.M. Conrad, Z. Djurcic, M. Fallot, et al. Reactor Simulation for Antineutrino Experiments using DRAGON and MURE. 2011, 1109.5379.

[129] Y. Nakahara et al. *ORNL/TR-2001/01*, 2001.

[130] V. Kopeikin, L. Mikaelyan, and V. Sinev. Reactor as a source of antineutrinos: Thermal fission energy. *Phys.Atom.Nucl.*, 67:1892–1899, 2004, hep-ph/0410100.

[131] K. Schreckenbach, H.R. Faust, F. von Feilitzsch, A.A. Hahn, K. Hawerkamp, and J.L. Vuilleumier. Absolute measurement of the beta spectrum from 235u fission as a basis for reactor antineutrino experiments. *Physics Letters B*, 99(3):251 – 256, 1981.

[132] K. Schreckenbach, G. Colvin, W. Gelletly, and F. Von Feilitzsch. DETERMINATION OF THE ANTI-NEUTRINO SPECTRUM FROM U-235 THERMAL NEUTRON FISSION PRODUCTS UP TO 9.5-MEV. *Phys.Lett.*, B160:325–330, 1985.

[133] A.A. Hahn, K. Schreckenbach, G. Colvin, B. Krusche, W. Gelletly, et al. ANTI-NEUTRINO SPECTRA FROM PU-241 AND PU-239 THERMAL NEUTRON FISSION PRODUCTS. *Phys.Lett.*, B218:365–368, 1989.

[134] W. Mampe et al. The double focusing iron-core electron-spectrometer "bill" for high resolution (n, e) measurements at the high flux reactor in grenoble. *Nuclear Instruments and Methods*, 154(1):127 – 149, 1978.

[135] P. Vogel and John F. Beacom. Angular distribution of neutron inverse beta decay, anti-neutrino(e) + p $\rightarrow$ e+ + n. *Phys.Rev.*, D60:053003, 1999, hep-ph/9903554.

[136] A. Pichlmaier, V. Varlamov, K. Schreckenbach, and P. Geltenbort. Neutron lifetime measurement with the UCN trap-in-trap MAMBO II. *Phys.Lett.*, B693:221–226, 2010.

[137] S.A. Fayans. RADIATIVE CORRECTIONS AND RECOIL EFFECTS IN THE REACTION anti-electron-neutrino + P → N + E+ AT LOW-ENERGIES. (IN RUSSIAN). *Sov.J.Nucl.Phys.*, 42:590, 1985.

[138] Y. Abe et al. First Test of Lorentz Violation with a Reactor-based Antineutrino Experiment. 2012, 1209.5810.

[139] V.V. Sinev. Measuring of fissile isotopes partial antineutrino spectra in direct experiment at nuclear reactor. 2009, 0902.3781.

[140] B. Achkar, R. Aleksan, M. Avenier, G. Bagieu, J. Bouchez, et al. Comparison of anti-neutrino reactor spectrum models with the Bugey-3 measurements. *Phys.Lett.*, B374:243–248, 1996.

[141] F.P. An et al. A side-by-side comparison of Daya Bay antineutrino detectors. 2012, 1202.6181.

[142] A.S. Cucoanes. The nucifer experiment: Non-proliferation with reactor antineutrinos. *AIP Conf.Proc.*, 1441:438–440, 2012.

[143] V.N Ivanchenko. Geant4 toolkit for simulation of hep experiments. *Nuclear Instruments and Methods in Physics Research Section A: Accelerators, Spectrometers, Detectors and Associated Equipment*, 502(2 - 3):666 – 668, 2003. Proceedings of the VIII International Workshop on Advanced Computing and Analysis Techniques in Physics Research.

[144] G. Horton-Smith. Glg4sim: a generic liquid-scintillator anti-neutrino detector ("genericland") geant4 simulation. http://neutrino.phys.ksu.edu/ GLG4sim/, 2005.

[145] P. Papka, T.A.D. Brown, B.R. Fulton, D.L. Watson, S.P. Fox, et al. Decay path measurements for the 2.429-MeV state in Be-9: Implications for the astrophysical alpha + alpha + n reaction. *Phys.Rev.*, C75:045803, 2007.

[146] D.R. Tilley, J.H. Kelley, J.L. Godwin, D.J. Millener, J.E. Purcell, et al. Energy levels of light nuclei A=8,9,10. *Nucl.Phys.*, A745:155–362, 2004.

[147] Y. Abe, C. Aberle, J.C.dos Anjos, J.C. Barriere, M. Bergevin, et al. Direct Measurement of Backgrounds using Reactor-Off Data in Double Chooz. 2012, 1210.3748.

[148] F. James. Minuit: Function minimization and error analysis reference manual. `http://wwwasdoc.web.cern.ch/wwwasdoc/minuit/minmain.html`, 2000.

[149] G.L. Fogli, E. Lisi, A. Marrone, D. Montanino, and A. Palazzo. Getting the most from the statistical analysis of solar neutrino oscillations. *Phys.Rev.*, D66:053010, 2002, hep-ph/0206162.

[150] D. Stump, J. Pumplin, R. Brock, D. Casey, J. Huston, et al. Uncertainties of predictions from parton distribution functions. 1. The Lagrange multiplier method. *Phys.Rev.*, D65:014012, 2001, hep-ph/0101051.

[151] Hiroshi Nunokawa, Stephen J. Parke, and Renata Zukanovich Funchal. Another possible way to determine the neutrino mass hierarchy. *Phys.Rev.*, D72:013009, 2005, hep-ph/0503283.

[152] Gary J. Feldman and Robert D. Cousins. A Unified approach to the classical statistical analysis of small signals. *Phys.Rev.*, D57:3873–3889, 1998, physics/9711021.

[153] P. Adamson et al. New constraints on muon-neutrino to electron-neutrino transitions in MINOS. *Phys.Rev.*, D82:051102, 2010, 1006.0996.

[154] R. Wendell et al. Atmospheric neutrino oscillation analysis with sub-leading effects in Super-Kamiokande I, II, and III. *Phys.Rev.*, D81:092004, 2010, 1002.3471.

[155] Thierry Lasserre, Guillaume Mention, Michel Cribier, Antoine Collin, Vincent Durand, et al. Comment on Phys. Rev. Lett. 108, 191802 (2012): 'Observation of Reactor Electron Antineutrino Disappearance in the RENO Experiment'. 2012, 1205.5626.

[156] D. Dwyer. Improved Measurement of Electron-antineutrino Disappearance at Daya Bay. `http://neu2012.kek.jp/neu2012/programme.html`, june 2012. Presentation slides at the Neutrino 2012 Conference at Kyoto, Japan.

[157] F.P. An et al. Improved Measurement of Electron Antineutrino Disappearance at Daya Bay. 2012, 1210.6327.

[158] T. Nakaya. New results from t2k. `http://neu2012.kek.jp/neu2012/programme.html`, june 2012. "Posted presentation slides of the Neutrino 2012 Conference at Kyoto, Japan".

[159] Pilar Coloma, Andrea Donini, Enrique Fernandez-Martinez, and Pilar Hernandez. Precision on leptonic mixing parameters at future neutrino oscillation experiments. *JHEP*, 1206:073, 2012, 1203.5651.

[160] D.V. Forero, M. Tortola, and J.W.F. Valle. Global status of neutrino oscillation parameters after Neutrino-2012. 2012, 1205.4018.

[161] G.L. Fogli, E. Lisi, A. Marrone, D. Montanino, A. Palazzo, et al. Global analysis of neutrino masses, mixings and phases: entering the era of leptonic CP violation searches. *Phys.Rev.*, D86:013012, 2012, 1205.5254.

[162] M.C. Gonzalez-Garcia, Michele Maltoni, Jordi Salvado, and Thomas Schwetz. Global fit to three neutrino mixing: critical look at present precision. 2012, 1209.3023.

[163] G.J. Feldman, J. Hartnell, and T. Kobayashi. A Review of Long-baseline Neutrino Oscillation Experiments. 2012, 1210.1778.

[164] Sanjib Kumar Agarwalla, Suprabh Prakash, Sushant K. Raut, and S. Uma Sankar. Potential of optimized NOvA for large theta(13) & combined performance with a LArTPC & T2K. 2012, 1208.3644.

[165] Hisakazu Minakata. Phenomenology of future neutrino experiments with large Theta(13). 2012, 1209.1690.

[166] Pilar Coloma, Patrick Huber, Joachim Kopp, and Walter Winter. Systematic uncertainties in long-baseline neutrino oscillations for large θ_{13}. 2012, 1209.5973.

[167] G. Rajasekaran. India based neutrino observatory. *AIP Conf.Proc.*, 721:243–246, 2004, hep-ph/0402246.

[168] J. Alonso et al. Expression of Interest for a Novel Search for CP Violation in the Neutrino Sector: DAEδALUS. *ArXiv e-prints*, June 2010, 1006.0260.

[169] T. Akiri et al. The 2010 Interim Report of the Long-Baseline Neutrino Experiment Collaboration Physics Working Groups. 2011, 1110.6249.

[170] K. Nakamura. Hyper-Kamiokande: A next generation water Cherenkov detector. *Int.J.Mod.Phys.*, A18:4053–4063, 2003.

[171] Y. Suzuki and K. Inoue. Kamioka Underground Observatories. *Eur.Phys.J.Plus*, 127:111, 2012.

[172] A. de Bellefon, J. Bouchez, J. Busto, Jean-Eric Campagne, C. Cavata, et al. MEMPHYS: A Large scale water Cerenkov detector at Frejus. 2006, hep-ex/0607026.

[173] Jean-Eric Campagne, M. Maltoni, M. Mezzetto, and T. Schwetz. Physics potential of the CERN-MEMPHYS neutrino oscillation project. *JHEP*, 0704:003, 2007, hep-ph/0603172.

[174] Emilio Ciuffoli, Jarah Evslin, and Hong Li. The Reactor Anomaly after Daya Bay and RENO. 2012, 1205.5499.

[175] Carlo Giunti and Marco Laveder. Effect of the reactor antineutrino anomaly on the first Double-Chooz results. *Phys.Rev.*, D85:031301, 2012, 1111.5211.

[176] M. Fallot, S. Cormon, M. Estienne, A. Algora, V.M. Bui, et al. New antineutrino energy spectra predictions from the summation of beta decay branches of the fission products. 2012, 1208.3877.

[177] Francis Halzen. Sterile Neutrinos and IceCube. 2011, 1111.0918.

[178] Arman Esmaili, Francis Halzen, and O.L.G. Peres. Constraining Sterile Neutrinos with AMANDA and IceCube Atmospheric Neutrino Data. 2012, 1206.6903.

[179] Soebur Razzaque and A. Yu. Smirnov. Searches for sterile neutrinos with IceCube DeepCore. *Phys.Rev.*, D85:093010, 2012, 1203.5406.

[180] V. Barger, Y. Gao, and D. Marfatia. Is there evidence for sterile neutrinos in IceCube data? *Phys.Rev.*, D85:011302, 2012, 1109.5748.

[181] T. Lasserre. Testing the Reactor and Gallium Anomalies with Intense (Anti)Neutrino Emitters. *ArXiv e-prints*, September 2012, 1209.5090.

[182] C. Grieb, J.M. Link, M.L. Pitt, R.S. Raghavan, D. Rountree, et al. LENS as a probe of sterile neutrino mediated oscillations. pages 483–492, 2007, 0705.2769.

[183] T.J.C. Bezerra, H. Furuta, and F. Suekane. Measurement of Effective Δm^2_{31} using Baseline Differences of Daya Bay, RENO and Double Chooz Reactor Neutrino Experiments. 2012, 1206.6017.

[184] S.T. Petcov and M. Piai. The LMA MSW solution of the solar neutrino problem, inverted neutrino mass hierarchy and reactor neutrino experiments. *Phys.Lett.*, B533:94–106, 2002, hep-ph/0112074.

[185] Sandhya Choubey, S.T. Petcov, and M. Piai. Precision neutrino oscillation physics with an intermediate baseline reactor neutrino experiment. *Phys.Rev.*, D68:113006, 2003, hep-ph/0306017.

[186] Liang Zhan, Yifang Wang, Jun Cao, and Liangjian Wen. Experimental Requirements to Determine the Neutrino Mass Hierarchy Using Reactor Neutrinos. *Phys.Rev.*, D79:073007, 2009, 0901.2976.

[187] Pomita Ghoshal and S.T. Petcov. Addendum: Neutrino Mass Hierarchy Determination Using Reactor Antineutrinos. *JHEP*, 1209:115, 2012, 1208.6473.

[188] Emilio Ciuffoli, Jarah Evslin, and Xinmin Zhang. Mass Hierarchy Determination Using Neutrinos from Multiple Reactors. 2012, 1209.2227.

[189] Seon-Hee Seo. Reno: Results and perspectives. `http://www.ba.infn.it/~now/now2012/web-content/TALKS/Tuesday11/plenary/Seo-RENO-NOW2012.pdf`, 2012.

[190] X. Qian, D. A. Dwyer, R. D. McKeown, P. Vogel, W. Wang, and C. Zhang. Mass Hierarchy Resolution in Reactor Anti-neutrino Experiments: Parameter Degeneracies and Detector Energy Response. *ArXiv e-prints*, August 2012, 1208.1551.

[191] Sergey I. Alekhin. Global fit to the charged leptons DIS data: alpha(s) parton distributions, and high twists. *Phys.Rev.*, D63:094022, 2001, hep-ph/0011002.

[192] Sergey I. Alekhin. Statistical properties of the estimator using covariance matrix. 2000, hep-ex/0005042.

[193] S.J. Brice. An Improved Way to Propagate π^+ Production Uncertainties. *MiniBooNE Tech Note*, 257.

[194] Leo A. Goodman. On the exact variance of products. *Journal of the American Statistical Association*, 55(292):pp. 708–713, 1960.

[195] Debian linux.

[196] LINBIT Software. Drbd.

[197] ClusterLabs. Pacemaker.

[198] Nagios.

[199] Nagiosgrapher project.

Part VI

Appendices

Appendix A

First Double Chooz Publication

The first oscillation analysis results from Double Chooz analysis were first presented in a preliminary form at the LowNu2011 conference in Seoul, South Korea, in November 2011. These results were later published as [16]. A facsimile of the publication may be found in Appendix K.1.

This section is included to provide contrast to the second analysis iteration described in Chapter 7, particularly regarding the oscillation analysis fit methods. For a more detailed description of the input analyses, consult the thesis of M. Toups [125].

A.1 Data Set

Data for this analysis were taken between April 13, 2011, and September 18, 2011. In all, physics data from 101.5234 days of detector run time were included, out of 159 calendar days.

A.2 Candidate Selection Cuts

A.2.1 First Publication Analysis

The following cuts were applied to data to define a set of Inverse Beta Decay candidates. Many use the reconstructed energy of an energy deposition in the Inner Detector E_{reco} in units of MeV, as defined in Sec. A.5.

- Prompt signal energy: $E_{\text{reco}} \in [0.7,\ 12.2]$ MeV.
- Delayed signal energy: $E_{\text{reco}} \in [6.0,\ 12.0]$ MeV.
- Time difference Δt between prompt and delayed: $\Delta t \in [2,\ 100]$ μsec.
- Time between prompt signal and the preceding muon: $\Delta t_\mu > 1$ msec. A muon is defined as any event having charge in the IV $Q_{IV} > 10000$ DUQ, or inner detector energy $E_{\text{reco}} > 30$ MeV.
- Spontaneous light noise rejection cuts.
  - PMT hits approximately homogeneous based on maximum charge on any single PMT Q_{max} and total charge Q_{tot} of all PMTs: $Q_{max}/Q_{tot} < 0.09$ for all events, and $Q_{max}/Q_{tot} < 0.06$ for delayed event.
  - PMT hits approximately simultaneous based on pulse start times T_{start} of each PMT: RMS(T_{start}) < 40 nsec.
- Multiplicity rejection cut: no valid trigger ($E_{\text{reco}} > 0.5$ MeV, and passes light noise cuts) in the 100 μsec before the prompt candidate, only one valid trigger in the $[2,\ 100]$ μsec window following the prompt event, and no valid trigger in a $[100,\ 400]$ μsec window following the prompt event.

A.2.2 Effects of IBD Selection on Detector Livetime

Each selection cut which imposes a veto time decreases the amount of detector livetime, down from a maximum possible live time equal to the run time of the detector. The resulting live time is used to calculate the number of expected background events in the IBD candidate sample (used in Sec. A.4), as well as to determine the normalization of the IBD signal expectation (described in Sec. A.3.2). Cuts which factor into determination of the live time include:

- Muon Veto: rejection of candidates within 1 msec after any muon.

Run Time [days]	101.5234
Live Time [days]	96.823
(Live Time)/Run Time Ratio	0.9547

Table A.1: Run time, and corrected live time numbers for the first Double Chooz analysis (cuts described in Sec. A.2.1). Described in detail in Sec. A.2.2.

- Second-order muon veto effect: due to "overlapping" muons which arrive sooner than 1 msec after another muon[1].

Table A.1 lists live time numbers for the analysis, along with comparisons of the live time as a fraction of detector run time. In these tables, "Run Time" is the recorded length of all physics runs which comprise the data set, and "First-Order Live Time" is the run time minus the dead time effected by all cuts except for the second-order muon veto effect. The "Second-Order Live Time" includes the second-order muon veto effect, and is calculated as 99.9% of the First-Order Live Time based on Poisson statistics of overlapping muons. The second-order live time numbers are used to determine the background expectations in Sec. A.4, while the (2^{nd}-Order live)/(run time) ratio is used to determine the signal normalization in Sec. A.3.2.

A.3 Signal Prediction

Prediction of the IBD signal component of all IBD candidates is achieved in two general steps: prediction of the number of IBD interactions in the detector by $\bar{\nu}_e$; and the prediction of the selection efficiency when the detector response and selection cuts are applied to those

[1]In practice, dead time due to muons is calculated as (number of muon triggers)×(1 ms veto window). However, it is possible for a second muon to arrive within that 1 ms window and start a new 1 ms veto window; the veto windows of each muon "overlap." This correction is calculated by using Poisson statistics and the rate of muon triggers in the detector to determine the average rate of overlapping muons, and the average additoinal deadtime incurred. A similar, but even more rare, effect can occur with triplets of overlapping muons; this is also accounted for.

events. This process utilizes the Double Chooz Monte Carlo, with corrections applied only when discrepancies between data and MC are measured.

A.3.1 Reactor Prediction

The reactor neutrino prediction and its accompanying uncertainties were generated using the prescription described in Chapter 6.

The degree of the uncertainty $\sigma_{P_{th}}$ on the thermal power $P_{th}^{R}(t)$ of reactor R was considered to be constant in time for the first analysis iteration.

For this data set, a total exposure of 15.34 GW-ton-years was collected after taking into account livetime considerations (see Sec. A.2.2). The total number of expected IBD candidates from each reactor are listed in Table A.5.

A.3.1.1 Reactor Uncertainty Propagation

Uncertainty contributions to the $\bar{\nu}_e$ signal were treated as described in Sec. 6.4.3. A MultiSim method using the selected signal Monte Carlo events of Eq. A.3 was used to convert the matrix $M_{ab}^{\text{rxt}}$from a binning in $E_{\bar{\nu}}$ to a matrix M_{ij}^{rxt} binned in E_{reco} (see Appendix C.3):

$$M_{ab}^{\text{rxt}} \xrightarrow[N_i^{\text{exp}} \text{ MC Events}]{\text{MultiSim}} M_{ij}^{\text{rxt}} \tag{A.1}$$

The resulting matrix M_{ij}^{rxt} represented a total uncertainty on the $\bar{\nu}_e$ signal rate of 1.745%. A breakout of the components of M_{ij}^{rxt} may be found in Table A.2.

A.3.2 Signal Selection Efficiency

The detector simulation is used to model all IBD candidate selection efficiencies at first order, with corrections applied only when necessary to account for known discrepancies between Monte Carlo and data.

The first correction applied is to account for the signal IBD sample having been generated according to detector run time, while the analysis is performed using detector live time. This is described in greater detail in Sec. A.2.2.

Further corrections are applied to account for differences in selection efficiency between the Monte Carlo simulation, and similar metrics measured from calibration data. In some

Source	Uncertainty [%]
Bugey4 Rate	1.42
$\langle E_f \rangle$	0.16
$\langle \sigma_f \rangle_k$ & σ_{IBD}	0.17
L_R	0.04
P_{th}^R	0.46
α_k^R	0.78
Total	1.745

Table A.2: Reactor uncertainty components, quoted as percentages of the total predicted signal rate.

cases a correction is not deemed necessary, but the a comparison between data and Monte Carlo simulation must still be made in order to establish uncertainty intervals on each effect. These effects are described in the following subsections, and include: target proton number (Sec. A.3.2.1); DAQ trigger efficiency (Sec. A.3.2.2); spill-in/spill-out effects (Sec. A.3.2.3); Gadolinium capture fraction (Sec. A.3.2.4); delayed coincidence Δt cut (Sec. A.3.2.5); delayed energy containment efficiency (Sec. A.3.2.6); and multiplicity cut (Sec. A.3.2.7). A full accounting of the corrections due to each effect, and their associated uncertainty contributions, can be found in Table A.3. Combining the numbers in Table A.3 with the (live time)/(run time) ratios of Table A.2.2 yields the normalization correction coefficient of 0.9243, which is applied to the reactor prediction described in Sec. A.3.1.

A.3.2.1 Target Proton Number

The number of free hydrogen nuclei in the neutrino target N_p, also called the target proton number, is needed to drive the prediction of the number of observed IBD signal events, as shown in Eq. 6.17.

Measurement of N_p and the estimate of its uncertainty are further described in Sec. 7.3.2.1. The final proton number used for the first analysis iteration was found to be $N_p = 6.7473 \times 10^{29}$ protons. The uncertainty on the total corrected mass measurement is 0.04%. The rel-

Source	Uncertainty	MC Correction Coeff.
Target Proton Number	0.3%	1.000
Electronics & Trigger & DAQ	0.4%	1.000
Spill-In/Spill-Out	0.4%	1./1.0072
$\frac{\text{Gd}}{\text{Gd+H}}$	0.58%	0.98
Δt Cut	0.5%	1.000
Delayed window n Capture Fraction	0.6%	1.000
Multiplicity Cut	Negligible	0.995
Signal Total	1.080%	0.9681

Table A.3: Monte Carlo signal selection efficiency corrections. Described in A.3.2. Uncertainties are quoted with relative to the total signal normalization. Total correction coefficient is applied to the reactor prediction to account for discrepancies between data and simulation.

ative uncertainties on the chemical composition and target mass combine to give the 0.3% uncertainty quoted in Table A.3.

While mentioned in Sec. 6.4.2 as contributing to the "reactor signal" uncertainty, the uncertainty on N_p is bundled with other "detector efficiency" uncertainties by collaboration convention, as it is a quantity describing a property of the detector itself. It is *not* included in the reactor uncertainty numbers quoted in Sec. A.3.1.1.

A.3.2.2 DAQ Trigger Efficiency

As described in Sec. 4.3, the Inner Detector DAQ reads out the pulse waveforms of all PMT's whenever the total integrated charge in either of two trigger groups is above 0.35 MeV. The summed integrated charge at low visible energies has some uncertainty, which gives rise to and uncertainty on the trigger efficiency at a given visible energy E_{reco}. The method for measuring the trigger efficiency and its uncertainty are further described in Sec. 7.3.2.2, though for this analysis the energy variable used was E_{reco}. By that method,

the trigger efficiency at the physics trigger threshold is 50% at 400 keV. The prompt E_{reco} range for oscillation analysis purposes begins at 0.7 MeV, where the quoted efficiency is $100\%^{+0.0\%}_{-0.1\%}$. The $\bar{\nu}_e$ interaction threshold is at $E_{\text{reco}} = 1.0$ MeV, where the quoted efficiency is 100% ± 0.0%. Thus, the trigger efficiency is found to be a negligible source of signal uncertainty, and is listed as such in Table A.3.

A.3.2.3 Spill-In/Spill-Out

Spill-In and Spill-Out are jargon describing two classes of IBD events which occur close to the NT/GC interface, described in more detail in Sec. 7.3.2.3.

During the first analysis iteration, the neutron transport model implemented in the Monte Carlo simulation was found to disagree at a non-negligible level with more accurate simulations available. A correction factor of 1/1.0072 (as listed in Table A.3) was applied to account for this effect. Studies were performed with IBD Monte Carlo events and variations of the parameters of each of the four above factors. From these studies, a symmetric uncertainty of 0.4% on the total signal normalization was established.

A.3.2.4 Gadolinium Capture Fraction

Neutrons produced by IBD interactions in the $\bar{\nu}_e$ target capture on either Gadolinium or Hydrogen in the vast majority of occurrences. The fraction of captures which occur on Gadolinium ϵ_{Gd} directly factors into the number of detected IBD candidates, and is defined:

$$\epsilon_{Gd} = \frac{C_{n-Gd}}{C_{n-Gd} + C_{n-H}} \tag{A.2}$$

where C_{n-Gd} and C_{n-H} are the numbers of neutrons which capture on Gadolinium and Hydrogen, respectively, in a particular period of time.

A measurement of ϵ_{Gd} in data is performed by examining calibration data produced by using a tagged ^{252}Cf radioactive source, which produces neutrons by fission. The spectrum of the neutron captures is fit to a series of Gaussian peaks at known energies of H and Gd neutron captures, and the integrals of the peaks are compared to the predicted yield ϵ_{Gd} for the data. This measurement is then compared to Monte Carlo events generated by a

simulated ^{252}Cf source, and the relative difference $(\epsilon_{Gd}^{data} - \epsilon_{Gd}^{sim})/\epsilon_{Gd}^{data}$ determines whether or not a correction must be applied to the signal prediction.

For this analysis iteration, a relative difference of ∼1.0% was measured, mandating that a correction factor of 0.98 be applied to the signal prediction. The uncertainty associated with this measurement was 0.58%.

A.3.2.5 Delayed Coincidence Δt Cut

Following an IBD interaction, the neutron captures on either Gadolinium or Hydrogen with a characteristic time determined by the relative concentrations of the two elements in the target scintillator. This characteristic time can be predicted from the chemical properties of the scintillator and implemented in the detector simulation. The potential effects of this systematic and the method for estimating its uncertainty are described in Sec. 7.3.2.5.

No correction factor was applied to the signal normalization based on these studies. The uncertainty on the signal normalization due to a possible systematic effect in the Δt distribution was found to be 0.5% relative to the total signal prediction.

A.3.2.6 Delayed Energy Containment Efficiency

Even with the design feature of the γ-catcher to maximize energy containment, it is still possible for γ rays emitted from n-Gd captures to escape conversion into visible light, *i.e.* from absorption in material. This mechanism and the method used to measure its effect are described in more detail in Sec. 7.3.2.6.

While no modification to the simulation was employed to account for relative measured differences between data and simulation, an uncertainty on the total signal normalization was estimated conservatively at 0.6% of the total signal rate based on these measurements.

A.3.2.7 Multiplicity Cut

Recalling from Section A.2.1, the multiplicity cut requires that no valid trigger ($E_{\rm reco} > 0.5$ MeV, and passes light noise cuts) occur in the 100 μsec window before the prompt event, and that there exist only one only one valid trigger in the [2, 100] μsec window following the prompt event, and no valid trigger in a [100, 400] μsec window following the prompt

event. This cut does not reduce any background, but eliminates ambiguious cases where two prompt events of different energies could "share" a delayed event.

The multiplicity cut imposes a correction on the normalization of the predicted IBD signal selection of 0.995, due to the lack of interleaved singles events in the Monte Carlo. This correction factor is based on the Poisson probability of a single event with the proper energy appearing within the 500 μsec isolation window imposed by the multiplicity cut. This correction has negligible uncertainty, due to the precise measurement of the single event rate.

A.3.3 Signal Prediction Summary

Following the considerations mentioned in Sec. A.3.1, the expected number of $\bar{\nu}_e$-induced IBD interactions in the detector N_a is calculated as given in Eq. 6.17, where the index a runs over the 38 bins in $E_{\bar{\nu}}$.

In practice, the number of protons N_{prot} used in calculating the N_a includes the neutrino target scintillator, target tank, gamma catcher, GC tank, and buffer oil. According to the N_a, Monte Carlo events are generated in these volumes according to the expected proton density and reactor power. In addition to the IBD kinematic quantities from the detector, each Monte Carlo event contains the true energy $E_{\bar{\nu}}$ and originating reactor R of, and the baseline L traveled by the progenitor $\bar{\nu}_e$. These Monte Carlo events are generated at 100-times expected statistics in order to limit any statistical fluctuations; their weights are scaled down when used in the final oscillation fit.

The Monte Carlo events are then processed through the GEANT4-based [143] detector simulation package, DCGLG4sim [144]. DCGLG4sim simulates how the scintillation and Cerenkov photons created following the IBD interactions propagate throughout the detector. The resulting simulation data are then used as input to the Double Chooz Read-out System Simulation (DCRoSS), which simulates the detector and electronics responses to the simulated photons collected by the PMTs. A suite of reconstruction algorithms are then applied, culminating in the final quantity of measured visible energy E_{reco} for each energy deposition.

The reconstructed Monte Carlo events then have the set of IBD candidate selection cuts

from Sec. A.2.1 applied to them. Thus, the only modifications to event weight which need to be applied are due to those effects which are not modeled in properly in the simulation chain, as described in Sec. A.3.2. This is accomplished by applying the signal normalization factor of 0.9243. The chain of processing from the calculated number of expected IBD events to an expected number of IBD candidates in the detector N_i^{exp} is as follows:

$$N_a^R \begin{pmatrix} E_{\bar{\nu}} \\ L \end{pmatrix} \xrightarrow[\text{CT}]{\text{GLG4sim, RoSS}} N_i^R \begin{pmatrix} E_{\bar{\nu}} \\ L \\ E_{\text{reco}} \end{pmatrix} \xrightarrow[\text{Sig. Norm. Factor}]{\text{IBD Cand. Sel.}} N_i^{\text{exp},R} \begin{pmatrix} E_{\bar{\nu}} \\ L \\ E_{\text{reco}} \end{pmatrix} \tag{A.3}$$

where the final index i runs over bins in reconstructed energy E_{reco}. The selected Monte Carlo IBD candidates represented as $N_i^{\text{exp},R}$ will be used as inputs to the final oscillation fit in Sec. A.6.

A.3.3.1 Efficiency Uncertainty Propagation

The effect of an error on the selection efficiency would act as a bias in the signal normalization. Thus, the uncertainties listed in Table A.3 are added in quadrature and propagated to the oscillation analysis as a covariance matrix derived from the shape of the predicted signal. This matrix is implemented as a normalization uncertainty with a total relative magnitude of:

$$\frac{\sigma_{\text{eff}}}{\sum_{i=1}^{18} \sum_{R=1,2} N_i^{\text{exp},R}} = 1.080\% \tag{A.4}$$

of the signal prediction, or 0.947% as compared to the 8,121 data candidates. The signal efficiency uncertainty is fully correlated between energy bins in the signal population:

$$M_{ij}^{\text{eff}} = \left(\sum_{R=1,2} N_i^{\text{exp},R} \right) \left(\frac{\sigma_{\text{eff}}}{\sum_{i=1}^{18} \sum_{R=1,2} N_i^{\text{exp},R}} \right)^2 \left(\sum_{R=1,2} N_j^{\text{exp},R} \right). \tag{A.5}$$

A.4 Background Measurements

Three main backgrounds were included in the oscillation fit, and constrained by measurements using the data. The background from accidental coincidences is described in

Sec. A.4.1, the cosmogenic ^{9}Li background is described in Sec. A.4.2, and the combined fast-neutron/stopping-muon correlated background is described in Sec. A.4.3. The final part of each of those sections describes how the uncertainty on each measurement is propagated into the final oscillation fit (Sec. A.6) as a covariance matrix, a fit parameter and pull term in the fit statistic, or a combination. It is worthwhile to note that the final measurements of the ^{9}Li and fast-neutron/stopping-muon backgrounds will be output parameters from the oscillation fit itself. Finally, a set of cross-checks of the background measurements is described in Sec. A.4.4.

A.4.1 Accidental Background

The accidental background contribution was measured by applying the neutrino selection cuts described in Sec. A.2 to data, but using a coincidence window separated by 1 second. This "off-time" window effectively measures the rate of random coincidences passing the neutrino selection cuts without the correlated events from real n-Gd captures of IBD-generated neutrons. A total of 198 off-time windows, each separated by 500 μs, were used to increase the statistics of the measurement, thereby improving its precision. The total rate for accidental background events in the prompt spectrum was measured to be $R_{\text{acc.}} = (0.33 \pm 0.03)$ events per day. Any light noise remaining after the cuts described in Sec. A.2 is included in this measurement.

A.4.1.1 Uncertainty Propagation

Since this measurement is from data, uncertainties on the binned accidental background spectrum are considered to be uncorrelated between bins. For the measured background rate of $R_{\text{acc.}} = 0.33$ events per day and uncertainty $\sigma_{R_{\text{acc.}}} = 0.03$ events per day, the covariance matrix associated with the accidental background population $N_i^{\text{acc.}}$ is:

$$M_{ij}^{\text{acc.}} = \delta_{ij} \sqrt{\frac{N_i^{\text{acc.}}}{\sum_k N_k^{\text{acc.}}}} \left(\frac{\sigma_{R_{\text{acc.}}}}{R_{\text{acc.}}} \right)^2 \sqrt{\frac{N_j^{\text{acc.}}}{\sum_k N_k^{\text{acc.}}}}. \tag{A.6}$$

A.4.2 Cosmogenic Lithium-9

The rate of ^{9}Li in the IBD candidate sample is constrained by observing the distribution in time Δt_μ of IBD-like interactions since the closest preceding muon in a 20-second time window, where the muon deposited more than 600 MeV of visible energy. The distribution of Δt_μ is fit to a combination of an exponential and a constant background:

$$f\left(\Delta t_\mu\right) = \left(\frac{A}{\tau_9}\exp\left(-\frac{\Delta t_\mu}{\tau_9}\right) + C\right)\left(1 - \frac{\Delta t_\mu}{T}\right) \tag{A.7}$$

where τ_9 is the 257 msec lifetime of ^{9}Li, A is proportional to the rate of ^{9}Li, C represents the constant background, and the term containing the run length $T = 3600$ seconds is a correction factor accounting for the finite lengths of physics runs. The fit value for A and its uncertainty are converted into a rate for ^{9}Li using the total live time of the data used to construct the fit. The total measured rate of cosmogenic isotopes was found to be 2.3 ± 1.2 events per day. Here the uncertainty has been symmetrized to allow proper implementation in the final oscillation fit.

A.4.2.1 Uncertainty Propagation

The ^{9}Li background is propagated to the final fit by combining a Monte Carlo-generated spectrum of events with the measured background rate. The spectrum is created by using a nuclear model to simulate ^{9}Li decays in the Inner Detector. This generator, dubbed DC-GenSpec, is based on nuclear decay data [145, 146], and allows for some nuclear parameters to be adjusted in order to evaluate potential effects on the end spectrum. The generated MC events are then processed through the detector response simulation and reconstruction, similar to the sequence of Eq. A.3. Following application of the IBD candidate selection cuts, the product is a high-statistics set of ^{9}Li events which would fit IBD candidate criteria. These events are re-weighted in order to make the integral of the spectrum fit the central-value expectation of ^{9}Li rate times detector live time. When binned, this normalized spectrum gives the central-valued prediction for the ^{9}Li background population $N_i^{\mathrm{Li,CV}}$.

Uncertainties on the ^{9}Li prediction are treated as two orthogonal components: a normalization component based on the uncertainty of the measured rate; and a spectral shape component.

For the measured background rate of $R_{\mathrm{Li}} = 2.3$ events per day and uncertainty $\sigma_{R_{\mathrm{Li}}} = 1.2$ events per day, the covariance matrix associated with the ^{9}Li background population $N_i^{\mathrm{Li,CV}}$ is:

$$M_{ij}^{\text{Li rate}} = N_i^{\mathrm{Li,CV}} \left(\frac{\sigma_{R_{\mathrm{Li}}}}{R_{\mathrm{Li}}} \right)^2 N_j^{\mathrm{Li,CV}} \tag{A.8}$$

In practice, the uncertainty on the ^{9}Li rate is implemented with a pulled fit parameter $\epsilon_{^9\mathrm{Li}}$ and corresponding pull term in the fit statistic, as described in Sec. A.6.2.1. Thus, in the fit implementation, the ^{9}Li spectrum enters as a dynamic set of values N_i^{Li} calculated as:

$$N_i^{\mathrm{Li}} = \epsilon_{^9\mathrm{Li}} N_i^{\mathrm{Li,CV}} \tag{A.9}$$

In cases where the matrix $M_{ij}^{\text{Li rate}}$ is used to represent the ^{9}Li rate uncertainty, the parameter $\epsilon_{^9\mathrm{Li}}$ is fixed to its null-effect value of 1.

The uncertainty on the spectral shape is determined by comparing the output of two Monte Carlo event sets with different nuclear decay parameters. The central-value ^{9}Li spectrum $N_i^{\mathrm{Li,CV}}$ is compared to a spectrum $N_i^{\mathrm{Li,alt}}$ with alternate nuclear decay parameters set to the limits of their uncertainty intervals. This provides for a correlated shape uncertainty with allowed deviations of up to 20% per bin. The matrix is then constructed:

$$M_{ij}^{\text{Li shape}} = \left(N_i^{\mathrm{Li,alt}} - N_i^{\mathrm{Li,CV}} \right) \times \left(N_j^{\mathrm{Li,alt}} - N_j^{\mathrm{Li,CV}} \right) \tag{A.10}$$

Since this uncertainty component is close to, but not exactly, a "spectral shape only" uncertainty, the sum of the elements of $M_{ij}^{\text{Li shape}}$ is near zero.

A.4.3 Fast Neutron & Stopping μ Backgrounds

Two irreducible correlated backgrounds are known to affect Double Chooz: fast neutron recoils (FN); and stopping muons (SM). For a more detailed decription of the mechanism of each, see Sec. 7.4.3.

Study of this background is then accomplished by examining IBD candidates in the energy region 12 MeV $< E_{\mathrm{reco}} <$ 30 MeV where no IBD signal events are expected. The spectrum is then extrapolated down into the IBD signal region 0.7 MeV $< E_{\mathrm{reco}} <$ 12.2 MeV presuming a flat spectral shape. With this method, the estimated rate of FN/SM events in the signal energy region is $(0.83 \pm 0.38)\,\mathrm{day}^{-1}$. In addition to the rate uncertainty, an

uncertainty on the shape of the spectrum is included by allowing the slope of the linear spectral shape to vary, using the measurement of a complimentary method which accounts for stopping μ differently as the 1σ deviation.

A.4.3.1 Uncertainty Propagation

Uncertainties on the FN/SM prediction are treated as two orthogonal components: a normalization component based on the uncertainty of the measured rate; and a spectral shape component.

For the measured background rate of $R_{\rm fn} = 0.83$ events per day and uncertainty $\sigma_{R_{\rm fn}} = 0.38$ events per day, the covariance matrix associated with the FN/SM background population $N_i^{\rm fn,CV}$ is:

$$M_{ij}^{\text{fn rate}} = N_i^{\rm fn,CV} \left(\frac{\sigma_{R_{\rm fn}}}{R_{\rm fn}}\right)^2 N_j^{\rm fn,CV} \tag{A.11}$$

In practice, the uncertainty on the FN/SM rate is implemented with a fit parameter $\epsilon_{\rm fn}$ and a corresponding pull term in the fit statistic, as described in Sec. A.6.2.1. Thus, in the fit implementation, the FN/SM spectrum enters as a dynamic set of values $N_i^{\rm fn}$ calculated as:

$$N_i^{\rm fn} = \epsilon_{\rm fn} N_i^{\rm fn,CV} \tag{A.12}$$

In cases where the matrix $M_{ij}^{\text{fn rate}}$ is used to represent the ^{9}Li rate uncertainty, the parameter $\epsilon_{\rm fn}$ is fixed to its null-effect value of 1.

The uncertainty on the spectral shape is determined by comparing the best-fit linear spectrum of two different analysis methods. A flat spectral shape is used as the central valued spectrum $N_i^{\rm fn,CV}$, while the alternate spectrum $N_i^{\rm fn,alt}$ is a linear fit where the stopping muon contribution has been accounted for in a different manner. To maintain a true "shape" uncertainty, $N_i^{\rm fn,alt}$ is scaled to the normalization of $N_i^{\rm fn,CV}$. The covariance matrix is then constructed:

$$M_{ij}^{\text{fn shape}} = \left(N_i^{\rm fn,alt} - N_i^{\rm fn,CV}\right) \times \left(N_j^{\rm fn,alt} - N_j^{\rm fn,CV}\right). \tag{A.13}$$

Since this uncertainty component is implemented as a "spectral shape only" uncertainty, with $N_i^{\rm fn,CV}$ and $N_i^{\rm fn,alt}$ having the same total normalization, the sum of the elements of $M_{ij}^{\text{fn shape}}$ is zero.

A.4.4 Cross-checks of Background Measurements

Two cross-checks of the measured background rates were made by independent means: an extrapolation of background rates from the measured rate of observed events as a function of reactor power, and a measurement of the observed rate during periods of time where both reactors were at near-zero thermal power.

A.4.4.1 Observed Candidate Rate vs. Expected $\bar{\nu}_e$ Rate

Plotting the observed IBD candidate rate versus expected event rate, as is done in Figure A.1, is loosely equivalent to plotting the IBD candidate rate versus average reactor power. At the minimal expected rate, where both reactors are at or near zero thermal power, the irreducible backgrounds dominate the observed IBD candidate rate. Thus, a linear fit to these data allows a measurement of the sum of all irreducible backgrounds to be made by extrapolation. This is the linear fit depicted on Figure A.1, and gives a best-fit value for the background rate of 3.2 ± 1.3 events per day.

A.4.4.2 Measured Candidate Rate with Both Reactors Off

Soon after the Nov. 2011 end of the data-taking period for the first Double Chooz analysis iteration, both reactors B1 and B2 were shut down for a period of $\sim$24 hours. This period yielded a physics data livetime of 0.84 days (22.5 hours) during which the dominant sources of expected IBD candidates are the irreducible backgrounds. Fewer than 0.3 residual $\bar{\nu}_e$ events are expected during this time period with the reactor cores idle from residual radioactive decays. Three events were found which passed the first four IBD candidate selection cuts listed in Sec. A.2.1. Two of these events were found to have prompt energies of 4.8 MeV and 9.4 MeV, and were reconstructed within 30 cm and 240 cm of the closest energetic muon. These factors suggest that these IBD candidates were cosmogenic ^{9}Li background events. The third candidate was found to have a prompt energy of 0.8 MeV, with its prompt and delayed components reconstructed 3.5 m distance from each other. This is suggestive of an accidental coincidence. Further analysis of these events was later presented in [147].

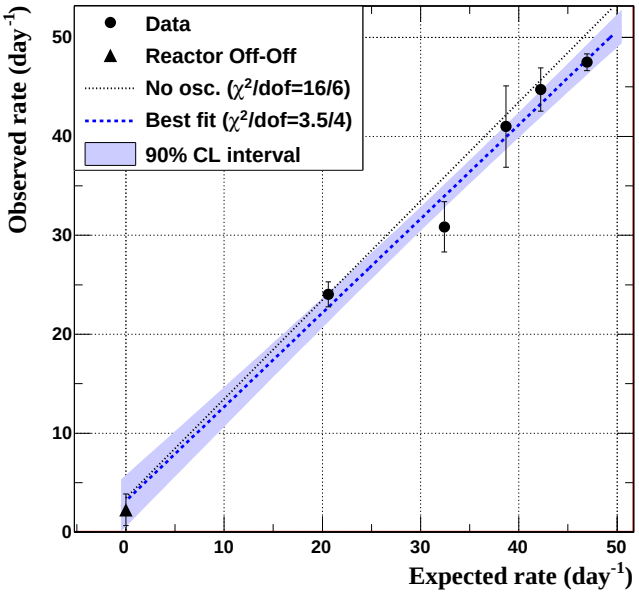

Figure A.1: Daily number of observed IBD candidate events plotted versus the expected number of $\bar{\nu}_e$ events. Dashed blue line shows the best fit to the data, with blue region giving the 90% confidence level band. Dotted line shows the expectation from the no-oscillation scenario. Best-fit parameters described in text of Sec. A.4.4. From [16].

A.5 Energy Scale

The definition of the visible energy E_{reco} for an energy deposition in the Inner Detector is found by summing the charge q_l in all channels l to yield a calorimetric measure of the total number of photoelectrons CaloPE $= \sum_l \frac{q_l}{\text{gain}_l(t)}$ and applying a set of corrections:

$$E_{\text{reco}} = \text{CaloPE} \times \text{Corr}_1\left(\text{CaloPE}, a_0, a_1, a_2\right) \times \text{Corr}_2\left(z, a_3, a_4, a_5\right) \times f^m_{\text{MeV}} \tag{A.14}$$

where Corr_1 and Corr_2 are spatial and energy-dependent correction functions:

$$\begin{aligned} \text{Corr}_1\left(\text{CaloPE}, a_0, a_1, a_2\right) &= a_0 \log\left(\text{CaloPE} - a_1\right) + a_2 && \text{(A.15)} \\ \text{Corr}_2\left(z, a_3, a_4, a_5\right) &= a_3 + z a_4 + z^2 a_5 && \text{(A.16)} \\ \vec{a} &= \{0.0286966,\ 56.1478,\ 0.842321, \\ &\quad 0.998201,\ -9.51483 \times 10^{-6},\ -3.25985 \times 10^{-8}\} && \text{(A.17)} \end{aligned}$$

and $f = 1/214$ MeV/PE sets the correspondence between detector response and absolute measured energy. The time-dependent gain gain_l for each channel l is determined from LED light-injection calibration data. The correction functions are futher described in subsequent subsections, with treatment of the total uncertainty described in Sec. A.5.2.

A.5.1 Detector Response Correction Functions

The correction functions Corr_1 and Corr_2 of Eqs. A.15 and A.16 are phenomenological corrections applied to Monte Carlo such that the modeled detector repsonse better matches data from calibration source deployments in the detector. For this analysis iteration, sources were deployed along the z-axis of the detector, as well as in the guide tube just outside the target vessel. The parameters $\vec{a}$ of each function as listed in Eq. A.17 are determined by the best-fit of both functions to the differences between data from calibration deployments, and simulated Monte Carlo calibration data. Detector response is considered nominal at the center of the detector. Uncertainties on the parameters of $\vec{a}$ are related by a 6-by-6 covariance matrix $M_{\vec{a}}$, which is block-diagonal in 3-by-3 blocks, as determined by the output of the fits to calibration data.

A.5.2 Uncertainty Propagation

The dominant uncertainties on the energy scale arise from the six fit parameters $\vec{a}$ of the correction functions Corr_1 and Corr_2 of Eqs. A.15 and A.16. These are propagated to the final fit using the MultiSim method. The energy scale covariance matrix was constructed from $\vec{a}$ and $M_{\vec{a}}$ using a MultiSim method (see Appendix C.4 for more detail). Sets of $u = [1, ..., U]$ random Gaussian throws $\{\vec{a}\}_u$ are made on the energy scale parameters $\vec{a}$ as drawn from $M_{\vec{a}}$. The correlated-random bin deviations $\{\delta N_i^{\mathrm{pred}}\}_u = \{N_i^{\mathrm{pred}}\}_u - \{N_i^{\mathrm{pred}}\}_{\vec{a}}$ are used to construct an average covariance matrix M_{ij}^{escale}:

$$M_{ij}^{\mathrm{escale}} = \frac{1}{U}\sum_{u=1}^{U}\left(\{\delta N_i^{\mathrm{pred}}\}_u \times \{\delta N_j^{\mathrm{pred}}\}_u\right) \tag{A.18}$$

The resulting M_{ij}^{escale} is 18-by-18 in dimension, binned in E_{reco}.

Traditionally, the energy scale is modulated in the final oscillation fit as a parameter P_E which scales the energy E_{reco}^0 of some events comprising the Monte Carlo prediction:

$$E_{\mathrm{reco}} = P_E E_{\mathrm{reco}}^0. \tag{A.19}$$

The parameter P_E is analogous to a_3 of $\vec{a}$ in effect, though not in central value. This scaling is only applied to events whose energies E_{reco}^0 are determined by the Monte Carlo reconstruction, and not by measurement in data (*e.g.* IBD signal events and ^{9}Li events, but not fast neutrons/stopping muons or accidentals).

In practice, it was found that allowing P_E to float as a pulled parameter of the χ^2 minimization fit led to instabilities of the minimizing software, MINUIT [148]. Much trial-and-error for MINUIT's operating parameters was required to produce representative output.

A.6 Oscillation Fit & Results

The oscillation fit was performed using the CUfits statistics toolkit (see Appendix B). CUfits is designed to re-weight an ensemble of Monte Carlo event populations, all of which are tabulated in Table A.4, according to a set of fit parameters. These re-weighted events are filled into a histogram representing the total signal-plus-background prediction N_i^{pred}

for the IBD candidates observed in the Double Chooz Far Detector:

$$N_i^{\text{pred}} = \sum_{R=1,2} N_i^{\bar{\nu},R}\left(\sin^2(2\theta_{13}), \Delta m^2_{31}, \alpha_E\right) + N_i^{\text{Li}}\left(\epsilon_{^9\text{Li}}, \alpha_E\right) + N_i^{\text{fn}}\left(\epsilon_{textfn}\right) + N_i^{\text{acc}} \quad \text{(A.20)}$$

where the index i runs over bins in visible energy E_{reco}. The predicted number of signal antineutrino events $N_i^{\bar{\nu},R}$ from each reactor R is calculated from the reactor expectation $N_i^{\text{exp},R}$ of Eq. A.3 by reweighting each event according to the effective two-neutrino survival probability:

$$\begin{aligned} N_i^{\bar{\nu},R} &= P\left(\bar{\nu}_e \to \bar{\nu}_e\right) N_i^{\text{exp},R} \\ &= \left(1 - \sin^2(2\theta_{13}) \sin^2\left(\frac{1.27 L_R \Delta m^2_{31}}{E_{\bar{\nu}}}\right)\right) N_i^{\text{exp},R} \quad \text{(A.21)} \\ & \quad \text{(A.22)} \end{aligned}$$

A summary of each initial event population at null-oscillation and with initial-valued fit parameters is given in Table A.5.

Population	Original Population	Fit Parameters
$N_i^{\bar{\nu},R}$	$N_i^{\text{exp},R}$	$\sin^2(2\theta_{13})$, P_E
N_i^{Li}	$N_i^{\text{Li,CV}}$	$\epsilon_{^9\text{Li}}$, P_E
N_i^{fn}	$N_i^{\text{fn,CV}}$	ϵ_{fn}
N_i^{acc}	–	–

Table A.4: Summary of final oscillation fit input event species, and their parametric dependencies.

The oscillation analysis fit proceeds by comparing to the observed number of IBD candidates in each bin N_i to the prediction N_i^{pred} and calculating a goodness-of-fit using one of the statistics described in Sec. A.6.2. By collaboration agreement made before "opening the box" and fitting to data, the Rate+Shape statistic of Eq. A.27 is used as the main-line analysis, with the Rate-only and Shape-only statistics of Eq. A.28 and A.29 used in complimentary analyses. In addition, reactor power information was kept blinded until the analysis methodology had been frozen. This decision was based on null oscillation sensitivity studies, the results of which showed the Rate+Shape fit to provide an optimally-sensitive

	Total
Live Time [days]	96.823
IBD Candidates	4121
Total $\bar{\nu}$	4009.96
Lithium-9	222.9
Fast-n & Stopping μ	79.5
Accidentals	32.00
Total Backgrounds	335.68
Total Prediction	4344

Table A.5: Summary of observed IBD candidates, with corresponding signal and background predictions. No oscillation fit parameter results have been applied.

measurement. These results are tabulated in Table A.6. The studies were performed with the actual systematic uncertainties used in the final oscillation analysis; these are summarized in Tale A.7.

	$\sin^2(2\theta_{13})$ 68% C.L.	$\sin^2(2\theta_{13})$ 90% CL
Rate Only	0.0816	0.1343
Shape Only	0.1555	0.2560
Rate+Shape	0.0511	0.0842

Table A.6: Summary of Null Oscillation sensitivity intervals at 68% and 90% CL for three different goodness-of-fit statistics, for the first Double Chooz analysis iteration.

The statistic is minimized numerically using MINUIT [148]. At each iteration of the minimization, N_i^{pred} is recalculated based on the values of the fit parameters listed in Table A.4. Following recalculation of N_i^{pred}, the fit statistic is evaluated for that iteration. A combination of MINUIT's HESSE and MIGRAD minimization algorithms [2] is employed until a set of best-fit parameters is established. The multi-dimensional uncertainty intervals

[2]Consult the MINUIT manual [148] for more details on each algorithm.

Source	Rate Uncertainty
Statistics	1.56%
Selection Efficiency	1.07%
Reactor	1.7%
Detector	1.66%
^{9}Li Background	1.5318%
Fast-n/Stopping-μ Background	0.4941%
Accidental Background	0.0074%
Total	2.6831%

Table A.7: Uncertainties from all sources contributing to the oscillation analysis. Numbers quoted are the relative uncertainty on contributed to the rate of events, as a percentage of the number of observed IBD candidates in each analysis.

on each parameter are then evaluated by using the HESSE algorithm to calculate the parameter covariance matrix. The results of this oscillation fit are described in detail in Sec. A.6.3.

In practice, uncertainty intervals are determined by evaluating the behavior of the fit statistic, generically called χ^2 for the purposes of this paragraph (the actual fit statistics used are described in Sec. A.6.2). At best-fit, the statistic takes a minimum value χ^2_{bf}. Uncertainty intervals are then evaluated in the multi-dimensional space of all floating fit parameters. The 1σ interval of a parameter is defined by the boundary where $\Delta\chi^2 = \chi^2 - \chi^2_{bf} = 1$ in the case of one unbounded parameter (see the "Statistics" section of [36]). With a proper error definition, these intervals are calculated by MINUIT's HESSE algorithm.

A break-out of the uncertainty interval on $\sin^2(2\theta_{13})$ into "statistical" and "systematic" parts is achieved by running a null-oscillation sensitivity study at 100-times expected statistics, and considering the resulting 68% C.L. sensitivity as the "purely systematic" component of the total uncertainty. A null-oscillation sensitivity is chosen over boosting the statistics of the observed data in order to prevent lending improper weight to statistical

fluctuations found in the data. This systematic part is subtracted in quadrature from the total uncertainty to yield the "statistical" component.

A.6.1 Parameter-Independent Covariance Matrix

The uncertainty on the signal and background predictions is initially defined by a covariance matrix M_{ij} [191, 192]. The matrix is 18×18 in dimension, corresponding to the number of energy bins indexed in i. The matrix is the sum of contributions from each systematic and statistical source of ucertainty, as prescribed in the previous sections. If no pull parameters are used to represent any uncertainties, the matrix has the form:

$$M_{ij}^{\text{No Pulls}} = M_{ij}^{\text{stat}} + M_{ij}^{\text{rxt}} + M_{ij}^{\text{eff}} + M_{ij}^{\text{Li rate}} + M_{ij}^{\text{Li shape}} + M_{ij}^{\text{fn rate}} + M_{ij}^{\text{fn shape}} + M_{ij}^{\text{escale}} \quad \text{(A.23)}$$

In practice, pull parameters and pull terms are used to represent some uncertainties, in which the components of the covaraince matrix corresponding to those systematics must be omitted from the sum. Thus, if the list of pull parameters described in Sec. A.6.2.1 is used, the matrix has the form:

$$M_{ij} = M_{ij}^{\text{stat}} + M_{ij}^{\text{rxt}} + M_{ij}^{\text{eff}} + M_{ij}^{\text{Li shape}} + M_{ij}^{\text{fn shape}} + M_{ij}^{\text{escale}} \quad \text{(A.24)}$$

The matrix in Eq. A.24 is used in the main oscillation analysis.

The statistical uncertainty component is defined by the Neyman χ^2 convention:

$$M_{ij}^{\text{stat}} = \delta_{ij}\sqrt{N_i N_j}. \quad \text{(A.25)}$$

where N_i is the measured number of IBD candidates in energy bin i. This matrix does not fluctuate as a function of the fit parameters, making the minimization procedure more efficient[3].

A.6.2 Definitions of χ^2 Statistics

Oscillation analyses were performed using three different χ^2 statistics. Each statistic contains a set of floating fit parameters in addition to the oscillation amplitude, called "pulled parameters", which are constrained by externally-specified data.

[3]At the time of the first analysis iteration, tools allowing the use of a dynamic χ^2 fit statistic (*a la* Sec. 7.7.1) were not yet proven.

While analyses were performed using each of these statistics, an agreement among the collaboration made in advance of the analysis stipulated that χ^2_{RS} of Eqn. A.27 would be used to determine the offical oscillation measurement.

A.6.2.1 Pull Term Contribution

It is possible to modifly the fit statistics to contain "pull terms" constraining the behavior of additional fit parameters. As described in previous sections, the fit parameters affect the values of the N_i^{pred}. In particular, a multiplier $\epsilon_{^9\text{Li}}$ on the ^{9}Li rate (Sec. A.4.2.1), a multiplier ϵ_{fn} on the FN/SM rate (Sec. A.4.3.1), the oscillation amplitude $\sin^2(2\theta_{13})$, and the energy scale P_E (Sec. A.5) were included as pulled parameters. For each parameter, a "pull term" or constraint term is added to the fit statistic. The pull term constrains the value of each parameter towards its central value while still allowing it to vary within the prescribed external uncertainty interval. This accounts for uncertainty on the parameter in the fit in a way that is roughly[4] equivalent to a contribution to the covariance matrix [149, 150].

For the first Double Chooz analysis iteration, the main result quoted employed a χ^2 statistic which did not use pulled parameters. Seperate fits were performed using the same fit statistic with parameters added in order to provide results on how well certain parameters were constrainted. The fits with additional parameters showed some numerical instability during the minimization process, preventing them from being used as the main result.

To keep later equations concise, we collect all pull terms into a separable term χ^2_{pulls} which will be included in other, later-described fit statistics. This portion of the statistics is denoted:

$$\chi^2_{\text{pulls}} = \frac{(\epsilon_{\text{fn}} - 1)^2}{\sigma^2_{\text{fn}}} + \frac{(\epsilon_{^9\text{Li}} - 1)^2}{\sigma^2_{^9\text{Li}}} + \frac{(P_E - P_{E,0})^2}{\sigma^2_{P_E}} \tag{A.26}$$

[4]The author doubts this assertion. The equivalence shown in [149] and [150] presumes that each pull term or contribution to the covariance matrix are independent, and known precisely at the beginning of the minimization procedure. This does not rigorously allow for the technique of re-calculating the values of other covariance matrix contributions based on the values of the pull paramters, as is described in Sec. 7.7.1. However, an argument can be made that the technique of Sec. 7.7.1 is appropriate to the situation at hand, and correct in that context. See Appendix G for more discourse on the requirements for complete equivalence in different uncertainty scenarios.

Each statistic is minimized with respect to all of these parameters during the fitting process. The parameters ϵ_{fn}, $\epsilon_{^9\mathrm{Li}}$, and P_E are bounded by uncertainty intervals determined as described in the above text. The mass splitting Δm^2_{31} is fixed to $2.4 \times 10^{-3}\mathrm{eV}^2$, close to the central value as measured by MINOS [83] at the time. Thus, the mass splitting was not a parameter of the fit for this analysis iteration.

It is worthwhile to note that while the pulled parameters must be minimized as part of the fit, they do not contribute a new degree of freedom if they are accompanied by a pull term in the statistic. In essence, a free parameter is added, but a data point is also added, with no net change in the number of degrees of freedom.

A.6.2.2 Rate + Shape Fit Statistic

The "rate + shape" chi-squared statistic was defined as:

$$\chi^2_{RS} = \sum_{i,j=1}^{18} \left(N_i - N_i^{\mathrm{pred}}\right) \times (M_{ij})^{-1} \left(N_j - N_j^{\mathrm{pred}}\right)^{\mathrm{T}} + \chi^2_{\mathrm{pulls}} \tag{A.27}$$

This statistic takes into account all potential spectral and temporal information contained in the binned data and the correlated uncertainties of the prediciton. Since pulled parameters are used, M_{ij} is as described in Eq. A.24.

A.6.2.3 Rate-Only Fit Statistic

The rate-only statistic compares the measured rate of IBD candidates to the predicted rate by summing over all energy bins i. For brevity of notation, we define:

$$\begin{aligned} N &= \sum_i N_i \\ N^{\mathrm{pred}} &= \sum_i N_i^{\mathrm{pred}} \end{aligned}$$

Also, we compactify the covariance matrix into a single measure of uncertainty M:

$$M = \sum_{i,j=1}^{18} M_{ij}$$

where M_{ij} is as described in Eq. A.24 on account of the use of pull parameters and pull terms. The "rate-only" chi-squared statistic is then defined as:

$$\chi^2_{RO} = \frac{\left(N - N^{\mathrm{pred}}\right)^2}{M} + \chi^2_{\mathrm{pulls}} \tag{A.28}$$

It is worth noting that the number of degrees of freedom in this fit is one, and the minimum value of χ^2_{RO} is always zero at best-fit.

A.6.2.4 Shape-Only Fit Statistic

The "shape-only" chi-squared statistic is intended to neglect any normalization information associated with the signal prediction.

First, we define a prediction renormalization factor η:

$$\eta = \frac{\sum_i N_i}{\sum_i \left(\sum_{R=1,2}^{\text{Reac.}} N_i^{\nu,R} + \sum_b^{\text{Bkgnds.}} N_i^b \right)}$$

This factor is used to ensure that the signal+background prediction has the same total normalization as the measured data, with the goal of removing normalization information from the fit[5]. The "shape-only" chi-squared statistic is then defined as:

$$\begin{aligned} \chi^2_{SO} \;=\; & \sum_{i,j=1}^{18} \left[\left(N_i - \eta \left(\sum_{R=1,2}^{\text{Reac.}} N_i^{\nu,R} + \sum_b^{\text{Bkgnds.}} N_i^b \right) \right) \right. \\ & \left. \times (M_{ij})^{-1} \left(N_j - \eta \left(\sum_{R=1,2}^{\text{Reac.}} N_j^{\nu,R} + \sum_b^{\text{Bkgnds.}} N_j^b \right) \right)^{\text{T}} \right] + \chi^2_{\text{pulls}} \end{aligned} \tag{A.29}$$

Since pull parameters and pull terms are used to represent some systematics, M_{ij} is given by Eq. A.24. Because the signal normalization is treated as a nearly-free parameter, this statistic has one fewer degree of freedom than χ^2_{RS} of Eq. A.27.

A.6.3 Results

Using the selected set of IBD candidates, and minimizing χ^2_{RS} of Eq. A.27 as the fit statistic, the best fit of the prediction to the data is found at $\sin^2(2\theta_{13}) = 0.086 \pm 0.041$ (stat.) $\pm$ 0.030 (syst.) at $\Delta m^2_{31} = 2.4 \times 10^{-3}$ eV^2, with χ^2_{RS}/d.o.f. = 26.6/18. As previously mentioned, seperate fits were performed with χ^2 statistics which did employ pulled parameters, and statistics which contained all uncertainty contributions in the covariance matrix. The latter approach was used for the main quoted results in [16], as well as for the frequentist

[5]The χ^2 statistic described in Sec. 7.7.2.4 is better designed for achieving this effect.

studies described in Sec. A.6.4. Results for each method are shown in Tables A.8 and A.9. The prompt spectrum at the best-fit pulls values is shown in Figure A.2.

Statistic	Best-Fit $\sin^2(2\theta_{13})$	1σ	1σ Stat.	1σ Syst.	90%CL	χ^2_{bf}/d.o.f.
Rate Only	0.1044	0.0813	0.0296	0.0757	0.1338	0.
Shape Only	0.1078	0.1680	0.1617	0.0458	0.2766	23.85/16
Rate + Shape	0.0856	0.0502	0.0411	0.0297	0.0826	23.71/17

Table A.8: Best-fit values of $\sin^2(2\theta_{13})$ for different fit statistics, with all uncertainties accounted for in the covariance matrix.

	$\sin^2(2\theta_{13})$	FN/SM [%]	^9Li [%]	Energy Scale [value]	$\chi^2_{\rm bf}$/d.o.f.
Rate-Only	0.1043±0.0849	100±46	100±52	0.997±0.007	0.
Rate+Shape	0.0854±0.051	95.2±38	81.5±25.5	0.998±0.005	23.66/17

Table A.9: Best-fit parameters for different fit statistics using pulled parameters and pull terms, for the first Double Chooz analysis.

Further information can be gained from examining the output fit parameters and their output uncertainty intervals in Table 7.19. In the main fit employing χ^2_{RS}, both the $\epsilon_{^9\rm Li}$ and P_E parameters have output uncertainty intervals smaller than the input uncertainties, indicating that they are constrained by the fit to a more strict degree than the initial uncertainty in the pull term alone allows.

A.6.4 Frequentist Confidence Intervals

In addition to the uncertainty intervals on θ_{13} established by the behavior of $\Delta\chi^2_{RS}$, confidence intervals were established for the oscillation analysis using a frequentist methodology, based off the techniques of [152]. The frequentist method utilizes the prediction $N_i^{\rm pred}$ and the covariance matrix M_{ij} representing all sources of uncertainty to simulate an ensemble of pseudoexperiments for each of a set of "true" values of $\sin^2(2\theta_{13})$. Confidence intervals are drawn by comparing the $\Delta\chi^2_{RS}$ value for the true experimental data to the distribution

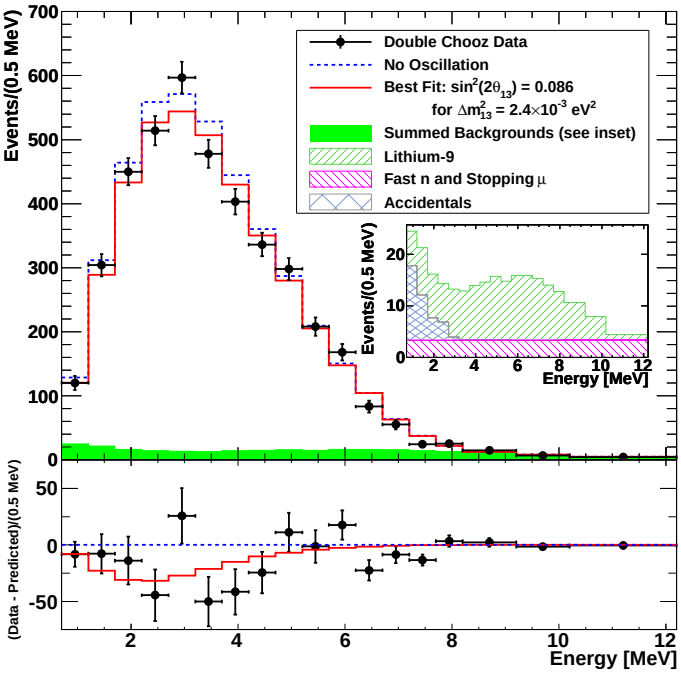

Figure A.2: Measured prompt energy spectrum (data points) superimposed on the expected prompt energy spectrum, including backgrounds (green region), for the no-oscillation (blue dotted curve) and best-fit (red solid curve) at $\sin^2(2\theta_{13}) = 0.086$ and $\Delta m^2_{31} = 2.4 \times 10^{-3}$ eV^2. Inset: stacked spectra of backgrounds. Bottom: differences between data and no-oscillation prediction (data points), and differences between best fit prediction and no-oscillation prediction (red curve). From [16].

of $\Delta\chi^2_{RS}$ values from the pseudoexperiments. This method is described in more detail in Appendix F.

A set of "true" values of $\sin^2(2\theta_{13})$ were tested along the range $0. \leq \sin^2(2\theta_{13}) \leq 0.25$. The allowed region for the data was determined at 90% C.L. to be $0.017 < \sin^2(2\theta_{13}) < 0.16$. Using the test point at $\sin^2(2\theta_{13}) = 0$, the null-oscillation hypothesis was ruled out at 94.6% C.L. It is expected that these 1σ confidence intervals differ slightly from those presented in Section A.6.3, since the frequentist method correctly covers intervals where the behavior of the χ^2 becomes nonlinear close to unphysical regions of parameter space.

A.6.5 Synthesized Quantities: R_{DC}, σ_f^{pred}, and $\sigma_f^{DC,far}$

Three intensive properties may be synthesized from the final fit information and data set. These quantities are useful in comparing the results of Double Chooz to other experimental results.

A.6.5.1 Ratio of Measured vs. Expected Events R_{DC}

The ratio of measured to expected events R_{DC} is straight-forward to calculate.

$$R_{DC} = \frac{(N_{\text{obs}} - N_{\text{bkg}})}{N_{\text{pred}}} \tag{A.30}$$

where N_{obs} is the number of observed events, N_{bkg} is the estimated number of background events (as , and N_{pred} is the number of predicted signal events. A total of 4121 ± 64.195 (statistical, 1.56%) events were observed. The number of predicted events, after processing through the MC and selections, and applying any necessary data-MC corrections, is $N_{\text{pred}} = 4009.96 \pm 108.87$ (systematic, 2.715%). The uncertainties on N_{pred} stem from the data-MC efficiency correction factors (1.1%), the reactor signal uncertainties (1.74%), and the detector covariance matrix (1.77%).

If the *a priori* background rates and uncertainties are used, the species populations for each of the backgrounds are: Lithium-9 (222.88 ± 116.30 events), Correlated Backgrounds (80.9 ± 37.5), and Accidentals (32.00 ± 2.91). Using these rates and uncertainties to calculate N_{bkg}, the result is:

$$R_{DC}^{\text{pre-pulls}} = 0.944 \pm 0.016 \text{ (stat.)} \pm 0.040 \text{ (syst.)} \tag{A.31}$$

The statistical and systematic uncertainties are 1.7% and 3.5% of the quantity, respectively.

If the backgrounds are determined by results of the pulls-based analysis of Sec. A.6.3), the species populations become: Lithium-9 (182.9 ± 48.1 events), Correlated Backgrounds (76.0 ± 30.8), and Accidentals (32.00 ± 2.91). Using these rates and uncertainties, the result is:

$$R_{DC}^{\text{post-pulls}} = 0.955 \pm 0.016 \text{ (stat.)} \pm 0.030 \text{ (syst.)} \tag{A.32}$$

The statistical and systematic uncertainties are 1.68% and 3.14% of the central value, respectively.

A.6.5.2 Predicted Mean Cross-Section per Fission σ_f^{pred}

As described in Sec. 6.3, the predicted mean cross-section per fission σ_f^{pred} (formula given in Eq. 6.11) is derived from knowledge of the antineutrino reference spectra, as well as Double Chooz's choice to anchor this quantity to the Bugey4 measured mean cross-section per fission $\sigma_f^{\text{Bugey4}} = 5.752 \pm 0.081 \times 10^{-43}$ cm^2/fission (1.4% relative error). The fuel composition for the first Double Chooz analysis iteration α_l^{DC}, averaged by baseline for the two Chooz reactors, have values of ^{235}U = 48.78%, ^{238}U = 8.67%, ^{239}Pu = 35.89%, and ^{241}Pu = 6.65%.

As fully described in Sec. 6.3, this quantity is calculated to be:

$$\sigma_f^{pred} = (5.703 \pm 0.108) \times 10^{-43}\text{cm}^2/\text{fission}. \tag{A.33}$$

The correction term versus σ_f^{Bugey4} is then:

$$\sigma_f^{pred} - \sigma_f^{\text{Bugey4}} = (-0.049 \pm 0.067) \times 10^{-43}\text{cm}^2/\text{fission}. \tag{A.34}$$

If the formalism of the Bugey4 anchor point is not used, the predicted mean cross-section per fission increases:

$$\sigma_f^{pred} = (6.209 \pm 0.170) \times 10^{-43}\text{cm}^2/\text{fission}. \tag{A.35}$$

A.6.5.3 Measured Mean Cross-section per Fission $\sigma_f^{DC,far}$

The measured cross-section per fission $\sigma_f^{DC,far}$ is derived from the background-subtracted number of events observed in the detector ($N_{\text{obs}} - N_{\text{bkg}}$), and other geometric, detector, and reactor considerations:

$$\sigma_f^{DC,far} = \frac{4\pi L_{avg}^2 \left(N_{\text{obs}}^{\nu} - N_{\text{bkg}}\right)}{N_p \epsilon N_f^{avg}} \tag{A.36}$$

where L_{avg}^2 is the average reactor-detector baseline-squared, N_p is the number of target protons in the detector, ϵ is the total efficiency of the detector derived from MC simulation, and N_f^{avg} is the baseline-averaged number of fissions in both of the reactors for the detector running period. Values, uncertainties, and sources for these numbers may be found in Tab. A.10. If the *a priori* background rates and uncertainties $N_{\text{bkg}}^{\text{pre-pulls}}$ are used, the result of the calculation is:

$$\sigma_f^{DC,far} = (5.383 \pm 0.091(\text{stat.}) \pm 0.189(\text{syst.})) \times 10^{-43}\text{cm}^2/\text{fission}. \tag{A.37}$$

The statistical and systematic uncertainties are 1.7% and 3.52% of the quantity, respectively.

If instead one uses the background rates and uncertainties as constrained by the pulls approach $N_{\text{bkg}}^{\text{post-pulls}}$ (Sec. A.6.3), the final result becomes:

$$\sigma_f^{DC,far} = (5.447 \pm 0.091(\text{stat.}) \pm 0.120(\text{syst.})) \times 10^{-43}\text{cm}^2/\text{fission}. \tag{A.38}$$

The statistical and systematic uncertainties are 1.7% and 2.2% of the quantity, respectively.

Quantity	**Value**	**Uncertainty**
N_{obs}	4121	1.56% (statistical)
$N_{\text{bkg}}^{\text{pre-pulls}}$	335.68	122.3 (3.64%)
$N_{\text{bkg}}^{\text{post-pulls}}$	290.9	57.19 (1.96%)
L_{avg}^2	$(105206.1)^2\,\text{cm}^2$	$\sqrt{(}0.2\% + 0.2\%) = 0.28\%$
N_p	6.733×10^{29} protons	0.3%
ϵ	$(4009.96/5318.22) = 0.754$	2.08%
N_f^{avg}	1.9264×10^{27}	0.76%

Table A.10: Input parameters to the calculation of the measured cross-section per fission $\sigma_f^{DC,far}$.

Appendix B

CUfits

CUfits is an oscillation analysis toolkit developed in `C++` and `ROOT` with some use of `RooFit`. Its development is managed in the Double Chooz Cluster United SVN Repository, though its use by any members of the collaboration is encouraged. CUfits was conceived and originally developed by Igor Ostrovskiy. CUfits was used to calculate the best-fit oscillation parameters in each of the first two Double Chooz oscillation analyses (described in Sections 7.7 and 7.7, with publication facsimiles in Appendix K). This appendix describes how CUfits is designed, and how it is used to perform an oscillation analysis.

B.1 Design

CUfits is designed around object-oriented programming principles. It is a toolkit of classes and namespaces which may be used in `ROOT` scripts or compiled `C++` programs to perform a variety of analysis tasks. The most common tasks performed are: an oscillation analysis performed by constructing and minimizing a χ^2 goodness-of-fit variable; and a frequentist oscillation analysis where a χ^2 variable is evaluated for a large set of pseudoexperiments in different simulated universes.

In the incarnation used to perform the second Double Chooz oscillation analysis, CUfits consists of a number of classes and two namespaces. Some key classes are:

- `CUhistMC`: A dynamic histogram object, populated with Monte Carlo events from `DataSet` objects with event weights dependent upon fit parameters and the oscillation

model.

- `CUchi2var`: Goodness-of-fit statistic which compares the binned prediction of a `CUhistMC` object with a vector of data bins. The pull terms of a full χ^2 function are not implemented in this object, but are added later by the `CUfcnMaker` utility class.

- `CUfcnMaker`: Utility class that assembles all necessary pieces of a full χ^2 function, in preparation for χ^2 minimization. Takes as input the `CUhistMC` prediction, desired form of the `CUchi2var` (rate-only, rate+shape, etc...), binned observed data, and a set of pull terms with uncertainties.

- `DataSet`: Monte Carlo data set of a particular event type (background type, or neutrino from either reactor). Signal events have an associated true neutrino energy and baseline. All events have an associated initial weight to assist with setting normalizations for different analyses from the same base event set.

- `CUphysics` namespace: Namespace of physics-related functions such as oscillation formulate and physical constants.

- `CUutils` namespace: Catch-all namespace of functions for data pre-processing, statistical methods, and diagnostic output.

Upon compilation of CUfits, these classes and namespaces are made available in a standalone library, for use in `ROOT` scripts or compiled `C++` executables.

The object-oriented nature of CUfits enables portability of inputs between different styles of analysis. For example, careful construction of a `ROOT` macro with CUfits objects allows one to specify at runtime whether to perform a null-oscillation sensitivity study or an "open-box" oscillation measurement with the same set of input predictions for either.Similarly, the code which might have been initially written to construct the CUchi2var and CUhistMC objects for a χ^2 minimization analysis can also be copied-and-pasted into a different program that performs a frequentist analysis with little to no modification.

B.2 Usage

The most common usage of CUfits is to construct an oscillation analysis where a χ^2 goodness-of-fit statistic is constructed, minimized, and its behavior evaluated to establish confidence intervals of the fit parameter being measured. The workflow of such a program is illustrated in Figure B.1, which will be used as a roadmap in the following description of an analysis.

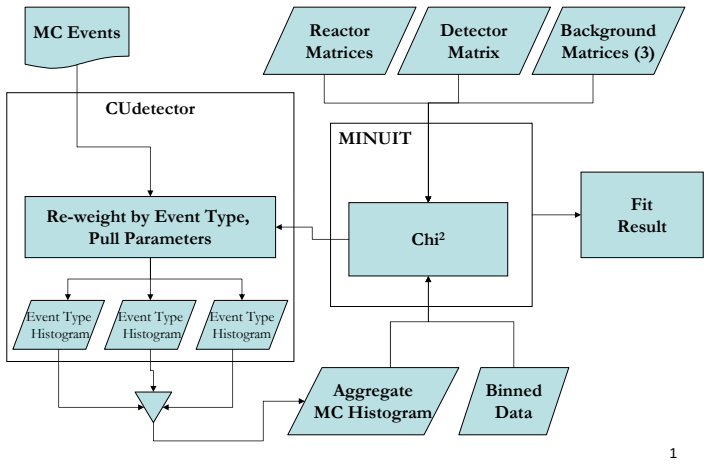

Figure B.1: Block diagram showing the workflow of a CUfits oscillation analysis.

The analysis begins with sets of Monte Carlo events representing the predicted signal and background populations. These are input from `ROOT` trees of a standardized format, and loaded into `DataSet` objects. Each species of event (background type, or origin reactor) is assigned an initial weight to allow specification by the user of the population's normalization. Typically, one `DataSet` is loaded per species per integration period.

All `DataSet` objects are associated with a `CUdetector`/`CUhistMC` object (the class name is dependent upon the version of CUfits; both have similar functionality). The `CUhistMC` dynamically recalculates bin contents as a function of different fit parameters. Among these parameters are the background rates, signal efficiency, and neutrino oscillation parameters;

the user may specify at runtime which fit parameters are to float. The `CUhistMC` object fills each event type into a set of respective histograms; these segregated histograms are useful in recalculating uncertainty contributions on each iteration of the χ^2 minimization. Finally, all event type histograms are summed into an aggregated signal+background prediction histogram. This final histogram is passed to the `CUchi2var` object.

At this point in the fitting program, and according to the user's specifications, the `CUfcnMaker` object has created a χ^2 formula object comprised of a `CUchi2var` object and several formula objects representing the pull terms. In doing so, the `CUfcnMaker` also associates a number of covariance matrices with the `CUchi2var` object. Typically, one covariance matrix is input for each of the following sources of systematic uncertainty: reactor signal; signal efficiency; detector response; and each of the three backgrounds. A statistical contribution to the total covariance matrix is calculated internally by the `CUchi2var` object. The different covariance matrices are stored in fractionalized forms, according to which event types they are associated with. Following the procedures of Section 7.7.1, they are de-fractionalized and effectively re-weighted on each iteration of the minimization as a function of the fit parameters.

Once both the `CUhistMC` bins and covariance matrices are updated, the `CUchi2var` calculates the goodness-of-fit. The input parameters to this calculation are managed by the `MINUIT` [148] numerical minimizer. A number of algorithms are employed in order to iteratively find the minimum of the χ^2 function and evaluate the uncertainty intervals on all parameters. The user may define which error interval definition is to be used, based on how many fit parameters are unconstrained. The `MINUIT` best-fit information is stored at the end of the fitting procedure, for later display according to the user's desired format.

Appendix C

The MultiSim Method

The MultiSim method[1] is a loosely-defined algorithm for translating a set of correlated variables and their uncertainties from one basis to another. In it, uncertainties are propagated directly from a set of data and associated covariance matrix using a formalism built on large numbers of simulations using correlated input parameters (MultiSim). This method has been employed for a number of different uses on the Double Chooz experiment, and has demonstrated versatility.

Subsection C.1 of this appendix will describe the MultiSim method in as general terms as possible, and introduce nomenclature which will be used throughout. The subsequent subsections C.2 through C.4.2 will give detailed accounting and examples of how the MultiSim method was used by the author and other members of the Double Chooz collaboration.

C.1 General Description of MultiSim Method

In the most general terms possible, the purpose of the MultiSim method is to translate correlated uncertainties from one variable basis to another. In doing so, it allows uncertainties to be propagated through complicated models, between different binnings, and between uintuitively-related variables. Operation of a MultiSim method requires three general inputs:

[1]This method was pioneered and named by the MiniBooNE experiment [193], where it was used to propagate uncertainties on pion production data to an expected neutrino flux.

- A set of central-valued input parameters $\vec{a}^{CV} = a_i^{CV}$, where $i = \{1, ..., N_a\}$.
- A description of the correlated uncertainties on the input parameters, typically in the form of a covariance matrix M_{ij}^a.
- A system response model (SRM) which depends upon the input parameters $\vec{a}$ and returns a set of output parameters $\vec{b} = b_u$, where $u = \{1, ..., N_b\}$.

The result of the MultiSim method will be a central-valued set of output parameters $\vec{b}^{CV} = b_u^{CV}$ and a covariance matrix M_{uv}^b representing the correlated uncertainties on the b_u^{CV}.

The MultiSim method operates as follows:

1. The matrix M_{ij}^a is Cholesky-decomposed into a lower-triangular matrix L such that $M^a = L\,(L)^T$. In order for this decomposition to be successful, M^a must be symmetric and positive-definite.
2. For a large number $N_{sim} \approx 10^4$ of "sims", each indexed by m, the following steps are taken:
   (a) Generate a vector of N_a uncorrelated normal random numbers $\vec{\rho}^m = \rho_i^m$, where $i = \{1, ..., N_a\}$.
   (b) Convert the uncorrelated ρ_i^m to a set of correlated, properly-scaled fluctuations δa_i^m of the a_i by left-multiplying: $\delta a_i^m = L_{ij}\rho_j^m$.
   (c) Use the shifted input parameters for the sim $a_i + \delta a_i^m$ as inputs for the SRM, to yield a set of outputs for the sim $\vec{b}^m = b_u^m$.
3. Use the central-value input values a_i^{CV} as input to the SRM to find the central-value output parameters $\vec{b}^{CV} = b_u^{CV}$
4. Find the average covariance matrix by comparing all sets of sim outputs b_u^m against the central value:

$$M_{uv}^b = \frac{1}{N_{sim}} \sum_{m=1}^{N_{sim}} \left(b_u^m - b_u^{CV}\right)\left(b_v^m - b_v^{CV}\right) \tag{C.1}$$

The functionality of the SRM is dependent upon the system being examined. As will be shown in the following sections, the SRM may involve Monte Carlo simulation of a detector

response, re-binning or reweighting of sets of events with pre-determined properties, or some other arbitrary system response. The number of sims N_{sim} required for an acceptable calculation of M^b_{uv} is a function of the number of input parameters N_a, and the desired precision to which the matrix M^b_{uv} is to be known. Here, precision is loosely defined as the degree to which the norm of M^b_{uv} will change between repeated calculations in which each calculation begins with a different random number seed. While no definitive quantitative studies have been carried out, qualitatively a larger N_a warrants a larger N_{sim}, and a smaller threshold on desired precision warrants a larger N_{sim}.

C.2 Applied to Neutrino Reference Spectra

(This application of the MultiSim method was not used in either of the Double Chooz analyses. It is included for completeness of the author's work, and since it is a logical precursor to the method described in Appendix C.3. The majority of this text may also be found as Double Chooz Document #2315.)

During analysis of single-detector Double Chooz data, it is necessary to propagate the uncertainties on the neutrino flux reference spectra to the final anticipated positron spectrum. In doing so, the uncertainties must be propagated through the inverse beta-decay (IBD) cross-section. Also, the binning and energy range of the final measured positron spectrum may differ from that of the initial neutrino spectrum data in order to increase the power of the analysis.

The most current data on antineutrino reference spectra emitted from reactor fuel components are those of Mueller et. al. [13], which are given in bins of 250 keV on a range between 2 and 8 MeV. Historically, these data have been fit to a set of exponential polynomials (one for each fuel component k) of form:

$$S_k(E_\nu, \vec{\alpha}_k) = \exp\left(\sum_{p=1}^{6} \alpha_{pk} E_\nu^{p-1}\right). \tag{C.2}$$

This analytical parametrization is desirable because it can be continuously multiplied against the IBD cross-section to get the predicted spectrum of events in the detector, binned arbitrarily. It has been observed in [97] that using the fit parameters $\vec{\alpha}_k$ to propagate un-

certainties from the converted ILL data to the final event spectrum leads to numerical instabilities. Those authors developed a method for interpolating the covariance matrix of the ILL data which circumvents those instabilities, and is thought to be equivalent to the method presented here.

Use of the MultiSim method avoids the numerical instabilities and binning issues previously described by forgoing the exponential-polynomial fitting entirely. The steps of the procedure are the following, hypothetically to be done for each isotope:

1. Generate a large-statistics data set of N_{evt} random events in E_ν by drawing from Eqn. C.2.

2. Draw from the converted-ILL data covariance matrix (using Cholesky decomposition of Eq. F.1, or otherwise) N_{sim} times and add these values to the converted-ILL central values. These represent N_{sim} "Simulated ILL + Conversion" experiments.

3. Fit a spline $SP(E_\nu, \vec{g}_n)$ to each of the $n = 1, 2, ..., N_{sim}$ simulated results. Here, each spline is defined by parameters $\vec{g}_n$.

4. Use the interpolated spline values to re-weight the data set using the ratio:

$$R_{strict} = \frac{SP(E_\nu, \vec{g}_n)}{S_k(E_\nu, \vec{\alpha}_k)} \tag{C.3}$$

   One might also consider fitting the CV converted-ILL data to a spline $SP(E_\nu, \vec{g}_{CV})$ and reweighting the events using an "approximate" ratio:

$$R_{approx} = \frac{SP(E_\nu, \vec{g}_n)}{SP(E_\nu, \vec{g}_{CV})} \tag{C.4}$$

   The differences between these reweighting schemes, including how the "approximate" method produces more accurate results, will be explored in Section C.2.1. Events having E_ν outside the span of the converted-ILL data are reweighted using the ratio evaluated at the closest available data point. Cross-section and flux considerations make these events have little weight in the final event spectrum.

5. Re-weight each event set using the IBD cross-section $\sigma_{IBD}(E_\nu)$, or another appropriate cross-section.

6. Generate the covariance matrix for the final event spectrum. This is done by producing a histogram of the CV data set N_i^{CV} and histograms of each of the reweighted data sets N_i^n, where i is over bins in E_ν. Note that the binning chosen here can be whatever binning is desired for the analysis at hand. The matrix is formed by taking the differences between each of the "fake data" histograms and the CV data histogram, and averaging:

$$M_{ij} = \frac{1}{N_{sim}} \sum_{n=1}^{N_{sim}} \left(N_i^n - N_i^{CV}\right)\left(N_j^n - N_j^{CV}\right) \tag{C.5}$$

C.2.1 Application & Results

As an example investigation, this method was applied to the ^{235}U reference spectrum from [13]. The original correlation matrix for these data can be found in Fig. C.1. The algorithm was implemented as a ROOT macro, fitting quintic natural splines to the converted-ILL data. A data set of 60,000 events was generated using the exponential-polynomial formalism. After a number of trials, N_{sim} =20,000 was selected as a sufficient number of MultiSims to produce a stable matrix.

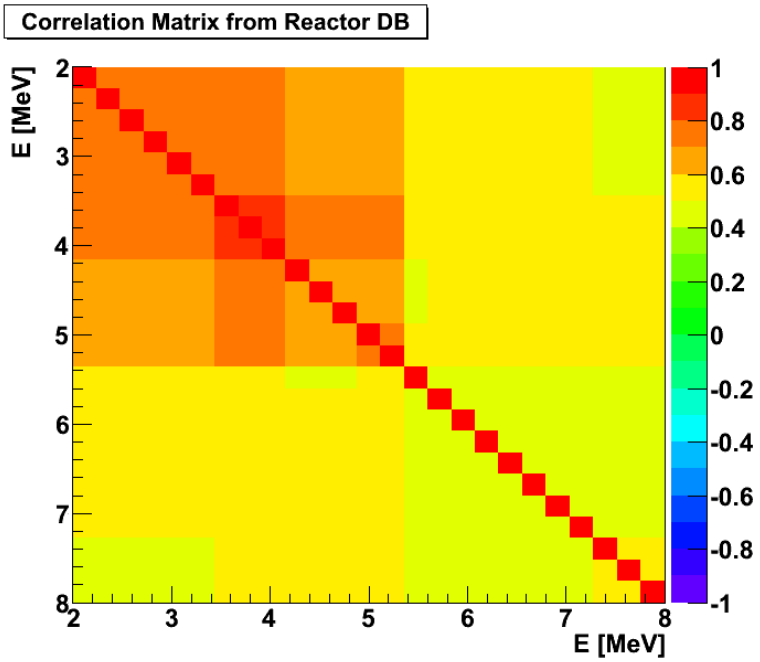

Figure C.1: The correlation matrix for the ^{235}U reference spectrum produced in [13].

Results for a number of bins and energy range equal to the original converted-ILL data can be found as correlation matrices in Figures C.2 and C.3. In comparison to the original correlation matrix, the approximate method's results are qualitatively closer than those of the strict method. In particular, the strict method introduces anti-correlations at higher energy values. These are thought to be artifacts stemming from the residues between the converted-ILL data points and the exponential-polynomial fit. While the approximate matrix is qualitatively more similar to the original, it is not an exact propagation, as can be seen in Figure C.4.

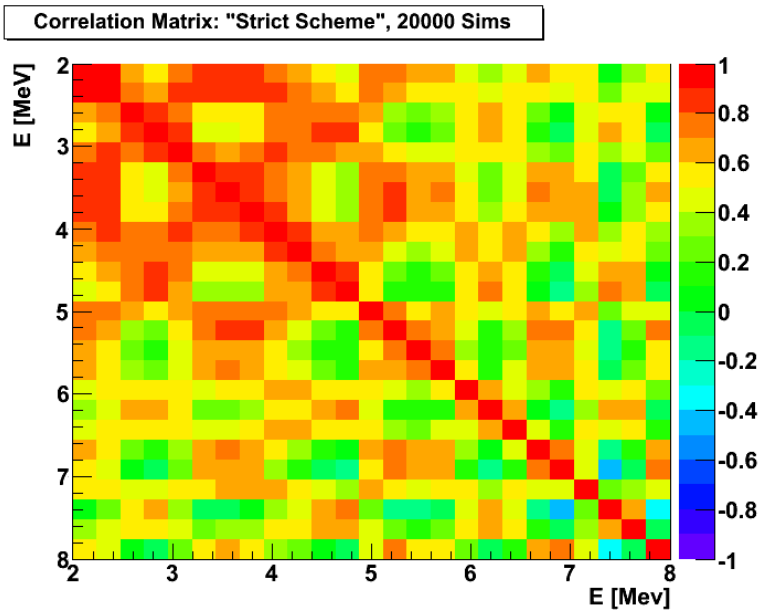

Figure C.2: The correlation matrix produced by the MultiSim method using R_{strict}. The binning and energy range shown here is identical to that of the original converted-ILL data, shown in Figure C.1. Of particular note are the anomalous anti-correlations at high energies.

As previously described, this method allows the user to choose any binning and energy limits on the final covariance matrix. Figure C.5 shows results from the approximate method being applied over the extended 1.75-10 MeV energy range, into a total of 200 bins. For this data set, an increased number of 200,000 events were generated, in order ensure events at high energies (> 9 MeV).

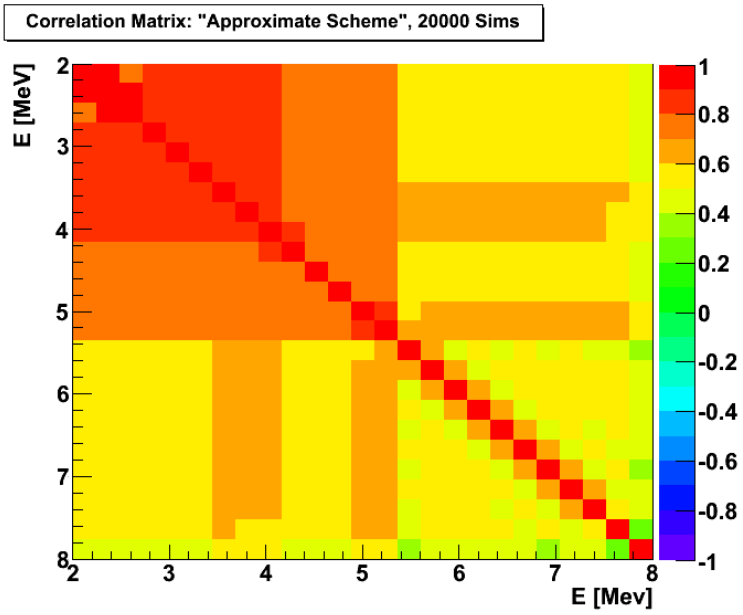

Figure C.3: The correlation matrix produced by the MultiSim method using R_{approx}. The binning and energy range shown here is identical to that of the original converted-ILL data, shown in Figure C.1.

C.2.2 Summary

This MultiSim-based method may be useful for propagating uncertainties on the antineutrino reference spectra to the expected event spectrum, as these investigations have demonstrated. While some unphysical anti-correlations appear when the method is executed using R_{strict}, results using R_{approx} are close to the original correlation matrix. This method allows uncertainties to be propagated to a final expected spectrum with an arbitrary energy range and binning.

C.3 Applied to Reactor Uncertainties

Following the formalism of Chapter 6, it is straight-forward to calculate the expected spectrum N_a of neutrino interactions binned in neutrino energy $E_{\bar{\nu}}$, and accompanying covariance matrix M_{ab}^{rxt}, where the index a runs over the 72 bins in $E_{\bar{\nu}}$ and integration period (using the notation of Sections 7.3.1.1 and 7.3.3). In practice, the final fit is performed

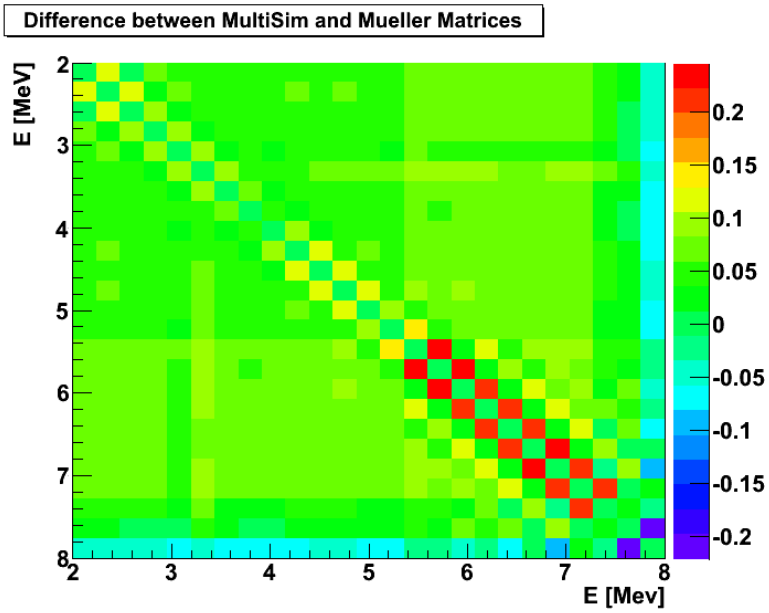

Figure C.4: The difference in elements between the "approximate" MultiSim method correlation matrix (shown in Fig. C.3) and the original reference spectrum correlation matrix (shown in Fig. C.1).

using events binned in reconstructed energy $E_{\rm vis}$, as described in Section 7.7. Thus, it is necessary to use the MultiSim method to translate $M^{\rm rxt}_{ab}$ to a matrix binned in $E_{\rm vis}$.

The System Response Model in this application is a set of selected signal Monte Carlo events which have as data members both the true neutrino energy $E_{\bar{\nu}}$ and the reconstructed energy $E_{\rm vis}$. The inputs are the initial neutrino spectrum N_a binned in $E_{\bar{\nu}}$, and the accompanying covariance matrix $M^{\rm rxt}_{ab}$. The desired output is a new matrix $M^{\rm rxt}_{ij}$ where i and j run over 36 bins in $E_{\rm vis}$, to accompany the signal prediction $N^{{\rm exp},R}_i$. Use of the MultiSim method proceeds in a very similar manner to the implementation described in Section C.2. The method described below has been implemented as the `RTMultiSim` class, part of the `DCRxtrTools` suite of the `DOGS` Double Chooz Offline Software package.

The simulations are generated by Cholesky decomposing[2] the input $M^{\rm rxt}_{ab}$ (*a la* Eq. F.1)

[2]In practice, the matrix $M^{\rm rxt}_{ab}$ does not always decompose on the first try, due to its form being nearly not positive-definite. To ensure positive-definiteness, it is often necessary to add small ($\sim 10^{-8} \times N_a$) augmentations to the diagonal of the matrix. These additions negligibly affect the norm of the matrix and

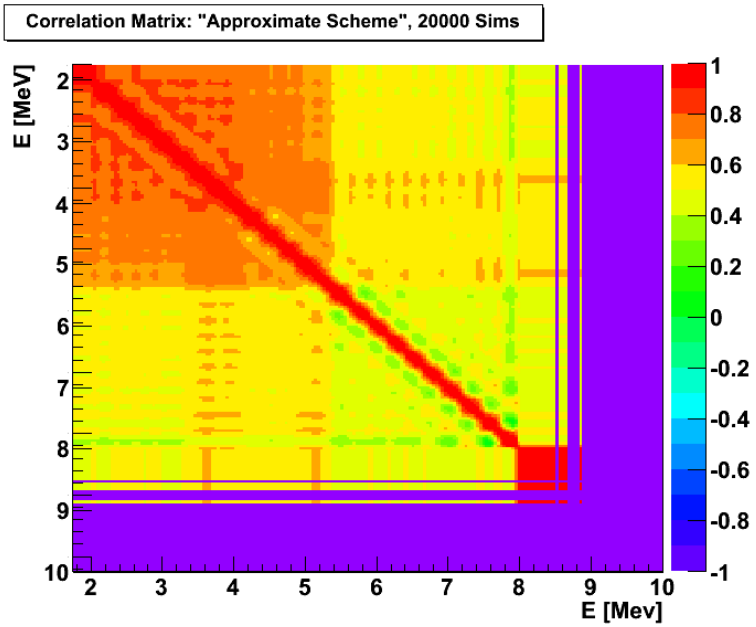

Figure C.5: The correlation matrix produced by the MultiSim method using R_{approx} with an extended energy range and sharpened binning. Purple indicates regions where no events were present in the original data set. Note the regions of strong correlation at high and low energies, due to events in those regions having their reweighting values tied to that of the closest existing bin.

and creating a set of random deviations δN_a of the input spectrum N_a. The deviated spectrum $N_a + \delta N_a$ is then fit to a spline. An energy-dependent ratio of this spline to a spline fit of the central-valued N_a is then used as the basis for re-weighting the Monte Carlo events, similar to the "approximate" scheme described in Section C.2. The output reweighted bins $\{N_i\}_u$ from each sim $u \in [1, ..., N_{sims}]$ are them compared to the output bins of central-value spectrum N_i^{CV} and the average covariance matrix M_{ij}^{rxt} is calculated:

$$M_{ij}^{\mathrm{rxt}} = \frac{1}{N_{sims}} \sum_{u=1}^{N_{sims}} \left(\{N_i\}_u - N_i^{\mathrm{CV}}\right) \times \left(\{N_j\}_u - N_j^{\mathrm{CV}}\right) \times \tag{C.6}$$

The resulting M_{ij}^{rxt} is 36×36 in dimension to cover both integration periods, binned in E_{reco}.

the behavior of the random throws, but ensure that the Cholesky decomposition can proceed.

Since the the number of inputs is large (length($\vec{a}$) = 72), a large N_{sims} is required to achieve good precision in the norm of M_{ij}^{rxt}. As shown in Figure C.6, sets of simulations beginning with different random number seeds can take very different norm values. It is not until $N_{sims} \approx 10^5$ that the norm of the matrix is dependable to four or five significant digits. Achieving this level of precision requires significant computation, so optimization of the MultiSim algorithm implementation and use of parallel processing is desirable.

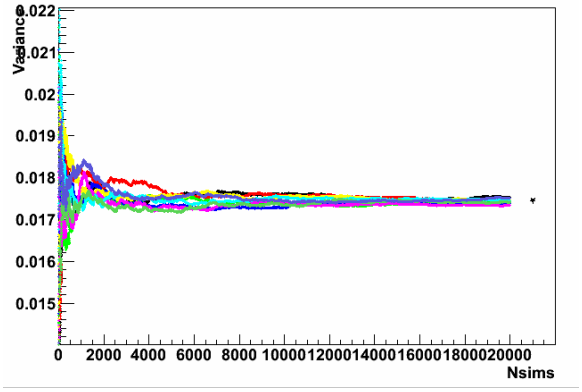

Figure C.6: Variance of the predicted IBD rate, as a fraction of the total rate, as a function of the number of simulations N_{sims} which are averaged to construct the matrix. Different colored lines represent sets of simulations begun with different random number seeds. Star is the final variance when all sets of simulations are averaged together. The different sets of simulations do converge asymptotically towards a final value, though the rate of convergence gets progressively slower.

C.4 Applied to Energy Scale Uncertainties

The MultiSim method was used in both the first and second Double Chooz analysis iterations to propagate uncertainties on the energy scale to the final oscillation fit, as mentioned in Sec. A.5.2 and 7.5.5, respectively.

Section C.4.1 will describe how it was used to propagate the uncertainties on six optical model parameters of the Monte Carlo to a final energy scale matrix. Section C.4.2 will describe how the method was used to propagate the uncertainty on a single classical energy scale parameter, with some commentary on how the method behaves when treating energy

nonlinearities.

C.4.1 First Double Chooz Publication

During the first Double Chooz analysis iteration, the MultiSim method was employed to propagate uncertainties on the fit parameters of the phenomenological detector response correction functions to the final reconstructed IBD candidate spectrum, as mentioned in Section A.5.2. The MultiSim method was used to propagate uncertainties on phenomenological fits of data/MC discrepancies to a final covariance matrix relating the bins of the final fit.

Recall from Section A.5that the energy scale for the first analysis was dependent on two correction functions Corr_1 and Corr_2, representing corrections on the spatial and energy-dependent components of the detector response, dependent upon six parameters $\vec{a}$:

$$\mathrm{Corr}_1\left(\mathrm{CaloPE}, a_0, a_1, a_2\right) = a_0 \log\left(\mathrm{CaloPE} - a_1\right) + a_2 \tag{C.7}$$

$$\mathrm{Corr}_2\left(z, a_3, a_4, a_5\right) = a_3 + z a_4 + z^2 a_5 \tag{C.8}$$

$$\begin{aligned}\vec{a} = \{&0.0286966,\ 56.1478,\ 0.842321,\\ &0.998201,\ -9.51483\times10^{-6},\ -3.25985\times10^{-8}\}\end{aligned} \tag{C.9}$$

The dominant uncertainties on the energy scale arise from the six fit parameters $\vec{a}$. These are related by a 6×6 covariance matrix $M_{\vec{a}}$, which is block-diagonal with two 3×3 blocks. The $\vec{a}$ and $M_{\vec{a}}$ comprise the input parameters and uncertainty description. The System Response Model is comprised of Monte Carlo events with associated in reconstructed energies E_{reco}, Corr_1 and Corr_2, and the binning that they are filled into.

Sets of $u = [1, ..., U]$ random Gaussian throws $\{\vec{a}\}_u$ are made on the energy scale parameters $\vec{a}$ as drawn from $M_{\vec{a}}$. From these draws, the energies of each event is modified and rebinned. The correlated-random bin deviations $\{\delta N_i^{\mathrm{pred}}\}_u = \{N_i^{\mathrm{pred}}\}_u - \{N_i^{\mathrm{pred}}\}_{\vec{a}}$ are used to construct an average covariance matrix M_{ij}^{escale}:

$$M_{ij}^{\mathrm{escale}} = \frac{1}{U}\sum_{u=1}^{U}\left(\{\delta N_i^{\mathrm{pred}}\}_u \times \{\delta N_j^{\mathrm{pred}}\}_u\right) \tag{C.10}$$

The resulting M_{ij}^{escale} is 18-by-18 in dimension, binned in E_{reco}.

C.4.2 Second Double Chooz Publication

During the second Double Chooz analysis iteration, initial treatment of the energy scale uncertainty was prescribed as an uncertainty interval on a classical energy scale variable P_E (see Eq. 7.17 of Section 7.5.5). One might recall that this scaling is only applied to events whose energies E^0_{vis} are determined by the Monte Carlo reconstruction, and not by measurement in data (*to wit*, IBD signal events and ^{9}Li events, but not fast neutrons/stopping muons or accidentals). As tabulated in Table 7.10, the total uncertainty was evaluated as $\sigma_{P_E}/P_E = 1.13\%$.

The MultiSim method was used to convert deviations on the single energy scale parameter P_E to a covariance matrix. While the results of using a MultiSim are comparable to using an average of $\pm 1\sigma$ shifts of this parameter (see Figure 7.22), the MultiSim method was chosen on account of its ability to include nonlinear behaviors of the bins during its averaging process.

The MultiSim method for generating a matrix based on P_E proceeded as follows. In the nomenclature of Section C.1, the central-valued input parameter and uncertainty interval was $P_E = 1.0000 \pm 0.0113$. Since there is only one parameter in this model, there are no correlations of input parameters to be considered. The System Response Model is comprised of Monte Carlo events with associated in reconstructed energies E_{vis}, and the binning that they are filled into. We denote the binning with P_E at its central value as $\{N_i^{\text{pred}}\}_{P_E=1}$; these are the output variables of the SRM. The MultiSim method in this usage case is meant to address the correlations between the output variables due to the nature of the binned event species. This usage is similar to that of the reactor uncertainty propagation described in Section C.3 in that the MC events themselves are used as the backbone of the SRM.

Sets of $u = [1, ..., U]$ random Gaussian throws $\{P_E\}_u$ are made on the energy scale parameter P_E, producing sets of bin deviations $\{\delta N_i^{\text{pred}}\}_u = \{N_i^{\text{pred}}\}_u - \{N_i^{\text{pred}}\}_{P_E=1}$. After a sufficient number of simulations, the $\{\delta N_i^{\text{pred}}\}_u$ are used to construct an average covariance matrix M_{ij}^{escale}:

$$M_{ij}^{\text{escale}} = \frac{1}{U} \sum_{u=1}^{U} \left(\{\delta N_i^{\text{pred}}\}_u \times \{\delta N_j^{\text{pred}}\}_u \right). \tag{C.11}$$

In the case of DC2ndPub, the resulting M_{ij}^{escale} is 36×36 in dimension, to span both

integration periods.

Since the model is determined by only a single input parameter, a relatively low number of sims ($\sim 10^3$) is needed to accurately determine M_{ij}^{escale}. However, it is notable that this method does not address deviations which might be caused by nonlinearities in the energy scale, as the method of Section C.4.1 does. If such nonlinearities are included in the simulation by the addition of more parameters, it becomes impossible to deconstruct the matrix into components and bin shifts for use in association with pull terms, as described in Section 7.5.5.

Appendix D

DCRxtrTools Neutrino Event Generator & Uncertainty Calculator

`DCRxtrTools` is a toolkit for neutrino event generation and signal uncertainty calculation, written in `C++` with `ROOT`. `DCRxtrTools` provides a direct interface between the Double Chooz Reactor Database, Detector Database, GLG4sim detector geometry, and the DOGS Monte Carlo format. The goal of this appendix[1] is to explain how `DCRxtrTools` calculates an expected neutrino flux, generates Monte Carlo events, and propagates uncertainties into a covariance matrix binned in E_ν^{true}. `DCRxtrTools`was developed with the specific purpose of enabling the Rate+Shape fit used in each of the Double Chooz oscillation analysis iterations, where rigorous treatment of correlated signal uncertainties is necessary.

D.1 Description of Operation

This section provides an overview of `DCRxtrTools`' operation, focusing on inputs, outputs, and general strategy. Input data to `DCRxtrTools` are described in Sec. D.1.1, output prod-

[1]Much of this appendix originally appeared as Double Chooz Tech Note co-authored with Mike Shaevitz, David Lhuillier, and Camillo Mariani.

ucts are described in Sec. D.1.2, and an overview of the calculation methodology is covered in Sec. D.1.3.

D.1.1 Inputs

Inputs to `DCRxtrTools` can be broken into the following categories: detector-related parameters; reactor-related parameters; antineutrino interaction type; uncertainty calculation method; and integration period run sorting rules. Each are described in the following subsections.

D.1.1.1 Detector Parameters

Relevant detector parameters taken as input by `DCRxtrTools` include:

- Run number, start time and duration, for all physics runs, as accessed from the a MySQL database. Run durations are calculated during Common Trunk data processing.
- Detector geometry, taken from DCGLG4sim via a user-generated GDML file.
- Specification of macroscopic detector parameters, input via an ASCII file.
  - Detector position and orientation in the world frame, with respect to the reactors.
  - Which detector sub-volumes should be considered when generating events.
  - Detector efficiency, and uncertainty on efficiency.
  - Uncertainty on the number of target particles (protons, in the case of IBD interactions).
- A list of run numbers to be processed, input via an ASCII file.

D.1.1.2 Reactor Parameters

Reactor-related parameters taken as input by `DCRxtrTools` include:

- Fission Rates for the four principal reactor fuel nuclides. These are generated by the Reactor Working Group using MURE or DRAGON, and stored on a MySQL database.

- Antineutrino reference spectra for each of the principal fuel nuclides. These are accessed from the same database as the fission rates.
- Specification of macroscopic reactor parameters, input via an ASCII file:
  - Reactor position in the world frame, with respect to the detectors.
  - Reactor dimensions (approximated as a rectangular prism).
  - Reactor power uncertainty.
  - Uncertainty on the fission rates/fuel load out.
- EXALT power measurement data, accessed from the `dcreactordb`.

Reference Spectra

As described in Section 6.1.2, reference spectra for the antineutrino spectra $S_k(E)$ emitted by the four principal fuel nuclides k are sourced from [96] (for $k =^{235}\mathrm{U},^{239}\mathrm{Pu},^{241}\mathrm{Pu}$) and [13] (for $k =^{238}\mathrm{U}$). As these data were synthesized from ILL data with a short, finite irradiation time, off-equilibrium effects are applied following [13] presuming an approximate 100 day irradiation time. Due to the finite binning and limited energy range of the reference spectra, interpolation and extrapolation is required to cover the full energy region of interest (see section D.4 for more details).

The configuration of `DCRxtrTools` may be changed to use any set of reference spectra available on the Reactor Group database. This includes all spectra calculated in Ref. [13], Ref. [96], or the original reference spectra of Refs. [14, 132, 133].

Fission Rates

Calculation of the α_k^R (and to some extent, P_{th}^R) requires knowing the fission rates f_k of the four principal fuel nuclides k in the reactor. These data are generated external to `DCRxtrTools` the Reactor Working Group using either of the core simulation codes MURE or DRAGON. Due to the finite time step resolution of these simulation codes, `DCRxtrTools` rescales the simulated fission rates f_k^{sim} to effective fission rates f_k^{eff} based on additional data of short-timescale power measurements from the EXALT database (details in Sec. D.5). To

this extent, the f_k^{eff}, α_k^R and P_{th}^R are all presumed to be constant over periods of time $\lesssim 1$ hour.

D.1.1.3 Interaction & Cross-Section

The cross-section is programmed as a class deriving from the `RTInteraction` virtual class. When programmed, the interaction class must have a function whose return value is the cross section in units of cm^2 as a function of E_ν^{true} in MeV. For more detailed discussion of the cross-section used for the Double Chooz publications, see Section 6.1.2.

At the moment, the products of the neutrino interaction are limited to the positron and neutron which come from an IBD interaction, due to limitations in the output data structure. However, it is straight-forward to extend the data format to allow for general particle types to be output, and the `RTInteraction` base class has no such constraints.

D.1.1.4 Calculation Process

The Calculation Process is the implementation of event rate calculations and uncertainty propagation. It is defined as a class which inherits from the `RTCalcProcess` virtual class, to allow run time switching between different calculation processes without recompilation. Two such classes have been implemented: `RTMultiB4`, a prediction anchored to the Bugey4 measurement that also accommodates multiple integration periods (see Section; and `RTCPILL`, an prediction anchored to the raw normalizations of the ILL reference spectra.

D.1.1.5 Integration Period Sorting Rules

If multiple data integration periods are to be used, a set of rules for sorting detector runs must be specified. This is done by defining classes which derive from an `RTRunSorter` virtual base class. The rule set for sorting runs is user-defined, and may involve any information from the detector or reactor objects. Examples of sorting rules have depended on reactor power as in the case of the second Double Chooz analysis detailed in Section 7.6, or or sidereal time as in the case of the analysis published in [138].

D.1.2 Outputs

The principal outputs of `DCRxtrTools` are:

- A set of Monte Carlo event files, with each file representing the set of events expected during a particular run of the detector. Each file is tagged with the corresponding run number.
- A file containing the aggregate mean expected event distribution (binned in E_ν^{true}) and a covariance matrix representing the total uncertainty on that distribution (in the same binning).

The covariance matrix may optionally be split into three component matrices, following the prescription of Appendix H. Conversion of the covariance matrix from a binning in E_ν^{true} to one in $E_{e^+}^{\text{reco}}$ may be carried out using the methods described in section D.3.1.

Additionally, some simulation input parameters and diagnostic summaries are displayed in the terminal output of the program. This includes summaries of each component of the covariance matrix generated, in most cases.

D.1.3 General Process

Before beginning event generation, `DCRxtrTools` downloads and caches any data which must be acquired from databases, and performs and necessary pre-processing. This involves re-scaling fission rates based on EXALT power data (see Section D.5), and re-binning the neutrino reference spectra (see Section D.4) and cross-section to the user-specified binning.

The primary of `DCRxtrTools`'s calculations is to merge the periods of time defined by physics data-taking runs of the detector with those where the reactor is producing a flux. This detector run-centric approach is motivated by the known time-dependence of various detector parameters, and that they are typically cataloged by run number.

For each detector run, the following steps are taken:

1. Check each reactor to see if it was producing an antineutrino flux during the run time in question. If so, execute the next two steps for each of the reactors.

2. Calculate the expected number of neutrinos during the run, and create the appropriate number of events (for more detail, see section D.2).

3. Store any contributions to the total uncertainty by passing relevant information to the `RTCalcProcess`-derived class (for more detail, see section D.3).

4. Save all generated events as `NuGenThInfo` objects into a DOGS-format `.root` file, labeled by detector run number.

Following the processing of all runs for the detector in question, a final covariance matrix and mean event distribution is saved into a separate file (see section D.3).

D.2 Monte Carlo Event Generation

Monte Carlo event generation is dependent upon several combined factors: detector run time and number of target particles; the antineutrino flux emitted by the reactor during the detector run time; the defined interaction cross-section; the defined interaction product particles. Generally, the process may be described as having the following steps:

1. The time of the detector run is accessed from the `RTDetector` object.

2. Using the run time, a time-dependent set of fission rates and a set of reference spectra are generated from the `RTReactor` object.

3. The continuous form of the cross-section is accessed from the `RTInteraction` object.

4. All necessary information is passed by the `RTCalcProcess::CreateNus()` virtual method to the defined calculation process class.

5. The reference spectra are multiplied against the cross-section, with the resulting product used to create a histogram binned in E_ν^{true}.

6. The `CreateNus()` function calculates the expected number of events for the detector run. Event times and parent nuclides are generated by random pulls from the fission rates histogram.

7. The parent nuclide information of each event is then used to generate event energies by random pulls from the proper reference spectra.

8. Product particles of the antineutrino interaction in the detector are generated based on E_ν^{true} and the direction vector drawn between the reactor and detector.

9. This process is repeated for each reactor, and the events from both reactors are sorted by time stamp and stored into a single MC event file.

Once the total expected rate of antineutrino events N_ν^{exp} is known, production neutrino events becomes a matter of generating random numbers. First, an integer number of events to generate N_ν^{rand} is pulled by using N_ν^{exp} as the argument of a Poissonian pull. The events are then generated by the following process:

1. A histogram of the mean fission rates is created, binned by isotope and time for the duration of the detector run.

2. The bins of each isotope k are further weighted by the mean cross-section per fission of that isotope, $\langle\sigma_f\rangle_k$.

3. Random draws from this histogram using the native `TH2::Random()` produce an isotope index k and a time stamp for an event.

4. Based on the isotope index, another random pull is made from the corresponding $\langle\sigma_f\rangle_k^i$ to yield a neutrino energy for the event.

5. A random creation point is generated inside the reactor "core", using a flat 3-dimensional distribution (fission barycenter effects are considered negligible).

6. An interaction vertex is randomly generated inside the detector, with the position draws weighted by a proton density map of the relevant detector sub-volumes.

7. Using the neutrino energy and the vector connecting the creation and interaction points, the kinematic quantities of the resulting neutron and positron are calculated. A rotation is applied to the neutron and positron momentum vectors, to properly orient them with the `DCGLG4sim` coordinate system.

Steps 3 through 7 are repeated until N_ν^{rand} events have been generated. These events are stored, and the process may be repeated for any other reactors which were producing neutrinos during the particular detector run.

D.3 Uncertainty Propagation

The structure of `DCRxtrTools` allows for different uncertainty-handling methods to be interchanged via the `RTCalcProcess` virtual class. Uncertainty information is passed on a by-run basis to the defined `RTCalcProcess`-derived class via the `RTCalcProcess::AddRunInfo()` pure virtual method. After all runs have been considered, a final covariance matrix and mean expected event histogram is generated via the `RTCalcProcess::CreateFinalMatrix()` pure virtual method.

The Double Chooz collaboration has decided to use the Bugey4 measurement of neutrino rate as an anchor point on the normalization of the neutrino flux. This methodology is described in Section 6.3, and implemented in `DCRxtrTools` as the `RTCPMultiB4` class. A prediction of the neutrino flux and uncertainties without this anchor point (as described in Section 6.4.2) is also implemented as the `RTCPILL` class.

D.3.1 Propagation from $E_\nu^{\mathbf{true}}$ to $E_{e^+}^{\mathbf{reco}}$

The covariance matrix and mean expected spectrum calculated by `DCRxtrTools` are binned in E_ν^{true}. In practice, analyses will likely be carried out by fitting event distributions in a reconstructed energy: either $E_{e^+}^{\text{reco}}$ or E_ν^{reco}. For this reasons it is then necessary to apply further processing to the matrix M_{ij}^{tot} in order to provide a fit-ready matrix. This conversion is carried out using a MultiSim method as described in Section C.3.

D.4 Rebinning of Reference Spectra and Uncertainties

Current antineutrino reference spectra for the principal reactor fuel nuclides ([13, 96]) are typically binned in E_ν^{true} over the energy range between 2 and 8 MeV, with bin widths on the order of 250 keV. To allow flexibility in choosing a binning for final analyses, it is

necessary to develop techniques for rebinning these reverence spectra and their associated uncertainties. In this section,we describe those methods implemented in `DCRxtrTools`.

It is worthwhile to note that the use of a MultiSim method to convert the signal covariance matrix from E_ν^{true} to $E_{e^+}^{\text{reco}}$ as described in Section C.3 renders these techniques superfluous. The binning of the neutrino prediction can be chosen to match that of the reference spectra, thereby avoiding any potential biases that arise from these methods, since the MultiSim method can convert the resulting matrix to an arbitrary binning in $E_{e^+}^{\text{reco}}$.

D.4.1 Rebinning Reference Spectra

For newly-defined bins within the range of energies covered by the data of [13] and [96], we make use of linear interpolation at the center of the new bin to establish its value. This is implemented by converting the reference spectrum data to a `TH1D` histogram and utilizing the `TH1::Interpolate()` method. It is recognized that since the reference spectrum data represent mean values within their bins, this approach is not strictly rigorous. It is thought that any biases contributed by its use are on the sub-percent level, though alternative approaches are being investigated.

Since the reference spectra are limited in energy range to between 2 and 8 MeV, we are forced to use the polynomial fits to these data in order to extrapolate over the full region of interest for reactor studies (1.8 to >9 MeV). If a bin of the desired binning exists outside of the region where reference spectrum data exist, we integrate the fit polynomial over the bin's energy range and divide by the bin width, setting this mean value to be the content of that bin.

D.4.2 Rebinning Covariance Matrices

Following rebinning of the reference spectra, it is also necessary to rebin the accompanying covariance matrix that relates them. The technique implemented in `DCRxtrTools` utilizes the prescription of [97]. The covariance matrix is first converted to a correlation matrix. This correlation matrix is converted to a `TH2D` histogram object, and bilinear interpolation via the `TH2::Interpolate()` method is used to establish the bin correlations at the center of each new bin. Once complete, a histogram of the original diagonal variances is

interpolated and used to convert the correlation matrix back to a covariance matrix. Other methods have been investigated for rebinning uncertainty matrices (*e.g.* as described in Section C.2) but this method of interpolation is attractive for its ease of implementation and low computational requirements.

In energy regimes where interpolation is needed (as described in section D.4.1), each bin is assigned a 20% uncertainty which is fully-correlated with all other bins in that interpolated region. This is conservative, while at the same time usually applies to regions of the spectrum where few neutrino events take place. The one exception is typically the lowest-energy bin above the IBD threshold, which is moderately populated and highly sensitive to oscillation effects.

D.5 Power-Scaling of Fission Rates

Properly simulating the antineutrino flux emitted by a reactor requires knowledge of the rate of fissions of the four principle fuel nuclides. These rates are produced via simulation, whether by the deterministic code DRAGON or the Monte Carlo-based simulation MURE. The reactor power tends to act as an overall normalization on the four fission rates and can evolve quickly in time (∼15 minute timescales). The abundance of each fission species α_k^R in the reactor R (see Eq. 6.2) tend to evolve on a slower timescale, showing significant changes on the timescale of days.

Due to computational constraints, it is impractical to run iterative reactor simulations with time steps on the same timescale as power evolutions. It is sufficient to run the simulations with time steps on the same order as fission species abundance changes if the fission rates produced can later be re-scaled based on the short timescale power measurements. This is the approach taken by `DCRxtrTools` when loading fission rates and EXALT power data from the Reactor Working Group Database.

The algorithm behaves according to the following steps:

1. Fission rates from simulation with 24- or 48-hour time steps are downloaded from the reactor database. This provides four mean fission rates f_k^{sim} for the time step, as well as the mean simulated power for the time step P_{th}^{sim}.

2. EXALT power data with 15-minute to 12-hour time steps are downloaded from the reactor database. This provides measured values of the thermal power P_{th}^{meas}.

3. The timestamps of each data set are compared: data points falling outside of the intersection of the time ranges are discarded, to improve performance.

4. For each short-timescale step of the EXALT data, the simultaneous f_k^{sim} and P_{th}^{sim} are found by timestamp comparison. In cases where the EXALT time step straddles the boundary of two simulation time steps, the f_k^{sim} and P_{th}^{sim} corresponding to the beginning of the EXALT time step are used.

5. Effective fission rates f_k^{eff} are calculated:

$$f_k^{\text{eff}} = \frac{P_{th}^{\text{meas}}}{P_{th}^{\text{sim}}} f_k^{\text{sim}} \tag{D.1}$$

6. The effective fission rates f_k^{eff} are loaded into a `TH2` histogram, binned in nuclide and time according to the EXALT time steps, for use in event generation (see sec. D.2) and uncertainty propagation (see sec. D.3).

Appendix E

OV Online Monitor

The OV Online Monitor (OV Monitor) was developed in C++ with use of ROOT and the Double Chooz Online Monitor Framework [126] libraries. Its design goal is to provide real-time visualizations of Outer Veto status in a manner that is useful to both shifters and experts, and automatically scalable to different OV configurations including the Near Detector. The OV Monitor is designed to independently read the binary data stream of the OVDAQ in parallel to the EventBuilder, with data also coming from the OV High Voltage system. The monitor has been in standard use since the Outer Veto electronics were in a test stand configuration at Nevis Labs, through OV commissioning, and in day-to-day operation at the Double Chooz site.

All code associated with the OV Monitor are are stored in the DC Online SVN Repository, under the `$DCONLINE_PATH/DCOV/OVMonitor` directory.

E.1 Architecture

The OV Monitor rusn as a standalone process on a machine with disk access to the OV DAQ data stream, and the OV HV Controller Card. It then communicates visual data objects via TCP sockets with the Double Chooz Online Monitor Server, which acts as depot for these data objects and serves them to remote visualization clients. This data flow is illustrated in the middle pane of Figure E.1. The rest of this section will focus on the internal architecture of the OV Monitor, leaving descriptions of the Online Monitor Framework to Figure E.1,

its citations, and [126].

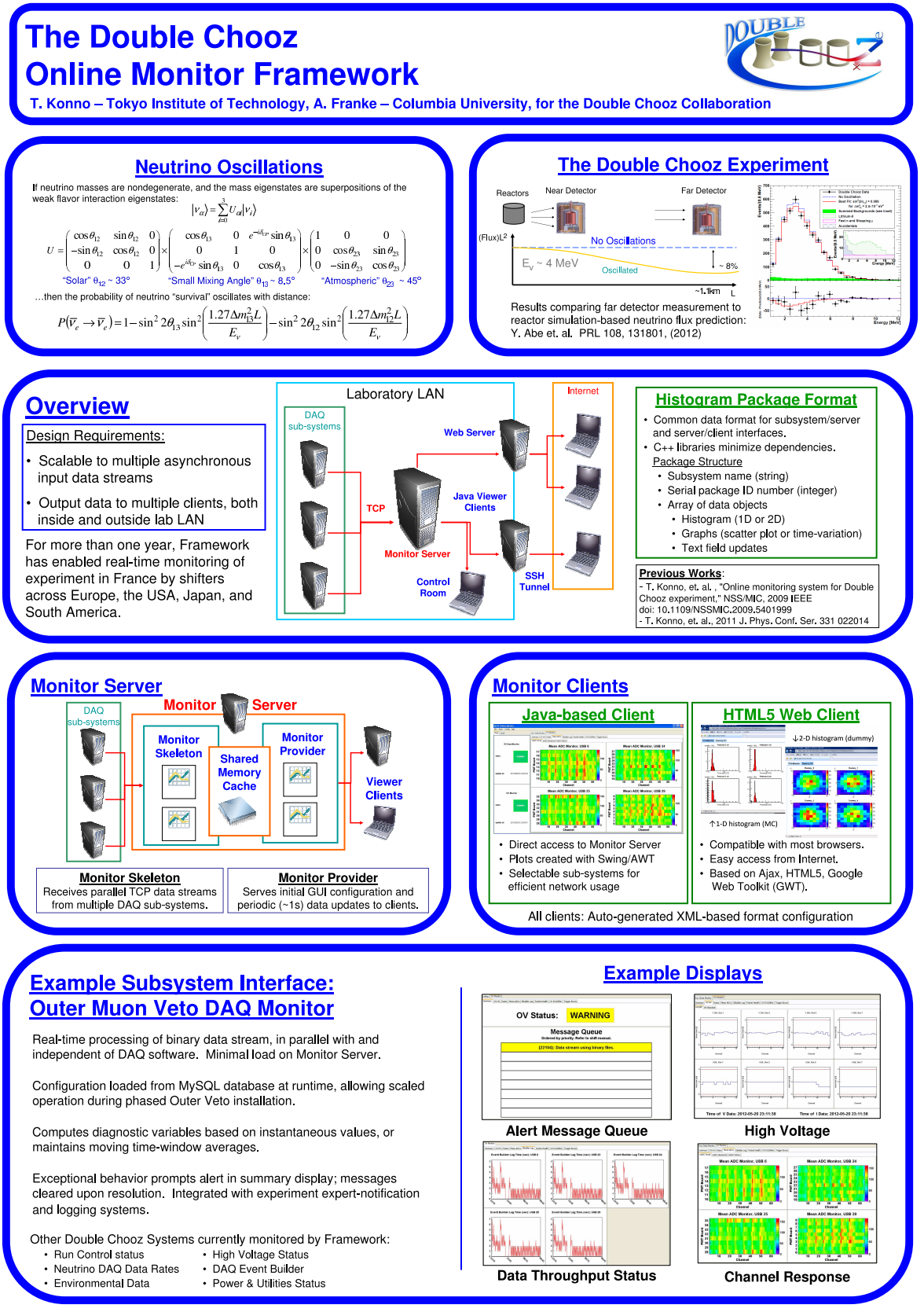

Figure E.1: Poster describing the OV Online Monitor, and Double Chooz Monitor Framework, presented at the Computing in High Energy Physics (CHEP) 2012 conference, May

The OV Monitor is compiled as a standalone C++ executable, whose `main` process spawns a single `OVMonitorThread` object. The `OVMonitorThread` queries a MySQL database to retrieve data on the current configuration of the Outer Veto. The configuration also contains thresholds for different alarmed quantities to be monitored once data-taking begins. Based on that configuration, dynamic numbers of `USB`, `PMTBoard`, and `TriggerBoard` objects are instantiated. The latter two classes derive from a virtual `Board` class. Many other member objects are related to how the data will ultimately be transmitted to the DC Monitor Skeleton; the organization and associations of these objects automatically determine the format of the visualizations on the remote client, as designed in [126].

Once the configuration is loaded, the OV Monitor begins an unending loop in which it searches for all properly-formatted OV binary data files in a specified target directory. In typical operation, the target directory the same directory where the OV EventBuilder places files when that process is finished reading them. If a certain delay condition is met, the OV Monitor will presume that the EventBuilder has crashed, and will directly probe the directory where binary data are placed by the OV DAQ. When data files are found, they are decoded and relevant packet data are associated with the `USB`, `PMTBoard`, and `TriggerBoard` objects. Data are accumulated in a moving time-window configuration: four 30-second "time slices" are cached, in a rotating manner. On some executions of the unending data-reading loop, synthesized data metrics are compared to alarm threshholds, and alarm messages are queued as needed. Finally, every iteration of the loop prompts checks of various server connections and system statuses. At the end of a loop iteration where a change in status is noted or data are found, a package of updated visualization objects are sent to the DC Monitor Skeleton, forcing an update of that process.

The OV Monitor is designed to be fault-tolerant. Many types of connection and system exceptions are handled internally, and retries attempted. The OV Monitor process itself is run as part of Linux's `init` service, with a configuration that restarts the OV Monitor if the process terminates. This is accomplished by placing a utility script `OVMonitor` in the `/etc/init.d` directory, and setting it to be invoked perpetually by adding the line:

```
om:234:respawn:/etc/init.d/OVMonitor start
```

to the file `/etc/inittab`. This script and documentation on its configuration are stored

in the Double Chooz Online SVN Repository, under the `$DCONLINE_PATH/DCOV/OVMonitor` directory.

E.2 Data Handling & Visualization

The OV Monitor presents data visually with an emphasis on two purposes: summarizing data effectively for the lay shifter so that exceptions can easily and clearly be communicated, while also providing detailed and relevant visualizations for the expert to assist in debugging tasks. Since data are communicated from the OV Monitor process to the Monitor Skeleton and remote viewers as pre-defined histogram objects, the visual format of the displays is somewhat fixed. Data objects are grouped by topical similarity into tabs and sub-tabs. Due to design constraints, only one tab is visible to the remote client at a time. Some screenshots of the OV Monitor in operation are shown in the lower sections of Figure E.1.

For a person on shift, the most-often-viewed tab is the Summary Tab, which displays a large "status indicator" in color and text, as well as a message queue to display a prioritized list of currently-existing alarm or exception states. Other tabs show different metrics for each stage of the OV data chain, with increasing levels of data granularity on subtabs as an expert might desire.

Within each tab, the number of data objects to be displayed is determined by configuration settings loaded from a MySQL server instance at startup. This allows the OV Monitor to be automatically scalable to different OV configurations with little to no modificaiton of source code. The configuration is read from the same database tables as are used by the OV DAQ itself, such that necessary system configuration changes are automatically propagated to the OV Monitor. This feature will also allow the OV Monitor to be used with minimial modification for the Near Detector OV, and has allowed the OV to run in a reduced configuration since mid-2012 when a PMT Board failed and prompted re-configuration of a daisy chain.

In maintaining the short-term, real-time focus of the OV Monitor, no data are logged beyond exception messages. Alarms and exceptions are often propagated to the Online Log Message Server or Gaibu Server as needed. Since the OV Monitor reads the same binary

data as is used by the EventBuilder and offline processing tools, historical data are readily available by reprocessing.

Appendix F

Drawing Confidence Intervals using a Frequentist Method

Data from the first and second Double Chooz analyses were analyzed using a frequentist method to establish confidence intervals on a measurement. A frequentist method compares the goodness-of-fit of the data's best fit to a large sample of fits to randomized "pseudo-experiments" in order to determine whether or not the fit to data is better than might be provided by chance. This methodology is based on the work in Ref. [152]. A frequentist method is useful because it ensures proper coverage of the allowed inclusion region for the specified confidence interval even when the goodness-of-fit statistic may behave poorly near the physical limits of parameter space.

This section briefly describes the frequentist method used in the first and second Double Chooz analyses. In those publications, it was used to establish one-dimensional confidence intervals in $\sin^2(2\theta_{13})$ and evaluate the exclusion of the null-oscillation hypothesis (see results in Sections A.6.4 and 7.7.4).

F.1 Procedure for Drawing Confidence Intervals

The procedure for drawing confidence intervals using a frequentist approach proceeds in the following manner:

1. Set the desired confidence level for the acceptance region C (*e.g.* if a 90%C.L. confi-

dence interval is desired, $C = 0.90$).

2. For each point in the parameter space, generate a set of N_{ex} pseudoexperiments $\{u\}$. The oscillation parameters of these pseudoexperiments are to be set at those of the point in parameter space; all other parameters (including statistical fluctuations) are to be randomized.

3. Calculate a goodness-of-fit statistic (*e.g.* $\Delta\chi^2$) for each pseudoexperiment u.

4. Calculate the critical value $\Delta\chi^2_C$ of the fit statistic where a fraction C of the pseudoexperiments u have $\Delta\chi^2(u) < \Delta\chi^2_C$.

5. If the goodness-of-fit statistic of the data $\Delta\chi^2(d) < \Delta\chi^2_C$, then that point in parameter space is within the inclusion interval of the predefined confidence level.

The following subsections will describe these steps in further detail. Descriptions will cater to the case of generating a confidence interval in $\sin^2(2\theta_{13})$ at a fixed Δm^2_{31}, as was done for the Double Chooz publications.

F.1.1 Generation of Pseudoexperiments

Each pseudoexperiment u at a particular value of $\sin^2(2\theta_{13})$ is constructed from expected fluctuations of the signal+background prediction $N_i^{\text{pred}}\left(\sin^2(2\theta_{13}), \Delta m^2_{31}\right)$ based on uncertainty estimates. In practice, those uncertainties are encoded in a covariance matrix M_{ij}. Correlated random fluctuations $\delta N_i^{\text{pred}}\left(u, \sin^2(2\theta_{13}), \Delta m^2_{31}\right)$ of the $N_i^{\text{pred}}\left(\sin^2(2\theta_{13}), \Delta m^2_{31}\right)$ may be generated based on the Cholesky Decomposition of M_{ij} as follows. Note that if M_{ij} should be calculated based on $\sin^2(2\theta_{13})$ and Δm^2_{31} and their effect on $N_i^{\text{pred}}\left(\sin^2(2\theta_{13}), \Delta m^2_{31}\right)$.

Cholesky decomposition produces a lower-triangular matrix L_{ij} (or upper-triangular matrix U_{ij}) such that:

$$M_{ij} = L_{ik}\left(L_{kj}\right)^{\mathrm{T}} = \left(U_{ik}\right)^{\mathrm{T}} U_{kj} \tag{F.1}$$

provided that M_{ij} is positive-definite. Correlated random fluctuations δN_i^{pred} are generated by multiplying L_{ij} against a vector of normal random numbers a_j:

$$\delta N_i^{\text{pred}} = L_{ij} a_j. \tag{F.2}$$

The "data" of pseudoexperiment u are then constructed by applying the correlated random shifts to the prediction:

$$N_i^{\text{pred}}\left(u, \sin^2(2\theta_{13}), \Delta m^2_{31}\right) = N_i^{\text{pred}}\left(\sin^2(2\theta_{13}), \Delta m^2_{31}\right) + \delta N_i^{\text{pred}}\left(u, \sin^2(2\theta_{13}), \Delta m^2_{31}\right). \tag{F.3}$$

This process is repeated $\mathcal{O}(10^4)$ times to generate an ensemble of pseudoexperiments $\{u\}$ at the presumed-true values of $\sin^2(2\theta_{13})$ and Δm^2_{31}.

F.1.2 Goodness-of-Fit Statistic Comparison

Each pseudoexperiment u is fit with an oscillation model, following the prescription of the analysis being performed, to generate a goodness-of-fit statistic for that pseudoexperiment. For each Double Chooz analysis, the fit statistic used was:

$$\Delta\chi^2(u) = \chi^2\left(u, \sin^2(2\theta_{13})\right) - \chi^2\left(u, \max\left(\sin^2(2\theta_{13})^{best}, 0\right)\right) \tag{F.4}$$

where $\chi^2\left(u, \sin^2(2\theta_{13})\right)$ is the goodness-of-fit of u at the true value of $\sin^2(2\theta_{13})$, and $\chi^2\left(u, \max\left(\sin^2(2\theta_{13})^{best}, 0\right)\right)$ is the goodness-of-fit of u at the best-fit $\sin^2(2\theta_{13})^{best}$ limited to the physical region of parameter space.

Once $\Delta\chi^2(u)$ has been calculated for each pseudoexperiment, we construct a "critical value" of the fit statistic $\Delta\chi^2_C\left(\sin^2(2\theta_{13}), \Delta m^2_{31}\right)$ based on the confidence interval C desired. The value is constructed such that $\Delta\chi^2(u) < \Delta\chi^2_C\left(\sin^2(2\theta_{13}), \Delta m^2_{31}\right)$ for a fraction C of all the pseudoexperiments $\{u\}$. This critical value is a function of the oscillation parameters.

F.1.3 Drawing Confidence Intervals

The value $\Delta\chi^2_C\left(\sin^2(2\theta_{13}), \Delta m^2_{31}\right)$ is calculated for many points in the oscillation parameter space, based on sets of pseudoexperiments being generated at each point, as described in the previous two subsections. The confidence interval is drawn by comparing the goodness-of-fit statistic of the observed data $\Delta\chi^2(d)$ to these critical values. If $\Delta\chi^2(d) < \Delta\chi^2_C\left(\sin^2(2\theta_{13}), \Delta m^2_{31}\right)$ at a particular point in oscillation parameter space, then that point is said to lie within the inclusion interval at the prescribed confidence level C. This process may be repeated for different values of C using the same sets of pseudoexperiments to generate inclusion contours at different confidence levels.

F.2 Procedure for Testing the Null-Oscillation Hypothesis

The procedure for comparing a set of measured Double Chooz data to the null-oscillation hypothesis is very similar to the procedure outlined in Section F.1 if applied only to a single point ($\sin^2(2\theta_{13}) = 0$) in parameter space, but without a prescribed desired confidence level. the procedure proceeds as follows:

1. For the null-oscillation hypothesis $\sin^2(2\theta_{13}) = 0$, generate a set of N_{ex} pseudoexperiments $\{u\}$. All other parameters (including statistical fluctuations) are to be randomized.

2. Calculate a goodness-of-fit statistic (*e.g.* $\Delta\chi^2$) for each pseudoexperiment u.

3. Calculate the fraction of pseudoexperiments F which have a goodness-of-fit less than that of the data. This fraction defined the confidence with which the null-oscillation hypothesis is rejected. (*e.g.* if $F = 0.995$, then the null-oscillation hypothesis is rejected at 99.5% C.L.).

The number of generated pseudoexperiments N_{ex} should be large, $\mathcal{O}(10^4)$, to suppress statistical fluctuations in F.

Appendix G

Pulls vs. Covariance χ^2

Based on ambiguously-qualified assertions in literature, χ^2 fit statistics which utilize a covariance matrix to represent correlated uncertainties are often considered to be analytically equivalent to χ^2 fit statistics which use pull parameters and pull terms to the same end. In this memo, we[1] use two simple single-bin χ^2 statistics to show that this presumed equivalence does not hold in practice for many common uncertainty scenarios. We then review the conditions which are required for the χ^2 equivalence to be true.

G.1 Motivation

In performing oscillation analyses, two types of χ^2 goodness-of-fit statistics are commonly used: those utilizing a covariance matrix to represent correlated uncertainties, and those utilizing "pull parameters" and "pull terms" (a.k.a. nuisance parameters) to achieve the same end. Historically, it has often been asserted[2] that these methods to constructing a χ^2 statistic are analytically equivalent. Two literature sources, [150] and [149], are often cited as containing proofs of this assertion. However, the assertion of equivalence is rarely accompanied by reminders of what assumptions have been made in [150] and [149] regarding the construction of the χ^2, the nature of the uncertainties, or natures of the signal and background which make up the predicted variables.

[1]The author would like to thank M. Toups and R. Carr for useful discussion on this topic.

[2]The author freely admits to having made this assertion on numerous occasions.

In Sec. G.2, this assertion is tested using a pair of single-bin χ^2 statistics, and shown to be untrue for some sets of assumptions. Finally, in Sec. G.3, we review what conditions are required for equivalence between the two χ^2 formulations, and make recommendations for analysis methodologies where this equivalence is not present. Code for all these investigations is contained in the appendix to this document.

G.2 Tests With Two Simple χ^2 Statistics

To test the equivalence of covariance approach and pulls approach, we employ two simple, single-bin, toy "oscillation" models. In each model, we use the asymmetric 68% C.L. interval produced in a null-oscillation sensitivity study as the metric for χ^2 behavior. Sec. G.2.1 examines a toy model comprised of a signal with oscillation effects and two backgrounds with accompanying uncertainties, while Sec. G.2.2 examines a toy model consisting of a signal with oscillations and two multiplicative normalization uncertainties. Since the two toy models contain uncertainties of inherently different natures, the results from each toy model should not be directly compared.

G.2.1 Uncertainties on Linear Parameters

The toy model predicts a number of events N_p with contributions from a neutrino signal S with survival fraction η, and two backgrounds B_a and B_b:

$$N_p = S\eta + B_a\epsilon_a + B_b\epsilon_b \tag{G.1}$$

where $\epsilon_a = 1.00 \pm 0.03$ and $\epsilon_b = 1.00 \pm 0.04$ are parameters which vary the normalization of each background within uncertainties. In practice, $S = 50000$, $B_a = B_b = 25000$, and the observation $N_o = N_p|_{\epsilon_a=\epsilon_b=\eta=1}$. For brevity, we define $\Delta = N_o - N_p$.

Three different χ^2 statistics are examined:

$$\chi^2_{\text{matrix}} = \left.\frac{\Delta^2}{B_a^2\sigma_a^2 + B_b^2\sigma_b^2 + \sigma^2_{\text{stat}}}\right|_{\epsilon_a=\epsilon_b=1} \tag{G.2}$$

$$\chi^2_{\text{1pull}} = \left.\frac{\Delta^2}{B_b^2\sigma_b^2 + \sigma^2_{\text{stat}}}\right|_{\epsilon_b=1} + \left(\frac{1-\epsilon_a}{\sigma_a}\right)^2 \tag{G.3}$$

$$\chi^2_{\text{2pulls}} = \frac{\Delta^2}{\sigma^2_{\text{stat}}} + \left(\frac{1-\epsilon_a}{\sigma_a}\right)^2 + \left(\frac{1-\epsilon_b}{\sigma_b}\right)^2 \tag{G.4}$$

In these definitions, the statistical uncertainty σ_{stat} can follow either the Pearson convention ($\sigma^2_{\text{stat}} = N_p$) or the Neyman convention ($\sigma^2_{\text{stat}} = N_o$).

A minimization in the parameters of the fit is performed with the MIGRAD algorithm, then the asymmetric sensitivity interval on the survival fraction parameter η is found using the MINOS algorithm.

Results for this model using the three different χ^2 constructions of Eqs. G.2, G.3, and G.4 are shown in Table G.1. For all cases involving the Neyman σ_{stat} convention, the three χ^2 definitions behave equivalently. However, when the Pearson convention is used, the three χ^2 definitions begin to show slight discrepancies between their results. The asymmetric (symmetric) behavior of the Pearson (Neyman) interval for any one χ^2 definition is expected.

	Pure-Matrix Static Eq. G.2	B_a Pull, B_b Matrix Eq. G.3	B_a Pull, B_b Pull Eq. G.4
Pearson	+2.57976%	+2.57942%	+2.57882%
Statistics	-2.57776%	-2.57810%	-2.57870%
Neyman	+2.57876%	+2.57876%	+2.57876%
Statistics	-2.57876%	-2.57876%	-2.57876%

Table G.1: Asymmetric null-oscillation 68% C.L. sensitivity intervals for different χ^2 formulations using the toy model of Eq. G.1, quoted in percent uncertainty on the survival fraction parameter η.

G.2.2 Uncertainties on Multiplicative Parameters

The second toy model predicts a number of events N_p with contributions from a neutrino signal S with survival fraction η, and two signal efficiency coefficients R and ϵ:

$$N_p = S\eta R\epsilon \tag{G.5}$$

where $\epsilon = 1.00 \pm 0.03$ and $R = 1.00 \pm 0.04$ are parameters which vary the normalization of the signal *a la* a reactor prediction normalization and a detection efficiency factor. In practice, $S = 50000$, and the observation $N_o = N_p|_{\epsilon=R=\eta=1}$. For brevity, we define $\Delta = N_o - N_p$.

Five different χ^2 statistics are examined:

$$\chi^2_{\text{static matrix}} = \left.\frac{\Delta^2}{S^2\left(\sigma_R^2 + \sigma_\epsilon^2\right) + \sigma_{\text{stat}}^2}\right|_{\epsilon=R=1} \tag{G.6}$$

$$\chi^2_{\text{reweight matrix}} = \left.\frac{\Delta^2}{N_p^2\left(\sigma_R^2 + \sigma_\epsilon^2\right) + \sigma_{\text{stat}}^2}\right|_{\epsilon=R=1} \tag{G.7}$$

$$\chi^2_{\text{1pull, fix. mat.}} = \left.\frac{\Delta^2}{S^2\sigma_R^2 + \sigma_{\text{stat}}^2}\right|_{R=1} + \left(\frac{1-\epsilon}{\sigma_\epsilon}\right)^2 \tag{G.8}$$

$$\chi^2_{\text{1pull, rew. mat.}} = \left.\frac{\Delta^2}{N_p^2\sigma_R^2 + \sigma_{\text{stat}}^2}\right|_{R=1} + \left(\frac{1-\epsilon}{\sigma_\epsilon}\right)^2 \tag{G.9}$$

$$\chi^2_{\text{2pulls}} = \frac{\Delta^2}{\sigma_{\text{stat}}^2} + \left(\frac{1-\epsilon}{\sigma_\epsilon}\right)^2 + \left(\frac{1-R}{\sigma_R}\right)^2 \tag{G.10}$$

In these definitions, the statistical uncertainty σ_{stat} can follow either the Pearson convention ($\sigma^2_{\text{stat}} = N_p$) or the Neyman convention ($\sigma^2_{\text{stat}} = N_o$). It is important to note that the χ^2 constructions in Eqs. G.6 and G.8 use a "static" covariance matrix normalized by the constant S, while the χ^2 constructions of Eqs. G.7 and G.9 both use a "reweighted" covariance matrix which is normalized by the fit parameter-dependent N_p.

A minimization in the parameters of the fit is performed with the MIGRAD algorithm, then the asymmetric sensitivity interval on the survival fraction parameter η is found using the MINOS algorithm.

Results for this model using the five different χ^2 constructions of Eqs. G.6, G.7, G.8, G.9, and G.10are shown in Table G.2. Discrepancies between the behaviors of all χ^2 definitions

are notable; nearly none of the definitions are precisely equivalent with each other.

	Pure-Matrix, Static Eq. G.6	Pure-Matrix, Reweighted Eq. G.7	ϵ Pull, Static R Matrix Eq. G.8	ϵ Pull, Reweighted R Matrix Eq. G.9	ϵ Pull, R Pull Eq. G.10
Pearson Statistics	+5.02096% -5.01896%	+5.28446% -4.78058%	+5.11376% -4.93228%	+5.22075% -4.83297%	+5.22006% -4.83357%
Neyman Statistics	+5.01996% -5.01996%	+5.28340% -4.78153%	+5.11312% -4.93293%	+5.22006% -4.83358%	+5.22006% -4.83358%

Table G.2: Asymmetric null-oscillation 68% C.L. sensitivity intervals for different χ^2 formulations using the toy model of Eq. G.5, quoted in percent uncertainty on the survival fraction parameter η.

G.2.2.1 Test of a Single Multiplicative Parameter

A common variation on the toy model of Eq. G.5 might involve merging the parameters ϵ and R into a single multiplicative parameter $E_{\epsilon R} = \epsilon R$, thus:

$$N_p = S\eta E_{\epsilon R} \tag{G.11}$$

and combining[3] the uncertainties on those two parameters:

$$\left(\frac{\sigma_{E_{\epsilon R}}}{E_{\epsilon R}}\right)^2 \approx \left(\frac{\sigma_\epsilon}{\epsilon}\right)^2 + \left(\frac{\sigma_R}{R}\right)^2 \tag{G.12}$$

Thus, for our purposes, $E_{\epsilon R} = 1.00 \pm 0.05$, and we maintain $S = 50000$, and the observation $N_o = N_p|_{E_{\epsilon R}=1}$. We still use $\Delta = N_o - N_p$.

[3] A recipe for exact combination can be found in [194].

Three different χ^2 statistics are examined:

$$\chi^2_{\text{static matrix}} = \left.\frac{\Delta^2}{S^2\sigma^2_{E_{\epsilon R}} + \sigma^2_{\text{stat}}}\right|_{E_{\epsilon R}=1} \tag{G.13}$$

$$\chi^2_{\text{reweight matrix}} = \left.\frac{\Delta^2}{N_p^2\sigma^2_{E_{\epsilon R}} + \sigma^2_{\text{stat}}}\right|_{E_{\epsilon R}=1} \tag{G.14}$$

$$\chi^2_{\text{pull}} = \frac{\Delta^2}{\sigma^2_{\text{stat}}} + \left(\frac{1 - E_{\epsilon R}}{\sigma_{E_{\epsilon R}}}\right)^2 \tag{G.15}$$

In these definitions, the statistical uncertainty σ_{stat} can follow either the Pearson convention ($\sigma^2_{\text{stat}} = N_p$) or the Neyman convention ($\sigma^2_{\text{stat}} = N_o$). It is important to note that the χ^2 construction in Eq. G.13 uses a "static" covariance matrix normalized by the constant S, while the χ^2 construction of Eq. G.14 uses a "reweighted" covariance matrix which is normalized by the fit parameter-dependent N_p.

A minimization in the parameters of the fit is performed with the MIGRAD algorithm, then the asymmetric sensitivity interval on the survival fraction parameter η is found using the MINOS algorithm.

Results for this model using the three different χ^2 constructions of Eqs. G.13, G.14, and G.15 are shown in Table G.3. A few features are notable. First, the results in Table G.3 associated with Eq. G.13 and G.14 are identical to those in Table G.2 associated with Eq. G.6 and G.7, respectively. This particular equivalence is as expected, since the covariance matrices in each of those equations are numerically identical, and are reweighted identically where appropriate. However, it is important to note the lack of equivalence in results between those associated with Eqs. G.14 and G.15. Similarly, it is notable that the "pure pulls" approach associated with Eq. G.10 in Table G.2 is not found to be equivalent to the "pure combined pull" approach associated with Eq. G.15 in Table G.3. These two final points suggest that combining degenerate multiplicative sources of uncertainty by summing their matrices or combining their pull terms may introduce an approximation, and should be done with caution.

	Matrix, Static Eq. G.13	Matrix, Reweighted Eq. G.14	Pull Term Eq. G.15
Pearson	+5.02096%	+5.28446%	+5.28341%
Statistics	-5.01896%	-4.78058%	-4.78152%
Neyman	+5.01996%	+5.28340%	+5.28340%
Statistics	-5.01996%	-4.78153%	-4.78153%

Table G.3: Asymmetric null-oscillation 68% C.L. sensitivity intervals for different χ^2 formulations using the toy model of Eq. G.11, quoted in percent uncertainty on the survival fraction parameter η.

G.3 Commentary

If the proofs in [150] and [149] are rigorous are valid, why so many discrepancies between the different results in Table G.1, and between those in Table G.2? The proofs in those sources function under the assumption that any potential shifts due to uncertainties, whether correlated or not, are absolutely known *a priori*. In χ^2 constructions where the Pearson prescription is used for σ_{stat}, this is distinctly not the case: the uncorrelated uncertainty must be calculated at each iteration of the minimization as η (at least) changes. A similar case arises when the correlated uncertainties due to systematics are recalculated as a function of η or other systematic parameters, as in any of the χ^2 constructions with "reweighted" covariance matrices. A covariance matrix known *a priori* allows the proofs in [150] and [149] to treat the systematic parameters as an analytically-solvable set of linear equations. Without the *a priori* covariance matrix, the set of relationships becomes nonlinear, and the treatment breaks down. Thus, the χ^2 constructions are no longer equivalent.

For an in-depth examination of the behavior of χ^2 statistics with different styles of systematic uncertainties, see [192]. One key recommendation of that reference is that any components of the covariance matrix which are not known *a priori* should be recomputed at each iteration of the minimization, or else the statistic will stray from rigorous behavior. Even with recalculation of the covariance matrix at each iteration, the statistic is still only

an approximates the true random behaviors of the set of measurements. In short, the fewer pull parameters that are used in a fit statistic, the more of an approximation the χ^2 construction will be, and the less the uncertainty intervals produced by it should be trusted.

G.4 Code

Code for these investigations was written in ROOT, using RooFits.

G.4.1 Linear Uncertainties

The following code was used to perform the calculations described in Sec. G.2.1.

G.4.2 Multiplicative Uncertainties

The following code was used to perform the calculations described in Sec. G.2.2.

G.4.3 Single Multiplicative Uncertainty

The following code was used to perform the calculations described in Sec. G.2.2.1.

Appendix H

Covariance Matrix Component Break-Out

It is possible [1] for a covariance matrix to be decomposed into three different components representing different effects of uncertainties on the data. A "normalization" part which changes all bins by an overall normalization factor. A "shape" part which changes bin contents in a way that conserves the total number of events among all bins. Finally, a "mixed" part represents uncertainties which change the number of events in different bins by different normalization factors.

[1] This method is taken from BooNE Tech Note 253, by Mike Shaevitz, where credit for the idea is given to Rex Tayloe and Teppei Katori.

H.1 Method

For an $n \times n$ covariance matrix M_{ij} the component matrices are given by the following formulae:

$$M_{ij}^{\text{norm}} = \frac{N_i N_j}{N_T^2} \sum_{k=1}^{n} \sum_{l=1}^{n} M_{kl} \tag{H.1}$$

$$M_{ij}^{\text{shape}} = M_{ij} - \frac{N_j}{N_T} \sum_{k}^{n} M_{ik} - \frac{N_i}{N_T} \sum_{k}^{n} M_{kj} + \frac{N_i N_j}{N_T^2} \sum_{k}^{n} \sum_{l}^{n} M_{kl} \tag{H.2}$$

$$M_{ij}^{\text{mixed}} = \frac{N_j}{N_T} \sum_{k}^{n} M_{ik} + \frac{N_i}{N_T} \sum_{k}^{n} M_{kj} - 2\frac{N_i N_j}{N_T^2} \sum_{k}^{n} \sum_{l}^{n} M_{kl} \tag{H.3}$$

where $N_T = \sum_{i}^{n} N_i$. The matrix components sum to the original matrix: $M_{ij} = M_{ij}^{\text{norm}} + M_{ij}^{\text{shape}} + M_{ij}^{\text{mixed}}$.

H.2 Limitations

A limiting case of this method arises when the total distribution N_i is comprised of two separate contributing distributions, *e.g.* N_i^{sig} and N_i^{bkg}. Let each distribution have its own corresponding covariance matrix: $M_{ij} = M^{\text{sig}})ij + M_{ij}^{\text{bkg}}$. Let it be the case that N_i^{bkg} is generally much less than N_i^{sig} (*e.g.* the ^{9}Li background under Double Chooz's IBD signal, with a typical signal/background ratio of $\sim$40).

The limiting case arises if $\sum_{i,j} M_{ij}^{\text{bkg}} \gtrsim \sum_{i,j} M_{ij}^{\text{sig}}$, *i.e.* the total "normalization" uncertainty of M_{ij} is dominated by the contribution from M_{ij}^{bkg}. In this case, constructing a "normalization" matrix M_{ij}^{norm} using Eq. H.1 results in a matrix which may have diagonal elements that are greater than the diagonal elements of M_{ij}. This is unphysical, as it would require the impossible condition of one of the associated M_{ij}^{shape} or M_{ij}^{mix} to have negative diagonal elements.

As of this writing, there is no precise condition or threshold where this limiting case can be identified.

Appendix I

Second Publication Data Release

Following the second Double Chooz Analysis (see Section 7), the collaboration decided to make publicly available its numerical data and fit results to enable use of Double Chooz's results by the theoretical and phenomenological communities. The data were to allow a full reproduction of the results published in [8], and provide minimal abilities for phenomenologists to modify the oscillation model used to fit the data.

The data were publicly released via a web page hosted on Double Chooz's website: `http://www.doublechooz.org/Public/English//DataRelease/DC2ndPubDataRelease.php`. A screen shot of this web page may be seen in Figure I.1. The website was assembled by the author, in collaboration with Maya Carter, a summer undergraduate researcher at Nevis Labs, and Joshua Spitz (MIT).

The following data were included as part of the release:

- All detected IBD candidates. Associated data with each event included reconstructed energy, reconstructed position, OV coincidence, and run number of detection.
- Predicted signal events. Associated data with each event included reconstructed energy, true neutrino energy, baseline, and run number.
- Predicted background events.
- Covariance matrices for all systematic uncertainties, and statistical uncertainties.

In addition to these data, a minimal fitting program based off of the CUfits package (see

Appendix B) was publicly released. The fitter reproduces the method and results used for the final oscillation fit of the second analysis, as described in Sec. 7.7. The fitter uses object-oriented programming principles to allow straight-forward replacement of the standard 2-neutrino oscillation model with more exotic physics models.

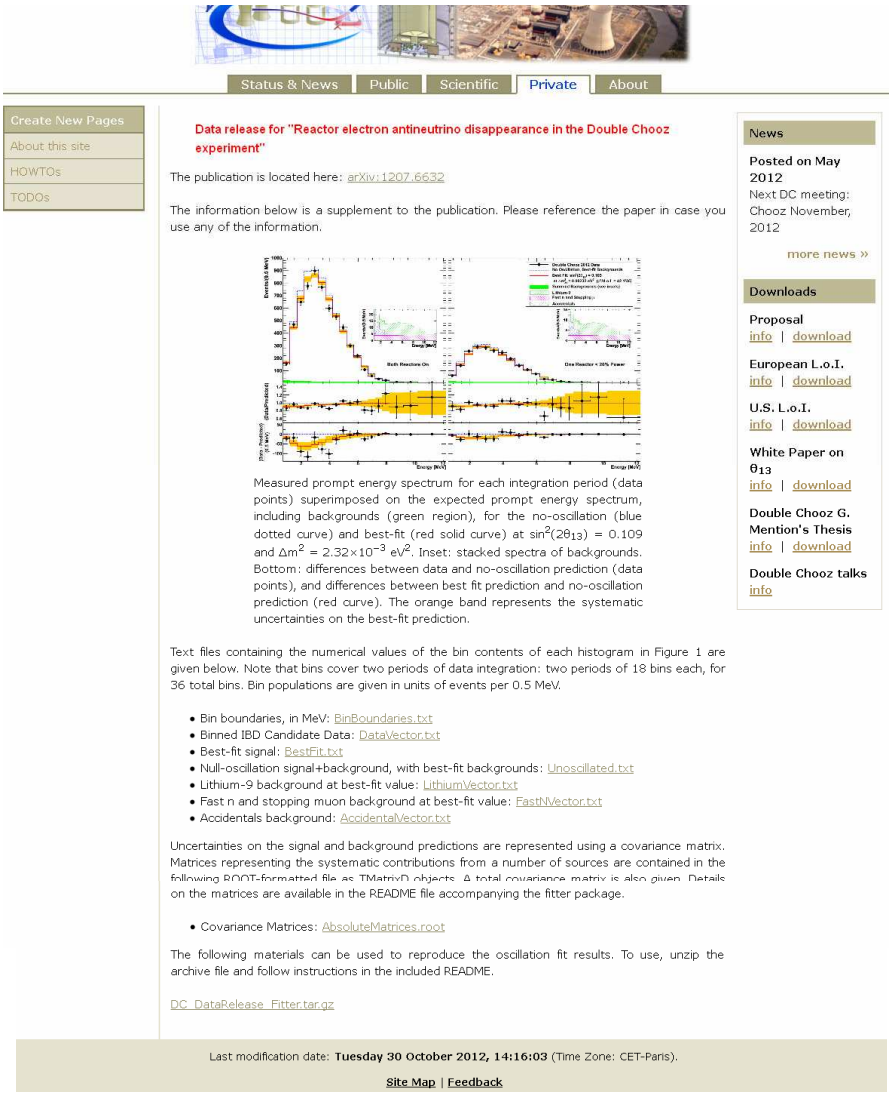

Figure I.1: Screen shot of the data release web page for the second Double Chooz publication.

Appendix J

IT Infrastructure

In support of the Outer Veto and Double Chooz in general, information technology infrastructure was deployed in the Double Chooz Far Laboratory to help fill computing needs. These systems were first realized as part of the Outer Veto test stand at Nevis, and later moved to the Double Chooz Far Hall as part of the multi-step Outer Veto installation. Additionally, documentation for the machines and hosted systems was prepared to enable future administration.

J.1 Outer Veto Computers

Three commodity 1U servers were installed in the Far Hall to host the Outer Veto DAQ, associated monitoring systems, and general Double Chooz systems. Each server uses Debian Linux [195] version 5.03 "lenny", though the hardware configuration of each server is slightly different, depending on role.

- `dcfovdaq`: Named for its use in hosting the principal components of the OV DAQ. It has an additional USB interface installed to allow acquisition from all USB data streams, as well as redundancy.
- `dcfovmon`: Named for its use in hosting the monitoring components of the OV DAQ. To this end, it is directly connected via dedicated Gigabit Ethernet link to `dcfovdaq`. Contains an additional USB interface which is not used, and also contains an extra

400MB hard disk to serve as one component of the replicated MySQL server instance (see Sec. J.2).

- `dcfovserv`: Named for its use in hosting many "server"-type processes. Contains a High Voltage interface card for use in communicating with the OV HV Mainframe. Also contains an extra 400MB hard disk to as part of the replicated MySQL server instance (see Sec. J.2).

While the machines are not directly interchangable, their configurations do afford some degree of redundancy.

J.2 High-Availability MySQL Server

A number of Double Chooz systems have been configured to utilize a MySQL database for storage or archiving of data and operating parameters. An on-site server instance has been realized to enable these systems, hosted on the Outer Veto computers. The design goal for the server instance was optimal uptime, so as not to impact the total uptime of all dependent detector systems. To this end, a High-Availability clustering configuration was implemented. The overall performance of this implementation has been mixed.

This implementation of a MySQL server instance with high-availability principles in mind strives towards two goals: minimization of downtime through automation and redundancy; and replication of data to minimize the chance of data loss. The latter is achieved through backup methods described in Sec. J.2.1.

Generally, the high-availability cluster is built upon the following components: at least two interchangeable computing nodes; a set of services which are to be hosted on those nodes; and management software which automatically determines on which node the services are to be run, in a fault-tolerant manner. In this setup, the computing nodes are `dcfovmon` and `dcfovserv`, each of which has installed in it a 400MB hard disk to be dedicated to MySQL data. Each node has the following software installed: MySQL server, DRBD disk replication manager [196], and Pacemaker cluster manager [197].

The necessary services are configured via Pacemaker's cluster configuration file: `ping` instances to determine network connectivity; a Master/Slave DRBD resource; a file sys-

tem to be mounted after the DRBD resource has established a Master; a MySQL server instance. The `/etc/mysql/my.cnf` files on each are identical. This configuration allows the Pacemaker cluster manager to start and stop the different services in a fault-tolerant way on either of the two nodes.

Operation proceeds in the following way. The DRBD disk replication utility ensures that each of the 400MB data drives on `dcfovmon` and `dcfovserv` are replicated to the sector level in a synchronous way. The synchronicity helps ensure identical data on each disk at any point in time, provided that the DRBD daemons are connected and communicating. With DRBD verified to be operating, Pacemaker mounts the filesystem on the read-/write-able DRBD Master, and starts a MySQL server instance which uses that filesystem as its data directory. A dynamic IP address also follows the MySQL server instance, ensuring that hosts contacting `dcfmysql.in2p3.fr` will always reach the node where the server instance is live. Thus, in normal operation, queries will always go to a live server instance, and that server instance will always have access to the current set of table data.

Operation of this system over time showed that MySQL livetime was not the factor most limiting of detector operation. Indeed, a faulty UPS system and unforseen routine power cuts have been the largest contributors to detector downtime. In this case, the additional operational overhead involved in safely shutting down and restarting the high-availability cluster on each power cycle event is considerable. The reccommendation from this author is that the Near Detector have a dedicated MySQL server which is not part of a HA cluster, but does have sufficient health monitoring and a good backup scheme to allow for quick recovery after significant fail-over events.

J.2.1 Backup Scheme

The backup scheme for the MySQL server inplements multiple layers of redundancy to minimize the potential for data loss. The first level of backup is the use of DRBD in the high-availability setup, which ensures that a single catastrophic disk failure will not destroy the on-site data. Second, replication to a MySQL server instance at CCIN2P3 in Lyon, France, provides an off-site backup with little to no lag time from when writes are made to the server instance on `dcfmysql`. Finally, periodic backups of the CCIN2P3 database

are made by the staff at that facility, ensuring backup capabilities in the event of data corruption.

J.3 Nagios Resource Monitoring

With a large number of computer systems operating in the Double Chooz Far Laboratory, each with many mission-critical hosted services and components, monitoring of each of these components is necessary to provide warning of impending failures, and to provide diagnostic information in the case of a failure. To provide this service, the Nagios software platform was selected. Nagios [198] is an open-source, enterprise-grade IT infrastructure monitoring package. Its open-source nature allows for flexibility in configuration, and its widespread use in industry helps provide documentation and a support base.

A Nagios Server instance was installed on a computer in the Double Chooz Control Room at the power plant site, from the Debian repositories. On each host to be monitored by Nagios, a daemon client named NRPE was installed, again from the standard repositories. Periodically, the Nagios server queries the NRPE client on each host, and passes a command which in turn checks an aspect of the system. System checks are defined by programs or scripts installed on the host being monitoried; as long as the output of the script is properly formatted, almost any component of the system can be monitoried with a bespoke script. The server then logs the query results, and checks whether they are outside predefined warning or critical specifications. The addition of the `nagiosgrapher` [199] utility to the server instance allowed the outputs to be logged for one year, and graphed in time. The Nagios server provides automatic email notifications if any metrics are out of spec, and provides a web-based dispaly of all measured statuses.

Appendix K

Double Chooz Publications

K.1 First Double Chooz Publication

This section contains a facsimile of the first Double Chooz publication, published as [16].

Indication for the disappearance of reactor $\bar{\nu}_e$ in the Double Chooz experiment

Y. Abe,[28] C. Aberle,[21] T. Akiri,[4,15] J.C. dos Anjos,[5] F. Ardellier,[15] A.F. Barbosa,[5,*] A. Baxter,[26] M. Bergevin,[9] A. Bernstein,[16] T.J.C. Bezerra,[30] L. Bezrukhov,[14] E. Blucher,[6] M. Bongrand,[15,30] N.S. Bowden,[16] C. Buck,[21] J. Busenitz,[2] A. Cabrera,[4] E. Caden,[10] L. Camilleri,[8] R. Carr,[8] M. Cerrada,[7] P.-J. Chang,[17] P. Chimenti,[34] T. Classen,[9,16] A.P. Collin,[15] E. Conover,[6] J.M. Conrad,[20] S. Cormon,[25] J.I. Crespo-Anadón,[7] M. Cribier,[15,4] K. Crum,[6] A. Cucoanes,[25,15] M.V. D'Agostino,[3] E. Damon,[10] J.V. Dawson,[4,36] S. Dazeley,[16] M. Dierckxsens,[6] D. Dietrich,[33] Z. Djurcic,[3] M. Dracos,[24] V. Durand,[15,4] Y. Efremenko,[27] M. Elnimr,[25] Y. Endo,[29] A. Etenko,[19] E. Falk,[26] M. Fallot,[25] M. Fechner,[15] F. von Feilitzsch,[31] J. Felde,[9] S.M. Fernandes,[26] D. Franco,[4] A.J. Franke,[8] M. Franke,[31] H. Furuta,[30] R. Gama,[5] I. Gil-Botella,[7] L. Giot,[25] M. Göger-Neff,[31] L.F.G. Gonzalez,[35] M.C. Goodman,[3] J.TM. Goon,[2] D. Greiner,[33] B. Guillon,[25] N. Haag,[31] C. Hagner,[11] T. Hara,[18] F.X. Hartmann,[21] J. Hartnell,[26] T. Haruna,[29] J. Haser,[21] A. Hatzikoutelis,[27] T. Hayakawa,[22,15] M. Hofmann,[31] G.A. Horton-Smith,[17] M. Ishitsuka,[28] J. Jochum,[33] C. Jollet,[24] C.L. Jones,[20] F. Kaether,[21] L. Kalousis,[24] Y. Kamyshkov,[27] D.M. Kaplan,[13] T. Kawasaki,[22] G. Keefer,[16] E. Kemp,[35] H. de Kerret,[4,36] Y. Kibe,[28] T. Konno,[28] D. Kryn,[4] M. Kuze,[28] T. Lachenmaier,[33] C.E. Lane,[10] C. Langbrandtner,[21] T. Lasserre,[15,4] A. Letourneau,[15] D. Lhuillier,[15] H.P. Lima Jr,[5] M. Lindner,[21] Y. Liu,[2] J.M. López-Castanõ,[7] J.M. LoSecco,[23] B.K. Lubsandorzhiev,[14] S. Lucht,[1] D. McKee,[2,17] J. Maeda,[29] C.N. Maesano,[9] C. Mariani,[8] J. Maricic,[10] J. Martino,[25] T. Matsubara,[29] G. Mention,[15] A. Meregaglia,[24] T. Miletic,[10] R. Milincic,[10] A. Milzstajn,[15,*] H. Miyata,[22] D. Motta,[15,*] Th.A. Mueller,[15,30] Y. Nagasaka,[12] K. Nakajima,[22] P. Novella,[7] M. Obolensky,[4] L. Oberauer,[31] A. Onillon,[25] A. Osborn,[27] I. Ostrovskiy,[2] C. Palomares,[7] S.J.M. Peeters,[26] I.M. Pepe,[5] S. Perasso,[10] P. Perrin,[15] P. Pfahler,[31] A. Porta,[25] W. Potzel,[31] R. Queval,[15] J. Reichenbacher,[2] B. Reinhold,[21] A. Remoto,[25,4] D. Reyna,[3] M. Röhling,[33] S. Roth,[1] H.A. Rubin,[13] Y. Sakamoto,[32] R. Santorelli,[7] F. Sato,[29] S. Schönert,[31] S. Schoppmann,[1] U. Schwan,[21] T. Schwetz,[21] M.H. Shaevitz,[8] D. Shrestha,[17] J-L. Sida,[15] V. Sinev,[14,15] M. Skorokhvatov,[19] E. Smith,[10] J. Spitz,[20] A. Stahl,[1] I. Stancu,[2] M. Strait,[6] A. Stüken,[1] F. Suekane,[30] S. Sukhotin,[19] T. Sumiyoshi,[29] Y. Sun,[2] Z. Sun,[15] R. Svoboda,[9] H. Tabata,[30] N. Tamura,[22] K. Terao,[20] A. Tonazzo,[4] M. Toups,[8] H.H. Trinh Thi,[31] C. Veyssiere,[15] S. Wagner,[21] H. Watanabe,[21] B. White,[27] C. Wiebusch,[1] L. Winslow,[20] M. Worcester,[6] M. Wurm,[11] E. Yanovitch,[14] F. Yermia,[25] K. Zbiri,[25,10] and V. Zimmer[31]

(Double Chooz Collaboration)

[1] *III. Physikalisches Institut, RWTH Aachen University, 52056 Aachen, Germany*
[2] *Department of Physics and Astronomy, University of Alabama, Tuscaloosa, Alabama 35487, USA*
[3] *Argonne National Laboratory, Argonne, Illinois 60439, USA*
[4] *APC, AstroParticule et Cosmologie, Université Paris Diderot, CNRS/IN2P3, CEA/IRFU, Observatoire de Paris, Sorbonne Paris Cité, 75205 Paris Cedex 13, France*
[5] *Centro Brasileiro de Pesquisas Fisicas, Rio de Janeiro, RJ, cep 22290-180, Brazil*
[6] *The Enrico Fermi Institute, The University of Chicago, Chicago, IL 60637, USA*
[7] *Centro de Investigaciones Energéticas, Medioambientales y Tecnológicas, CIEMAT, E-28040, Madrid, Spain*
[8] *Columbia University; New York, NY 10027, USA*
[9] *University of California, Davis, CA-95616-8677, USA*
[10] *Physics Department, Drexel University, Philadelphia, Pennsylvania 19104, USA*
[11] *Institut für Experimentalphysik, Universität Hamburg, 22761 Hamburg, Germany*
[12] *Hiroshima Institute of Technology, Hiroshima, 731-5193, Japan*
[13] *Department of Physics, Illinois Institute of Technology, Chicago, Illinois 60616, USA*
[14] *Institute of Nuclear Research of the Russian Aacademy of Science, Russia*
[15] *Commissariat à l'Energie Atomique et aux Energies Alternatives, Centre de Saclay, IRFU, 91191 Gif-sur-Yvette, France*
[16] *Lawrence Livermore National Laboratory, Livermore, CA 94550, USA*
[17] *Department of Physics, Kansas State University, Manhattan, Kansas 66506, USA*
[18] *Department of Physics, Kobe University, Kobe, 657-8501, Japan*
[19] *NRC Kurchatov Institute, 123182 Moscow, Russia*
[20] *Massachusetts Institute of Technology; Cambridge, MA 02139, USA*
[21] *Max-Planck-Institut für Kernphysik, 69029 Heidelberg, Germany*
[22] *Department of Physics, Niigata University, Niigata, 950-2181, Japan*
[23] *University of Notre Dame, Notre Dame, IN 46556-5670, USA*
[24] *IPHC, Université de Strasbourg, CNRS/IN2P3, F-67037 Strasbourg, France*
[25] *SUBATECH, CNRS/IN2P3, Université de Nantes, Ecole des Mines de Nantes, F-44307 Nantes, France*
[26] *Department of Physics and Astronomy, University of Sussex, Falmer, Brighton BN1 9QH, United Kingdom*
[27] *Department of Physics and Astronomy, University of Tennessee, Knoxville, Tennessee 37996, USA*
[28] *Department of Physics, Tokyo Institute of Technology, Tokyo, 152-8551, Japan*
[29] *Department of Physics, Tokyo Metropolitan University, Tokyo, 192-0397, Japan*

[30] Research Center for Neutrino Science, Tohoku University, Sendai 980-8578, Japan
[31] Physik Department, Technische Universität München, 85747 Garching, Germany
[32] Tohoku Gakuin University, Sendai, 981-3193, Japan
[33] Kepler Center for Astro and Particle Physics, Universität Tübingen, 72076, Tübingen, Germany
[34] Universidade Federal do ABC, UFABC, Sao Paulo, Santo André, SP, Brazil
[35] Universidade Estadual de Campinas-UNICAMP, Campinas, SP, Brazil
[36] Laboratoire Neutrino de Champagne Ardenne, domaine d'Aviette, 08600 Rancennes, France
(Dated: March 15, 2012)

The Double Chooz Experiment presents an indication of reactor electron antineutrino disappearance consistent with neutrino oscillations. An observed-to-predicted ratio of events of 0.944 ± 0.016 (stat) $\pm$ 0.040 (syst) was obtained in 101 days of running at the Chooz Nuclear Power Plant in France, with two 4.25 GW_{th} reactors. The results were obtained from a single 10 m^3 fiducial volume detector located 1050 m from the two reactor cores. The reactor antineutrino flux prediction used the Bugey4 flux measurement after correction for differences in core composition. The deficit can be interpreted as an indication of a non-zero value of the still unmeasured neutrino mixing parameter $\sin^2 2\theta_{13}$. Analyzing both the rate of the prompt positrons and their energy spectrum we find $\sin^2 2\theta_{13} = 0.086 \pm 0.041$ (stat) ± 0.030 (syst), or, at 90% CL, $0.017 < \sin^2 2\theta_{13} < 0.16$.

PACS numbers: 14.60.Pq,13.15.+g,25.30.Pt,95.55.Vj,28.41.Ak
Keywords: neutrino oscillations, neutrino mixing, reactor

We report first results of a search for a non-zero neutrino oscillation [1] mixing angle, θ_{13}, based on reactor antineutrino disappearance. This is the last of the three neutrino oscillation mixing angles [2, 3] for which only upper limits [4, 5] are available. The size of θ_{13} sets the required sensitivity of long-baseline oscillation experiments attempting to measure CP violation in the neutrino sector or the mass hierarchy.

In reactor experiments [6, 7] addressing the disappearance of $\bar{\nu}_e$, θ_{13} determines the survival probability of electron antineutrinos at the "atmospheric" squared-mass difference, Δm^2_{atm}. This probability is given by:

$$P_{surv} \approx 1 - \sin^2 2\theta_{13} \sin^2(1.267 \Delta m^2_{atm} L/E) \,, \qquad (1)$$

where L is the distance from reactor to detector in meters and E the energy of the antineutrino in MeV. The full formula can be found in Ref. [1]. Eq. 1 provides a direct way to measure θ_{13} since the only additional input is the well measured value of $|\Delta m^2_{atm}| = (2.32^{+0.12}_{-0.08}) \times 10^{-3}$ eV^2 [8]. Other running reactor experiments [9, 10] are using the same technique.

Electron antineutrinos of < 9 MeV are produced by reactors and detected through inverse beta decay (IBD): $\bar{\nu}_e + p \rightarrow e^+ + n$. Detectors based on hydrocarbon liquid scintillators provide the free proton targets. The IBD signature is a coincidence of a prompt positron signal followed by a delayed neutron capture. The $\bar{\nu}_e$ energy, $E_{\bar{\nu}_e}$, is reconstructable from E_{prompt}, the positron visible energy ($E_{\bar{\nu}_e} \cong E_{prompt} + 0.78$ MeV).

Recently, indications of non-zero θ_{13} have been reported by two accelerator appearance experiments: T2K [11] and MINOS [12]. Global fits (see e.g. [13, 14]) indicate central values in the range $0.05 < \sin^2 2\theta_{13} < 0.10$, accessible to the Double Chooz experiment [15, 16].

We present here our first results with a detector located $\sim$ 1050 m from the two 4.25 GW_{th} thermal power reactors of the Chooz Nuclear Power Plant and under a 300 MWE rock overburden. The analysis is based on 101 days of data including 16 days with one reactor off and one day with both reactors off.

The antineutrino flux of each reactor depends on its thermal power and, for the four main fissioning isotopes, ^{235}U, ^{239}Pu, ^{238}U, ^{241}Pu, their fraction of the total fuel content, their energy released per fission, and their fission and capture cross-sections. The fission rates and associated errors were evaluated using two predictive and complementary reactor simulation codes: MURE [17, 18] and DRAGON [19]. This allowed a study of the sensitivity to the important reactor parameters (*e.g.*. thermal power, boron concentration, temperatures and densities). The quality of these simulations was evaluated through benchmarks [20], and comparisons with Electricité de France (EDF) assembly simulations. The maximum discrepancies observed were included in the fission rate systematic error.

MURE was used to develop a 3D simulation of the reactor cores. EDF provided the information required to simulate the fission rates including initial burnups of assemblies. To determine the inventories of each assembly composing the core at the startup of the data-taking cycle, assembly simulations were performed and the inventories at the given burnup computed. The energies per fission computed by Kopeikin [21] and nuclear data evaluated from the JEFF3.1 database [22] were used. The evolutions of the core simulations with time were performed using the thermal power and the boron concentration from the EDF database averaged over 48 h time steps, yielding the relative contributions to fissions of the four main isotopes.

The associated antineutrino flux was computed using

* Deceased.

the improved spectra from [23], converted from the ILL reference electron spectra [24–26], and the updated *ab initio* calculation of the ^{238}U spectrum [27]. The ILL spectra were measured after irradiating U or Pu for $\sim$ 1 day. Contributions from β-decays with lifetimes longer than these irradiation times were accounted for as prescribed in [27].

The Double Chooz detector system (Figure 1) consists of a main detector, an outer veto, and calibration devices. The main detector comprises four concentric cylindrical tanks filled with liquid scintillators or mineral oil. The innermost 8 mm thick transparent (UV to visible) acrylic vessel houses the 10 m^3 ν-target liquid, a mixture of n-dodecane, PXE, PPO, bis-MSB and 1 g gadolinium/l as a beta-diketonate complex. The scintillator choice emphasizes radiopurity and long term stability [28]. The ν-target volume is surrounded by the γ-catcher, a 55 cm thick Gd-free liquid scintillator layer in a second 12 mm thick acrylic vessel, used to detect γ-rays escaping from the ν-target. The light yield of the γ-catcher was chosen to provide identical photoelectron (pe) yield across these two layers [29]. Outside the γ-catcher is the buffer, a 105 cm thick mineral oil layer. It shields from radioactivity of photomultipliers (PMTs) and of the surrounding rock, and is one of the major improvements over the CHOOZ experiment [4]. 390 10-inch PMTs [30–32] are installed on the stainless steel buffer tank inner wall to collect light from the inner volumes. These three volumes and the PMTs constitute the inner detector (ID).

Outside the ID, and optically separated from it, is a 50 cm thick "inner veto" liquid scintillator (IV). It is equipped with 78 8-inch PMTs and functions as a cosmic muon veto and as a shield to spallation neutrons produced outside the detector. The detector is surrounded by 15 cm of demagnetized steel to suppress external γ-rays. The main detector is covered by an outer veto system (not used in this analysis).

The readout is triggered by custom energy sum electronics [33–35]. The ID PMTs are separated into two groups of 195 PMTs uniformly distributed throughout the volume and the PMT signals in each group are summed. The signals of the IV PMTs are also summed. If any of the three sums is above a set energy threshold, the detector is read out with 500 MHz flash-ADC electronics [36, 37] with customized firmware and a deadtime-free acquisition system. Upon each trigger, a 256 ns interval of the waveforms of both ID and IV signals is recorded. The low trigger rate (120 Hz) allowed the ID readout threshold to be set at 350 keV, well below the 1.02 MeV minimum energy of an IBD positron, greatly reducing the threshold systematics.

The experiment is calibrated by several methods. A multi-wavelength LED–fiber light injection system (LI) produces fast light pulses illuminating the PMTs from fixed positions. Radio-isotopes ^{137}Cs, ^{68}Ge, ^{60}Co, and ^{252}Cf were deployed in the target along the vertical symmetry axis and, in the gamma catcher, through a rigid loop traversing the interior and passing along boundaries with the target and the buffer. The detector was monitored using spallation neutron captures on H and Gd, residual natural radioactivity, and daily LI runs. The stability of the peak energy of neutron captures on Gd in IBD candidates is shown in Figure 2. The energy response was found to be stable within 1% over time.

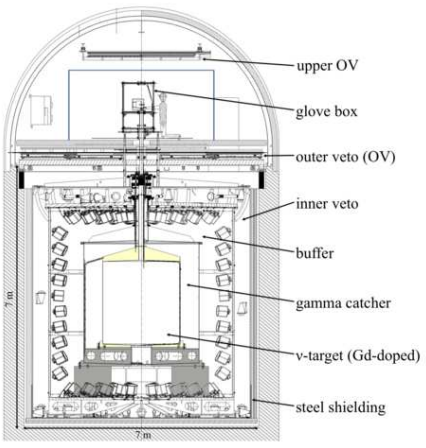

FIG. 1. A cross-sectional view of the Double Chooz detector system.

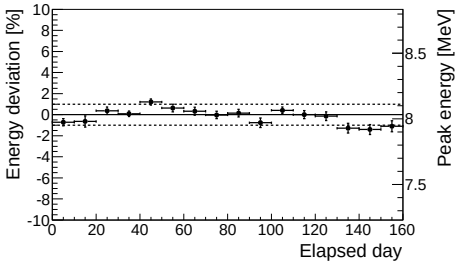

FIG. 2. The peak of the energy of neutron captures on Gd in IBD events(right scale) and its deviation from its average value(left scale) as a function of elapsed(calendar) day.

The signature of IBD events is a delayed coincidence between a prompt positron energy deposition, E_{prompt}, and a delayed energy deposition, E_{delay}, due to the neutron capture on H or Gd within Δt_{e^+n}. The fiducial volume is constrained to the target vessel without position cuts by requiring a $\bar{\nu}_e$ event to have a capture on Gd, identified by its emission of $\sim$ 8 MeV in γ rays. The

analysis compares the number and energy distribution of detected events to a prediction based on the reactor data.

Energy measurements are based on the total charge, Q_{tot}, collected by the PMTs and corrected for gain variations. The energy is reconstructed scaling Q_{tot} by a constant, adjusted so that the energy of the gamma emitted following neutron capture on H reconstructs to 2.22 MeV at the target center. This corresponds to ~ 200 pe/MeV. Our Monte Carlo (MC), based on GEANT4 [38], is used to model the detector response and to calculate its acceptance. It uses parameters for quenching [39], absorption, re–emission, refraction, etc. determined from laboratory measurements of the detector liquids. Comparisons between actual and simulated calibration data were used to develop a parametric function to correct the simulation, and to assess the uncertainties in the energy reconstruction. The function is a product of two factors. One, dependent on energy, ranges from 0.97 to 1.05 for 0.7-10.0 MeV. The other, dependent on position, ranges from 0.94 to 1.00 over the target volume.

The following criteria are applied to select $\bar{\nu}_e$ candidates. Triggers within a 1000 μs window following a cosmic muon crossing the IV or the ID (46 s^{-1}) are rejected to limit spallation neutron and cosmogenic backgrounds. This requirement is followed by five selections: 1) a cut rejecting events caused by some sporadically glowing PMT bases, resulting in light localized to a few PMTs and spread out in time: Q_{max}/Q_{tot} <0.09 (0.06) for the prompt (delayed) energy and rms(t_{start})< 40 ns, where Q_{max} is the maximum charge recorded by a single PMT and rms(t_{start}) is the standard deviation of the times of the first pulse on each PMT; 2) 0.7 MeV<E_{prompt}<12.2 MeV; 3) 6.0 MeV <E_{delay}<12.0 MeV; 4) 2 μs < Δt_{e+n} < 100 μs, where the lower cut eliminates correlated noise and the upper cut is determined by the $\sim$ 30 μs capture time on Gd; 5) a multiplicity cut to reject correlated backgrounds defined as no additional valid trigger from 100 μs preceding the prompt candidate to 400 μs after it. Applying selections (1-5) yields 4121 candidates or 42.6 ± 0.7 events/day, uniformly distributed within the target, for an analysis live time of 96.8 days.

Contributions from background events surviving these cuts have been estimated as follows. Uncorrelated coincidences result mainly from the random association of a prompt energy deposition due to radioactivity (7.6 s^{-1}) and a later candidate neutron capture ($\simeq$20/hour). This background is measured by applying selection cuts (1-5) but modifying selection (4) such that the $2-100$ μs time window is shifted by 1000 μs relative to the prompt trigger. To improve the precision of this background measurement, 198 such windows, each shifted from the previous one by 500 μs, were used, leading to 0.33 ± 0.03 events per day.

Fast neutrons induced by muons traversing the rock can interact in the target producing a recoil proton and, later, be captured, simulating an IBD event. We estimate this rate to be 0.83 ± 0.38 events per day (including a contribution from stopping muons) by applying cuts (1-5), but modifying selection (2) such that 12.2 MeV <E_{prompt}< 30 MeV, and then extrapolating to the signal region, assuming a flat energy spectrum. We account for an uncertainty in this extrapolation, and for the contribution of stopping muons, by including a shape error ranging up to $\pm$70% of the flat extrapolation at lower energies.

^{9}Li β-n emitters are produced preferentially by energetic muons. They were studied by searching for a triple delayed coincidence between a muon depositing > 600 MeV in the detector and a $\bar{\nu}_e$-like pair of events, where the delay between the muon and prompt event is dictated by the 178 ms ^{9}Li halflife, which precludes vetoing on all muons. Fitting the resulting time distribution with a flat component and an exponential with the ^{9}Li lifetime results in an estimated rate of 2.3 ± 1.2 events/day. This rate is assigned the energy spectrum of the ^{9}Li decay branches. A shape uncertainty of up to 20% is introduced to account for uncertainties in some decay branches. ^{8}He is not considered since it is less abundantly produced [40]. The total background rate, 3.46 ± 1.26 d^{-1}, is summarized in Table I.

The overall background envelope is independently verified by analyzing 22.5 hours of both-reactors-off data (< 0.3 residual $\bar{\nu}_e$ events). Two $\bar{\nu}_e$ candidates, with prompt energies of 4.8 MeV and 9.8 MeV, pass cuts (1-5). They were associated within 30 cm and 220 ms with the closest energetic muon, and are thus likely to be associated with ^{9}Li.

TABLE I. The breakdown of the estimated background rate. Additional shape uncertainties are described in the text.

Background	Rate/day	Syst. Uncertainty (% of signal)
Accidental	0.33 ± 0.03	< 0.1
Fast neutron	0.83 ± 0.38	0.9
^{9}Li	2.3 ± 1.2	2.8

The following detector-related corrections and efficiencies as well as their uncertainties were evaluated using the MC. The energy response introduces a 1.7% systematic uncertainty determined from fits to calibration data. The number of free protons in the target scintillator, 6.747×10^{29} based on its weight measurement, has an uncertainty of 0.3%, originating from the knowledge of the scintillator hydrogen ratio. A dedicated simulation including molecular bond effects [41] indicates that the number of IBD events occurring in the gamma catcher with the neutron captured in the target (spill in) exceeds the number of events in the target with the neutron escaping to the gamma catcher (spill out) by $1.4\% \pm 0.4\%$, 0.8% lower than our standard MC prediction which was therefore reduced accordingly. Above the 700 keV analysis threshold, the trigger efficiency is $100.0^{+0}_{-0.4}\%$, assessed with a low threshold prescaled trigger. Calibration data taken with the ^{252}Cf source were used to check the MC for any biases in the neutron selection criteria

and estimate their contributions to the systematic uncertainty. The fraction of neutron captures on Gd is found to be $(86.0 \pm 0.5)\%$ near the center of the target, 2.0% lower than the simulation prediction which was reduced accordingly with a relative systematic uncertainty of 0.6%. The simulation reproduces the 96.5% efficiency of the Δt_{e^+n} cut with an uncertainty of 0.5% and the 94.5% fraction of neutron captures on Gd accepted by the 6.0 MeV cut with an uncertainty of 0.6%. The MC normalization was adjusted for the muon veto (-4.5%) and the multiplicity veto (-0.5%) dead-times.

TABLE II. Contributions of the detector and reactor errors to the absolute normalization systematic uncertainty.

Detector		Reactor	
Energy response	1.7%	Bugey4 measurement	1.4%
E_{delay} Containment	0.6%	Fuel Composition	0.9%
Gd Fraction	0.6%	Thermal Power	0.5%
Δt_{e^+n}	0.5%	Reference Spectra	0.5%
Spill in/out	0.4%	Energy per Fission	0.2%
Trigger Efficiency	0.4%	IBD Cross Section	0.2%
Target H	0.3%	Baseline	0.2%
Total	2.1 %	Total	1.8%

The full covariance matrix of the emitted $\bar{\nu}_e$ spectra was computed as prescribed in [27]. MURE provided the fractions of fissions per isotope ^{235}U=48.8%, ^{239}Pu=35.9%, ^{241}Pu=6.7%, and ^{238}U=8.7% and the fission rate covariance matrix. The resulting relative uncertainties on the above fission fractions are $\pm 3.3\%$, $\pm 4\%$, $\pm 11.0\%$ and $\pm 6.5\%$, respectively. The error associated with the thermal power is $\pm 0.46\%$ at full power [42, 43], fully correlated between the two cores.

To avoid being affected by possible very short baseline $\bar{\nu}_e$ oscillations [4, 44, 45], we adopt the reactor $\bar{\nu}_e$ spectrum of [23, 27], but the global normalization is fixed by the Bugey4 rate measurement [46] with its associated 1.4% uncertainty. A relative correction of $(0.9 \pm 1.3\%)$ of the Bugey4 value accounts for the difference in core inventories. The IBD differential cross section is taken from [47], using 881.5 ± 1.5 s [1] as the neutron lifetime. The systematic uncertainties are summarized in Table II. The expected no-oscillation number of $\bar{\nu}_e$ candidates is 4344 ± 165, including background.

The measured daily rate of IBD candidates as a function of the no-oscillation expected rate for different reactor power conditions is shown in Figure 3. The extrapolation to zero reactor power of the fit to the data (including the both-reactors-off) yields 3.2 ± 1.3 events per day, in excellent agreement with our background estimate and the both-reactors-off data.

Our measurement can be expressed as an observed IBD cross section per fission, σ_f^{DC}, a quantity which depends on the number of events observed, the number of target protons, the detector efficiency, the number of fissions occurring during our measurement and the distance to the reactors, yielding $\sigma_f^{DC} = (5.383 \pm 0.210)\, 10^{-43}$ cm^2/fission. The Bugey4

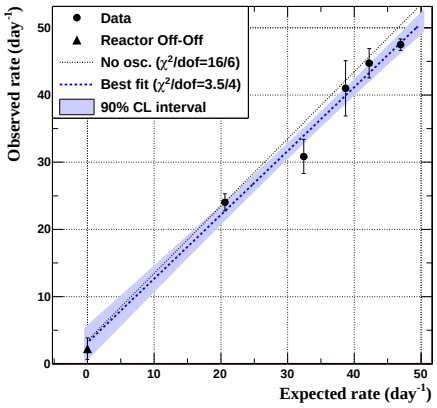

FIG. 3. Daily number of $\bar{\nu}_e$ candidates as a function of the expected number of $\bar{\nu}_e$. The dashed line is a fit to the data, the band is the 90% C.L. of this fit. The dotted line is the expectation in the no-oscillation scenario. The triangle indicates the measurement with both reactors off.

measurement, corrected to match our fractions of isotopes quoted above, yields a cross section per fission of $(5.703 \pm 0.108)\, 10^{-43}$ cm^2/fission. The ratio of these two measurements is independent of any possible very short baseline oscillations. (Without Bugey4 normalization, the prediction, for our running conditions and using the reference spectra [23, 27], is $(6.209 \pm 0.170)\, 10^{-43}$ cm^2/fission).

The ratio of observed to expected events is $R_{DC} = 0.944 \pm 0.016$ (stat) ± 0.040 (syst), corresponding to $\sin^2 2\theta_{13} = 0.104 \pm 0.030$ (stat) ± 0.076 (syst) for $\Delta m^2_{13} = 2.4 \times 10^{-3}$ eV^2.

The analysis is improved by comparing the positron spectrum in 18 variably sized energy bins between 0.7 and 12.2 MeV to the expected number of $\bar{\nu}_e$ events, again using $\Delta m^2_{13} = 2.4 \times 10^{-3}$ eV^2. The analysis, performed with a standard χ^2 estimator, uses four covariance matrices to include uncertainties in the antineutrino signal, detector response, signal and background statistics, and background spectral shape. With very few positrons expected above 8 MeV, the region $8-12.2$ MeV reduces the uncertainties in the correlated backgrounds with some additional contribution to the statistical uncertainty.

The best fit results in $\sin^2 2\theta_{13} = 0.086 \pm 0.041$ (stat) ± 0.030 (syst) with a χ^2/DOF of 23.7/17, whereas the $\sin^2 2\theta_{13} = 0.0$ hypothesis results in a χ^2/DOF of 26.6/18. Using a frequentist approach [48] we find an allowed region of $0.017 < \sin^2 2\theta_{13} < 0.16$ at 90% CL, and exclude the no

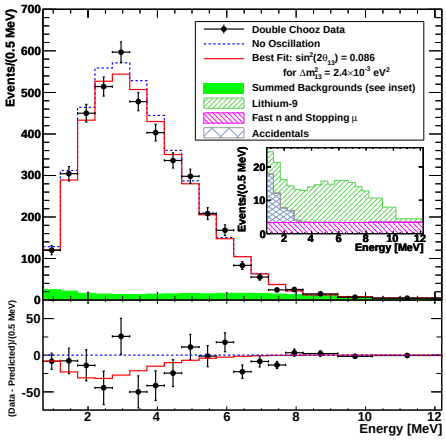

FIG. 4. Top: Expected prompt energy spectra, including backgrounds, for the no-oscillation case and for the best fit $\sin^2 2\theta_{13}$, superimposed on the measured spectrum. Inset: stacked histogram of backgrounds. Bottom: Difference between data and the no-oscillation spectrum (data points) and difference between the best fit and no-oscillation expectations (curve)

oscillation hypothesis at the 94.6% C.L.

We determine our best estimate of the $\bar{\nu}_e$ and background rates with a pulls-based approach [49], the results of which are shown in Table III. From the best fit we obtain a contribution from ^{9}Li reduced by ∼19%, and with an uncertainty decreased from 52% to 26%. The fast neutron value is decreased by 5% with almost unchanged uncertainty.

TABLE III. Summary of the effect of a pulls term approach on the fast neutron and ^{9}Li backgrounds and on the energy scale. Uncertainty values are in parentheses.

	Fast n. Bkg(%)	^{9}Li (%)	EScale (value)
Rate only	100 (46)	100 (52)	0.997 (0.007)
Rate + Shape	95.2 (38)	81.5 (25.5)	0.998 (0.005)

Figure 4 shows the measured positron spectrum superimposed on the expected spectra for the no-oscillation hypothesis and for the best fit (including fitted backgrounds).

Combining our result with the T2K [11] and MINOS [12] measurements leads to $0.003 < \sin^2 2\theta_{13} < 0.219$ at the 3σ level.

In summary, Double Chooz has searched for $\bar{\nu}_e$ disappearance using a 10 m^3 detector located 1050 m from two reactors. A total of 4121 events were observed where 4344 ± 165 were expected for no-oscillation, with a signal to background ratio of ≈11:1. In the context of neutrino oscillations, this deficit leads to $\sin^2 2\theta_{13} = 0.086 \pm 0.041$ (stat) $\pm$ 0.030 (syst), based on an analysis using rate and energy spectrum information. The no-oscillation hypothesis is ruled out at the 94.6% C.L. Double Chooz continues to run, to reduce statistical and background systematic uncertainties. A near detector will soon lead to reduced reactor and detector systematic uncertainties and to an estimated 1σ precision on $\sin^2 2\theta_{13}$ of ~ 0.02.

We thank all the technical and administrative people who helped build the experiment and the CCIN2P3 computer center for their help and availability. We thank, for their participation, the French electricity company EDF, the European fund FEDER, the Région de Champagne Ardenne, the Département des Ardennes and the Communauté des Communes Rives de Meuse. We acknowledge the support of CEA and CNRS/IN2P3 in France, MEXT and JSPS of Japan, the Department of Energy and the National Science Foundation of the United States, the Ministerio de Ciencia e Innovación (MICINN) of Spain, the Max Planck Gesellschaft and the Deutsche Forschungsgemeinschaft DFG (SBH WI 2152), the Transregional Collaborative Research Center TR27, the Excellence Cluster "Origin and Structure of the Universe" and the Maier-Leibnitz-Laboratorium Garching, the Russian Academy of Science, the Kurchatov Institute and RFBR (the Russian Foundation for Basic Research), the Brazilian Ministry of Science, Technology and Innovation (MCTI), the Financiadora de Estudos e Projetos (FINEP), the Conselho Nacional de Desenvolvimento Científico e Tecnológico (CNPq), the São Paulo Research Foundation (FAPESP) and the Brazilian Network for High Energy Physics (RENAFAE) in Brazil.

[1] K. Nakamura et al., J. Phys. G **37**, 075021 (2010).
[2] B. Pontecorvo, JETP **34**, 172 (1958).
[3] Z. Maki, M.Nakagawa, and S. Sakata, Prog. Theor. Phys. **28**, 870 (1962).
[4] M. Appolonio et al., Phys. Lett. **B466**, 415 (1999).
[5] F. Boehm et al., Phys.Rev. Lett. **84**, 3764 (2000).
[6] H. Minakata, H. Sugiyama, O. Yasuda, K. Inoue, and F. Suekane, Phys. Rev. D **68**, 033017 (2003), URL `http://link.aps.org/doi/10.1103/PhysRevD.68.033017`.
[7] H. Minakata, H. Sugiyama, O. Yasuda, K. Inoue, and F. Suekane, Phys. Rev. D **70**, 059901 (2004), URL `http://link.aps.org/doi/10.1103/PhysRevD.70.059901`.
[8] P. Adamson et al. (MINOS Collaboration), Phys. Rev. Lett. **106**, 181801 (2011).
[9] X. Guo et al. (Daya Bay Collaboration) (2006), arXiv:hep-ex/0701029.
[10] J. K. Ahn et al. (RENO Collaboration) (2010), arXiv:hep-ex/1003.1391.
[11] K. Abe et al. (T2K Collaboration), Phys. Rev. Lett. **107**, 041801 (2011).

[12] P. Adamson et al., Phys. Rev. Lett. **107**, 181802 (2011), hep-ex/1108.0015v1.
[13] T. Schwetz et al. (2011), arXiv:hep-ph/1108.1376v1.
[14] G. L. Fogli et al. (2011), arXiv:hep-ph/1106.6028v2.
[15] F. Ardellier et al. (Double Chooz Collaboration) (2006), hep-ex/0606025v4.
[16] G. Mention, Ph.D. thesis (2005), URL `http://tel.archives-ouvertes.fr/tel-00010528/fr/`.
[17] O. Meplan, Tech. Rep. LPSC 0912 and IPNO-09-01 (2009).
[18] MURE, *Mcnp utility for reactor evolution: couples monte-carlo transport with fuel burnup calculations* (2009), URL `http://www.nea.fr/tools/abstract/detail/nea-1845`.
[19] R. R. G. Marleau and A. Hebert, Tech. Rep. IGE-157 (1994).
[20] C. Jones et al. (2011), arXiv:nucl-ex/1109.5379v1.
[21] V. Kopeikin et al., *Reactor as a source of antineutrinos: Thermal fission energy* (2004), hep-ph/0410100v1.
[22] *Jeff and eff projects http://www.oecd-nea.org/dbdata/jeff/*, URL `http://www.oecd-nea.org/dbdata/jeff/`.
[23] P. Huber, Phys. Rev. C **84**, 024617 (2011).
[24] W. G. K. Schreckenbach, G. Colvin and F. von Feilitzsch, Phys. Lett. B **160** (1985).
[25] A. F. von Feilitzsch and K. Schreckenbach, Phys. Lett. B **118** (1982).
[26] A. A. Hahn et al., Phys. Lett. B **218** (1989).
[27] T. Mueller et al., Phys. Rev. C **83**, 054615 (2011).
[28] C. Aberle et al., *Large scale gadolinium-beta-diketonate based organic liquid scintillator production for antineutrino detection.* (2011), arXiv:1112.5941. Submitted to JINST.
[29] C. Aberle et al., Chem. Phys. Lett. **516**, 257 (2011).
[30] T. Matsubara et al., Nucl. Instrum. Meth. in Physics Research **A661**, 16 (2011), 1104.0786[phys.ins-det].
[31] C. Bauer et al., JINST **6**, P06008 (2011), 1104.0758.
[32] E. Calvo et al., Nucl. Instrum. Meth. in Physics Research **A621**, 222 (2010), 0905.3246[phys.ins-det].
[33] C. Kuhnt, Master's thesis (2010), URL `http://www.physik.rwth-aachen.de/fileadmin/user_upload/www_physik/Institute/Inst_3B/Fo`
[34] F. Beissel et al., *The trigger and timing system of the double chooz experiment. in preparation.*
[35] B. Reinhold, Ph.D. thesis, RWTH Aachen University (2009).
[36] A. Cabrera et al., Nucl. Instrum. Meth. in Physics Research **A617**, 473 (2010).
[37] T. Akiri, Ph.D. thesis (2010), URL `http://tel.archives-ouvertes.fr/tel-00580175/fr/`.
[38] S. Agostinelli et al., Nucl.Instrum.Meth. in Physics Research **A506**, 250 (2003).
[39] C. Aberle et al., JINST **6**, P11006 (2011).
[40] S. Abe et al., Phys. Rev. C **81**, 025807 (2010).
[41] J. P. Both et al., Tech. Rep. CEA-REPORT: CEA-R-6044, DTI, CEA/Saclay, France (2003).
[42] S. F. E. Tournu et al., EPRI 2001.1001470, Palo Alto, CA. (2001).
[43] Standard AFNOR XP X 07-020, Palo Alto, CA. (1996).
[44] G. Mention et al., Phys. Rev. D **83**, 073006 (2011).
[45] C. Giunti and M. Laveder (2011), hep-ph/1111.5211v2.
[46] Y. Declais et al., Phys. Lett. **B338**, 383 (1994).
[47] P. Vogel and J. F. Beacom, Phys. Rev. D **60**, 053003 (1999).
[48] G. J. Feldman and R. D. Cousins, Phys. Rev. D **57**, 3873 (1998).
[49] D. Stump et al., Phys. Rev. D **65**, 014012 (Appendix B) (2001).

K.2 Second Double Chooz Publication

This section contains a facsimile of the second Double Chooz publication, published as [8].

Reactor $\bar{\nu}_e$ disappearance in the Double Chooz experiment

Y. Abe,[30] C. Aberle,[21] J.C. dos Anjos,[5] J.C. Barriere,[15] M. Bergevin,[9] A. Bernstein,[16] T.J.C. Bezerra,[28] L. Bezrukhov,[14] E. Blucher,[6] N.S. Bowden,[16] C. Buck,[21] J. Busenitz,[2] A. Cabrera,[4] E. Caden,[10] L. Camilleri,[8] R. Carr,[8] M. Cerrada,[7] P.-J. Chang,[17] P. Chimenti,[33] T. Classen,[9,16] A.P. Collin,[15] E. Conover,[6] J.M. Conrad,[20] J.I. Crespo-Anadón,[7] K. Crum,[6] A. Cucoanes,[25,15] M.V. D'Agostino,[3] E. Damon,[10] J.V. Dawson,[4,36] S. Dazeley,[16] D. Dietrich,[32] Z. Djurcic,[3] M. Dracos,[24] V. Durand,[15,4] J. Ebert,[11] Y. Efremenko,[27] M. Elnimr,[25] A. Etenko,[19] M. Fallot,[25] M. Fechner,[15] F. von Feilitzsch,[26] J. Felde,[9] D. Franco,[4] A.J. Franke,[8] M. Franke,[26] H. Furuta,[28] R. Gama,[5] I. Gil-Botella,[7] L. Giot,[25] M. Göger-Neff,[26] L.F.G. Gonzalez,[34] M.C. Goodman,[3] J.TM. Goon,[2] D. Greiner,[32] N. Haag,[26] C. Hagner,[11] T. Hara,[18] F.X. Hartmann,[21] J. Haser,[21] A. Hatzikoutelis,[27] T. Hayakawa,[22] M. Hofmann,[26] G.A. Horton-Smith,[17] A. Hourlier,[4] M. Ishitsuka,[30] J. Jochum,[32] C. Jollet,[24] C.L. Jones,[20] F. Kaether,[21] L.N. Kalousis,[24] Y. Kamyshkov,[27] D.M. Kaplan,[13] T. Kawasaki,[22] G. Keefer,[16] E. Kemp,[34] H. de Kerret,[4,36] Y. Kibe,[30] T. Konno,[30] D. Kryn,[4] M. Kuze,[30] T. Lachenmaier,[32] C.E. Lane,[10] C. Langbrandtner,[21] T. Lasserre,[15,4] A. Letourneau,[15] D. Lhuillier,[15] H.P. Lima Jr,[5] M. Lindner,[21] J.M. López-Castanõ,[7] J.M. LoSecco,[23] B.K. Lubsandorzhiev,[14] S. Lucht,[1] D. McKee,[17] J. Maeda,[31] C.N. Maesano,[9] C. Mariani,[8,35] J. Maricic,[10] J. Martino,[25] T. Matsubara,[31] G. Mention,[15] A. Meregaglia,[24] T. Miletic,[10] R. Milincic,[10] H. Miyata,[22] Th.A. Mueller,[28] Y. Nagasaka,[12] K. Nakajima,[22] P. Novella,[7] M. Obolensky,[4] L. Oberauer,[26] A. Onillon,[25] A. Osborn,[27] I. Ostrovskiy,[2] C. Palomares,[7] I.M. Pepe,[5] S. Perasso,[10] P. Perrin,[15] P. Pfahler,[26] A. Porta,[25] W. Potzel,[26] J. Reichenbacher,[2] B. Reinhold,[21] A. Remoto,[25,4] M. Röhling,[32] R. Roncin,[4] S. Roth,[1] Y. Sakamoto,[29] R. Santorelli,[7] F. Sato,[31] S. Schönert,[26] S. Schoppmann,[1] T. Schwetz,[21] M.H. Shaevitz,[8] S. Shimojima,[31] D. Shrestha,[17] J-L. Sida,[15] V. Sinev,[14,15] M. Skorokhvatov,[19] E. Smith,[10] J. Spitz,[20] A. Stahl,[1] I. Stancu,[2] L.F.F. Stokes,[32] M. Strait,[6] A. Stüken,[1] F. Suekane,[28] S. Sukhotin,[19] T. Sumiyoshi,[31] Y. Sun,[2] R. Svoboda,[9] K. Terao,[20] A. Tonazzo,[4] M. Toups,[8] H.H. Trinh Thi,[26] G. Valdiviesso,[5] C. Veyssiere,[15] S. Wagner,[21] H. Watanabe,[21] B. White,[27] C. Wiebusch,[1] L. Winslow,[20] M. Worcester,[6] M. Wurm,[11] F. Yermia,[25] and V. Zimmer[26]

(Double Chooz Collaboration)

[1] *III. Physikalisches Institut, RWTH Aachen University, 52056 Aachen, Germany*
[2] *Department of Physics and Astronomy, University of Alabama, Tuscaloosa, Alabama 35487, USA*
[3] *Argonne National Laboratory, Argonne, Illinois 60439, USA*
[4] *APC, AstroParticule et Cosmologie, Université Paris Diderot, CNRS/IN2P3, CEA/IRFU, Observatoire de Paris, Sorbonne Paris Cité, 75205 Paris Cedex 13, France*
[5] *Centro Brasileiro de Pesquisas Fisicas, Rio de Janeiro, RJ, cep 22290-180, Brazil*
[6] *The Enrico Fermi Institute, The University of Chicago, Chicago, IL 60637, USA*
[7] *Centro de Investigaciones Energéticas, Medioambientales y Tecnológicas, CIEMAT, E-28040, Madrid, Spain*
[8] *Columbia University; New York, NY 10027, USA*
[9] *University of California, Davis, CA-95616-8677, USA*
[10] *Physics Department, Drexel University, Philadelphia, Pennsylvania 19104, USA*
[11] *Institut für Experimentalphysik, Universität Hamburg, 22761 Hamburg, Germany*
[12] *Hiroshima Institute of Technology, Hiroshima, 731-5193, Japan*
[13] *Department of Physics, Illinois Institute of Technology, Chicago, Illinois 60616, USA*
[14] *Institute of Nuclear Research of the Russian Academy of Science, Russia*
[15] *Commissariat à l'Energie Atomique et aux Energies Alternatives, Centre de Saclay, IRFU, 91191 Gif-sur-Yvette, France*
[16] *Lawrence Livermore National Laboratory, Livermore, CA 94550, USA*
[17] *Department of Physics, Kansas State University, Manhattan, Kansas 66506, USA*
[18] *Department of Physics, Kobe University, Kobe, 657-8501, Japan*
[19] *NRC Kurchatov Institute, 123182 Moscow, Russia*
[20] *Massachusetts Institute of Technology; Cambridge, MA 02139, USA*
[21] *Max-Planck-Institut für Kernphysik, 69117 Heidelberg, Germany*
[22] *Department of Physics, Niigata University, Niigata, 950-2181, Japan*
[23] *University of Notre Dame, Notre Dame, IN 46556- 5670, USA*
[24] *IPHC, Université de Strasbourg, CNRS/IN2P3, F- 67037 Strasbourg, France*
[25] *SUBATECH, CNRS/IN2P3, Université de Nantes, Ecole des Mines de Nantes, F-44307 Nantes, France*
[26] *Physik Department, Technische Universität München, 85747 Garching, Germany*
[27] *Department of Physics and Astronomy, University of Tennessee, Knoxville, Tennessee 37996, USA*
[28] *Research Center for Neutrino Science, Tohoku University, Sendai 980-8578, Japan*
[29] *Tohoku Gakuin University, Sendai, 981-3193, Japan*
[30] *Department of Physics, Tokyo Institute of Technology, Tokyo, 152-8551, Japan*
[31] *Department of Physics, Tokyo Metropolitan University, Tokyo, 192-0397, Japan*
[32] *Kepler Center for Astro and Particle Physics, Universität Tübingen, 72076, Tübingen, Germany*
[33] *Universidade Federal do ABC, UFABC, Saõ Paulo, Santo André, SP, Brazil*

[34] Universidade Estadual de Campinas-UNICAMP, Campinas, SP, Brazil
[35] Center for Neutrino Physics, Virginia Tech, Blacksburg, VA
[36] Laboratoire Neutrino de Champagne Ardenne, domaine d'Aviette, 08600 Rancennes, France
(Dated: August 31, 2012)

The Double Chooz experiment has observed 8,249 candidate electron antineutrino events in 227.93 live days with 33.71 GW-ton-years (reactor power × detector mass × livetime) exposure using a 10.3 m^3 fiducial volume detector located at 1050 m from the reactor cores of the Chooz nuclear power plant in France. The expectation in case of θ_{13}= 0 is 8,937 events. The deficit is interpreted as evidence of electron antineutrino disappearance. From a rate plus spectral shape analysis we find $\sin^2 2\theta_{13} = 0.109 \pm 0.030(\text{stat}) \pm 0.025(\text{syst})$. The data exclude the no-oscillation hypothesis at 99.8% CL (2.9σ).

I. INTRODUCTION

In the three neutrino paradigm, there are three mixing angles that can be measured in neutrino oscillation experiments. For many years, the CHOOZ reactor neutrino experiment [1] had the best limit on the value of θ_{13}. Recently, the value of θ_{13} has been shown to be non-zero by the combination of fits to KamLAND and solar [2–4], MINOS [5], T2K [6] and, more precisely, by the new generation of reactor antineutrino disappearance experiments: Double Chooz [7], Daya Bay [8] and RENO [9].

The Double Chooz analysis is unique among reactor experiments in its fit to the energy spectrum. In the previous reactor measurements of θ_{13}, Double Chooz presented both a rate-only analysis and an analysis using both the rate and the shape of the energy spectrum, while Daya Bay and RENO presented rate-only analyses. The disappearance of reactor electron antineutrinos has a well-defined effect on the shape of that spectrum. The use of the energy distribution to constrain the oscillation parameters requires a good understanding of the energy response of the detector and of the accuracy of the Monte Carlo. That understanding is achieved through multiple calibration techniques, in time, space and energy.

This paper continues the analysis reported in [7] with a larger data set, a new energy scale definition, reduced background rates and improved systematic uncertainties. Additionally, the running period has been subdivided into a two-reactor-on period and a one-reactor-on period in the oscillation fit to help separate signal and background.

Reactor antineutrinos are observed using the inverse beta decay (IBD) reaction $\bar{\nu}_e + p \rightarrow e^+ + n$ in which there is a positron whose signal is promptly seen, and a neutron, whose delayed signal is seen after a mean time of about 30 μs from its capture in the gadolinium-doped target. The prompt energy of the positron allows us to determine the antineutrino energy and observe the antineutrino spectrum. The energy deposited by the positron including annihilation is related to antineutrino energy $E_{\bar{\nu}_e}$ by $E_{\text{prompt}} = E_{\bar{\nu}_e} - T_n - 0.8$ MeV where T_n denotes the average neutron recoil energy and is small compared to $E_{\bar{\nu}_e}$.

The previous analysis represented 15.34 GW-ton-years of exposure, taking into account the reactor livetime and the detector fiducial mass. Here we re-analyze that data set together with an additional 18.37 GW-ton-years giving a total of 33.71 GW-ton-years. In addition the analysis of 22.5 hours of both-reactors-off data allows a cross check of our estimates of the correlated and accidental backgrounds.

The structure of the paper is as follows. In Section II we review the experimental setup and detector. Section III covers the measurements and simulations of the Chooz reactors used to predict the unoscillated neutrino spectrum, as well as the model used to describe the detector. Event reconstruction including the energy determination of candidate events is described in Section IV. The steps that are used to identify reactor neutrino candidates are covered in Section V. Section VI presents the extraction of neutrino mixing parameters from the measured antineutrino rate and energy distribution.

II. DETECTOR AND METHOD DESCRIPTION

A. Overview

The Double Chooz detector system [10] consists of a main detector, an outer veto, and calibration devices (Figure 1). The main detector is made of four concentric cylindrical tanks with a chimney in the center at the top and is filled with liquid scintillators or mineral oil.

The innermost 8 mm thick transparent (UV to visible) acrylic vessel contains 10.3 m^3 gadolinium loaded liquid scintillator called the ν-target (NT). The NT volume is surrounded by the γ-catcher (GC), a 55 cm thick Gd-free liquid scintillator layer in a second 12 mm thick acrylic vessel, used to detect gamma rays escaping from the ν-target. Outside the γ-catcher is the buffer, a 105 cm thick mineral oil layer. It shields from radioactivity of photomultiplier tubes (PMTs) and surrounding rock, and is one of the major improvements over the CHOOZ experiment [1]. The 390 10-inch PMTs [11–13] are installed on the inner wall of the stainless steel buffer tank to collect light from the inner volumes. These three volumes and PMTs constitute central detector system referred to as the inner detector (ID). Outside the ID, and optically separated from it by a stainless steel vessel, is a 50 cm thick inner veto (IV) liquid scintillator. It is equipped with 78 8-inch PMTs and functions as a cosmic muon

veto and as an active shield to spallation neutrons produced outside the detector. The detector is covered and surrounded by 15 cm of demagnetized steel to suppress external gamma rays. The main detector is covered by an outer veto system (OV) described in Section II G.

B. Radiopurity

All parts of the Double Chooz detector have been thoroughly screened for their content of radioactive isotopes prior to their installation. The screening was carried out by direct gamma spectroscopy with a variety of germanium detectors in underground laboratories. Among them were the large HPGe detector for the non-destructive radioassay at Saclay [14] and the GeMPI detector at Gran Sasso [15] with a sensitivity of about $10\,\mu$Bq/kg for U and Th. In addition, neutron activation analyses have been performed for dedicated parts of the inner detector: the acrylics for NT and GC vessels as well as the wavelength shifter PPO [16]. The irradiations were done at the FRM II research reactor in Garching, Germany by a thermal neutron flux of $1.63{\cdot}10^{13}\,\mathrm{cm}^{-2}{\cdot}\mathrm{s}^{-1}$, with subsequent gamma spectroscopy in the Garching underground laboratory [17].

The PMT glass and cavern rock are the main sources of the gamma ray background. The PMT glass was made from low activity sands using a platinum coated furnace to reduce contamination. Radioactivity of the glass samples was measured during development of the low activity glass and production of the PMTs [18]. The average measurements were 13 ppb, 61 ppb and 3.3 ppb for ^{238}U, ^{232}Th and ^{40}K, respectively assuming radio-equilibrium, which are much smaller than regular PMT glass.

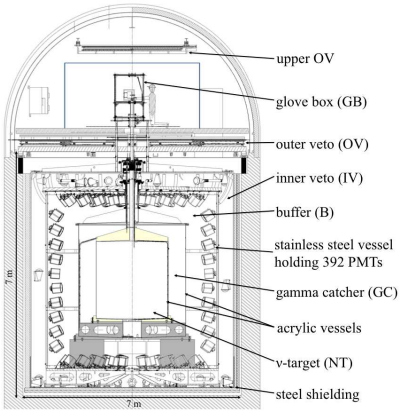

FIG. 1. A cross-sectional view of the Double Chooz detector system.

The design goal of Double Chooz concerning radiopurity is no more than ∼0.8 accidental background events per day. Along with the radiopurity screenings, Double Chooz maintained strict clean-room conditions during the setup of the detector with an ISO-level up to 6. The analysis of BiPo coincidences in the detector data yields concentrations of U and Th in NT and GC below the design goal of 10^{-13} g/g. The accidentals rate is measured to be $< 0.5\ \mathrm{d}^{-1}$, well below our design goal. The daily rate of correlated background events stemming from (α, n)-reactions of ^{210}Po on ^{13}C is estimated to be smaller than $0.020\ \mathrm{d}^{-1}$ (scaled from the result of KamLAND [19]), which is negligibly small compared to the neutrino signal.

C. Double Chooz Liquids

The CHOOZ experiment was limited in sensitivity by the optical instability of its gadolinium-loaded (Gd) scintillator [20]. Therefore a new type of metal loaded organic liquid scintillator was developed for Double Chooz [16]. The target scintillator used in the NT must fulfill the basic requirements of Gd solubility in the solvent of choice, optical transparency, radiopurity and chemical stability. In addition, the organic liquid must be compatible with the detector materials in contact with the scintillator, mainly acrylics. Safety considerations influenced the scintillator design as well.

Since the rare earth Gd does not dissolve in the required amount in the organic solvents used for liquid scintillators, a metalorganic complex is formed providing higher solubility. In particular, the complex of choice is a metal-β-diketone, Gd(thd)$_3$, Gd(III)-tris-(2,2,6,6-tetramethyl-heptane-3,5-dionate). Such complexes are known for their stability and high vapor pressure. This allowed us to purify the material by sublimation reducing radioimpurities U, Th and K. The Gd concentration in the NT is 0.123% by weight, which corresponds to about 1 g/liter.

As scintillator solvent for the NT we have chosen an ortho-phenylxylylethane (o-PXE)/n-dodecane mixture at a volume ratio of 20/80. To shift the scintillation light into a more transparent region, wavelength shifters are added. In both scintillators we use PPO (2,5-diphenyloxazole) as primary fluor and bis-MSB (4-bis-(2-methylstyryl)benzene) as secondary wavelength shifter.

The light yield and density of the GC liquid ($22.5\ \mathrm{m}^3$) were matched simultaneously to the NT values [21]. To achieve this goal, a medicinal white oil was added as a third solvent to the GC. The light yield of the GC is optimized for homogeneous detector response using Monte Carlo simulations. To avoid mechanical stress on the detector vessels the densities of all four detector liquids were matched at the detector temperature of about 15 °C to $0.804 \pm 0.001\ \mathrm{g/cm}^3$.

The attenuation lengths for wavelengths in the region of scintillator emission are well above the dimensions of

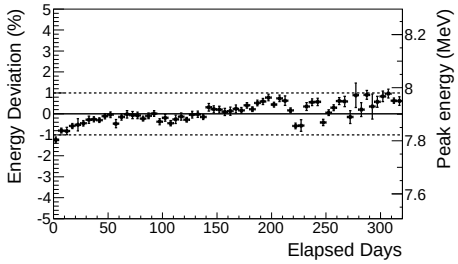

FIG. 2. Average target detector response evolution in time, as measured by the mean energy of the Gd-capture peak arising from interaction of spallation neutrons in the NT.

the corresponding vessels. Optical stability of the scintillators is demonstrated in Figure 2, where the stability of the peak energy of neutron captures on Gd is shown. The energy response of the detector was found to be stable within 1% over the data-taking period of about one year.

The absolute number of H nuclei ("proton number") as well as the precision on its knowledge are crucial parameters. The error on the proton number is minimized by using well defined and pure chemicals in combination with a precise knowledge of the weights of each chemical added in the scintillator production. The amount of NT scintillator was determined after thermalization by a weight measurement with a precision of 0.04%. The hydrogen fraction in the NT is 13.6% by weight, known with 0.3% relative precision. This error includes the uncertainties originating from the weights of the scintillator ingredients. In addition, the error takes into account the knowledge of the hydrogen content of not fully defined impurities in the chemicals which are on the per mil level for the main components [16].

A mixture of solvents was used in all detector volumes to allow for density matching. The 110 m^3 of buffer liquid contain a medicinal white oil (53% by volume) and an n-alkane mixture (47% by volume). This liquid was optimized for transparency and low aromaticity to minimize scintillation light production in the buffer. The veto volume is filled with 90 m^3 of liquid scintillator, a mixture of linear alkyl benzene (LAB) and n-alkanes, with 2 g/l PPO as fluor and 20 mg/l bis-MSB as secondary wavelength shifter.

D. ID Photomultiplier Tubes

The inner detector uses 390 Hamamatsu R7081 10-inch PMTs [22] to view the target volume. The glass is a low background type, contributing only a few Hz of singles rate in the detector. The PMTs are operated with a gain of 10^7 at the PMT anode. They are submerged in a paraffin oil buffer liquid. The base circuit is enclosed in a transparent epoxy resin. Some PMTs are observed to generate light flashes from their base circuit through the epoxy resin, causing false triggers. HV for the 14 worst PMTs was turned off. Since the signal pattern is different from that of the neutrino signal, the false events are safely removed from the neutrino sample as described in Section IV D. The 800 PMTs for both this and an eventual near detector were characterized carefully [11, 12, 23]. The following characteristics were measured: for one photoelectron signals, the ratio of the one photoelectron peak to the valley between that peak and the pedestal was 4, with 1/4 photoelectron thresholds; the quantum efficiency × collection efficiency (efficiency that photoelectrons produced in the cathode are collected by the first dynode) was 23%; transit time spread was 3 ns (FWHM); the afterpulse probability was in average 2.7%; the charge output was linear up to 300 photoelectrons per PMT; dark hit rate was approximately 2 kHz measured 20 hours after turning on the HV. Each PMT is shielded by a mu-metal cylinder to suppress effects from the gamma shield and the earth's magnetic field [13] and is equipped with an angle-adjustable mounting jig. The PMTs are angled to collect light more uniformly from the detector.

E. The Inner Veto

The IV is a cylindrical stainless steel vessel (radius 3.3 m and height 6.8 m) surrounding the ID and optically separated by the buffer tank. It shields the ID with a 50 cm thick layer of liquid scintillator against external radioactivity and spallation neutrons created by cosmic muons. At the same time it acts as an active detector identifying cosmic muons crossing it. The design of the IV was optimized by the use of a MC simulation [24], where the emphasis was on a high number of detected photoelectrons (PE) per MeV deposited in the IV volume and on a high efficiency in rejecting muons and correlated background events produced by them. The resulting configuration of the IV consists of 78 PMTs, divided into three parts: the top has 24 PMTs, the side walls have 12 PMTs at the mid way point and the bottom has 42 PMTs. The 78 8-inch PMTs (Hamamatsu R 1408), which were previously used in the IMB and Super-Kamiokande experiments, were tested and modified for use in Double Chooz [25]. Each IV PMT and its base are contained in a stainless steel encapsulation, with a transparent PET window at the front end. The capsules are filled with mineral oil to match the optical properties of the surrounding scintillator. All surfaces of the IV are painted with highly reflective white coating (AR100/CLX coating from MaxPerles [26]), the side walls of the buffer vessel are covered with reflective VM2000 sheets. Using the OV, the muon rejection efficiency was found to be larger than 99.99% for muons

crossing the IV volume.

F. Electronics and Data Acquisition

The full readout and data acquisition (DAQ) for both the ID and the IV detectors are depicted in Figure 3. The functional principle is that digitization of PMT signals (see Section II D) is done by flash-ADC electronics. As shown in Figure 3, from left to right, the electronics elements are the High Voltage (HV) splitter, the HV supply, the Front-End electronics (FEE), the Trigger system [27] and the flash-ADC digitizing electronics [28, 29] (ν-FADC). Each PMT has a single cable for both PMT signal (5 mV per PE) and HV ($\sim$ 1.3 kV). A custom made HV-splitter circuit decouples both components. The HV is provided by CAEN-A1535P [30] supplies. PMT signals are optimized (amplified, clipped, baseline restored and coherent noise filtered) by the FEE for digitization. The FEE also delivers sum signals, whose amplitude is proportional to charge, that are fed into a custom trigger system. The circuit generating the sum signal subtracts the input amplitude after about 100 ns. This capability allows the trigger input signals to suffer from minimal overshoot that can lead to trigger dead-time. This same feature works as a high-pass filter: slow signals (frequency $\lesssim$ 1 MHz) cannot cause a trigger. The ID PMTs are separated into two ID super-groups at the trigger level, uniformly distributed across the volume. Either super-group can cause a trigger of the ID based on energy and sub-group multiplicity information. The ID triggers at energies about 350 keV. The trigger efficiency is 100.0% above the analysis threshold 0.7 MeV with negligible uncertainty. Both energy and sub-group multiplicity information are used to cause IV triggers. The IV triggers at $\sim$ 10 MeV which corresponds to 8 cm of a minimum ionizing muon track. The ν-FADC system relies on 64 CAEN-Vx1721(VME64x) [30] waveform digitizers. Each card has 8 channel with 8-bit flash-ADC (FADC) at 500 MS/s. Each channel holds up to 1024 4 μs waveforms without readout. When triggered, the 256 ns waveform is recorded, containing $>$ 90% of the scintillation light emitted. Up to $\sim$ 3 MeV, a single-PE is deposited per channel, each having $\sim$ 40 mV amplitude corresponding to around 10 samples per PE. FADC amplitude saturation leads to some degree of non-linearity for $>$ 100 MeV energies. Above 500 MeV, up to a 40% non-linearity has been estimated.

The FADC baselines are observed to be stable, showing variations below 1 ADC. After power-cycling, small (sub-mV) DC shifts in the baseline are observed. Due to under-sampling of the baseline, these shifts can cause a bias in the reconstructed charge estimation. This bias manifests itself as an effective non-linearity for signals below 2 PEs and has been thoroughly studied, measured and calibrated out, as described in Section Section IV E.

All systems (trigger, ID and IV) are readout by the same DAQ upon any trigger of either the ID or IV. The system is deadtime free, as demonstrated by two monitor systems running at 2 Hz. The dead time monitor waveforms are, in addition, used to randomly sample the detector providing extra baseline monitoring, background and dark-current information.

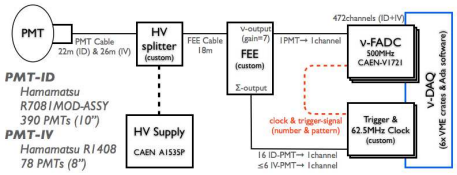

FIG. 3. Block diagram of the Double Chooz readout and DAQ systems.

G. The Outer Veto

The OV is installed above the ID, IV and 15 cm of shielding steel. A lower outer veto is mounted directly above the shielding and provides (x, y) coordinate for muons passing through a 13 m $\times$ 7 m area centered on the chimney; a 110 cm $\times$ 30 cm region around the chimney is left open. The lower outer veto has been installed for 68.9% of the data presented here, and is used to help reduce background levels quoted in [7]. An upper outer veto, again measuring (x, y) coordinates, has been mounted above the chimney and glove box used for source insertion, to cover this area. The upper outer veto was not present for this analysis.

The outer veto is assembled from modules containing 64 scintillator strips, each 5 cm $\times$ 1 cm $\times$ 320 cm or 360 cm. Each strip was extruded with a hole running through its length, through which a 1.5 mm diameter wavelength-shifting fiber was threaded. Modules are built out of two superimposed 32-strip layers with the top layer offset by 2.5 cm from the bottom layer. The 64 fibers are coupled at one end to a Hamamatsu H8804 multi-anode photomultiplier tube (M64); the other fiber ends are mirrored. The OV modules are positioned over the inner detector in two layers, one with strips oriented in the x direction and one in the y direction. Each M64 is connected to a custom front-end board with a MAROC2 ASIC [31] and an FPGA. The MAROC2 allows adjustment of the electronic gain of each of the 64 channels, which is needed to correct for the factor of 2 pixel-to-pixel gain variation in the M64. Signals that exceed a common threshold are sent to a multiplexed 12-bit ADC, providing charge information for hit strips.

H. Calibration Systems

The experiment is calibrated using light sources, radioactive (point-like) sources, and cosmic rays.

A multi-wavelength LED–fiber system (LI) is used to inject light into the inner detector and the inner veto from a set of fixed points. The optical fibers of the LI are routed inside the detector and the fiber ends are attached to the PMT covers. Some of the injection points are equipped with diffuser plates to widely illuminate the detector. The other ends of the fibers are connected to blue and UV LEDs (385, 425 and 470 nm wavelengths for the ID, and 365 and 475 nm for the IV) whose flash rate, light intensity and pulse width are controlled remotely. Data are taken with the LI systems regularly. The LI data are used to measure the PMT and readout electronics gains and the time offsets and to monitor the stability of those gains and offsets.

Radio-isotopes ^{137}Cs, ^{68}Ge, ^{60}Co, and ^{252}Cf, sealed in miniature capsules, have been deployed in the NT and GC. The visible energy response is measured with a 0.662 MeV gamma (Cs–137), 2×0.511 MeV annihilation gammas (Ge–68), which also corresponds to the threshold for inverse beta decay, the combination of 1.173 MeV and 1.333 MeV gammas (Co–60), and the 2.223 MeV gamma from neutron capture on hydrogen (Cf–252). The detector response to neutrons is calibrated using ^{252}Cf. Source rates are at the level of 50 Bq.

Deployments in the NT are realized by lowering the sources from a glove box at the detector top through the detector chimney. A motorized pulley-and-weight system, operated from a glove box, is used to position sources at positions along the target symmetry axis. The range of deployments is from 1 cm above the NT bottom up to the chimney; the positions of the source are known within 1 mm. In the GC, the source is attached to a motor-driven wire and guided through a rigid hermetic looped tube (GT). The sources are inserted in the GT near the chimney top. The loop traverses interior regions of the GC and passes near boundaries with the NT and the buffer. The position of the source along the loop is known to 1 cm, and in the NT boundary region, the perpendicular distance between the source and the target wall is known within 2 mm. The materials of the source capsules and deployment systems in the NT and GC are modeled by the detector simulation.

Cosmic rays are analyzed to identify stopping muons, spallation neutrons, and cosmogenic radioactive isotopes. Several thousand spallation neutrons per day are captured on hydrogen and gadolinium in the ID.

The use of the calibration data for issues of energy uniformity, stability, non-linearity and absolute calibration is described in Section IV E. The neutron detection efficiency from ^{252}Cf is described in Section V F. Good control of uncertainties on detection efficiency is essential for sensitivity to neutrino disappearance with a single detector. The detailed calibration data allow a precise energy-shape fit to the prompt neutrino candidates for the most sensitive extraction of θ_{13}.

III. REACTOR AND DETECTOR MODELS

A. Thermal Power

Double Chooz's sources of antineutrinos are the reactor cores B1 and B2 at the Électricité de France (EDF) Centrale Nucléaire de Chooz. Antineutrinos are produced in nuclear reactors by the β-decay of the fission products. Four main isotopes, ^{235}U, ^{239}Pu, ^{238}U, and ^{241}Pu, provide >99.7% of the fissions and antineutrinos.

Chooz B1 and B2 are N4 type pressurized water reactor (PWR) cores, and as such are two of the most powerful cores in the world with nominal thermal power outputs of 4.25 GW_{th} each. The instantaneous thermal power of each reactor core P_{th}^{R} is provided by EDF as a fraction of the total power and is evaluated over time steps of <1 minute. The instantaneous thermal power is derived from the in-core instrumentation with the most important variable being the temperature of the water in the primary loop.

The in-core instrumentation calibration is tested weekly using the heat balance in the secondary loop, which is heated by the primary loop containing water heated by fissions. In the secondary loop, steam is generated to drive turbines. By using measurements of the heat flow in the secondary loop, the thermal power can be measured. This test is performed with the reactor running at full power. The uncertainty at lower power is therefore slightly larger. The in-core instrumentation is re-calibrated if it deviates by more than the uncertainty in the heat balance measurement.

Since the accuracy of the thermal power measurement determines the maximum power at which the core can operate, EDF has performed a detailed study of the uncertainty in this measurement [32–34]. The dominant uncertainty on the weekly heat balance at the secondary loops comes from the measurement of the water flow. At the nominal full power of 4250 MW the final uncertainty is 0.5% (1 σ C.L.). Since the amount of data taken with one or two cores at intermediate power is small, this uncertainty is used for the mean power of both cores. This is smaller than the typical uncertainty for PWRs of 0.7% [35] and reflects optimizations in the pipe geometry of the secondary loop, as well as great care taken to understand the sensor uncertainties, including full-scale test stands for the most critical sensors.

B. Mean Cross Section per Fission

The mean cross section per fission is effectively a spectrum averaged cross section. It is given by

$$\langle \sigma_f \rangle = \sum_k \alpha_k \langle \sigma_f \rangle_k = \sum_k \alpha_k \int_0^\infty dE\, S_k(E)\, \sigma_{IBD}(E) \tag{1}$$

where α_k is the fractional fission rate of the k^{th} isotope ($k = {}^{235}$U, ^{239}Pu, ^{238}U, ^{241}Pu), $S_k(E)$ is the reference spectrum of the k^{th} isotope and σ_{IBD} is the inverse beta decay cross section. The determinations of the α_k require the simulation of the reactor core (Section III C).

The antineutrino spectrum for each fission isotope is the result of the beta decays of many different fission products. For ^{235}U, ^{239}Pu, and ^{241}Pu, the reference antineutrino spectra are derived from measurements of the β spectra at the ILL research reactor [36–38]. In the case of ^{238}U, an ab initio calculation of the spectrum is used [39]. The conversion of the β spectra to antineutrino spectra has recently been improved by using more data on the many β transitions and higher order energy corrections [39, 40]. We use the conversion scheme of [40] including corrections for off-equilibrium effects[41]. The uncertainty on these spectra is energy dependent but is on the order of 3%. The new technique for the analysis of the β spectra has led to an overall change in the normalization of the $S_k(E)$ that, when applied to previous reactor antineutrino experiments, results in measurements that are lower than predictions for experiments at short baselines [41].

C. Fission Rate Computation

The fractional fission rates α_k of each isotope are needed in order to calculate the mean cross section per fission of (Equation 1). They are also required for the calculation of the mean energy released per fission for reactor R:

$$\langle E_f \rangle_R = \sum_k \alpha_k \langle E_f \rangle_k. \tag{2}$$

The mean energies released per fission per isotope $\langle E_f \rangle_k$ are summarized in Table I. The thermal power one would calculate given a fission is relatively insensitive to the specific fuel composition since the $\langle E_f \rangle_k$ differ by <6%; however, the difference in the detected number of antineutrinos is amplified by the dependence of the norm and mean energy of S_k(E) on the fissioning isotope. For this reason, much effort has been expended in developing simulations of the reactor cores to accurately model the evolution of the α_k.

Double Chooz has chosen two complementary codes for modeling of the reactor cores: MURE and DRAGON [42–45]. MURE is a 3D full core simulation which uses Monte Carlo techniques to model the neutron transport in the core. DRAGON is a 2D simulation which models the individual fuel assemblies. Using some approximations, it solves the neutron transport equation in the core. These two codes provide the needed flexibility to extract fission rates and their uncertainties. These codes were benchmarked against data from the Takahama-3 reactor and were found to be consistent other codes commonly used in the reactor industry for reactor modeling within the uncertainty in the Takahama data [46].

The construction of the reactor model requires detailed information on the geometry and materials comprising the core. The Chooz cores are comprised of 205 fuel assemblies. For every reactor fuel cycle, approximately one year in duration, one third of the assemblies are replaced with assemblies containing fresh fuel. The other two thirds of the assemblies are redistributed to obtain a homogeneous neutron flux across the core. The Chooz reactor cores contain four assembly types that differ mainly in their initial ^{235}U enrichment. These enrichments are 1.8%, 3.4% and 4%.

The data set presented here spans fuel cycle 12 for core B2 and cycle 12 and the beginning of cycle 13 for B1. EDF provides Double Chooz with the locations and initial burnup of each assembly. Based on these maps, a full core simulation was constructed using MURE for each cycle. In addition, the beginning-of-fuel-cycle composition needs to be determined based on the burnup of each assembly. To accomplish this, an assembly-level reference simulation is run using both MURE and DRAGON for each of the four fuel assembly types. The results of the reference simulations are compared to EDF's own simulation code APOLLO2-F from which the burnup values are derived. The uncertainty due to the simulation technique is evaluated by comparing the DRAGON and MURE results for the reference simulation leading to a small 0.2% systematic uncertainty in the fission rate fractions α_k.

Once the initial fuel composition of the assemblies is known, MURE is used to model the evolution of the full core in time steps of 6 to 48 hours, depending on the operating conditions of the reactor. The results from each simulation time step are written to a database. This allows the α_k's, and therefore the predicted antineutrino flux, to be calculated. The results averaged over the current data set are shown in Table I.

The systematic uncertainties on the α_k's are determined by varying the inputs and observing their effect on the fission rate relative to the nominal simulation. The uncertainties considered are those due to the thermal power, boron concentration, moderator temperature and density, initial burnup error, control rod positions, choice of nuclear databases, choice of the energies released per fission, and statistical error of the MURE Monte Carlo. The systematic errors associated with each input are considered independently and the uncertainties propagated quadratically. The correlation coefficients among isotopic fission rates due to the thermal power constraint are also computed, and a covariance matrix is constructed with these contributions in order to properly account for those

TABLE I. Mean energy released per fission $\langle E_f \rangle_k$ from [47] and fractional fission rate $\langle \alpha_k \rangle$ of the isotope k for this data.

Isotope	$\langle E_f \rangle_k$ (MeV)	$\langle \alpha_k \rangle$
^{235}U	201.92±0.46	0.496±0.016
^{239}Pu	209.99±0.60	0.351±0.013
^{238}U	205.52±0.96	0.087±0.006
^{241}Pu	213.60±0.65	0.066±0.007

correlations. The uncertainties in the α_k's are listed in Table I. The two largest contributions come from the moderator density and control rod positions.

D. Bugey4 Normalization and Antineutrino Rate Calculation

In the current, far-only, phase of Double Chooz, the rather large uncertainties in the reference spectra of Section III B limited our sensitivity to θ_{13}. To mitigate this effect, the normalization of the cross section per fission for each reactor is "anchored" to the Bugey4 rate measurement at 15 m [48]:

$$\langle \sigma_f \rangle_R = \langle \sigma_f \rangle^{Bugey} + \sum_k (\alpha_k^R - \alpha_k^{Bugey}) \langle \sigma_f \rangle_k. \quad (3)$$

where R stands for each reactor. The second term corrects for the difference in fuel composition between Bugey4 and each of the Chooz cores. This treatment takes advantage of the high accuracy of the Bugey4 anchor point (1.4%) and suppresses the dependence on the predicted $\langle \sigma_f \rangle_R$. This is due to the smallness of the correction term $(\alpha_k^R - \alpha_k^{Bugey})$. At the same time, the analysis becomes insensitive to possible oscillations at shorter baselines due to heavy $\Delta m^2 \sim 1\ eV^2$ sterile neutrinos.

The expected number of antineutrinos with no oscillation in the i^{th} energy bin with the Bugey4 anchor point becomes:

$$N_i^{exp,R} = \frac{\epsilon N_p}{4\pi} \frac{1}{{L_R}^2} \frac{P_{th}^R}{\langle E_f \rangle_R} \times \left(\frac{\langle \sigma_f \rangle_R}{\left(\sum_k \alpha_k^R \langle \sigma_f \rangle_k\right)} \sum_k \alpha_k^R \langle \sigma_f \rangle_k^i \right) \quad (4)$$

where ϵ is the detection efficiency, N_p is the number of protons in the target, L_R is the distance to the center of each reactor, and P_{th}^R is the thermal power. The variable $\langle E_f \rangle_R$ is the mean energy released per fission defined in Equation 2, while $\langle \sigma_f \rangle_R$ is the mean cross section per fission defined in Equation 3. The three variables P_{th}^R, $\langle E_f \rangle_R$ and $\langle \sigma_f \rangle_R$ are time dependent with $\langle E_f \rangle_R$ and $\langle \sigma_f \rangle_R$ depending on the evolution of the fuel composition in the reactor and P_{th}^R depending on the operation of the reactor.

A covariance matrix $M_{ij}^{exp} = \delta N_i^{exp} \delta N_j^{exp}$ is constructed using the uncertainties listed in Table II. This matrix is constructed in terms of real energy and is converted into reconstructed energy by running multiple simulations drawn from a Cholesky decomposition of M_{ij}^{exp}. For these simulations, the full detector Monte Carlo described below is used. The use of Equation 4 to construct the covariance matrix allows time and spectral information to propagate to the final analysis.

TABLE II. The uncertainties in the antineutrino prediction. All uncertainties are assumed to be correlated between the two reactor cores. They are assumed to be normalization and energy (rate and shape) unless noted as normalization only.

Source	Normalization Only	Uncertainty [%]
P_{th}	yes	0.5
$\langle \sigma_f \rangle^{Bugey}$	yes	1.4
$S_k(E)\sigma_{IBD}(E_\nu^{true})$	no	0.2
$\langle E_f \rangle$	no	0.2
L_R	yes	<0.1
α_k^R	no	0.9
Total		1.8

The IBD cross section used is the simplified form from Vogel and Beacom [49] :

$$\sigma_{IBD}(E_\nu^{true}) = E_{e^+} K \sqrt{E_{e^+}^2 - m_e^2} \quad (5)$$

where

$$E_{e^+} = \frac{1}{2}\left(\sqrt{m_n^2 - 4m_p\left(-E_\nu + \Delta + \frac{\Delta^2 - m_e^2}{2m_p}\right)} - m_n \right) \quad (6)$$

and m_e and E_{e^+} are the positron mass and energy. The variables m_n and m_p are the masses of the neutron and proton with $\Delta = m_n - m_p$. The constant K is inversely proportional to the neutron lifetime. We use the MAMBO-II measurement of the neutron lifetime [50] and find $K = 0.961 \times 10^{-43}$ cm^2 MeV^{-2}.

E. Detector Model

We model the detector response using a detailed Geant4 [51] simulation with enhancements to the scintillation process, photocathode optical surface model, and thermal neutron model. Apart from these additions, the physics list is similar to Geant4's `QGSP_BERT_HP` reference physics list [52], without processes for high-mass hadrons. Our custom scintillation process implements detailed light waveforms, spectra, re-emission, and Birks-law [53] quenching. Our photocathode model is based on a standard mathematical model of a thin, semitransparent surface with absorption and refractive index [54], and also includes the collection efficiency for photoelectrons as a function of position of emission on the photocathode. Our custom neutron thermalization process implements molecular elastic scattering for neutrons under 4 eV and a

radiative capture model with improved final state gamma modeling.

The simulation models the detector geometry to a fine level of detail, particularly with regard to the geometry of the phototubes and mu-metal shields and of all materials near the active volume such as tank walls and supports. The orientation and positions of the phototube assemblies were set using data from a photographic survey with sub-mm accuracy. The dimensions of the tank walls and supports were checked by experimenters during assembly and installation, and placement also verified by photographic survey.

Simulated IBD events are generated with run-by-run correspondence of MC to data, with fluxes and rates calculated as described in Section III D. Radioactive decays in calibration sources and spallation products were simulated using detailed models of nuclear levels, taking into account branching ratios and correct spectra for transitions [55].

Optical parameters used in the detector model are based on detailed measurements made by the collaboration. The relative light yield of the NT compared to the GC was measured using a Compton backscatter peak method in order to select scattered electrons with fixed energy [21]. Tuning of the absolute and relative light yield in the simulation was done with calibration data. The scintillator emission spectrum was measured using a Cary Eclipse fluorometer [56]. The photon emission time probabilities used in the simulation are obtained with a dedicated laboratory setup [16]. For the ionization quenching treatment in our MC, the light output of the scintillators after excitation by electrons [57] and alpha particles [58] of different energies was measured. The non-linearity in light production in the simulation has been adjusted to match these data. The attenuation and re-emission probabilities of each of the scintillator components in the relevant wavelength range are implemented in the MC. The fine-tuning of the total attenuation was made using measurements of the complete scintillators [16]. Other measured optical properties include reflectivities of various detector surfaces and indices of refraction of detector materials.

F. Readout System Simulation

The Readout System Simulation (RoSS) accounts for the response of elements associated with detector readout, such as from the PMTs, FEE, FADCs, trigger system and DAQ. The simulation relies on the measured probability distribution function (PDF) to empirically characterize the response to each single PE as measured by the full readout channel. The Geant4-based simulation calculates the time at which each PE strikes the photocathode of each PMT. RoSS converts this time-per-PE into an equivalent waveform as digitized by FADCs. A dedicated setup was built to measure most of the necessary PDFs as well as to tune the design of the full readout chain. Channel-to-channel variations, such as gains, baselines, noise, single PE widths, etc., are taken into consideration, to accurately predict dispersion effects. This capability allows the simulation to exhibit non-linearity effects as observed in the data, as described in Section II F. After calibration, the MC and data energies agree within 1%. About 25% of the width of the calibrated H-capture (2.2 MeV γ line) results from readout effects; i.e., effects beyond photon-statistics fluctuations.

G. Monte Carlo $\bar{\nu}_e$ Event Generation

A set of Monte Carlo $\bar{\nu}_e$ events representing the expected signal for the duration of physics data-taking is created based on the formalism of Equation 4. The calculated IBD rate is used to determine the rate of interactions. Parent fuel nuclide and neutrino energies are sampled from the calculated neutrino production ratios and corresponding spectra, yielding a properly normalized set of IBD-progenitor neutrinos.

Once generated, each event-progenitor neutrino is assigned a random creation point within the originating reactor core. The event is assigned a weighted-random interaction point within the detector based on proton density maps of the detector materials. In the center-of-mass frame of the $\nu - p$ interaction, a random positron direction is chosen, with the positron and neutron of the IBD event given appropriate momenta based on the neutrino energy and decay kinematics. These kinematic values are then boosted into the laboratory frame. The resulting positron and neutron momenta and originating vertex are then available as inputs to the Geant4 detector simulation. "Truth" information regarding the neutrino origin, baseline, and energy are propagated along with the event, for use later in the oscillation analysis.

IV. RECONSTRUCTION

A. Pulse Reconstruction

The pulse reconstruction provides the signal charge and time in each PMT. Pulser triggers are taken with a rate of 1 Hz in order to provide accurate information about the baseline for each of the 468 readout channels. The baseline mean (B_{mean}) and rms (B_{rms}) are computed using the full readout window (256 ns).

The integrated charge (q) is defined as the sum of digital counts in each waveform sample over the integration window, once the pedestal has been subtracted. The pedestal is computed as the integration of B_{mean} over the same window. In order to improve the charge resolution, the size of the integral window has been set to a 112 ns subsample of the readout one, based on the width of the single PE signals.

In order to find the pulses within the readout window, a dynamic window algorithm is used. The algo-

rithm searches for the 112 ns window which maximizes the integral. In the absence of an actual PE signal, this algorithm would reconstruct the largest noise fluctuation, leading to a bias in the charge reconstruction. To address this, we introduce two requirements: ≥ 2 ADC counts in the maximum bin, and $q > B_{rms} \times \sqrt{N_s}$, where N_s is the number of integrated waveform samples (56 for a 112 ns window). For each pulse reconstructed, the start time is computed as the time when the pulse reaches 20% of its maximum. This time is then corrected by the PMT-to-PMT offsets obtained with the LI system.

B. Vertex Reconstruction

Vertex reconstruction in Double Chooz is not used for event selection, but is used for event energy reconstruction. It is based on a maximum charge and time likelihood algorithm which utilizes all hit and no-hit information in the detector. Assuming the event to be a point-like source of light characterized by the set

$$\mathbf{X} = (x_0, y_0, z_0, t_0, \Phi) \tag{7}$$

where (x_0, y_0, z_0) is the event position in the detector, t_0 is the event time and Φ is the light intensity per unit solid angle (expressed in photons/sr), the amount of light and prompt arrival time at the i-th PMT can be predicted as

$$\mu_i = \Phi\, \epsilon_i\, \Omega_i\, A_i \tag{8}$$

and

$$t_i^{(pred)} = t_0 + \frac{r_i}{c_n} \tag{9}$$

respectively, where ϵ_i is the quantum efficiency of the PMT, Ω_i is the solid angle subtended by the PMT at a distance r_i from the event vertex, A_i is the light transmission amplitude, and c_n is the effective speed of light in the medium.

The event likelihood is defined as

$$\mathcal{L}(\mathbf{X}) = \prod_{q_i=0} f_q(0;\mu_i) \prod_{q_i>0} f_q(q_i;\mu_i) f_t(t_i; t_i^{(pred)}, \mu_i) \tag{10}$$

where the first product goes over the PMTs that have not been hit, while the second product goes over the remaining PMTs that have been hit (i.e., have a non-zero recorded charge q_i at the registered time t_i). $f_q(q_i;\mu_i)$ is the probability to measure a charge q_i given an expected charge μ_i, and $f_t(t_i; t_i^{(pred)}, \mu_i)$ is the probability to measure a time t_i given a prompt arrival time t_i^{pred} and predicted charge μ_i. These are obtained from MC simulations and verified against the physics and calibration data. The task of the event reconstruction is to find the best possible set of event parameters $\mathbf{X}_{min}$ which maximizes the event likelihood $\mathcal{L}(\mathbf{X})$, or equivalently, minimizes the negative log-likelihood function

$$F(\mathbf{X}) = -\ln \mathcal{L}(\mathbf{X}) = -\sum_i \ln f_q(q_i;\mathbf{X}) - \sum_{q_i>0} \ln f_t(t_i;\mathbf{X}) = F_q(\mathbf{X}) + F_t(\mathbf{X}). \tag{11}$$

Note that the event reconstruction can be performed using either one or both of the two terms in the expression above, F_q for a charge-only reconstruction, or F_t for a time-only reconstruction; utilizing both components enhances the accuracy and stability of the algorithm.

The performance of the Double Chooz reconstruction has been evaluated in situ using radioactive sources deployed at known positions along the z-axis in the target volume, and off-axis in the guide tubes. The sources are reconstructed with a spatial resolution of 32 cm for ^{137}Cs, 24 cm for ^{60}Co, and 22 cm for ^{68}Ge.

C. Muon tagging and reconstruction

Cosmic muons passing through the detector or the nearby rock induce backgrounds which are discussed in the next section. A through-going (stopping) muon typically deposits 160 MeV (80 MeV) in the IV which triggers above about 10 MeV. The IV trigger rate is 46 s^{-1}. All muons in the ID are tagged by the IV except some stopping muons which enter the chimney. Muons which stop in the ID and their resulting Michel e can be identified by demanding a large energy deposition (roughly a few tens of MeV) in the ID. An event is tagged as a muon if there is > 5 MeV in the IV or > 30 MeV in the ID.

Several tracking algorithms have been developed to reconstruct these muons. IV reconstruction is based on a maximum likelihood algorithm utilizing the arrival times of the earliest photons to hit each PMT, while ID reconstruction utilizes the spatial pattern of hit times. The forward wavefront of scintillation light from a relativistic track propagates at the Cerenkov angle, thus allowing the same algorithm to be used for tracks in the NT, GC, and non-scintillating buffer. Using MC and the OV as reference, the lateral resolution at the detector center has been determined to be 35 cm for ID and 60 cm for IV muons.

D. Light Noise Rejection

The background known as *light noise* is caused by a sporadic spontaneous flashes of some PMT bases. The characteristic signature is light mainly localized to one PMT base and spread out in time among the other PMTs after many reflections from the detector surfaces. This background can be discriminated from physics events based on the fact that the detected light is spread less homogeneously across the detector for light noise events. Light noise is rejected by demanding both a small value of

$Q_{\max}/Q_{\rm tot}$, where $Q_{\max}$ is the maximum charge recorded by a single PMT and $Q_{\rm tot}$ is the total ID charge collected in a trigger, and large values of rms($t_{\rm start}$), which is the standard deviation of the distribution of the start time ($t_{\rm start}$) of the first pulse on each PMT.

E. Energy Reconstruction

The visible energy (E_{vis}) provides the absolute calorimetric estimation of the energy deposited per trigger. E_{vis} is a function of the calibrated PE (total number of photoelectrons):

$$E_{vis} = PE^m(\rho, z, t) \times f_u^m(\rho, z) \times f_s^m(t) \times f_{MeV}^m, \quad (12)$$

where $PE = \sum_i pe_i = \sum_i q_i/gain_i(q_i)$. Coordinates in the detector are ρ and z, t is time, m refers to data or Monte Carlo (MC) and i refers to each good channel. The correction factors f_u, f_s and f_{MeV} correspond, respectively, to the spatial uniformity, time stability and PE/MeV calibrations. Four stages of calibration are carried out to render E_{vis} linear, independent of time and position, and consistent between data and MC. Both the MC and data are subjected to the same stages of calibration.

The sum over all good channels of the reconstructed raw charge (q_i, see Section IV A) from the digitized waveforms is the basis of the energy estimation. Good channels are those identified and tagged as well behaved by fast online analysis based on waveform information. Only a very few channels are sporadically not good and are, thus, excluded from the calorimetric estimation. The limited sampling of the waveform baseline estimation can be biased [28] leading to a non-linearity at about 1 PE charge equivalent. Figure 4 shows the effect for a representative channel. A similar curve is used to calibrate the MC. The PE calibrated charge (pe_i) is defined as $pe_i = q_i/gain_i(q_i)$. One $gain_i(q_i)$ curve is generated upon each power-cycle episode. Due to the average light level (~ 230 PE/MeV), the non-linear bias of the single-PE calibration can have up to a 10% effect for energies below 3 MeV, if not corrected.

The PE response is position dependent for both MC and data. Calibration maps were created such that any PE response for any event located at any position (ρ,z) can be converted into its response as if measured at the center of the detector ($\rho = 0, z = 0$): $PE^m_{\odot} = PE^m(\rho, z) \times f_u^m(\rho, z)$. The calibration map's correction for each point is labeled $f_u^m(\rho, z)$. Independent uniformity calibration maps $f_u^m(\rho, z)$ are created for data and MC, such that the uniformity calibration serves to minimize any possible difference in position dependence of the data with respect to MC. The capture peak on H (2.223 MeV) of neutrons from spallation and antineutrino interactions provides a precise and copious calibration source to characterize the response non-uniformity over the full volume (both NT and GC). The calibration map for data is shown in Figure 5. A similar map

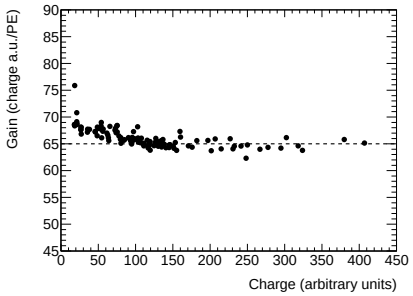

FIG. 4. Demonstration of the linear PE calibration for one channel. The gain versus charge is shown. The dashed line highlights the constant component (linear behavior) of the gain observed at large charges. The calibration parametrizes this curve to correct the non-linear component (deviation from constant) of the gain, making the PE corrected energy scale linear to within 2%.

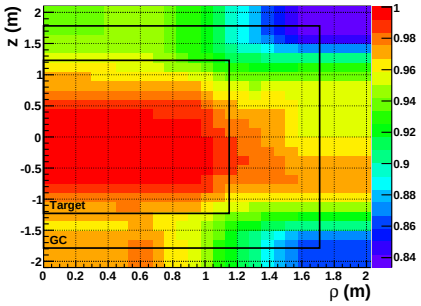

FIG. 5. Detector calibration map, in cylindrical coordinates (ρ,z), as sampled with spallation neutrons capturing in H across the ID. Response variations are quantified as the fractional response with respect to the detector center. Largest deviation in NT are up to 5%. A similar map is constructed with MC for calibration of its slightly different response uniformity pattern.

was measured and applied to MC. A 2D-interpolation method was developed to provide a smooth application of the calibration map at any point (ρ, z).

The detector response stability was found to vary in time due to two effects, which are accounted for and corrected by the term $f_s^m(t)$. First, the detector response can change due to variations in readout gain or scintillator response. This effect has been measured as a $+2.2\%$ monotonic increase over 1 year using the response of the spallation neutrons capturing on Gd within the NT, shown in Figure 2. Second, a few readout chan-

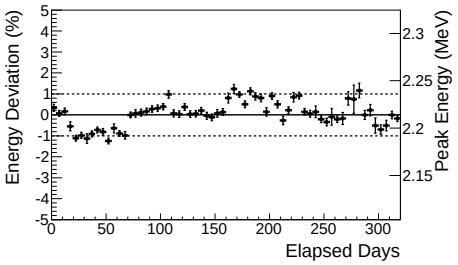

FIG. 6. Stability of the reconstructed energy as sampled by the evolution in response of the spallation neutron H-capture after stability calibration. The observed steps correspond to power-cycle periods. The systematic uncertainty on the energy stability is estimated at 0.61%.

TABLE III. Energy scale systematic errors.

	Error (%)
Relative Non-Uniformity	0.43
Relative Instability	0.61
Relative Non-Linearity	0.85
Total	1.13

nels varying over time are excluded from the calorimetry sum, and the average overall response decreases by 0.3% per channel excluded. The MC is stable, so this correction is applied only to data. The stability calibration is relative to a specific reference time t_0. Therefore, any response $PE_{\odot}(t)$ is converted to the equivalent response at t_0, as $PE^m_{\odot t_0} = PE^m_{\odot}(t) \times f^m_s(t)$. The t_0 was defined as the day of the first Cf source deployment, during August 2011. The remaining instability after calibration is shown in Figure 6, as sampled with H-capture from spallation neutrons, and is used for the stability systematic uncertainty estimation.

The number $PE_{\odot t_0}$ per MeV is determined by an absolute energy calibration independently, for the data and MC. The response in $PE_{\odot t_0}$ for H-capture as deployed in the center of the NT is used for the absolute energy scale. The absolute energy scales are found to be 229.9 $PE_{\odot t_0}$/MeV and 227.7 $PE_{\odot t_0}$/MeV, respectively, for the data and MC, demonstrating agreement within 1% prior to this calibration stage.

Discrepancies in response between the MC and data, after calibration, are used to estimate these uncertainties within the prompt energy range and the NT volume. Table III summarizes the systematic uncertainty in terms of the remaining non-uniformity, instability and non-linearity. The relative non-uniformity systematic uncertainty was estimated from the calibration maps using neutrons capturing on Gd, after full calibration. The rms deviation of the relative difference between the data and MC calibration maps is used as the estimator of the non-uniformity systematic uncertainty, and is 0.43%. This result is consistent with the analysis of all calibration sources along the z-axis (NT) and GT (GC). The relative instability systematic error, discussed above, is 0.61%. Responses are equalized at 2.223 MeV, but small data/MC discrepancies in the absolute energy scale can still arise from the relative non-linearity across the prompt energy spectrum. This possibility was explored by using all calibration sources in the energy range 0.7 – 8 MeV with deployments along the z-axis and GT. Some relative non-linearity was observed ($< 0.2\%$/MeV) but the pattern diminished when integrated over the full volume. A 0.85% variation consistent with this non-linearity was measured with the z-axis calibration system, and this is used as the systematic error for relative non-linearity in Table III. Consistent results were obtained when sampling with the same sources along the GT.

V. NEUTRINO DATA ANALYSIS

A. $\bar{\nu}_e$ Candidate Selection

The $\bar{\nu}_e$ candidate selection procedure starts in a similar way as [7]. Events with an energy below 0.5 MeV, where the trigger efficiency is not 100%, or identified as light noise ($Q_{\max}/Q_{\rm tot} > 0.09$ or $\mathrm{rms}(t_{\rm start}) > 40$ ns) are discarded. Triggers within a 1 ms window following a tagged muon are also rejected (see Section IV C), in order to reduce the correlated and cosmogenic backgrounds. The effective veto time is 4.4% of the total run time. Defining $\Delta T \equiv t_{\rm delayed} - t_{\rm prompt}$, further selection consists of 4 cuts:

1. time difference between consecutive triggers (prompt and delayed): 2 μs $< \Delta$T $<$ 100 μs, as shown in Figure 7, where the lower cut reduces correlated backgrounds and the upper cut is determined by the approximately 30 μs capture time on Gd;

2. prompt trigger: 0.7 MeV $< E_{\rm prompt} <$ 12.2 MeV, as illustrated in Figure 8;

3. delayed trigger: 6.0 MeV $< E_{\rm delayed} <$ 12.0 MeV (Figure 8) and $Q_{\max}/Q_{\rm tot} <$0.055;

4. multiplicity: no additional triggers from 100 μs preceding the prompt signal to 400 μs after it, with the goal of reducing the correlated background.

The IBD efficiencies for these cuts are listed in Table IV.

A preliminary sample of 9021 candidates is obtained by applying selections (1–4). In order to reduce the background contamination in the sample, candidates are rejected according to two extra cuts not used in [7]. First, candidates within a 0.5 s window after a high energy muon crossing the ID ($E_\mu > 600$ MeV) are tagged as cosmogenic isotope events and rejected, increasing the

Cut	Efficiency %
E_{prompt}	100.0 ± 0.0
E_{delayed}	94.1 ± 0.6
ΔT	96.2 ± 0.5
Multiplicity	99.5 ± 0.0
Muon veto	90.8 ± 0.0
Outer Veto	99.9 ± 0.0

TABLE IV. Cuts used in the event selection and their efficiency for IBD events. The OV was working for the last 68.9% of the data.

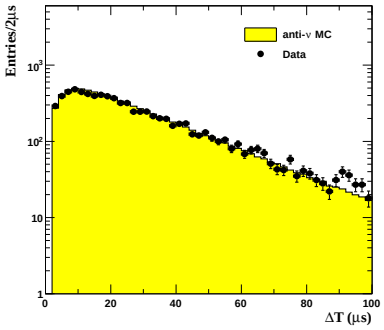

FIG. 7. Time difference between prompt and delayed triggers. Black dots and solid histogram show data and MC results, respectively.

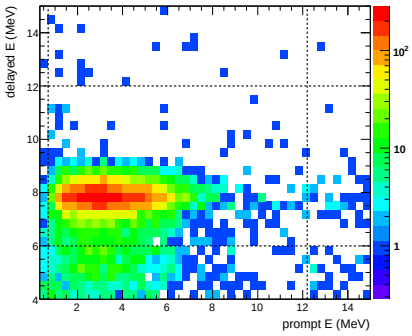

FIG. 8. Delayed energy versus prompt energy for time-correlated triggers. Vertical and horizontal dashed lines show the cuts applied for $\bar{\nu}_e$ candidates selection.

effective veto time to 9.2%. Second, candidates whose prompt signal is coincident with an OV trigger are also excluded as correlated background. Applying the above vetoes yields 8249 candidates or a rate of 36.2 ± 0.4 events/day, uniformly distributed within the target, for an analysis livetime of 227.93 days. This rate is lower than the one presented in [7] due to a longer data taking period with one reactor being off, as well as to the new cuts reducing the background contamination. Following the same selection procedure on the $\bar{\nu}_e$ MC sample yields 8439.6 expected events in the absence of oscillation.

B. Accidental Background

The main source of accidental coincidences is the random association of a prompt trigger from natural radioactivity and a later neutron-like candidate. This background is estimated by applying the neutrino selection cuts described in Section V A but using coincidence windows shifted by 1 s in order to remove correlations in the time scale of n-captures in H and Gd. The statistics of the sample is enhanced by using 198 windows each shifted from the previous one by 500 μs. The radioactivity rate between 0.7 and 12.2 MeV is 8.2 s^{-1}, while the singles rate in 6 - 12 MeV energy region is 18 h^{-1}. Both rates are quite stable along the data taking period. Finally, the accidental background rate is found to be 0.261 ± 0.002 events per day. The reproducibility of our result and any possible systematic effect are studied by repeating the procedure 30 times, i.e., taking 30 times 198 consecutive time windows. The dispersion of these 30 measurements is consistent with only statistical error, so, no systematic deviation is found.

Figure 9 shows the accidental prompt spectrum and the energy distribution for natural radioactivity scaled to the number of accidental events; the agreement is excellent. The distribution is peaked at low energies below 3 MeV. The remaining light noise is included in the accidental background sample. Using the correlation between both variables $Q_{\max}/Q_{\text{tot}}$ and $\text{rms}(t_{start})$, its contribution to the accidental sample is estimated to be lower than 1%.

C. Cosmogenic Isotopes Background

The radioisotopes ^{8}He and ^{9}Li are products of spallation processes on ^{12}C induced by cosmic muons crossing the scintillator volume. The βn-decays of these isotopes constitute a background for the antineutrino search. βn-emitters can be identified from the time- and space- correlation to their parent muon. Due to their relatively long lifetimes (^{9}Li: $\tau = 257$ ms, ^{8}He: $\tau = 172$ ms), an event-by-event discrimination is not possible. For the

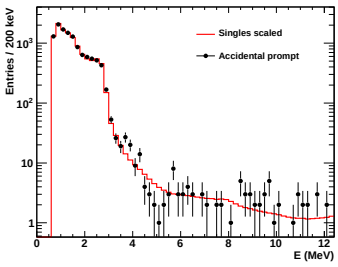

FIG. 9. The accidental prompt spectrum (black circles) superimposed to the radioactivity energy distribution measured in Double Chooz scaled to the same number of entries (red line).

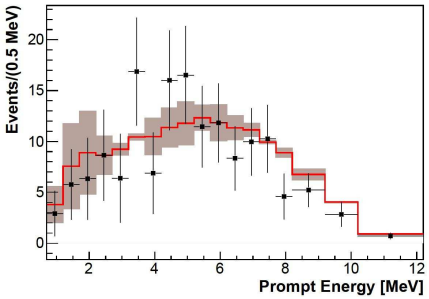

FIG. 10. The prompt β spectrum of the βn-emitters ^{8}He and ^{9}Li from data (black squares) and Monte Carlo (red line), assuming ^{9}Li is the dominant contribution.

muon rates in our detector, vetoing for several isotope lifetimes after each muon would lead to an unacceptably large loss in exposure. Instead, the rate is determined by an exponential fit to the $\Delta t_{\mu\nu} \equiv t_\mu - t_\nu$ profile of all possible muon-IBD candidate-pairs.

The analysis is performed for three visible energy E_μ^{vis} ranges that characterize subsamples of parent muons by their energy deposition, not corrected for energy non-linearities, in the ID:

1. Showering muons crossing the target value are selected by $E_\mu^{vis} > 600\,\mathrm{MeV}$ and feature an increased probability to produce cosmogenic isotopes. The $\Delta t_{\mu\nu}$-fit returns a precise result of 0.95 ± 0.11 events/day for the βn-emitter rate.

2. In the E_μ^{vis} range from 275 to 600 MeV, muons crossing GC and target still give a sizable contribution to isotope production of 1.08 ± 0.44 events/day. To obtain this result from a $\Delta t_{\mu\nu}$ fit, the sample of muon-IBD pairs has to be cleaned by a spatial cut on the distance of closest approach from the muon to the IBD candidate of $d_{\mu\nu} < 80\,\mathrm{cm}$ to remove the majority of uncorrelated pairs. The corresponding cut efficiency is determined from the lateral distance profile obtained for $E_\mu^{vis} > 600\,\mathrm{MeV}$. The approach is validated by a comparative study of cosmic neutrons that show an almost congruent profile with very little dependence on E_μ^{vis} above 275 MeV.

3. The Cut $E_\mu^{vis} < 275\,\mathrm{MeV}$ selects muons crossing only the buffer volume or the rim of the GC. For this sample, no production of βn-emitters inside the target volume is observed. An upper limit of < 0.3 events/day can be established based on a $\Delta t_{\mu\nu}$ fit for $d_{\mu\nu} < 80\,\mathrm{cm}$. Again, the lateral distribution of cosmic neutrons has been used for determining the cut efficiency.

The overall rate of βn-decays found is $2.05^{+0.62}_{-0.52}$ events/day. The result of a similar analysis based on the IV muon tracking agrees within the uncertainty.

Accidental coincidences containing the β-decay of the isotope ^{12}B either as prompt or as delayed event feature a time correlation to the parent muons producing the ^{12}B. In the $\Delta t_{\mu\nu}$ profile, these events are represented by a decay function with $\tau(^{12}B) = 29\,\mathrm{ms}$. However, these events were removed very efficiently from the data set used for ^{9}Li analysis by imposing a maximum distance cut of 90 cm between prompt and delayed events, introducing a negligible inefficiency of $\sim$1%.

The correlation of a cosmogenic isotope to the showering muons has been exploited to impose a partial veto of this background for the final fit analysis. Vetoing all IBD candidates within 0.5 s following a muon of $E_\mu^{vis} > 600\,\mathrm{MeV}$, 0.89 ± 0.10 events d^{-1} of βn-decays are removed from the data sample. The residual cosmogenic isotope background rate has been determined to 1.25 ± 0.54 events/day.

Finally, the correlation of parent muons and βn-emitters has been used to extract the prompt β spectrum from the data. Figure 10 shows a sample spectrum obtained for $E_\mu > 620\,\mathrm{MeV}$, a distance cut of 0.7 m and a $\Delta t_{\mu\nu}$ cut of 600 ms. The contamination of the sample by random coincidences has been statistically subtracted. Good agreement is found for the MC spectrum used in the final fit analysis.

D. Fast Neutrons and Stopping Muon Background

Most correlated backgrounds are rejected by the 1 ms veto time after each tagged muon. The remaining events arise from cosmogenic events whose parent muon either misses the detector or deposits an energy low enough to escape the muon tagging. Two contributions have been found: fast neutrons (FN) and stopping muons (SM).

FN are created by muons in the inactive regions surrounding the detector. Their large interaction length allows them to cross the detector and capture in the ID, causing both a prompt trigger by recoil protons and a delayed trigger by capture on Gd. An approximately flat prompt energy spectrum is expected; a slope could be introduced by acceptance and scintillator quenching effects. The time and spatial correlation distribution of FN are indistinguishable from those of $\bar{\nu}_e$ events.

The selected SM arise from muons entering through the chimney, stopping in the top of the ID, and eventually decaying. The short muon track mimics the prompt event, and the decay Michel electron mimics the delayed event. SM candidates are localized in space in the top of the ID under the chimney, and have a prompt-delayed time distribution following the 2.2 μs muon lifetime.

The correlated background has been studied by extending the selection on $E_{\rm prompt}$ up to 30 MeV. No IBD events are expected in the interval 12 MeV $\leq E_{\rm prompt} \leq$ 30 MeV. FN and SM candidates were separated via their different correlation time distributions. A 97^{+3}_{-8}% pure sample of FN is obtained for $\Delta T > 10$ μs, and a (88 ± 7)% pure sample of SM is obtained for $\Delta T < 10$ μs. These samples of FN and SM can be used to estimate their rate. The observed prompt energy spectrum is consistent with a flat continuum between 12 and 30 MeV, which extrapolated to the IBD selection window provides a first estimation of the correlated background rate of $\approx$ 0.75 events/day. The accuracy of this estimate depends on the validity of the extrapolation of the spectral shape. Next we describe a measurement of the FN and SM spectral shapes including the IBD region, obtained by using the IV and OV to tag samples of FN and SM.

The DAQ reads out the IV upon any ID trigger, lowering the IV detection threshold to $\sim$ 1 MeV, and making the IV sensitive to FN via the detection of proton recoils and captures on H. The IV-tagging is implemented by demanding at least 2 IV PMT hits leading to (33 ± 5)% tagging efficiency with no contribution by single PMT energy depositions. There is a very low probability of accidental IV tagging due to any IV energy deposition in the 256 ns coincident readout window.

The OV-tagging, when available, is especially sensitive to SMs since the muon is often detected. (41 ± 23)% of the FN and SM candidates in the 12-to-30-MeV window are tagged by the OV, of which (74 ± 12)% are SM. OV-tagging has an accidental rate = 0.06% of the neutrino sample and can be used to veto events caused by muons.

Several FN and SM analyses were performed using different combinations of IV and OV tagging. The main analysis for the FN estimation relies on IV-tagging of the prompt triggers with OV veto applied for the IBD selection. Two sources of backgrounds on the tagged FN sample were identified and rejected. The first source is the combination of natural radioactivity in the IV in an accidental coincidence with a genuine IBD, and was reduced to 12% by imposing a time coincidence between the ID and IV energy depositions. The second source, a Compton scattering in both the IV and ID in an accidental coincidence with a Gd-capture, was reduced to 2% by imposing a cut on the spatial distance between the prompt and delayed candidate in the ID. The purity of the IV-tagged FN sample was 86%. The remaining background was measured in an off-time window and subtracted, thus minimizing distortions to the energy spectrum. The FN spectral shape was found to be in agreement with a linear model with a small positive slope. The measured total FN rate was (0.30 ± 0.14) events/day, including systematic uncertainties from the ΔT-based FN-SM separation, the IV-tagging efficiency, and background subtractions.

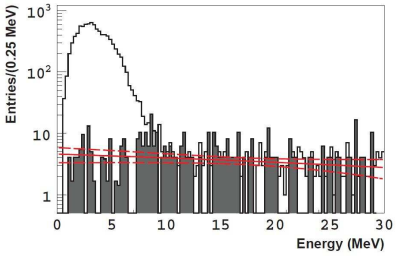

FIG. 11. FN and SM combined spectral model best fit (solid red) with $\pm 1\sigma$ (dashed red), energy distribution of tagged FN and SM population (gray histogram) and IBD spectrum.

Since there is no correlation between the SM prompt energy and the delayed energy deposit of the Michel electron, a pure sample of SM was obtained by selecting 20 MeV $\leq E_{\rm delayed} \leq$ 60 MeV. The spectral shape of SM prompt energy was found to be in agreement with a linear model with a small negative slope. The total SM rate was measured to be (0.34 ± 0.18) events/day, including systematic uncertainties.

Since the spectral shapes for both FN and SM are linear, a combined analysis was performed to obtain the total spectrum shown in Fig. 11 and the total rate estimation (0.67 ± 0.20) events/day summarized in Table V. Consistent results were obtained from different analysis techniques, which included IV- and OV-tagging without OV-vetoing. The OV veto reduces the rate of correlated backgrounds by about 30%.

E. Background Measurements

There are four ways that can be utilized to estimate backgrounds. Each independent background component can be measured by isolating samples and subtracting possible correlations. This is described for each component in Sections IV D, V C and V D. Second, we can measure each independent background component including spectral information when fitting for θ_{13} oscillations as is done in Section VI. Third, the total background rate is

measured by comparing the observed and expected rates as a function of reactor power. Fourth, we can use the both-reactor-off data to measure both the rate and spectrum.

The latter two methods are used currently as cross-checks for the background measurements due to low statistics and are described here. The measured daily rate of IBD candidates as a function of the no-oscillation expected rate for different reactor power conditions is shown in Figure 12. The extrapolation to zero reactor power of the fit to the data yields 2.9 ± 1.1 events per day, in excellent agreement with our background estimate. The overall rate of correlated background events that pass the IBD cuts is independently verified by analyzing 22.5 hours of both-reactors-off data. The expected neutrino signal is < 0.3 residual $\bar{\nu}_e$ events. Three events passed the first 4 cuts in Section V A. Two events with prompt energies of 4.8 MeV and 9.4 MeV were associated within 30 cm and 240 ms with the closest energetic muon, and are thus likely to be associated with ^{9}Li. Indeed, the second candidate is rejected by the showering muon veto. The third candidate at a prompt energy of 0.8 MeV features 3.5 m distance between prompt and delayed events and is therefore most likely a random coincidence. Immediately following the data set used in this paper, we obtained a larger data set with both-reactors-off. That will be the subject of a separate paper [59].

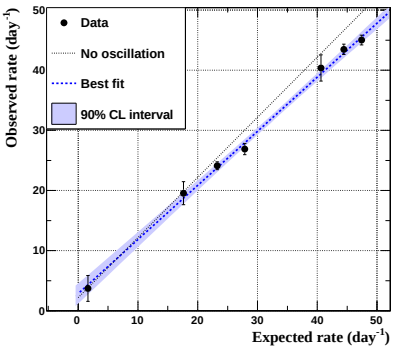

FIG. 12. Daily number of $\bar{\nu}_e$ candidates as a function of the expected number of $\bar{\nu}_e$. The dashed line shows the fit to the data, along with the 90% C.L. band. The dotted line shows the expectation in the no-oscillation scenario.

F. Neutron Detection Efficiency

Calibration data taken with the ^{252}Cf source were used to check the Monte Carlo prediction for any biases in the neutron selection criteria and estimate their contributions to the systematic uncertainty.

The fraction of neutron captures on gadolinium is evaluated to be 86.5% near the center of the target, 1.5% lower than the fraction predicted by simulation. Therefore the Monte Carlo simulation for the prediction of the number of $\bar{\nu}_e$ events is reduced by factor of 0.985. After the prediction of the fraction of neutron captures on gadolinium is scaled to the data, the prediction reproduces the data to within 0.3% under variation of selection criteria.

The ^{252}Cf is also used to check the neutron capture time, ΔT. The time difference between the prompt event and neutron capture signal for the californium calibration data is shown in Figure 13. The simulation reproduces the efficiency (96.2%) of the Δt_{e+n} cut with an uncertainty of 0.5% augmented with sources deployed through the NT and GC.

The efficiency for Gd capture events with visible energy greater than 4 MeV to pass the 6 MeV cut is estimated to be 94.1%. Averaged over the NT, the fraction of neutron captures on Gd accepted by the 6.0 MeV cut is in agreement with calibration data to within 0.7%.

The Monte Carlo simulation indicates that the number of IBD events occurring in the GC with the neutron captured in the NT (spill-in) slightly exceeds the number of events occurring in the target with the neutron escaping to the gamma catcher (spill-out), by $1.35\% \pm 0.04\%$(stat) $\pm$ 0.30%(sys). The spill-in/out effect is already included in the simulation and therefore no correction for this is needed. The uncertainty of 0.3% assigned to the net spill-in/out current was quantified by varying the parameters affecting the process, such as gadolinium concentration in the target scintillator and hydrogen fraction in the gamma-catcher fluid within its tolerances. Moreover the parameter variation was performed with multiple Monte Carlo models at low neutron energies.

VI. OSCILLATION ANALYSIS

The oscillation analysis is based on a combined fit to antineutrino rate and spectral shape. IBD candidates are selected as described in Section V A. The data are compared to the Monte Carlo signal and background events from high-statistics samples. The same selections are applied to both signal and background, with corrections made to Monte Carlo only when necessary to match detector performance metrics.

The oscillation analysis begins by separating the data into 18 variably-sized bins between 0.7 and 12.2 MeV. Two integration periods are used in the fit to help separate background and signal flux. One set contains data periods where one reactor is operating at less than 20% of

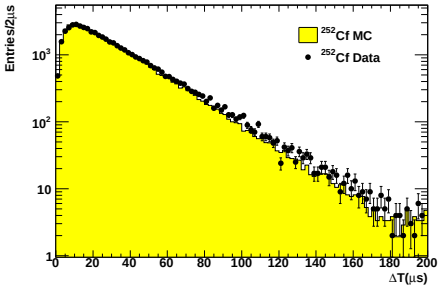

FIG. 13. Time difference between prompt and delayed events with ^{252}Cf at the detector center. The prompt time is determined by 7-30 MeV gamma ray.

its nominal thermal power, according to power data provided by EDF, while the other set contains data from all other times, typically when both reactors are running. All data end up in one of the two integration periods. Here, we denote the number of observed IBD candidates in each of the bins as N_i, where i runs over the combined 36 bins of both integration periods. The use of multiple periods of data integration takes advantage of the different signal/background ratios in each period, as the signal rate varies with reactor power while the backgrounds remain constant in time. This technique adds information about background behavior to the fit. The distribution of IBD candidates between the two integration periods is given in Table V.

A prediction of the observed number of signal and background events is constructed for each energy bin, following the same integration period division as the data:

$$N_i^{\rm pred} = \sum_{R=1,2}^{\rm Reactors} N_i^{\nu,R} + \sum_{b}^{\rm Bkgnds.} N_i^b \qquad (13)$$

where $N_i^{\nu,R} = P_(\bar{\nu}_e \to \bar{\nu}_e) N_i^{{\rm exp},R}$; $P_{\bar{\nu}_e \to \bar{\nu}_e}$ is the neutrino survival probability from the well-known oscillation formula and $N_i^{{\rm exp},R}$ is given by Equation 4. The index b runs over the three backgrounds: cosmogenic isotope; correlated; and accidental. The index R runs over the two reactors, Chooz B1 and B2.

Background populations were calculated based on the measured rates and the livetime of the detector during each integration period. Details on the signal prediction normalization can be found in Sec. III D. Predicted populations for both null-oscillation signal and backgrounds may be found in Table V.

Systematic and statistical uncertainties are propagated to the fit by the use of a covariance matrix M_{ij} in order to properly account for correlations between energy bins.

	Reactors Both On	**One Reactor $P_{th} < 20\%$**	**Total**
Livetime [days]	139.27	88.66	227.93
IBD Candidates	6088	2161	8249
ν Reactor B1	2910.9	774.6	3685.5
ν Reactor B2	3422.4	1331.7	4754.1
Cosmogenic Isotope	174.1	110.8	284.9
Correlated FN & SM	93.3	59.4	152.7
Accidentals	36.4	23.1	59.5
Total Prediction	6637.1	2299.7	8936.8

TABLE V. Summary of observed IBD candidates, with corresponding signal and background predictions for each integration period, before any oscillation fit results have been applied.

The sources of uncertainty A are listed in Table VI.

$$M_{ij} = M_{ij}^{\rm sig.} + M_{ij}^{\rm det.} + M_{ij}^{\rm stat.} + M_{ij}^{\rm eff.} + \sum_{b}^{\rm Bkgnds.} M_{ij}^{\rm b} \qquad (14)$$

Each term $M_{ij}^{\rm A} = {\rm cov}(N_i^{\rm pred}, N_j^{\rm pred})_A$ on the right-hand side of Equation 14 represents the covariance of $N_i^{\rm pred}$ and $N_j^{\rm pred}$ due to uncertainty A. The normalization uncertainty associated with each of the matrix contributions may be found from the sum of each matrix: these are summarized in Table VI. Many sources of uncertainty contain spectral shape components which do not directly contribute to the normalization error, but do provide for correlated uncertainties between the energy bins. The signal covariance matrix $M_{ij}^{\rm sig.}$ is calculated taking into account knowledge about the predicted neutrino spectra. The ^{9}Li matrix contribution contains spectral shape uncertainties estimated using different Monte Carlo event generation parameters, as described in Sec. III E. The slope of the FN/SM spectrum is allowed to vary from a nearly-flat spectrum following the measurements described in Section V D. Since accidental background uncertainties are measured to a high precision from many off-time windows, they are included as a diagonal covariance matrix.

The elements of the covariance matrix contributions are recalculated as a function of the oscillation and other parameters (see below) at each step of the minimization. This maintains the fractional systematic uncertainties as the bin populations vary from the changes in the oscillation and fit parameters.

A fit of the binned signal and background data to a two-neutrino oscillation hypothesis was performed by

Source	Uncertainty [%]
Reactor Flux	1.67%
Detector Response	0.32%
Statistics	1.06%
Efficiency	0.95%
Cosmogenic Isotope Background	1.38%
FN/SM	0.51%
Accidental Background	0.01%
Total	2.66%

TABLE VI. Summary of signal and background normalization uncertainties in this analysis relative to the total prediction.

minimizing a standard χ^2 function:

$$\chi^2 = \sum_{i,j}^{36} \left(N_i - N_i^{\rm pred}\right) \times (M_{ij})^{-1} \left(N_j - N_j^{\rm pred}\right)^{\rm T} + \frac{\left(\epsilon_{FN/SM} - 1\right)^2}{\sigma^2_{FN/SM}} + \frac{\left(\epsilon_{^9{\rm Li}} - 1\right)^2}{\sigma^2_{^9{\rm Li}}} + \frac{\left(\alpha_E - 1\right)^2}{\sigma^2_{\alpha_E}} + \frac{\left(\Delta m^2_{31} - \left(\Delta m^2_{31}\right)_{\rm MINOS}\right)^2}{\sigma^2_{\rm MINOS}} \quad (15)$$

The use of energy spectrum information in this analysis allows additional information on background rates to be gained from the fit, in particular because of the small number of IBD events between 8 and 12 MeV. The two fit parameters $\epsilon_{FN/SM}$ and $\epsilon_{^9{\rm Li}}$ are allowed to vary as part of the fit, and they scale the rates of the two backgrounds (correlated and cosmogenic isotope). The rate of accidentals is not allowed to vary since its initial uncertainty is precisely determined by the measurement method described in Sec. V B. The energy scale for predicted signal and ^{9}Li events is allowed to vary linearly according to the α_E parameter with an uncertainty $\sigma_{\alpha_E} = 1.13\%$. A final parameter constrains the mass splitting Δm^2_{31} using the MINOS measurement [60] of $\Delta m^2_{31} = (2.32 \pm 0.12) \times 10^{-3}$ eV^2, where we have symmetrized the error. This error includes the uncertainty introduced by relating the effective mass-squared difference observed in a ν_μ disappearance experiment to the one relevant for reactor experiments, and the ambiguity due to the type of the neutrino mass hierarchy, see e.g. [61]. Uncertainties for these parameters, $\sigma_{FN/SM}$, $\sigma_{^9Li}$, and $\sigma_{\rm MINOS}$, are listed as the initial values in Table VII.

The best-fit gives $\sin^2 2\theta_{13} = 0.109 \pm 0.030$ (stat.) $\pm$ 0.025 (syst) at $\Delta m^2_{31} = 2.32 \times 10^{-3}$ eV^2, with a χ^2/NDF = 42.1/35. We used the MINOS measured Δm^2_{31} value as a constraint for our θ_{13} measurement, but a two parameter fit without the MINOS Δm^2_{31} in the region $\Delta m^2_{31} < 0.01$ eV^2 gives a Δm^2_{31} value of $2.7 \pm 1.9 \times 10^{-3}$ eV^2, which is fully consistent with MINOS. The fit gives $\sin^2 2\theta_{13} = 0.093 \pm 0.078$ which is consistent with our fit for θ_{13} using MINOS.

Table VII gives the resulting values of the fit parameters and their uncertainties. Comparing the values with the ones used as input to the fit in Table V we conclude that the background rate and uncertainties are further constrained in the fit, as well as the energy scale.

The final measured spectrum and the best-fit spectrum are shown in Figure 14 for the new and old data sets, and for both together in Figure 15.

Fit Parameter	Initial Value	Best-Fit Value
^{9}Li Bkg. $\epsilon_{^9{\rm Li}}$	(1.25 $\pm$ 0.54) d^{-1}	(1.00 $\pm$ 0.29) d^{-1}
FN/SM Bkg. $\epsilon_{FN/SM}$	(0.67 $\pm$ 0.20) d^{-1}	(0.64 $\pm$ 0.13) d^{-1}
Energy Scale α_E	1.000 $\pm$ 0.011	0.986 $\pm$ 0.007
Δm^2_{31} (10^{-3} eV^2)	2.32 $\pm$ 0.12	2.32 $\pm$ 0.12

TABLE VII. Parameters in the oscillation fit. Initial values are determined by measurements of background rates or detector calibration data. Best-fit values are outputs of the minimization procedure.

An analysis comparing only the total observed number of IBD candidates in each integration period to the expectations produces a best-fit of $\sin^2 2\theta_{13} = 0.170 \pm 0.052$ at χ^2/NDF = 0.50/1. The compatibility probability for the rate-only and rate+shape measurements is about 30% depending on how the correlated errors are handled between the two measurements.

A re-processing of the data set used for the first Double Chooz publication [7] was performed using the current analysis techniques. A fit using only a single integration period yielded a best-fit value of $\sin^2 2\theta_{13} = 0.0744 \pm 0.046$ with χ^2/NDF = 18.3/17. An analysis of only the data taken since the first publication yielded a best-fit of $\sin^2 2\theta_{13} = 0.143 \pm 0.043$ with χ^2/NDF = 9.54/17. The data and best-fit spectra for each of these cases is shown in Figure 16.

Our predicted fission cross section is $5.723 \pm 0.096 \times 10^{-43}$ cm^2/fission using the Bugey4 anchoring measurement and corresponding to the values of α_k in Table I. The background subtracted reactor antineutrino event rate is 7751.9 events, corresponding to 91.85% of the rate expected in the absence of oscillations. Our measured fission cross section is 5.257 ± 0.056 (stat.) $\pm$ 0.105 (syst) $\times 10^{-43}$ cm^2/fission.

A further cross-check of the analysis was carried out by imposing cuts to eliminate the vast majority of the cosmogenic isotope background at the cost of reduced livetime. The best-fit case of this analysis was found at $\sin^2 2\theta_{13} = 0.109 \pm 0.044$ and $\Delta m^2_{31} = 2.32 \times 10^{-3}$ eV^2, in good agreement with the standard analysis.

Confidence intervals for the standard analysis were determined using a frequentist technique [62]. This approach accommodates the fact that the true χ^2 distributions may not be Gaussian and is useful for calculating the probability of excluding the no-oscillation hypothesis. This study compared the data to 10,000 simulations generated at each of 21 test points in the range $0 \leq \sin^2 2\theta_{13} \leq 0.25$. A $\Delta\chi^2$ statistic, equal to the difference between the χ^2 at the test point and the χ^2 at

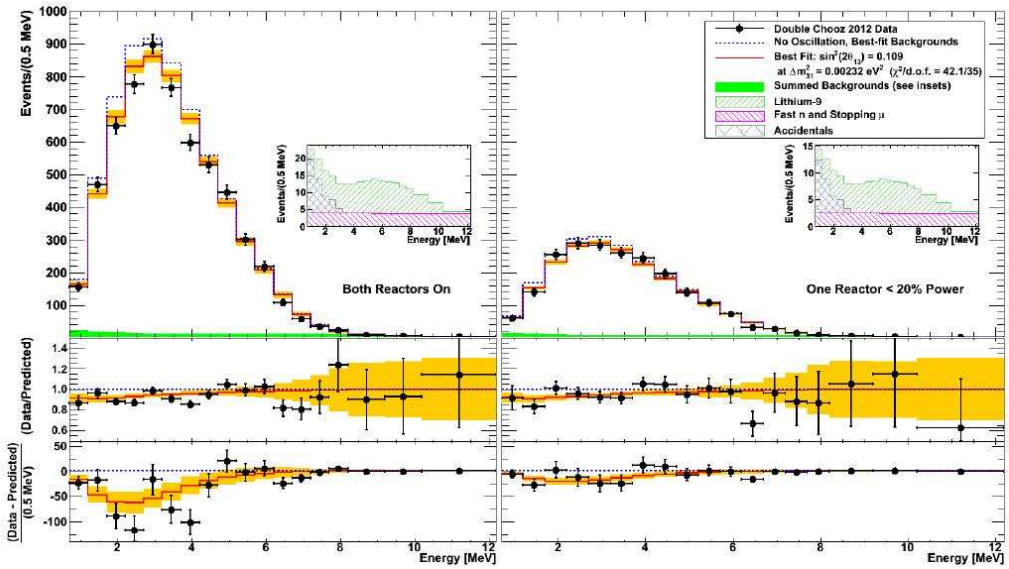

FIG. 14. Measured prompt energy spectrum for each integration period (data points) superimposed on the expected prompt energy spectrum, including backgrounds (green region), for the no-oscillation (blue dotted curve) and best-fit (red solid curve) at $\sin^2 2\theta_{13} = 0.109$ and $\Delta m^2_{31} = 2.32 \times 10^{-3}$ eV^2. Inset: stacked spectra of backgrounds. Bottom: differences between data and no-oscillation prediction (data points), and differences between best fit prediction and no-oscillation prediction (red curve). The orange band represents the systematic uncertainties on the best-fit prediction.

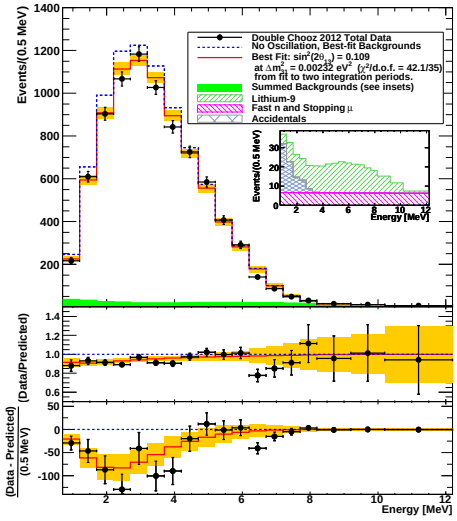

FIG. 15. Sum of both integration periods plotted in the same manner as Figure 14.

the best fit, was used to determine the region in $\sin^2 2\theta_{13}$ where the $\Delta\chi^2$ of the data was within the given confidence probability. The allowed region at 68% (90%) CL is $0.067\ (0.043) < \sin^2 2\theta_{13} < 0.15\ (0.18)$. An analogous technique shows that the data excludes the no-oscillation hypothesis at 99.8% (2.9σ).

VII. CONCLUSION

A comparison of this analysis result to other recent $\sin^2 2\theta_{13}$ measurements by other experiments is shown in Figure 17. The figure shows published results, though we note that new results from Daya Bay, MINOS and T2K have been shown at conferences but are not yet published [63]. The values for $\sin^2 2\theta_{13}$ from the various experiments are in excellent agreement with the results reported here. However this result is unique in its incorporation of energy dependence in the analysis.

Double Chooz has found evidence for a non-zero value of θ_{13} from the rate and energy spectrum of reactor neutrino candidates at a distance of 1050 m from two reactors. It is the first evidence for this parameter using the energy spectrum from reactor neutrinos, rather than simply their rate. We find a best fit value and 1σ error to be $\sin^2 2\theta_{13} = 0.109 \pm 0.030\ (\text{stat}) \pm 0.025\ (\text{syst})$. The data is inconsistent with the assumption that oscillations

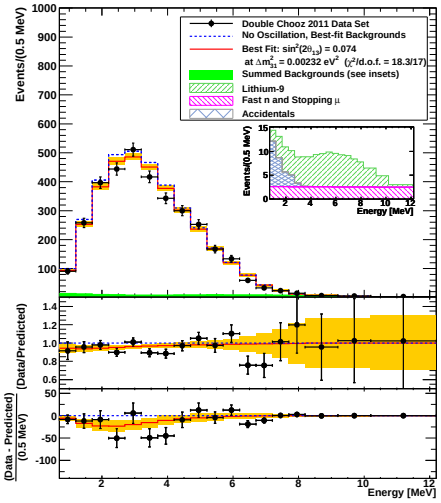

(a)First Publication Data Set

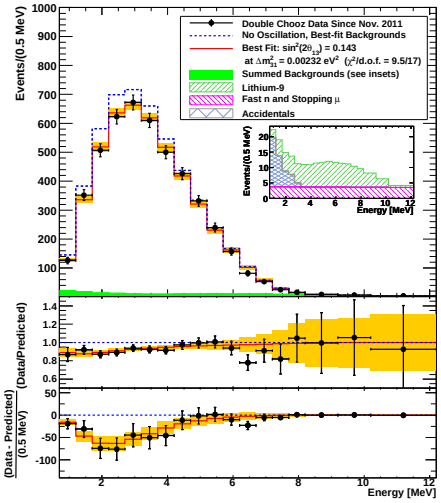

(b)Data Since First Publication

FIG. 16. Data and best-fit spectrum from applying current analysis techniques to the data set used to produce the first Double Chooz publication (a), and data taken since that publication (b), plotted in the same manner as Figure 14.

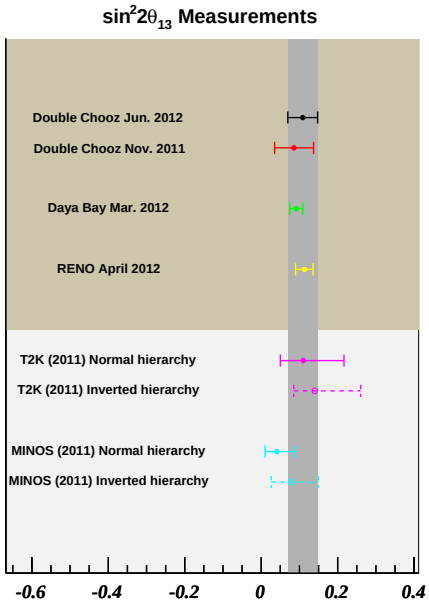

FIG. 17. Comparison of recent reactor- and accelerator-based measurements of $\sin^2 2\theta_{13}$ from this analysis, the first Double Chooz publication [7], Daya Bay [8], RENO [9], T2K [6], and MINOS [5]. Error bars correspond to 1σ. For T2K and MINOS the CP phase δ has been fixed (arbitrarily) to $\delta = 0$.

are absent with a CL of 99.8% CL (2.9σ).

We thank the French electricity company EDF, the European fund FEDER, the Région de Champagne Ardenne, the Département des Ardennes and the Communauté des Communes Rives de Meuse. We acknowledge the support of CEA and CNRS/IN2P3 in France, French LabEx UnivEarthS, Ministry of Education, Culture, Sports, Science and Technology of Japan (MEXT) and Japan Society for the Promotion of Science (JSPS), the Department of Energy and the National Science Foundation of the United States, the Ministerio de Ciencia e Innovación (MICINN) of Spain, the Max Planck Gesellschaft and the Deutsche Forschungsgemeinschaft DFG (SBH WI 2152), the Transregional Collaborative Research Center TR27, the Excellence Cluster "Origin and Structure of the Universe" and the Maier-Leibnitz-Laboratorium Garching, the Russian Academy of Science, the Kurchatov Institute and RFBR (the Russian Foundation for Basic Research), the Brazilian Ministry of Science, Technology and Innovation (MCTI), the Financiadora de Estudos e Projetos (FINEP), the Conselho Nacional de Desenvolvimento Científico e Tecnológico (CNPq), the São Paulo Research Foundation (FAPESP), the Brazilian Network for High Energy Physics (RENAFAE) in Brazil and the computer center CCIN2P3.

[1] M. Appolonio et al., Phys. Lett., B466, 415 (1999).
[2] G. L. Fogli, E. Lisi, A. Marrone, A. Palazzo and A. M. Rotunno, Phys. Rev. D84, 053007 (2011).
[3] The KamLAND Collaboration, Phys. Rev. D83, 052002 (2011).
[4] T. Schwetz et al., New J. Phys. 13, 109401 (2011).
[5] P. Adamson et al., Phys. Rev. Lett. 107, 181802 (2011).
[6] K. Abe et al., Phys. Rev. Lett. 107, 041801 (2011).
[7] Y. Abe et al., Phys. Rev. Lett. 108, 131801 (2012).
[8] F. P. An et al., Phys. Rev. Lett. 108, 171803 (2012).
[9] J. K. Ahn et al., Phys. Rev. Lett. 108, 191802 (2012).
[10] F. Ardellier et al., (Double Chooz Collaboration) (2006) hep-ex/0606025.
[11] T. Matsubara et al., Nucl. Instrum. Meth., A661, 16, 2011.
[12] C. Bauer et al., JINST, 6, P06008 (2011).
[13] E. Calvo et al., Nucl. Instrum. Meth., A621, 222 (2010).
[14] M. Fechner et al., Applied Radiation and Isotopes, 69(7), 1033 (2011).
[15] G. Heusser, M. Laubenstein, H. Neder, Radionuclides in the environment, Int. Conf. on Isotopes in Environmental Studies, edited by P. P. Povinec and J. A. Sanchez-Cabeza, Elsevier, Amsterdam 495 (2006).
[16] C. Aberle et al., JINST, 7, P06008 (2012).
[17] M. Hofmann, Ph.D. thesis, Technische Universität München (2012).
[18] Measured by A. Smith at the LBNL Low Background Facility with the MERLIN n-type HPGe detector.
[19] S. Abe et al., Phys. Rev. C81, 025807 (2010).
[20] M. Apollonio et al., Eur. Phys. J, C27, 331 (2003).
[21] C. Aberle, C. Buck, F.X. Hartmann and S. Schönert, Chem. Phys. Lett., 516, 257 (2011).
[22] http://jp.hamamatsu.com/resources/products/etd /pdf/LARGE_AREA_PMT_TPMH1286E05.pdf.
[23] F. Kaether and C. Langbrandtner, arXiv:1207.0378 (submitted to JINST).
[24] D. Dietrich et. al. "Monte Carlo aided design of the Inner Muon Veto detectors for the Double Chooz experiment" (2012), accepted for publication in JINST.
[25] K. Zbiri, arXiv:1104.4045 (2011).
[26] Max Perles et cie, http://www.maxperles.com/pdf /ftech_fr/ft_ar100clx_nov10.pdf (2012).
[27] F. Beissel et al., "The Trigger and Timing System of the Double Chooz Experiment" (submitted to JINST).
[28] A. Cabrera, Nucl. Instrum. Meth. Phys. Res., Sect. A 617, 473 (2010).
[29] T. Akiri, Ph.D. thesis, Universite Paris-Diderot, (2010).
[30] CAEN Corporation, http://www.caen.it/. The device was co-developed with APC.
[31] P. Barrillon et al., MAROC: Multi-Anode ReadOut Chip for MAPMTs, proceedings of 2007 IEEE conference (2007), P. Barrillon et al., 64-channel Front-End readout chip, MAROC2 datasheet, http://omega.in2p3.fr/.
[32] E. Tournu et al., EDF TechnicalNote (2001).
[33] Standard AFNOR XP X 07-020 (1996).
[34] Y. Caffari, J.M. Favennec, EDF tech-note H-P1C-2011-02007-FR.
[35] Z. Djurcic et al., J. Phys. G36, 045002 (2009).
[36] K. Schreckenbach, G. Colvin, and F. von Feilitzsch, Phys. Lett. 160B, 325 (1985).
[37] F. von Feilitzsch and K. Schreckenbach, Phys. Lett. 118B, 162 (1982).
[38] A. Hahn et al., Phys. Lett. B 218, 365 (1989).
[39] T. Mueller et al., Phys. Rev. C83, 054615 (2011).
[40] P. Huber, Phys. Rev. C84, 024617 (2011).
[41] G. Mention et al., Phys. Rev. D83, 073006 (2011).
[42] O. Meplan et al., in ENC 2005: European Nuclear Conference; Nuclear power for the XXIst century: from basic research to high-tech industry (2005).
[43] NEA-1845/01, documentation for MURE (2009).
[44] G. Marleau et al., Report IGE-157 (1994).
[45] C. Jones, "Prediction of the Reactor Antineutrino Flux for the Double Chooz Experiment", Ph.D. thesis, MIT (2012).
[46] C. Jones et al., arXiv:1109.5379v1 (2011).
[47] V. Kopeikin, L. Mikaelyan, and V. Sinev, Phys. At. Nucl. 67, 1892 (2004).
[48] Y. Declais et al., Phys. Lett. B338, 383 (1994).
[49] P. Vogel and J. F. Beacom, Phys. Rev. D60, 053003 (1999).
[50] A. Pichlmaier et al., Phys. Lett. B693, 221 (2010).
[51] J. Allison et al., IEEE Trans. Nucl. Sci. 53 No. 1, 270 (2006), S. Agostinelli et al., Nucl. Instrum. Meth. A506, 250 (2003).
[52] J. Apostolakis et al., "Geant4 Physics Lists for HEP," Nuclear Science Symposium Conference Record, IEEE, 833 (2008).
[53] J.B. Birks, Proc. Phys. Soc. A64, 874 (1951); 64, 511 (1951).
[54] D. Motta and S. Schönert, Nucl. Instrum. Meth. A539, (2005) 217.
[55] D. R. Tilley et al., Nucl. Phys. A745, 155 (2004), Y. Prezado, et al., Physics Letters B618, 43.50 (2005), P. Papka, et al., Phys. Rev. C 75, 045803 (2007).
[56] http://www.chem.agilent.com/en-US/Products/instruments/molecularspectroscopy/fluorescence/systems/caryeclipse/pages/default.aspx.
[57] C. Aberle, C. Buck, F.X. Hartmann, S. Schönert and S. Wagner, JINST 6, P11006 (2011).
[58] C. Aberle, Ph.D. thesis, Universität Heidelberg (2011).
[59] Y. Abe et al., in preparation.
[60] P. Adamson et al., Phys. Rev. Lett. 106, 181801 (2011).
[61] H. Nunokawa, S. Parke and R.Z. Funchal, Phys. Rev. D72, 013009 (2005).
[62] G.J. Feldman and R.D. Cousins, Phys. Rev. D57, 3873 (1998).
[63] Proceedings of the XXXV International Conference on Neutrino Physics and Astrophysics, June 3-9, 2012, Kyoto, Japan, to be published.